

Current-induced magnetization switching in a model epitaxial Fe/Au bilayer

Der Fakultät für Physik
der Universität Duisburg-Essen
zur Erlangung des akademischen Grades eines
Doktors der Naturwissenschaften
(Dr. rer. nat.)
vorgelegte Dissertation von

Pika Gospodarič
geb. in Ljubljana (Slowenien)

Gutachter: Prof. Dr. Claus M. Schneider (Universität Duisburg-Essen)
Gutachter: Prof. Dr. Jürgen Fassbender (Technische Universität Dresden)

Tag der mündlichen Prüfung: 14.06.2019

DuEPublico

Duisburg-Essen Publications online

UNIVERSITÄT
DUISBURG
ESSEN

Offen im Denken

ub | universitäts
bibliothek

Diese Dissertation wird über DuEPublico, dem Dokumenten- und Publikationsserver der Universität Duisburg-Essen, zur Verfügung gestellt und liegt auch als Print-Version vor.

DOI: 10.17185/duepublico/70573

URN: urn:nbn:de:hbz:464-20191017-094636-0

Alle Rechte vorbehalten.

Zusammenfassung

Die Verwendung neuartiger spintronischer Speicherkomponenten ist eine Möglichkeit, die Energie- und Leistungseffizienz datenverarbeitender Geräte in Zukunft weiter zu verbessern. Als vielversprechender Schreibmechanismus in einem spintronischen Speicher gilt das rein-elektrische Umschalten einer Magnetisierung induziert durch ein Spin-Bahn-Drehmoment (engl. Spin-orbit torque). Solche Spin-Bahn-Drehmomente können u.a. an Grenzoberflächen von Doppelschichten aus Schwermetallen und ferromagnetischen Metallen beobachtet werden.

Die vorliegende Arbeit ist eine Studie über das epitaktisch gewachsene Modellsystem aus dem Schwermetall Gold (Au) und dem Ferromagneten Eisen (Fe), welches mittels Magnetotransportmessungen und Kerr-Mikroskopie charakterisiert wurde. Zur Untersuchung der magnetischen und magnetoelektronischen Eigenschaften des Systems wurden die Au/Fe Doppelschichten, Au(4 nm)/Fe(1-1.5 nm)/MgO(001), mittels Fotolithographie in Hall-Barren strukturiert. Die Magnetotransportmessungen an den Hall-Barren zeigen, dass die Au/Fe-Doppelschicht zwei leichte Magnetisierungsachsen mit kubischer Anisotropie in der Filmebene besitzt, welche primär auf die magnetokristalline Anisotropie des Fe(001) Films zurückzuführen sind. In der gewählten Probengeometrie stimmen die leichten Magnetisierungsrichtungen mit den Extremwerten der transversalen Spannung überein, welche durch den planaren Hall-Effekt (PHE) induziert wird. Aufgrund dieser Koinkidenz zwischen Magnetisierungsrichtung und PHE-Spannung kann eine Reorientierung der Magnetisierung elektrisch detektiert werden. Anhand von optischer Kerr-Mikroskopie konnte die Bildung von streifenförmigen magnetischen Domänen mit 90°-Domänenwänden senkrecht zur langen Achse der Hall-Barren beobachtet werden. Durch den direkten Vergleich von der Transportmessungen und Kerr-Aufnahmen konnte weiterhin gezeigt werden, dass die Domänenkonfiguration im zentralen Bereich des Hall-Kreuzes einen maßgeblichen Einfluss auf die gemessene PHE-Spannung hat.

Basierend auf den gewonnenen Erkenntnissen wurde in einem weiteren Schritt der Einfluss elektrischer Ströme auf die Magnetisierung der Fe(001)-Schicht mittels kombinierter PHE-Messungen und Kerr-Mikroskopie systematisch untersucht: Bei Raumtemperatur induziert eine Stromdichte jenseits von 10^7 A/cm^2 ein Oersted-Feld, welches das Koerzitivfeld $B_c = 0.65 \pm 0.05 \text{ mT}$ in der Filmebene der Fe(001)-Schicht übersteigt und zu einer Reorientierung der Magnetisierung um 90° führt. Darüber hinaus kann eine Stromdichte von mehr als $1.4 \cdot 10^7 \text{ A/cm}^2$ mit wechselnder Polarität für ein reproduzierbares Schalten der Magnetisierung zwischen mehreren stabilen Zuständen verwendet werden. Die Ergebnisse der Kerr-Mikroskopie bestätigen, dass eine Variation der angelegten Stromdichte die Domänenkonfiguration am Hall-Kreuz verändert. Diese Änderungen in der Domänenkonfiguration können als Änderungen der PHE-Spannung detektiert werden und skalieren mit dem angelegten Strom. Transportmessungen bei $T < 50 \text{ K}$ zeigen das Vorhandensein eines zusätzlichen strominduzierten Feldes von bis zu 2.5 mT senkrecht zur Filmoberfläche.

Abstract

In electronics, the application of novel spintronic three-terminal memory devices is proposed to facilitate further improvements of the performance of electronic components. A promising write-mechanism in a spintronic memory is based on the purely electrical switching of the magnetization by *spin-orbit torque* (SOT) that can occur, for example, at the interface of heavy metal (HM)/ferromagnetic metal (FM) bilayers.

This thesis presents a study of the epitaxial model HM/FM system Au(4 nm)/Fe(1-1.5 nm)/MgO(001) using magneto-transport measurements and Kerr microscopy. The Au/Fe bilayers were photolithographically patterned into Hall bars in order to study their magnetic and magneto-transport properties. The Au/Fe bilayer Hall bars on MgO(001) substrate exhibit a strong in-plane easy magnetization axis and a cubic magnetic anisotropy in the film plane dominated by the magneto-crystalline term of the Fe(001) layer. In the chosen geometry of the samples the easy magnetization directions coincide with the extrema of the transversal voltage induced by the planar Hall effect (PHE). Therefore, a switching of the magnetization from one easy direction to another can be detected by measuring the PHE-voltage. Furthermore, Kerr microscopy revealed the formation of stripe-shaped magnetic domains separated by 90° domain walls aligned perpendicular to the Hall bar. A combined measurement of PHE-voltage and acquisition of Kerr images has shown that the measured PHE-voltage is most considerably affected by the domain configuration within the central area of the Hall cross.

Based on this findings, the influence of electrical currents on the magnetization in the Fe(001) layer was investigated via measurements of the PHE combined with Kerr microscopy. At room temperature, a current density beyond 10^7 A/cm² induces an Oersted field, which in the Fe(001) layer points in-plane in the direction perpendicular to the long axis of the Hall bar and can exceed the coercive field $B_c=0.65\pm 0.05$ mT for the 90° switch of the magnetization. Moreover, a current density beyond $1.4\cdot 10^7$ A/cm² with an alternating polarity can be employed for reproducible electrical switching of the magnetization in the Au/Fe/MgO(001) Hall bars between multiple stable states. Kerr microscopy confirmed that a variation of the applied current density changes the domain structure at the Hall bar cross. The change of the domain structure scales with the applied current density and can be read-out as a change in the PHE-voltage. The PHE measurements at $T<50$ K indicate a presence of an additional current-induced field up to 2.5 mT in the direction normal to the film surface.

Contents

1	Introduction	1
2	Theoretical background	4
2.1	Magnetism in 3d transition metals	4
2.1.1	Fundamentals of magnetism	4
2.1.2	Itinerant ferromagnetism	5
2.1.3	Magnetism in reduced dimensions	7
2.2	Magnetic anisotropy	9
2.2.1	Shape anisotropy	10
2.2.2	Magneto-crystalline anisotropy	10
2.2.3	Magneto-elastic anisotropy	12
2.2.4	Surface and interface anisotropy	12
2.3	Magnetic domains	13
2.4	Electrical transport in transition metal ferromagnets	15
2.4.1	Anisotropic magneto-resistance (AMR)	17
2.4.2	Planar Hall effect (PHE)	20
2.4.3	Anomalous Hall effect (AHE)	21
2.5	Current-induced magnetization switching in magnetic multilayers	22
2.5.1	Current-induced Oersted field in bilayers	23
2.5.2	Spin-orbit torques	24
3	The Au/Fe/MgO sample system	29
3.1	Review of literature	29
3.2	Growth characterization using surface analysis techniques	31
3.2.1	Microscopic study of Fe/Au(001) growth	31
3.2.2	Epitaxial growth of Fe and Au on MgO(001)	34
4	Experimental methods for magnetic characterization	40
4.1	Fabrication of Hall bars	40
4.2	Magneto-transport measurements	41
4.3	Kerr microscopy	43
4.3.1	Magneto-optical Kerr effect (MOKE)	43
4.3.2	Kerr microscopy experimental setup	45
5	Magnetic properties of Au/Fe/MgO(001)	50
5.1	Magnetic hysteresis in Kerr microscopy	50
5.2	Anomalous Hall effect characterization	56

5.2.1	Contributions to the magnetic anisotropy	58
5.3	In-plane magnetic anisotropy investigated via the planar Hall effect	61
5.3.1	Magnetic torque analysis of the in-plane anisotropy	65
5.4	Magnetic domain structure	69
5.4.1	Magnetic domains in Au/Fe(1.5 nm) Hall bars	69
5.4.2	Magnetic domains in Au/Fe(1.3 nm) Hall bars	74
5.4.3	Domain structure and the planar Hall effect	75
6	Magnetization switching in Au/Fe/MgO(001) by applied current density	81
6.1	Asymmetry of the high-current PHE hysteresis loops	82
6.1.1	Comparison to Stoner-Wohlfarth simulations	84
6.1.2	Dependence on the direction of the external magnetic field	88
6.1.3	Temperature dependence of the current-induced left-right asymmetry	89
6.1.4	Indication of a current-induced out-of-plane field	92
6.2	Characterization of the current-induced field in Kerr microscopy	97
6.3	Current-driven magnetization reorientation	105
6.4	Reversible magnetization switching with high current density	110
7	Summary and Outlook	117
	Appendix	I
	Appendix: Simulations of the magnetic potential energy	I
A	Stoner-Wohlfarth equation	I
B	Anomalous Hall effect hysteresis simulation	II
C	Planar Hall effect hysteresis simulation	IV
C.1	Current-induced in-plane field	VIII
C.2	Current-induced out-of-plane field	IX
	Bibliography	XIII
	Publications and Conference Contributions	XXXI
	Curriculum Vitae	XXXV
	Acknowledgements	XXXVII

1. Introduction

Life in the 21st century has become almost unimaginable without electronic devices. Their influence on our everyday life has been rapidly increasing since the late 1970's, when the first home computers became available (and affordable) for households. This milestone was a consequence of the accelerated development of integrated circuits, which was anticipated by Gordon E. Moore [1] already in 1965. His prediction is today known as Moore's law and foresees doubling of the number of transistors per integrated circuit approximately every second year, which is due to the continuous reduction of the components' size.

While the Moore's law has provided a guideline for the "road map" planned by the international semiconductor industry over the last three decades [2], the integrated circuits with Si-based complementary metal-oxide-semiconductor (CMOS) transistors are facing several challenges as the feature size approaches the quantum-effects limit. Some of the issues, which lead to a high power consumption with the large number of transistors on the chips (in billions), and to increased heating due to high current densities in the nm-sized interconnections are yet to be resolved [2, 3]. The new goals of the semiconductor industry set by the International Roadmap for Devices and Systems (IRDS) point to the solutions beyond the miniaturization of the feature size of integrated circuits [2, 4]. Not only new materials, but also completely new approaches are being actively developed in order to be applied in addition to the CMOS technology, such as quantum computing or neuromorphic computing.

A promising field of research offering a suitable new technology for electronic devices is *spintronics* [5]. The discovery of the *giant magneto-resistance (GMR)* in 1988 [6, 7] is often viewed as the cornerstone of the field. The main idea of spintronics is to consider the electron's additional degree of freedom, namely its spin, in electronic transport, and to develop new spin-based electronic components. The research on GMR has led to important further developments in spin-based electronics, such as tunneling magneto-resistance (TMR) [8–13] and the spin-transfer torque (STT) [14–17]. Based on these phenomena, a non-volatile, i.e. not requiring power to store information, magnetoresistive random-access memory (MRAM) has been developed [18, 19].

One of the proposed geometries for the novel spintronics-based memory devices includes three terminals, allowing to separate the channels for information writing and reading. While the read-out of data would be based on the TMR, writing of information can be based on one of the proposed in-plane current-induced magnetization switching mechanisms [5]: Oersted-field, STT or the recently discovered spin-orbit torque (SOT) [20, 21]. The latter has been extensively studied in multi-layered structures containing usually a layer of a ferromagnetic metal, sandwiched between a layer of a heavy metal and an insulating layer.

Interestingly, experimental work on such multi-layered systems showed that via

current-induced switching mechanisms multiple stable states of the ferromagnetic layer can be induced by applying a varying current density [5,22]. Such an analog-like response of magnetization to electric current may find applications in multi-level, non-volatile electronic memories. Moreover, the analog-like memory behavior mimics some functionalities of the synapses in the brain. Therefore, the current-driven switching devices have been proposed for potential *neuromorphic* applications [23,24]. In fact, Torrejon *et al.* [25] have demonstrated that a single spin-torque nano-oscillator (two ferromagnetic metal layers separated by a non-magnetic spacer) can perform recognition of a spoken vocal, a typical function of a neural network. When coupled to each other, a network of spintronic devices has prospects of application in bio-inspired (neuromorphic) computation [23–25].

Current-induced magnetization switching via SOT has been demonstrated in heterostructures of different material combinations [26]. The quality of the interface to the layer of magnetic material may have an influence on the efficiency of SOTs [26,27]. The interface between the GaAs(001) substrate and an epitaxial Fe thin film of high crystalline quality was shown to suffice for generation of interfacial SOT at room temperature [28], which could be employed for manipulation of the magnetization in the Fe layer. A single-crystalline bilayer system prepared in-situ can be studied using surface sensitive techniques, as for example angle-resolved photoemission spectroscopy (ARPES), in order to investigate the band-structure origin of SOT. Moreover, the magneto-crystalline anisotropy arising from the crystallinity of a magnetic film may lead to distinctive crystallographic axes, along which the magnetization can be remanently saturated, while the anisotropy fields present in a crystalline film may assist the current-induced torques to switch the magnetization even in the absence of external magnetic fields.

Single-crystalline Fe(001) thin films exhibit a well-defined four-fold magnetic anisotropy leading to two in-plane easy magnetization axes already at only a few monolayers thickness [29]. In a Hall bar geometry the in-plane orientation of the magnetization in the Fe layer can be confirmed by measuring the transversal voltage induced by the planar Hall effect (PHE). The four easy magnetization directions result in only two distinguishable PHE voltages in a *flat* Fe(001) film. Yoo *et al.* have shown that four different PHE levels can be achieved by growing Fe on a vicinal surface of GaAs single crystal [30,31]. However, varying PHE values are obtained also for different domain configurations in the Fe layer [32]. An Oersted field generated by a current through a micrometer-sized Au wire fabricated on top of the Fe(001) Hall bar was used to manipulate the domain configuration in the Hall cross region [22]. The Au wire was rotated by 45° with respect to the Fe wire and was separated from it with an insulating spacer. However, the domain configuration responsible for the intermediate PHE levels of Fe(001) has not been shown by the authors of Ref. [22] as well as the current-induced torques originating from a Au/Fe bilayer have, to our best knowledge, not been reported thus far.

The scope of this work is to study current-induced magnetization reorientation in a well-defined model epitaxial system containing a single-crystalline ferromagnetic metal

layer. In this study, the system of choice is an Fe layer with a thickness just above a nm, grown epitaxially on an insulating MgO(001) single crystal and capped with a Au layer. The crystal structures of these three materials have a small lattice mismatch and therefore epitaxial and single-crystalline films can be grown by molecular beam epitaxy (MBE). This work presents a study of the Au/Fe/MgO(001) system combining magneto-transport measurements and Kerr microscopy to investigate the manipulation of the magnetization in the Fe(001) layer induced by an in-plane current. The study emphasizes the importance of the PHE read-out principle for metallic bilayer systems with in-plane magnetization and elucidates the potential of the formation of domains in the magnetic layer as a mechanism of analog-like response of the magnetic system to the applied in-plane current.

The thesis is organized as follows:

Chapter 2 gives a short account of the theoretical background of magnetism in thin magnetic films as well as the theory of the electronic transport in transition metal ferromagnets based on the semiclassical picture. This is followed by an introduction to the current-induced magnetization switching in metallic heterostructures.

Chapter 3 reviews the previously reported properties of the Au/Fe/MgO(001) system and discusses the characteristics of its growth.

Chapter 4 introduces the main experimental methods of this work: magneto-transport measurements and Kerr microscopy. The photolithography of Hall bars is briefly described.

Chapter 5 presents the characterization of magnetic properties of Au/Fe/MgO(001) Hall bars. It begins with a Kerr microscopy analysis of magnetic anisotropy (Sec. 5.1). Magneto-transport measurements show a purely in-plane easy magnetization axis (Sec. 5.2) and a four-fold magneto-crystalline anisotropy in the film plane (Sec. 5.3). The domain structure in the Hall bars, its dependence on the Fe layer thickness and its influence on the measured PHE voltage is shown in Sec. 5.4.

Chapter 6 assigns the current-induced asymmetry in the PHE hysteresis loops to the Oersted field and discusses a possible indication of the increased spin Hall effect (SHE) in the Au layer at low temperatures (Sec. 6.1). The current-induced Oersted field is confirmed by transport-measurements combined with Kerr microscopy of the Hall bars (Sec. 6.2). Current-induced manipulation of the domain structure at the Hall cross is shown with current-driven hysteresis loops (Sec. 6.3) and by switching the system between multiple stable magnetic states using pulses of current density beyond $1 \cdot 10^7$ A/cm² (Sec. 6.4).

Chapter 7 summarizes the experimental results and observations and closes with the discussion of possible future experiments.

2. Theoretical background

The present chapter provides an overview of the basic theoretical concepts underlying the experimental results presented in this thesis. In particular, the theory of magnetism in 3d transition metals is introduced with an emphasis on the magnetic anisotropy and magnetic domains in thin films. Further, the magneto-resistance effects are discussed, which were used in the present work for investigations of magnetic properties and current-induced effects on the magnetization in magnetic multilayers. Finally, different mechanisms of current-induced magnetization switching using an in-plane current in magnetic heterostructures are introduced.

2.1 Magnetism in 3d transition metals

2.1.1 Fundamentals of magnetism

The theory of magnetism is based on the concept of spin, which is a characteristic property of an electron. At the single-atom level, the electrons arrange around the nucleus by filling the energy levels, i.e. orbitals. In general, the orbital filling follows the Hund's rules; the levels are filled starting with the lowest energy orbitals and each two electrons must acquire a different set of quantum numbers or must have the opposite spin (Pauli's exclusion principle). If an energy level is not fully filled and some of the electrons in this level have no pair with the opposite spin, the unpaired spins contribute to the overall magnetic moment of the atom.

If atoms with a magnetic moment build a magnetic solid, then this material exhibits a *magnetization* \vec{M} which is the magnetic moment of the solid per unit volume [33]. In an external magnetic field \vec{H} (which can be produced by electric currents or by permanent magnets) the magnetization \vec{M} of the solid and \vec{H} will be related as

$$\vec{B} = \mu_0(\vec{H} + \vec{M}), \quad (2.1)$$

where $\mu_0=4\pi\cdot 10^{-7}$ Vs/Am is the *permeability of vacuum* and \vec{B} is *magnetic induction* (often referred to as *magnetic field* since it stands for a magnetic field measured in a medium in units of tesla (T) [33]). The standard unit for magnetic field H and magnetization M is A/m. In *paramagnetic* and *diamagnetic* materials the magnetization depends linearly on the magnetic field \vec{H} with the *magnetic susceptibility* χ

$$\vec{M} = \chi\vec{H}. \quad (2.2)$$

Therefore, the magnetization \vec{M} in paramagnets and diamagnets is zero when the external field \vec{H} is zero.

However, in *ferromagnets*, the magnetization is finite even in the absence of a magnetic field at temperatures below a critical value called the Curie temperature T_C . The ferromagnets are conventionally classified into *itinerant* and *localized* ferromagnets. However, ferromagnetic materials in general show aspects of both regimes [34]. The origin of ferromagnetism in both regimes is the *exchange interaction*, which is a quantum-mechanical effect and it manifests itself differently in the two classes of ferromagnets.

In a crystal, the atomic orbitals of neighboring atoms hybridize. Depending on the atomic character, which can be assigned to the hybridized orbitals (also known as *bands*) the electrons may be either fixed at the locations of the atoms in the crystal or *delocalized* to the extent that they travel as nearly free electrons through the periodic potential of the atoms [33]. The latter, also known as the *itinerant* electrons, are the delocalized valence electrons in metals and are mainly responsible for ferromagnetism in the 3d-transition metals. Itinerant electrons may be thought of as electrons occupying the very last energy levels and participate also in transport, bonding and hybridization. In contrast, localized electrons, which occupy lower energy levels, are more tightly bound to the location of the atoms and are only weakly interacting. They can be described as a periodic lattice of individual spins and mostly explain ferromagnetism in e.g. rare earth metals with 4f- and 5f-unpaired electrons.

In the following, the *itinerant ferromagnetism* of the 3d-transition metals will be briefly reviewed, as an Fe layer in the studied system is of main interest in this work.

2.1.2 Itinerant ferromagnetism

In a simplified approximation (Sommerfeld model), the strongly delocalized conduction electrons in metals are assumed to move as free electrons not influenced by the periodic potential of the lattice. In this *free-electron* model, the atomic lattice is neglected, and the energy levels which can be occupied by the itinerant electrons are given by [35]

$$E(n_x, n_y, n_z) = \frac{\pi^2 \hbar^2}{2m_e L^3} (n_x^2 + n_y^2 + n_z^2), \quad (2.3)$$

which are the solutions of the commonly known *particle in the box problem*. In Eq. 2.3, m_e is the electron mass, L^3 is the volume of the material and n_i are integers defining a set of quantum numbers with the corresponding wave vector \vec{k}

$$\vec{k} = \frac{2\pi}{L} (n_x \hat{e}_x + n_y \hat{e}_y + n_z \hat{e}_z). \quad (2.4)$$

For a macroscopic system ($L \rightarrow \infty$) the wave vectors \vec{k} with the energy E_k become a continuum of states and the electrons in the volume L^3 fill this continuum up to the *Fermi*

energy E_F

$$E_F = \frac{\hbar^2 k_F^2}{2m_e}. \quad (2.5)$$

The Fermi energy depends on the density of electrons in the volume $n = N/L^3$, where N is the number of electrons. It can be derived that

$$k_F^3 = 3\pi^2 n. \quad (2.6)$$

A measure determining many properties of the material (e.g. the conductivity, optical and magnetic properties) is the density of states (DOS) at the Fermi energy. It can be derived that in the *free electron model* the DOS at the Fermi level g_{E_F} is

$$g_{E_F} = \left. \frac{dn}{dE} \right|_{E_F} = \frac{3}{2} \frac{n}{E_F}. \quad (2.7)$$

The *Pauli exclusion principle* states that no two electrons can have the same set of quantum numbers. Therefore, in a many-electron system, the electrons have to occupy different energy levels or have to have the opposite spin to fulfill the Pauli principle. In a non-magnetic metal the electronic bands are occupied by electrons with both spin states, spin up (\uparrow) and spin down (\downarrow), in equal numbers. In an external magnetic field, a certain amount of electrons aligns their spin to the external field (Pauli paramagnetism) [36].

In a ferromagnetic metal (FM) an intrinsic deficit of one of the spin states is found ($n_\uparrow \neq n_\downarrow$) leading to a finite magnetization $\vec{M} = \mu_B(n_\uparrow - n_\downarrow)$ of the system even in the absence of an external magnetic field. For this to happen, the total energy of the many-electron system, containing same-spin electrons with different \vec{k} values, has to have a lower energy compared to the state with all \vec{k} -states doubly-occupied, i.e. \uparrow and \downarrow spins per each \vec{k} -state. This condition is known as the *Stoner criterion*, which states that ferromagnetism is observed when

$$I \cdot g_{E_F} > 1. \quad (2.8)$$

Here, the parameter I is the Stoner parameter arising from the exchange interaction between electrons. The Stoner criterion in Eq. 2.8 states that the energy gain due to the larger number of occupied \vec{k} states must be overcompensated by the energy loss due to reduced electrostatic repulsion between the same spin electrons [34].

If the Stoner criterion is fulfilled, a ferromagnetic state of the system is stable and the spin \uparrow states occupy different energy levels as compared to the spin \downarrow states. In the Stoner model this difference in the energy of \uparrow and \downarrow spin states can be visualized as an energy shift Δ between the corresponding spin- \uparrow DOS and spin- \downarrow DOS, see Fig. 2.1. The energy splitting Δ is known as the *Stoner exchange energy* and is proportional to

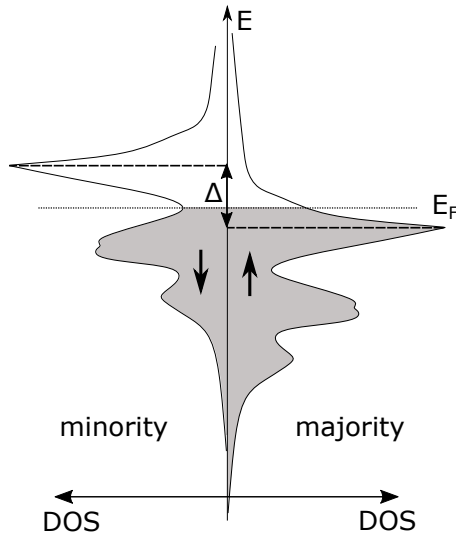


Figure 2.1: Exemplary *spontaneously-split* band structure of body-centered cubic (BCC)-Fe [37] for up spins \uparrow and down spins \downarrow . Due to the splitting (for exchange energy Δ) the Fermi energy E_F cuts the density of states (DOS) for each spin at different level, the down spins \downarrow are in deficit (minority spin) and the spin up \uparrow is the majority spin character.

I^1 . The Stoner criterion is met for the 3d transition metals Fe, Co and Ni, which are therefore ferromagnets at room temperature ($\Delta \sim 1$ eV). The prevailing itinerant regime of magnetism in these materials explains the non-integer value of their magnetic moment per atom ($2.2\mu_B$ for Fe), which reflects the hopping of the itinerant electrons between the atoms of the solid [36]. Ferromagnetism is observed also in alloys containing the three typical 3d FMs.

The Stoner model relates ferromagnetism to the DOS at the Fermi energy g_{E_F} , which is strongly dependent on the crystal structure². Moreover, the g_{E_F} at surfaces and in ultra-thin films is affected by the reduced number of the nearest neighbors. This can lead to changes of the magnetic properties as compared to the bulk. These effects will be addressed in the following section.

2.1.3 Magnetism in reduced dimensions

The research in the field of thin-film magnetism has been motivated by theoretical predictions about the characteristics of the magnetism in the ultra-thin regime (i.e. 2D magnetism), which differs from the 3D bulk magnetism [33]. In most cases, the reason for changed magnetic properties is the fact that in an ultra-thin film most of the atoms

¹In the Stoner model the exchange energy is the difference in energy before and after a single electron flips its spin in the field of all other electrons in the system [38].

²Change of the crystal structure of the material can change its magnetic properties. For example, BCC-Fe at ambient conditions is ferromagnetic, however at high temperatures and pressures a paramagnetic face-centered cubic (FCC)-Fe can be obtained.

are located at the surface. Atoms at the surface have less nearest neighboring atoms, i.e. lower coordination number, compared to the ones in the bulk. This translates into narrower width of the bands close to the Fermi level in the electronic structure and leads to an increase of the DOS g_{E_F} at the Fermi energy [33, 39]. Following from Eq. 2.8, increased g_{E_F} gives better chances for the Stoner criterion to be fulfilled and thus, more of the 3d transition metals are predicted to be ferromagnetic in the monolayer (ML) regime. It follows also that the magnetic moment of the typical transition metals, as well as for 4d and 5d metals is increased when grown as a single atomic layer (ML) [33, 38, 39].

The study of magnetic thin films became possible in the 1970's by the molecular beam epitaxy (MBE) deposition technique [40], which allows in-situ growth of films with high crystalline quality. Using MBE, ultra-thin films can be grown with a thickness down to a ML or multilayered structures can be prepared, in which materials with different properties can be “sandwiched” together. This technique thus enables one to tailor the magnetic properties of a material system.

The experimental studies of thin-film heterostructures revealed several coupling mechanisms and proximity effects at the interfaces. In heterostructures the hybridization of the d-states of the magnetic layer with the conduction bands of the non-magnetic layer can induce a magnetic moment from the ferromagnetic metal (FM) into the non-magnetic layer via the exchange interaction (*proximity effect*) [41]. The exchange coupling was also observed at the interface between a ferromagnet and an antiferromagnet, which results in an *exchange bias* field and is typically experimentally observed as an unidirectional shift in the magnetic hysteresis loop [42]. Of particular importance is the *interlayer exchange coupling*, which was reported first in Fe/Cr/Fe trilayers [43]. The Fe layers separated by Cr exhibit an antiferromagnetic arrangement for certain thicknesses of the Cr layer [43], which is related to the spin-dependent scattering of the conduction electrons at the interface between the FM and the non-magnetic metal. The interlayer exchange coupling led to the discovery of the giant magneto-resistance (GMR) [6, 7], which found applications in many devices, such as read heads in the hard disk drive (HDD) and information storage in the magnetoresistive random-access memories (MRAM-s). Albert Fert and Peter Grünberg were awarded the Nobel price for the discovery of GMR in 2007.

Another important aspect of the magnetic properties of thin films grown by MBE is the selection of a suitable substrate. By choosing different substrate materials, the MBE grown thin films on top can be driven into different crystallographic phases, i.e. *metastable phases*, which have a different crystal lattice compared to the bulk and may thus exhibit changed magnetic properties [33]. The driving mechanism for the altered crystal structure of the film is the mismatch-strain at the interface to the substrate. The mismatch strain is minimized by reducing the misfit of the crystal lattices of the substrate and the film in their symmetries and lattice parameters.

Furthermore, the reduced dimensions and the interface/surface effects can modify magnetic anisotropy of the thin film. In fact, in absence of magnetic anisotropies a long-range

ferromagnetic order is not stable in one- or two-dimensional spin system at a finite temperature according to the Mermin-Wagner theorem [44]. Magnetic anisotropy in thin magnetic films will be discussed in next section.

2.2 Magnetic anisotropy

Ferromagnetic objects in nature in general do not exhibit isotropic properties. For example, a high magnetic field is required to fully saturate the magnetization of the material along one direction, while a much lower magnetic field is sufficient for full saturation along another direction. Commonly, in zero field, the magnetization of a ferromagnet tends to align along certain axes, which are known as the *easy axes*. In contrast, the directions along which the fields required for saturation are highest are named the *hard axes*. The energy needed for the rotation of the magnetization from an easy axis into a hard axis is defined as *magnetic anisotropy* [38].

The Heisenberg model of exchange interaction between neighboring spins is isotropic and does not include spin-orbit interaction (SOI), which could describe the magnetic anisotropy [36]. Therefore, a phenomenological description is usually used to describe the magnetic energy in dependence on the magnetization direction. Because magnetic anisotropy energy E_{ani} should remain constant for inversion of the magnetization (i.e. in this model, there exist no easy magnetization directions but only easy magnetization *axes* [38]) it is an even function of the angle γ between the magnetization \vec{M} and the easy axis at $\gamma=0$ [38]. E_{ani} per unit volume is expressed as a multi-order expansion series of $\sin\gamma$

$$E_{ani} = K_1 \sin^2\gamma + K_2 \sin^4\gamma + K_3 \sin^6\gamma + \dots \quad (2.9)$$

with first-, second-, third-order etc. anisotropy constants K_1, K_2, K_3 ³ in SI units of J/m³. The number of the terms in E_{ani} depends on the specific geometry of the problem and mainly on the number of easy and hard axes present.

There exist different origins of magnetic anisotropy. These include effects arising from the shape of the sample, its crystal structure and any mechanical stress or strain. Important anisotropy factors for thin magnetic films are the surface and interface anisotropy contributions. Their magnitude and direction depend on the type of the surface or interface and on the thickness of the magnetic film. Often, a combination of different effects defines the direction and the magnitude of the total magnetic anisotropy in the system. For example, all mentioned effects may contribute to the first-order constant K_1 (which is usually the largest term of the expansion in Eq. 2.9 [38]) and would then be written as

$$K_1 = K_{sh} + K_{MCA} + K_{ME} + K_S/t \quad (2.10)$$

³The anisotropy constants are sometimes also named after the corresponding power of the sine function (e.g. second-, fourth-, sixth-order etc.).

with shape anisotropy K_{sh} , magneto-crystalline anisotropy K_{MCA} , magneto-elastic anisotropy K_{ME} and the surface and/or interface anisotropy constant K_S divided by the thickness t of the magnetic film. The individual contributions are further detailed in the following sections.

2.2.1 Shape anisotropy

The shape anisotropy arises from the magnetic dipolar interaction between the magnetization \vec{M} and the *demagnetizing field* H_d produced by the magnetization itself. A magnetic material with magnetization \vec{M} produces a magnetic *stray field* outside of the material and magnetic field H_d inside of it [38]. The Gauss' law of magnetism postulates $\nabla \cdot \vec{B} = 0$ and because $\vec{B} = \mu_0(\vec{H} + \vec{M})$ we can write

$$\nabla \cdot \vec{H} = -\nabla \cdot \vec{M}. \quad (2.11)$$

The magnetic energy of the field H_d inside of the material is [38]

$$E_d = -\frac{\mu_0}{2} \iiint_{\text{sample}} \vec{H}_d \vec{M} dV. \quad (2.12)$$

For thin magnetic films the shape anisotropy is derived from the difference in H_d for magnetization aligned to the film plane (H_d^{\parallel}) and magnetization perpendicular to the film plane (H_d^{\perp}). As it is shown in Ref. [38] the demagnetizing field H_d^{\parallel} is nearly zero, while a magnetization along the film normal produces a demagnetizing field of $\vec{H}_d^{\perp} = \vec{M}_S$, with the magnetization value at full saturation M_S , and thus leads to a higher magnetic potential energy E_d of the system. We can insert H_d in Eq. 2.12 and calculate E_{ani} , as the difference in energy between the state with magnetization along the easy axis (in the film plane) and hard axis (perpendicular to the plane). Therefore, the shape anisotropy contribution in magnetic thin films can be written as

$$K_{sh} = -\frac{\mu_0 M_S^2}{2}. \quad (2.13)$$

It is important to note that the mentioned derivation of K_{sh} holds only for thin films and a more general expression for the demagnetizing field is $H_{d,i} = D \cdot M_i$, where D is a demagnetizing factor [36]. A more detailed analysis of K_{sh} can be found in Ref. [36]. Nonetheless, the negative factor of K_{sh} promotes an in-plane orientation of the magnetization already with the smallest stray field.

2.2.2 Magneto-crystalline anisotropy

The easy magnetization axis in a infinite bulk crystal with no external forces or fields applied will be determined by the magneto-crystalline anisotropy (MCA). It is found that the

orientation of the easy magnetization axis depends on the material and its crystallographic structure. Therefore, the MCA has been attributed to the spin-orbit coupling (SOC), which can couple the spins in the system to the crystal lattice [45]. SOC describes the interaction of the two components of the magnetic moment, namely the spin moment \vec{m}_s and the orbital moment \vec{m}_l . The orbital moment \vec{m}_l depends on the symmetry of the bonding environment in the crystal and can differ in size for various crystallographic directions. The coupling of the \vec{m}_s to \vec{m}_l via SOC introduces favorable directions for \vec{m}_s and therefore influences magnetic anisotropy.

The SOC term is largest in the vicinity of the nucleus located at $r=0$, where the SOC Hamiltonian can be written as [38, 46]

$$H_{SOC} = \xi(r)\vec{L} \cdot \vec{S} \quad (2.14)$$

in a spherically symmetric model. $\xi(r)$ is the SOC constant, which in general depends on the distance r from the nucleus and, \vec{L} and \vec{S} are orbital and spin momentum operators for a multi-electron system. The constant ξ scales with the shell and the nuclear charge of the atom and is therefore expected to be large for atoms with large atomic number (i.e. heavy atoms). The MCA is defined as the energy ΔE , which is necessary (and therefore $\Delta E > 0$) for rotation of the magnetization from the easy direction to the hard direction and is given by the anisotropy of the SOC energy [38]

$$\Delta E_{SOC} = \langle H_{SOC} \rangle_{hard} - \langle H_{SOC} \rangle_{easy} = \xi[\langle \vec{L} \cdot \vec{S} \rangle_{hard} - \langle \vec{L} \cdot \vec{S} \rangle_{easy}] > 0. \quad (2.15)$$

In general, the nature of the MCA is not trivial, because it is based on relatively small effects in the electronic band structure [47] and, therefore, precise calculations of the MCA energy remain an important topic of theoretical efforts [38, 45]. A rigorous approach to calculating the MCA is to perform an *ab initio*-calculation of the total energy difference between states with different magnetization orientations. However, SOC is a relatively small effect in the transition metals (average ξ over the d-orbitals is of the order of 50-100 meV [48] and the MCA was reported to be in the order of 10^{-5} eV/atom [38]), thus it is difficult to investigate the origin of MCA in these materials. Under certain assumptions, the MCA is directly related to the anisotropy of the orbital moment \vec{m}_l , which was shown theoretically by Bruno [49]. In his model, the MCA energy is calculated from the band structure using perturbation theory. This approach can be applied for the transition metal ferromagnets due to the small SOC energy [45]. However, there are additional effects (e.g. anisotropy of the spin moment) which may contribute to the MCA and are neglected in the perturbation model [45].

Because of the complexity of the MCA there are no general trends for the easy magnetization axis. It has been observed that the MCA energy is for an order of magnitude smaller for Fe and Ni that have cubic crystal symmetry compared to the hexagonal close-packed symmetry of Co. For Fe(001) single crystals with the BCC crystal structure,

for example, a four-fold MCA is expected with easy magnetization axes along the Fe[100] and Fe[010] directions. Nonetheless, the MCA may considerably change for an Fe(001) thin film, at the surface or in a multilayer due to the breaking of the symmetry in the direction perpendicular to the layers [45], which induce changes to the electronic band structure. These effects will be briefly considered in the following in a phenomenological picture as additional terms to magnetic anisotropy. Nonetheless, in a quantum-mechanical view they all share a magneto-crystalline origin, i.e. they all depend on SOC.

2.2.3 Magneto-elastic anisotropy

Physically, the *magneto-elastic anisotropy (MEA)* arises from the same mechanism as the MCA [36, 38]. It can be considered as the MCA of a lattice with reduced symmetry. The reduction of symmetry is usually a consequence of the lattice mismatch between the magnetic film and the substrate or any other physically induced mechanical strain which changes the unit cell⁴. In most cases this results in an additional uniaxial magnetic anisotropy in the system. The crystal lattice often relaxes back to the unstrained unit cell for higher coverage and the MEA contribution to magnetic anisotropy decreases with film thickness.

2.2.4 Surface and interface anisotropy

Similarly to the MEA, the surface or interface anisotropy is also of a magneto-crystalline origin. It was first considered by Néel [50] in 1954, that at a surface or interface of a magnetic film magnetic anisotropy may change due to a different number of neighbors and different bonding conditions [38]. Later, there were many demonstrations of the magnetic easy axis turning from in-plane to out-of-plane when the film thickness was reduced below an interface-specific critical thickness (e.g. in Ref. [51]) and/or when the temperature was reduced below a critical value (e.g. in Ref. [52]). The in-plane to out-of-plane easy axis transition is known as the (polar) *spin reorientation transition (SRT)*.

The direction of the surface anisotropy and the amplitude of its constant K_S depend on the orientation of that surface in respect with the principle crystal axes [36]. Therefore, there is no general formula for the K_S . The surface/interface contribution to the anisotropy constant decrease with film thickness. A phenomenological formula can be used to describe the competition of K_S and the anisotropy contribution K_V from the bulk of the material [36]

$$K = K_V + \frac{K_S}{t}. \quad (2.16)$$

In Eq. 2.16 K_V includes the bulk MCA and the shape anisotropy and t is the magnetic film thickness. Usually, K_V and K_S prefer a different orientation of the easy magnetization axis.

⁴The opposite effect, i.e. an induced strain to the crystal lattice due the magnetization, is also possible. This is known as *magnetostriction* and is a consequence of the competition between the magneto-elastic energy, which is linear in strain ϵ_{ij} , and the elastic energy with quadratic strain dependence [48].

Therefore, when the thickness is sufficiently reduced to make the K_S/t term comparable to K_V the magnetization state may change, see Sec. 5.2.

Magnetic anisotropy terms in Fe thin films

In cubic crystals the bulk anisotropy K_V is of the fourth-order in the angular expansion in Eq. 2.9. Moreover, in 3d transition metals (and therefore also in bulk Fe) the MCA energy (typically some $\mu\text{eV}/\text{atom}$ [36,38,48]) is smaller compared to the surface anisotropy (in the order of some $\text{meV}/(\text{surface atom})$ [48])⁵. Therefore, the surface anisotropy K_S , which is a second-order effect, can dominate the anisotropy of cubic materials already at several MLs thickness [48] and turn the easy magnetization axis *out-of-plane*. The typical magnitude of K_S at the surface of 3d FMs is $\sim 0.5 \text{ mJ}/\text{m}^2$ [36]. Because the SOC is at the heart of the MCA, the interfaces to heavy metals were expected to result in a *perpendicular magnetic anisotropy (PMA)* for ultra-thin magnetic films [53]. However, Co and Fe thin films grown on oxide substrates (e.g. TaO_x , MgO_x , $\text{AlO}_x\dots$) also resulted in PMA [54]. The calculations confirmed the high K_S value for the interfaces with MgO and explain it with the hybridization of the out-of-plane oriented Fe 3d orbitals with O 2p orbitals of MgO which leads eventually to lowering of energy of the out-of-plane oriented orbitals for the magnetization perpendicular to the interface [53].

The in-plane SRT (i.e. rotation of the cubic in-plane magnetic anisotropy) was observed in Fe/Ag(001) [55,56] and in Fe/Au(001) [57]. Heinrich *et al.* associated the observed surface four-fold anisotropy to the *lower* Fe interface and therefore dependent on the growing conditions [56]. The main idea is, that the principal layers of the Fe film grow in an adapted Ag(001) FCC lattice and only gradually relax with thickness into the BCC lattice. In this view, the induced anisotropy belongs rather to the magneto-elastic class.

The Au/Fe/MgO(001) system, which is studied in this thesis, has small lattice parameter mismatch and exhibits a good epitaxy. Therefore, magnetic anisotropy of the Fe layer is expected to have the dominant contribution from the MCA. In ultra-thin film regime magnetic anisotropy of the Fe layer may exhibit additional contributions from the interface anisotropy (from the Au/Fe and Fe/MgO interfaces) as well as a considerable shape anisotropy contribution. The experimental characterization of magnetic anisotropy in the prepared Au/Fe/MgO(001) samples is given in Sec. 5.

2.3 Magnetic domains

In equilibrium, the magnetization of a magnetic system orients in a way to achieve a state with lowest magnetic potential energy [58]. A significant contribution to this energy is due to the stray field outside of the material induced by the magnetization itself (see

⁵This is related also to the *quenching* of the orbital magnetic moment due to the high symmetry of the cubic crystal lattice, see Ref. [38,45,48]

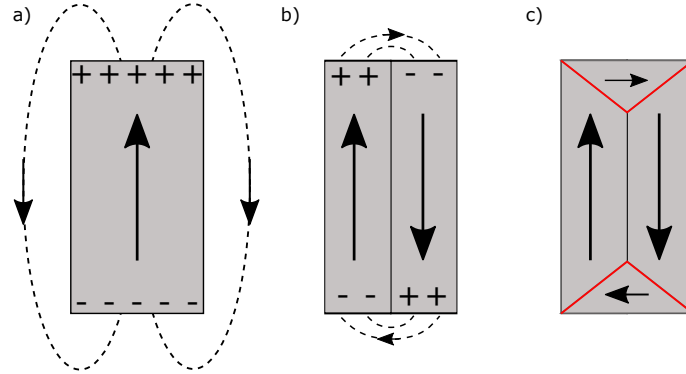


Figure 2.2: **a)** Elongated sample with homogeneous magnetization along the easy axis parallel to the long side. The magnetization produces magnetic poles and a magnetic stray field around the sample. **b)** By producing two magnetic domains with magnetization parallel to the easy magnetization axis and a 180° domain wall separating them, the stray field is reduced as sketched. **c)** A magnetic ring has the lowest magnetic energy; magnetic domains minimize the stray field and the magnetic potential energy by arranging in a circulating structure (also known as Landau pattern). The magnetization rotates for 90° (across red wall) and for 180° (across black wall).

Sec. 2.2). Because the stray field raises the magnetic potential energy, the magnetization tends to rotate in a way to minimize it. If magnetic anisotropy would have the dominant contribution to the magnetic energy, the magnetization in the sample would align to the easy magnetization axis homogeneously throughout the sample, Fig. 2.2 a. To reduce the stray field, regions with differently oriented magnetization often form as sketched in Fig. 2.2 b,c. These regions are termed *domains* and tend to arrange in a structure similar to a magnetic ring, which has the smallest stray field and therefore lowest magnetic energy.

In the regions between the domains the magnetization gradually rotates from one direction to another, e.g. a 90° rotation across the red borders and a 180° rotation across the black border in Fig. 2.2 c, to lower the exchange interaction energy. These areas are the *domain walls* and typically two types, namely the 90° (red) and 180° (black) domain walls, are observed.

The way how the magnetization rotates inside of a domain wall is determined by magnetic anisotropy and therefore varies between the bulk and a thin film and depends on the size of the sample. Ultra-thin magnetic films (with thickness up to 10 nm) do not support domain walls parallel to the film surface [38]. Moreover, for atomically thin films or small magnetic particles it may be energetically favorable not to break into domains at all [38]. Depending on the sample thickness the magnetization rotates either with magnetic moment always parallel to the wall (i.e. *Bloch wall*) or with magnetic moment rotating perpendicular to the wall (i.e. *Néel wall*). The domain walls of the latter type are observed in thin magnetic films with in-plane magnetic anisotropy so that the magnetization rotates within the film plane.

Because of the gradual reorientation of the magnetization inside of a domain wall, its

direction is not at all parts of the wall aligned along one of the easy magnetization axes of the material. The direction of the magnetization in a domain wall is thus easily influenced by magnetic fields applied either externally or internally via stray fields. For example, stray fields produced at defects of the film or at sharp edges (e.g. of lithographically patterned samples) can nucleate domain walls or pin already existing walls to the locations of the defects or edges. An externally applied field tilts the magnetization towards the direction parallel to the field and can in this way move the magnetic domain wall. The pinned domains as well as domain nucleation and growth during the magnetization reversal are manifested in magneto-transport measurements as gradual changes of the measured resistance or voltage because of the averaging of the measured quantity over a certain region of the sample, see Sec. 5. On the other hand, the domain formation can be visualized using Kerr microscopy as will be shown in Sec. 5.4 and in Ch. 6.

2.4 Electrical transport in transition metal ferromagnets

The magnetic characteristics of a material are often probed by measuring the dependence of its transport properties on external magnetic fields. In metals, the response of the electrons to externally applied electric and magnetic fields can be described in *the semiclassical model*, which employs the semiclassical equations of motion (see e.g. Ref. [35]) and relates the electronic transport to the electronic band structure [35]. The electronic structure of the metal is assumed to be known, i.e. the energy of an electron with wave vector \vec{k} in an electronic band with the index n is given as $\varepsilon_n(\vec{k})$ ⁶. In the semiclassical model, the energy and the momentum remain conserved, therefore the model describes the dynamics of electrons between collisions. The first semiclassical equation of motion defines the average velocity of an electron with wave vector \vec{k} as [35]

$$\vec{v}_n(\vec{k}) = \frac{1}{\hbar} \frac{\partial \varepsilon_n(\vec{k})}{\partial \vec{k}}. \quad (2.17)$$

Here it is assumed that the energy dispersion $\varepsilon_n(\vec{k})$ of each band n is known. Because of the periodicity of the crystal structure, the wave vectors within the same band n can differ in \vec{k} only up to the reciprocal lattice vector \vec{G} , i.e. the sets of labels (n, \vec{k}) and $(n, \vec{k} + \vec{G})$ describe the same state. In thermal equilibrium the density of electrons dn with mean velocity $v_n(\vec{k})$ in an infinitesimal volume $d\vec{k}$ in the \vec{k} -space is given by the Fermi distribution function $f(\varepsilon_n(\vec{k})) = f_n^0(\vec{k})$ [35]

$$dn = f_n^0(\vec{k}) \frac{d\vec{k}}{4\pi^3} = \frac{d\vec{k}/4\pi^3}{e^{(\varepsilon_n(\vec{k}) - \mu)/k_B T} + 1}. \quad (2.18)$$

⁶Index n stands for the independent solutions of the Schrödinger equation for the wavevector \vec{k} [35].

When an electric field \vec{E} and a magnetic field \vec{B} are applied to the sample, they induce an electric current density \vec{j} with components [59]

$$j_i = \sigma_{ij}(\vec{B})E_j = -e \sum_{\text{all electrons}} v_i = -\frac{e}{4\pi^3} \sum_n \int v_i(\vec{k}) f_n(\vec{k}) d^3k \quad (2.19)$$

with the magnetic field-dependent conductivity tensor elements σ_{ij} with indices $i=x,y,z$, and electron charge e . The coordinate system (x,y,z) is here defined irrespective of the crystal lattice orientation of the material. We used the Einstein notation for summation and the sum over all electrons transforms into the sum over all electronic bands n . It can be shown that the bands n with energy $\varepsilon_n(\vec{k}) < E_F$ for all \vec{k} , i.e. fully occupied bands, do not contribute to the electric transport. Therefore, the indices n should be limited to the partially filled bands only.

A finite σ_{ij} of a real material is a consequence of the imperfections of the crystal lattice at finite temperatures. This means that the electrons experience scattering on phonons, impurities and other deviations from a perfectly periodic lattice. These mechanisms may lead to transitions of the electrons into states with different n and \vec{k} . In the *relaxation-time approximation*, the scattering is accounted for by assuming a probability for such events in an infinitesimal time period dt to be dt/τ with *relaxation time* τ , which is, in general, dependent on n and \vec{k} ; $\tau = \tau_n(\vec{k})$ [35, 59]. Moreover, the resistivity tensor $\underline{\rho}$, which elements are defined as $E_i = \rho_{ij}j_j$, is the inverse tensor of $\underline{\sigma}$ with the following relation between their elements [60]

$$\begin{aligned} \rho_{ii} &= (\sigma_{jj}\sigma_{kk} - \sigma_{jk}\sigma_{kj}) / \Delta(\underline{\sigma}) \\ \rho_{ij} &= (\sigma_{ik}\sigma_{kj} - \sigma_{ij}\sigma_{kk}) / \Delta(\underline{\sigma}), \end{aligned} \quad (2.20)$$

where $\Delta(\underline{\sigma})$ stands for the determinant of the $\underline{\sigma}$.

An assumption of the relaxation-time approximation is that, after application of any external fields or temperature gradients to the system, the collisions of electrons are the driving mechanism towards the local thermodynamic equilibrium. Therefore, it can be shown that the non-equilibrium distribution $f_n(\vec{k})$ of the electron density can be written as the equilibrium distribution function $f_n^0(\vec{k})$ with a small correction, which can be expressed using $\tau_n(\vec{k})$. By solving the Boltzmann transport equation for $f_n(\vec{k})$ out of equilibrium (see e.g. Ref. [35]), one can obtain the expression for the elements of the conductivity tensor

$$\sigma_{ij} = \sum_n e^2 \int \frac{d\vec{k}}{4\pi^3} \tau_n(\vec{k}) v_n^i(\vec{k}) v_n^j(\vec{k}) \left(-\frac{\partial f^0}{\partial \varepsilon} \right)_{\varepsilon = \varepsilon_n(\vec{k})}. \quad (2.21)$$

The sum in Eq. 2.21 is over the bands n , which are partially occupied and the derivative of the distribution function over ε has negligible values except for ε values within an interval $k_B T$ around Fermi level ε_F [35].

Equation 2.21 shows the dependence of the tensor $\underline{\underline{\sigma}}$ on the electronic band structure of the sample, which is directly related to the crystal structure. Only when the current density \vec{j} is strictly parallel to the external field \vec{E} , the conductivity tensor $\underline{\underline{\sigma}}$ is diagonal, see Eq. 2.19. In a crystal with cubic symmetry and $i=x,y,z$ set along the principle directions of the crystal, Eq. 2.21 gives zero non-diagonal elements for tensor $\underline{\underline{\sigma}}$. This can be expected when the symmetry of the system leads to the same electronic structure along all the principle axes of the crystal. However, the symmetry of the crystal can be broken, for example, by an external magnetic field.

In general, changes of the resistance induced by an external magnetic field are known as *magneto-resistance* and can be observed in many, also non-magnetic, materials. In ferromagnets, the external magnetic field influences also the orientation and magnitude of the total magnetization, which often leads to additional magneto-resistance effects, some of which will be discussed in next sections. Because of the spontaneous magnetization, the electronic bands of a ferromagnet experience a spin-dependent energy splitting (see Fig. 2.1), which already changes the DOS close to the Fermi level and thus also affects the tensor $\underline{\underline{\sigma}}$. Moreover, the band dispersion along different \vec{k} directions (e.g. k_x , k_y and k_z) can vary depending on the spatial orientation of the magnetization in the crystal. In the example of the cubic crystal with x,y,z along the principle axes, a different electronic structure would lead to different $\underline{\underline{\sigma}}$ tensor elements along the diagonal and, thus, to non-zero off-diagonal elements. This would mean, that an electric field applied along $i=x$, for example, induces an electric field also in the directions y and z .

For instance, in a thin Fe film grown on Au(001) we observed SOI-induced gaps in the band structure, which were opening or closing depending on the rotation of the spontaneous magnetization axis [47]. Figure 2.3 shows the cuts through the Fe(001) Fermi surface for a magnetization being saturated parallel to k_y (a) and parallel to k_x (b) as observed in angle-resolved photoemission spectroscopy (ARPES) experiment and calculated using the *GW* approximation of the density functional theory including the SOI (c), see more in Ref. [47]. When comparing the electronic structure along the line marked B, the spin-orbit gap observed for $\vec{M} \parallel \hat{y}$ closes if the magnetization is rotated to \hat{x} . Such differences in the band dispersion close to the Fermi level may translate into different σ_{ij} elements and in this way contribute to the magneto-resistance effects.

2.4.1 Anisotropic magneto-resistance (AMR)

The conductivity tensor $\underline{\underline{\sigma}}$ (and thus also the resistivity tensor $\underline{\underline{\rho}}$) introduced in Eq. 2.19 has a magnetic field dependence. In non-magnetic materials a constant slow increase or decrease of the resistance is observed when an external magnetic field is increased. This is the *normal (ordinary)* magneto-resistance caused by the Lorentz force (for the increasing resistance or *positive* magneto-resistance) or by the spin disorder (for the decreasing resistance or *negative* magneto-resistance). The normal magneto-resistance is observed also in ferromagnets at applied magnetic fields beyond saturation.

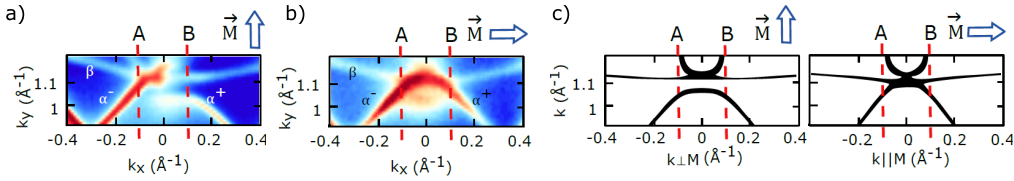


Figure 2.3: Angular-resolved photoemission spectroscopy (ARPES) maps of Fe(001) thin film in the (k_x, k_y) -momentum space for magnetization saturated parallel to **a)** the y-axis and **b)** to x-axis. **c)** The corresponding bulk Fe electronic structures in the chosen region of the \vec{k} space calculated in the framework of the GW approximation to the density functional theory in the generalized gradient approximation (GGA) including the spin-orbit interaction, adapted from Ref. [47].

In ferromagnets, the resistivity depends on the orientation of the magnetization \vec{M} with respect to the applied current direction. For polycrystalline ferromagnets, the largest difference in resistivity is observed between the resistivity ρ_{\parallel} measured when the magnetization is saturated parallel to the applied current direction and the resistivity ρ_{\perp} for magnetization pointing perpendicular to the current. This phenomenon is called the *anisotropic magneto-resistance (AMR)* and was observed first in 1856 by William Thomson (Lord Kelvin) [61]. The AMR effect disappears above the Curie temperature T_C where the magnetic ordering vanishes and is therefore related to the spontaneous magnetization \vec{M} [60].

In fact, AMR arises due to anisotropic scattering mechanisms caused by SOI. The principle effect of SOI is the coupling of the spin- and orbital-angular momenta of electrons, which can lead to spin-mixed states that allow scattering with a spin-flip. In transition metal ferromagnets the dominant spin-flip scattering mechanism is between the states with s-like and d-like orbital characters. It has been shown [38, 59, 60] that this scattering mechanism depends strongly on the wavevector \vec{k} , spin orientation \vec{s} , and the orbital angular momentum of the electronic states and, therefore, gives rise to anisotropic scattering. For example, the majority spins (whose direction is defined by \vec{M}) from “s-like” states have a higher probability for s-d scattering when they are traveling parallel to \vec{M} [59]. This leads to $\rho_{\parallel} > \rho_{\perp}$, which is commonly observed in FMs [59, 62].

In the case of a single crystal material the resistivities ρ_{\parallel} and ρ_{\perp} can be calculated by solving the Boltzmann equation in the relaxation-time approximation (as briefly introduced in Sec. 2.4), where the band n- and wavevector \vec{k} -dependent relaxation time $\tau_n(\vec{k})$ is included, see Eq. 2.21. Moreover, in ferromagnetic single crystals and epitaxial films AMR exhibits a more complex dependence on the directions of the applied current and \vec{M} in respect with the crystallographic axes [62]. Additional *crystalline* contributions arise, which can cancel out if the current is applied along one of the crystallographic axes and the magnetization is kept within one of the high-symmetry planes [63, 64]. The crystalline contributions are null in polycrystalline materials due to averaging over all orientations of the crystal. In the following, the crystalline contributions will not be considered.

In this section we will use a phenomenological description to derive the equations for the magneto-resistance effects in a thin ferromagnetic film with an in-plane magnetization \vec{M} (which can be saturated by an external field or set by magnetic anisotropy). We define the coordinate system, such that $\hat{x} \parallel \vec{M}$ and \hat{z} is parallel to the film normal. Following the derivation in Ref. [60], a phenomenological resistivity tensor $\underline{\underline{\rho}}$ can be defined for a current density \vec{j}

$$\begin{pmatrix} E_x \\ E_y \\ E_z \end{pmatrix} = \begin{pmatrix} \rho_{\parallel} & 0 & 0 \\ 0 & \rho_{\perp} & \rho_H \\ 0 & -\rho_H & \rho_{\perp} \end{pmatrix} \begin{pmatrix} j_x \\ j_y \\ j_z \end{pmatrix}. \quad (2.22)$$

Equation 2.22 gives $E = E_x = \rho_{\parallel} j_x$ for $\vec{j} \parallel \vec{M} \parallel \hat{x}$ and $\vec{E} = \rho_{\perp} j_y \hat{y} - \rho_H j_y \hat{z}$ for $\vec{j} \parallel \hat{y} \perp \vec{M}$. A current density applied in the direction perpendicular to \vec{M} induces an electric field also in the direction, which is transversal to \vec{j} and \vec{M} . This additional field scales with the current density by the factor ρ_H , which includes the ordinary Hall effect (induced by an external magnetic field perpendicular to current) and the anomalous Hall effect (AHE), which will be discussed in Sec. 2.4.3. In this section, the discussion will be limited to the fields induced in the plane of the film, where due to the in-plane \vec{M} the ordinary and the anomalous Hall effects vanish.

To define the resistivity tensor for an arbitrary in-plane angle φ between the current density \vec{j} and \vec{M} , ρ is calculated in a new coordinate system rotated for the angle φ around the sample normal \hat{z} by multiplying it with the rotation matrix $R(\varphi)$ (see Ref. [60])

$$\rho(\varphi) = R^{-1}(\varphi)(\rho(\varphi = 0))R(\varphi) = \quad (2.23)$$

$$\begin{pmatrix} \rho_{\perp} \sin^2 \varphi + \rho_{\parallel} \cos^2 \varphi & (\rho_{\parallel} - \rho_{\perp}) \sin \varphi \cos \varphi & -\rho_H \sin \varphi \\ (\rho_{\parallel} - \rho_{\perp}) \sin \varphi \cos \varphi & \rho_{\perp} \cos^2 \varphi + \rho_{\parallel} \sin^2 \varphi & \rho_H \cos \varphi \\ \rho_H \sin \varphi & -\rho_H \cos \varphi & \rho_{\perp} \end{pmatrix}.$$

In order to obtain the equations for the electric fields induced by a current density \vec{j} applied along \hat{x} of the new coordinate system (see sketch in Fig. 2.4), we insert the Eq. 2.23 into Eq. 2.22 and obtain

$$\begin{pmatrix} E_x \\ E_y \\ E_z \end{pmatrix} = \begin{pmatrix} \rho_{\perp} \sin^2 \varphi + \rho_{\parallel} \cos^2 \varphi & (\rho_{\parallel} - \rho_{\perp}) \sin \varphi \cos \varphi & -\rho_H \sin \varphi \\ (\rho_{\parallel} - \rho_{\perp}) \sin \varphi \cos \varphi & \rho_{\perp} \cos^2 \varphi + \rho_{\parallel} \sin^2 \varphi & \rho_H \cos \varphi \\ \rho_H \sin \varphi & -\rho_H \cos \varphi & \rho_{\perp} \end{pmatrix} \begin{pmatrix} j_x \\ 0 \\ 0 \end{pmatrix} = \quad (2.24)$$

$$= \begin{pmatrix} \rho_{\perp} \sin^2 \varphi + \rho_{\parallel} \cos^2 \varphi \\ (\rho_{\parallel} - \rho_{\perp}) \sin \varphi \cos \varphi \\ \rho_H \sin \varphi \end{pmatrix} j_x = \begin{pmatrix} \rho_{xx} \\ \rho_{xy} \\ \rho_{xz} \end{pmatrix} j_x.$$

From Eq. 2.24 the dependence of the longitudinal resistivity ρ_{xx} and the transversal resistivities ρ_{xy} and ρ_{xz} on the in-plane magnetization angle φ can be obtained. In the

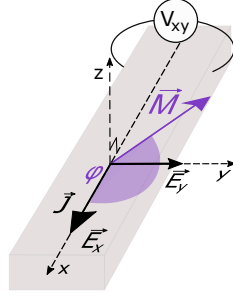


Figure 2.4: Sketch of the measurement of the transversal voltage V_{xy} by applying a longitudinal current \vec{j} along the x-direction in a thin-film material with the normal \hat{z} and an in-plane magnetization \vec{M} (violet arrow).

AMR experiment ρ_{xx} is measured as function of φ , which can be controlled by rotating the magnetization with an external magnetic field B

$$\begin{aligned}\rho_{xx}(\varphi) &= \rho_{\perp} \sin^2 \varphi + \rho_{\parallel} \cos^2 \varphi = \\ &= \rho_{\perp} + (\rho_{\parallel} - \rho_{\perp}) \cos^2 \varphi.\end{aligned}\quad (2.25)$$

An average resistivity ρ_{avg} is usually defined and the AMR signal is calculated as

$$\rho_{avg} = \frac{1}{3} \rho_{\parallel} + \frac{2}{3} \rho_{\perp} \quad (2.26)$$

$$\text{AMR}(\%) = \frac{\rho(B)}{\rho_{avg}} * 100. \quad (2.27)$$

The measured AMR value depends strongly on the type of the involved scattering processes. Scattering on impurities is dominant at low temperatures and the AMR reaches values beyond 10% [62]. Electric transport in thin films FMs at room temperature involves among other also scattering on phonons, film surface and structural defects, which reduce the AMR value to a few percent. For Fe films with thicknesses below 10 nm, the obtained AMR value was between 0.07 % and 0.15 % [62,65] and up to 1 % at 30 K, if capped with MgO [66].

2.4.2 Planar Hall effect (PHE)

Now we will have a look at the transversal resistivity ρ_{xy} , which describes the dependence on the in-plane magnetization angle φ of the electric field induced along the \hat{y} -axis by a current density j applied along the \hat{x} -axis. From Eq. 2.24 we obtain

$$E_y = \rho_{xy} j_x = (\rho_{\parallel} - \rho_{\perp}) j_x \sin \varphi \cos \varphi = (\rho_{\parallel} - \rho_{\perp}) j_x \frac{1}{2} \sin 2\varphi. \quad (2.28)$$

The observation of a *transversal* electric field E_y induced by a longitudinal current j_x in a thin film with in-plane \vec{M} is the *so-called* pseudo or planar Hall effect (PHE). The

name stems from the similarity of the effect to the normal Hall effect, which can be measured also in non-magnetic metals. In the *ordinary* Hall effect an external magnetic field applied perpendicular to the current induces a transversal (or Hall) voltage in the direction perpendicular to both, the electric current and the external field direction.

PHE in ferromagnetic metals stems from the AMR, which was shown by Seemann *et al.* [67] by comparing experimental PHE and AMR ratios to *ab initio* calculations. The relation between PHE and AMR can be seen also from the phenomenological derivation in Sec. 2.4.1, where the PHE amplitude is related to the difference between ρ_{\parallel} and ρ_{\perp} induced by the in-plane \vec{M} ⁷. For $(\rho_{\parallel} - \rho_{\perp}) > 0$ the maximum of PHE is observed for $\varphi=45^\circ$ and the minimum for $\varphi=-45^\circ$ between $\vec{j} \parallel \hat{x}$ and \vec{M} . The PHE relates the in-plane orientation of \vec{M} to a measurable transversal voltage V_{xy} , which corresponds to the induced E_y . Moreover, an opposite sign of the V_{xy} is measured for $\varphi=\pm 45^\circ$, which is of essential importance for the interpretation of the experimental results presented in this thesis.

2.4.3 Anomalous Hall effect (AHE)

The second transversal resistivity ρ_{xz} in Eq. 2.24 relates the electric field induced along the \hat{z} -axis to the current density along \hat{x}

$$E_z = \rho_{xz}j_x = \rho_H j_x \sin\varphi. \quad (2.29)$$

The $\sin\varphi$ -dependence of E_z comes from the fact that E_z is related only to the component of \vec{M} perpendicular to j_x . In a typical measurement of the ordinary and anomalous Hall effects a magnetic field B_z is applied normal to the film of a conductive material (along \hat{z} in Fig. 2.4) and the induced electric field is measured along the axis perpendicular to both, j_x and B_z , e.g. in Fig. 2.4 along the \hat{y} -axis (E_y). The same relation as in Eq. 2.29 holds also for E_y if \vec{M} has a component along the \hat{z} axis and φ is the out-of-plane tilt of \vec{M} . In the geometry with \vec{B} and \vec{M} with components along the film normal the empirical expression for the resistivity ρ_H can be found in literature [33, 69]

$$\rho_H = R_0 B_z + \mu_0 R_{AHE} M_z, \quad (2.30)$$

where B_z and M_z are the z-components of \vec{B} and \vec{M} . The first term stands for the ordinary Hall effect, which is a consequence of the Lorentz force $\vec{F} = e(\vec{E} + \vec{v} \times \vec{B})$ on the charge carriers in the material due to \vec{B} and \vec{E} . The second term in Eq. 2.30 accounts for the *extraordinary or anomalous Hall effect (AHE)*, an additional contribution to ρ_H , which is usually observed in ferromagnets and leads to a non-zero ρ_H even in the absence of \vec{B} .

A finite ρ_H in the absence of external field is observed for ferromagnetic thin films

⁷In general, PHE is related to the anisotropy of the scattering conditions. It has been shown recently, that anisotropy in scattering can be induced also in a non-magnetic topological insulator material by an external field, which induces PHE [68].

with a magnetization easy axis, which has a projection along the film normal (e.g. in films with PMA or with an easy axis tilted in the out-of-plane direction). In the typical AHE experiment, the induced electric field E_y is detected as a transversal voltage $V_{xy} = E_y \cdot w$ (w is the distance between the transversal contacts). A linear background of the V_{xy} measurement is expected, stemming from the ordinary Hall effect (first term in Eq. 2.30). The additional AHE term in Eq. 2.30 depends on the z-component of \vec{M} and is observed as a hysteresis loop for films with PMA or with an out-of-plane projection of the easy axis. In the films with in-plane easy axis no hysteresis is observed, because there is no remanence of \vec{M} along the normal of the film.

The theoretical understanding of the origin of AHE is not trivial. In general, AHE is a SOC-mediated effect, which is observed in materials with broken time-reversal symmetry [70]. In a simplified picture, SOC leads to spin-dependent scattering of conduction electrons in a material [70]. In ferromagnets, the number of spin- \uparrow electrons is not equal to the number of spin- \downarrow electrons. Different scattering conditions for different spin characters can thus lead to a non-zero AHE voltage. However, the AHE contribution to V_{xy} exhibits a dependence on a number of material properties (e.g. longitudinal resistivity ρ_{xx}) [71]. Moreover, AHE can be observed also in antiferromagnets [72, 73] or in paramagnets [74].

The theoretical description of AHE differentiates between the *intrinsic* contributions arising purely from the electronic structure and additional terms, which account for the scattering mechanisms on the impurities. Due to the strong system-dependence of different contributions to the AHE, different formalisms have been employed in the efforts to provide a complete theoretical description of the phenomenon. Last theoretical developments employ a topological formulation of the AHE by including the Berry phase of the electronic states in rigorous treatments of the electronic transport, such as the fully quantum mechanical Kubo formalism of conductivity (elaborated reviews on AHE can be found in Ref. [69–71, 75]).

2.5 Current-induced magnetization switching in magnetic multilayers

An important technological application of magnetic thin films is their use for information storage (e.g. in HDD and magnetoresistive random-access memory (MRAM)). The magnetic information storage is based on reversing the magnetization of a magnetic material between two states, which represent a “bit” of information (the first magnetization state is “0” and the second state is “1”). In this section, purely electrical concepts of magnetization switching are introduced, which use a charge current applied parallel to the layers of a heterostructure to generate a torque on the magnetization of the ferromagnetic layer. It is now a common understanding that if a ferromagnetic metal (FM) thin film is interfaced to a material with high SOI, e.g. a heavy metal (HM), enhanced SOC-assisted torques on the magnetic moments can be generated by the applied in-plane current. The

big breakthrough for the SOI-assisted torque or spin-orbit torque (SOT) were the experimental demonstrations of current-induced domain-wall motion with speeds of up to 400 m/s in Co/Pt nanowires [76] and current-induced switching of the magnetization of the ferromagnetic CoFeB interfaced to tantalum (Ta) [77].

In addition, in FM/non-magnetic metal (NM) bilayers the classical *Oersted field switching* can also be induced by an in-plane current. In combination with the SOT, the Oersted field can either assist or hinder the switching depending on the relative directions of the generated torques.

2.5.1 Current-induced Oersted field in bilayers

An electric current flowing through a conducting wire generates a magnetic field (a discovery made by Hans Christian Oersted in 1820 [38]). The theory behind the magnetic field produced by a constant electric current was further developed by Biot and Savart. The *Biot-Savart law* defines the spatial distribution of the magnetic field around a conductor with a constant current density [38]. It can be shown that the Oersted (or Biot-Savart) field at distance R perpendicular to a round wire carrying a current I is $B_{wire} = (\mu_0 I)/(2\pi R)$ [38]. The direction of \vec{B}_{wire} is along the tangent of a circle with its center at the wire. Similarly, the Oersted field produced by an infinite conductive sheet can be written as $B_{sheet} \approx \mu_0 j t/2$ where j is the current density through the sheet with thickness t . The Oersted field \vec{B}_{sheet} lies within the plane parallel to the sheet and points in opposite directions, but perpendicular to the current direction, on each side of the wire, see Fig. 2.5 a.

Now we consider a bilayer with a FM and a NM thin film layers. A current density j_C flows along \hat{x} through the NM layer with thickness t_{NM} and its normal along \hat{z} (note that the current of electrons j_e has the opposite sign compared to the current of the positive charges j_C). Then, the Oersted field B_{Oe} can be written as (see also sketch in Fig. 2.5)

$$B_{Oe} = \begin{cases} \frac{\mu_0 j_C}{2} t_{NM}, & \text{if } z > t_{NM}/2 \\ \mu_0 j_C z, & \text{if } -t_{NM}/2 < z < t_{NM}/2 \\ -\frac{\mu_0 j_C}{2} t_{NM}, & \text{if } z < -t_{NM}/2 \end{cases} \quad (2.31)$$

under the assumption that we can approximate the NM layer with an infinite conducting sheet. The Oersted field is directed along \hat{y} and has opposite sign on top and on the bottom of the NM layer. It averages to zero inside of the NM layer. Equation 2.31 is a good approximation also for a finite conducting sheet, if the distance from the sheet is much smaller compared to its length and width. For a conducting sheet with finite width, the direction of the Oersted field generated by $j_C \parallel \hat{x}$ would circulate around the layer as sketched in Fig. 2.5 a.

The strength of B_{Oe} at the FM layer position depends on the current distribution in the NM/FM bilayer and needs to be considered especially carefully for systems where the

NM layer has a much higher conductivity compared to the FM layer. If this is the case, the Oersted field generated by the NM layer may exert a torque $\vec{T} = \vec{m} \times \vec{B}_{Oe}$ on the magnetic moment $\vec{m} = \vec{M}/V$ of the FM layer with volume V , which can cause precession and, for a sufficiently strong B_{Oe} , also a complete reorientation of the magnetic moment towards a different easy direction, i.e. magnetization switching. Note that, the Oersted field induced by a current through a singular FM layer averages to zero inside the layer and thus cannot induce a switch of the magnetization.

2.5.2 Spin-orbit torques

The *spin-orbit torque (SOT)* phenomenon is a recent promising development in the field of spintronics. The basic concept of SOT is the conversion of a charge current into a spin accumulation or a spin current, which generates a torque on the magnetization. The origin of this conversion, however, is twofold as we shall see in the following. The research on SOTs has been mostly focused on NM/FM/insulator multilayers. Among the variety of material combinations, the Pt/Co/AlO_x heterostructure was established as a model system for SOT [21, 78–80]. Later the focus shifted to Ta or W capped CoFeB/MgO [77, 78, 81–83]. The effects of SOT are most prominent for heterostructures containing 5d metals, especially for high resistive W or Ta or for more conductive Pt and Pd due to the strong SOC and high density of states close to the Fermi level in these two metals. However, SOTs have been demonstrated also in other materials, for example in antiferromagnets [84, 85] or topological insulators/FM structures [86] to name a few. A thorough comparison of the SOT efficiency in different heterostructures can be found in the review article by Manchon et al. [26].

SOT induced by spin Hall effect

The SOT was first observed in HM/FM bilayers and it was assigned to the spin accumulation due to the *spin Hall effect (SHE)* in the HM. As early as 1971 [87] it has been already shown that strong SOI in HM can generate a spin current, when an unpolarized charge current is applied parallel to the layer. The mechanisms responsible for the spin current can be spin-dependent scattering of the conduction electrons (extrinsic effect) or existence of spin-dependent velocities of the conduction electrons in the direction perpendicular to the current (intrinsic effect related to the electronic band structure) [88]. The SHE in the HM layer induces a spin current \vec{j}_S in the direction normal to the layers with spin polarization \vec{S} perpendicular to both the charge current \vec{j}_e as well as \vec{j}_S (see Fig. 2.5 b).

At the interface the spin current diffuses into the FM layer, where its spin can interact with the local magnetic moments. The basic idea is sketched in Fig. 2.5 c. When electrons with spin vector \vec{S}_1 travel through a magnetic medium with magnetic moments \vec{m} , their spins undergo a reorientation towards the direction of \vec{m} due to the exchange interaction. Because the full process is spin conserving, the loss of the transversal component of the

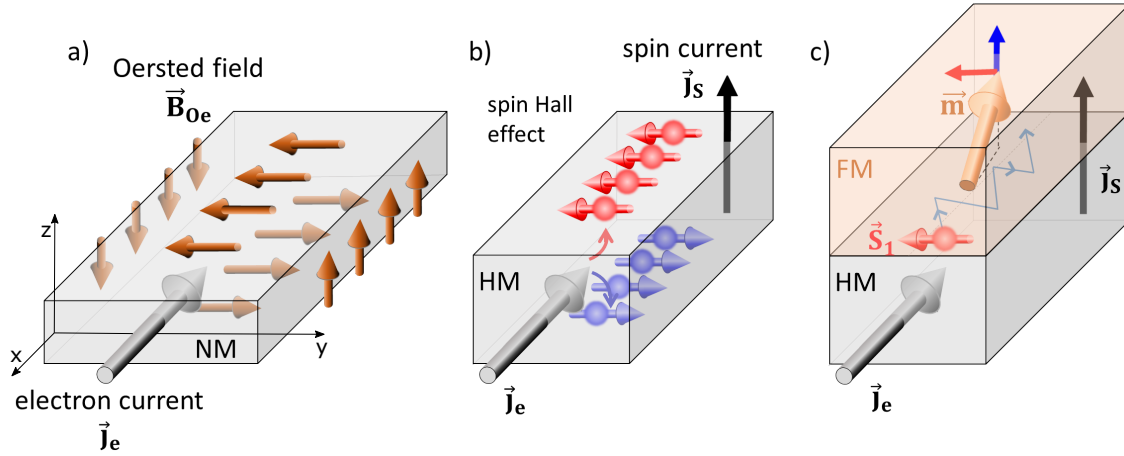


Figure 2.5: **a)** Sketch of the Oersted field induced by an electron current $\vec{j}_e \parallel (-\hat{x})$ applied to a non-magnetic metal (NM) layer. **b)** The spin Hall effect (SHE) in a heavy metal (HM) material. Due to a strong spin-orbit interaction, the electrons with opposite spin preferentially scatter into opposite directions, which leads to a spin current \vec{j}_s in the direction perpendicular to applied \vec{j}_e . **c)** If the HM layer has an interface to a ferromagnet (FM), the spin current \vec{j}_s diffuses also into the FM layer. During each scattering event of the electrons, the angular momentum can be transferred to the magnetic moment \vec{m} of the FM layer. This acts as a *spin-orbit torque* (SOT) to the total magnetization of FM. The SOT can have two perpendicular components (blue and red arrow).

spin of the incident electrons is transferred to the magnetization of the magnetic layer in the form of a *spin transfer torque* (STT). In the SOT-picture this torque is known as the *in-plane or Slonczewski torque*, because its plane is defined by \vec{m} and the spin of the incoming electrons (red arrow in Fig. 2.5 c). In this way, its direction is determined by the direction of \vec{m} and therefore rotates if \vec{m} changes direction.

Moreover, at the edges of the HM layer the spin current induced by SHE generates a spin accumulation with opposite spin orientation at each edge (as sketched in Fig. 2.5 b). A spin imbalance at an inversion asymmetric interface may drive competing interfacial effects, one of which will be considered in the following. Therefore, it is reasonable to expect additional contributions for the SHE-SOT.

SOT induced by inverse spin galvanic effect

When the NM/FM heterostructure is not inversion symmetric (e.g. a thin FM layer with one interface to HM and other to an insulator) the spin can accumulate even without SHE. This mechanism can be viewed as an *inverse spin galvanic effect* (*iSGE*) [89] or the *Edelstein-Rashba effect* [90].

A very schematic and simplified, but often used illustration of the iSGE-induced spin accumulation is to consider the *Rashba-Bychkov* SOI at an interface with inversion asymmetry (see Ref. [26] and the references therein). Rashba-Bychkov SOI locks the spin of the states perpendicular to their wavevector \vec{k} creating the spin-texture as sketched in Fig.

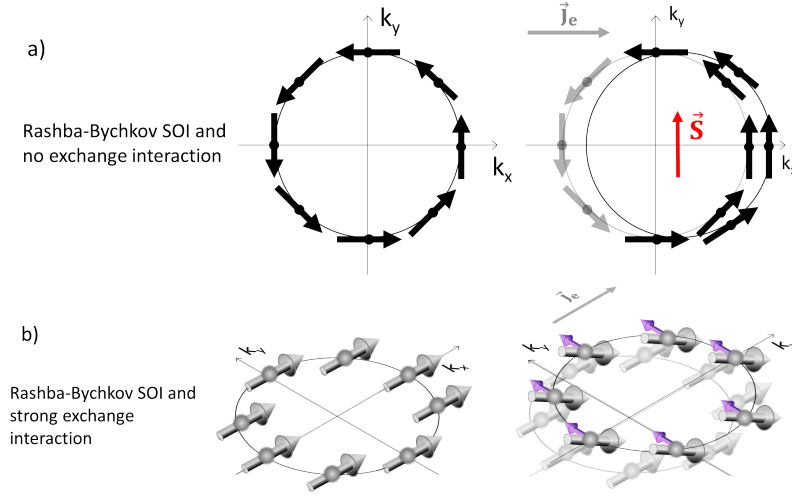


Figure 2.6: The illustration of the two limiting cases of the spin-orbit torque induced by the inversed spin galvanic effect (iSGE). **a)** In the limit of the strong SOI and small exchange interaction, the direction of the spins of electrons are locked perpendicular to their momentum vector \vec{k} by the Rashba-Bychkov SOI at an interface with inversion asymmetry. When an electric field is applied so that the electrons move along the x-direction, the \vec{k} -vectors are repopulated such that there is a higher occupancy of the states with positive k_x . Because spins are locked to the \vec{k} -vectors, the imbalance in the density of \vec{k} induces an imbalance in the density of spin leading to a total spin moment \vec{S} (red). **b)** In the limit of strong exchange interaction and small SOI, the spins of the electrons align with the exchange field direction (here along k_x). When the electrons are accelerated with an external electric field, the SOI induces a magnetic field along the y-direction (purple arrows). This field exerts a torque on the spins, which tilt and acquire a z-component. Based on Ref. [26, 91].

2.6 a for one of the chiral states. In equilibrium, the sum over all spins is zero. When an electric field is applied along the x-axis, the states at the Fermi level are shifted in momentum space according to the applied electric field ($\frac{d\vec{k}}{dt} \propto e\vec{E}$). The states with k_x component parallel to the electron flow will become more populated than the states with opposite k_x . Because the spin of the states is locked to \vec{k} , the imbalance in the distribution of \vec{k} induces also a spin imbalance in the direction perpendicular to \vec{j}_e .

In the above picture the exchange interaction was neglected under the assumption that it is a small correction compared to the SOI. The obtained expression for the spin accumulation \vec{S} is in this case independent of the magnetic moment \vec{m} . In the other limit, where the SOI is a small correction to energy compared to the exchange interaction, the spins of the electrons will tilt according to the direction of the total magnetization of the FM in equilibrium (see Fig. 2.6b). The SOI in the system can be viewed as an effective field of the periodic lattice acting on the spin of the electron, when the electron moves through the lattice with momentum \vec{k} . When the electrons change their momentum \vec{k} due to the applied electric field \vec{E} , the SOI-field acquires an additional component along the y-direction [26] (violet arrow in Fig. 2.6b). The spin tilts in response to the field and

acquires a component along the z-direction, perpendicular to both \vec{m} and \vec{j}_e (for more details see Ref. [26,92]). When integrated over all \vec{k} the acquired z-component of the spin angular momentum gives a total spin accumulation S_z .

General equations for SOTs

Based on either of the two discussed physical origins of SOT it can be shown that two different terms of SOT can be derived (see Ref. [26] and references therein). In the iSGE-picture these two terms are obtained in the two limits of the SOI strength. In the strong SOI limit, the expression for the current-induced spin accumulation exhibits no dependence on the magnetic moment \vec{m} and therefore acts as an effective magnetic field on the magnetic moments. This term was named the *field-like (FL) SOT*. In the second limit (i.e. strong exchange interaction limit), the expression for the spin accumulation depends on \vec{m} . The SOT generated by this spin accumulation thus depends on the orientation of \vec{m} . It can, in fact, decrease to zero when the applied field \vec{E} and \vec{m} are perpendicular [26]. In analogy, it acts on the magnetic moment as a damping torque and it was given the name *damping-like (DL) SOT*. In the quantum-mechanical treatment of transport (by e.g. applying the Kubo formalism), the contributions can be split into interband and intraband terms. The latter contribution depends on the level of disorder, therefore it is also known as the extrinsic term and contributes to the FL-SOT [26]. The DL-SOT is related to the interband contribution, which has only weak dependence on disorder and can be associated to the Berry curvature of the electronic states [26,93].

Moreover, the SHE-SOT can also generate both, a DL and a FL SOT. The first was discussed above, while the latter can be schematically introduced by considering the SHE-generated spin accumulation at the edges of the HM (as sketched in Fig. 2.5 b). If the edge of the HM is an inversion asymmetric interface, the spin accumulation implies similar considerations as the iSGE-induced spin imbalance (see Fig. 2.6 and the explanation in text). Therefore, it is reasonable to expect a field-like contribution also for the SHE-SOT.

In order to quantitatively characterize the SOTs it is suitable to use a general expression for SOT \vec{T}

$$\vec{T} = \underbrace{\tau_{FL}(\vec{m} \times \vec{\zeta})}_{\text{“field-like”}} + \underbrace{\tau_{DL}\vec{m} \times (\vec{m} \times \vec{\zeta})}_{\text{“damping-like”}} \quad (2.32)$$

where the first term can be attributed to the FL SOT with a scaling parameter τ_{FL} and the second term to the DL SOT with the parameter τ_{DL} . The vector $\vec{\zeta}$ is a unit vector along the current-induced transverse spin polarization $\vec{\zeta} \parallel \hat{z} \times \vec{j}_C$. The parameters τ_{FL} and τ_{DL} are to the first order independent of \vec{m} .

The two terms of the SOT in Eq. 2.32 can be written in terms of an effective field using the classical definition of the magnetic torque $\vec{T} = \vec{M} \times \vec{B}$. For \vec{j}_C applied along the

x direction the spin polarization $\vec{\zeta} = \hat{y}$ and Eq. 2.32 gives [26]

$$\vec{B}_{FL} = \tau_{FL}\hat{y} \quad (2.33)$$

$$\vec{B}_{DL} = \tau_{DL}\vec{m} \times \hat{y} \quad (2.34)$$

The two fields $\vec{B}_{DL,FL}$ typically reach values of 0.1-10 mT for a current density of 10^7 A/cm² [26]. A thorough summary of the investigated heterostructures and the obtained efficiencies of the DL and FL SOT can be found in the review article by Manchon *et al.* [26]. The field-like effective field \vec{B}_{FL} is either parallel or antiparallel to \hat{y} depending on the sign of τ_{FL} . In the iSGE picture, the inversion asymmetry at the HM/FM interface results in an electric field with the direction pointing towards the surface with a lower work function [94] (in the case of Au/Fe heterostructure the interface electric field would point towards Fe layer). This can determine the sign of the effective field at the interface. The \vec{B}_{FL} effective field can be assisted or opposed by the B_{Oe} . The damping-like field \vec{B}_{DL} , on the other hand, assists or acts against the Gilbert damping. In most cases, the sign of \vec{B}_{DL} is defined by the SHE in the bulk HM. A good example is the comparison of the SOT observed in HM/FM heterostructures with Pt to the SOT in heterostructures with Ta. Pt and Ta have an opposite sign of the SHE and consistently, also the effective fields reverse [95, 96].

In the commonly used ultra-thin film FM/NM bilayers for SOT studies a simple separation of the two components does not disentangle the two origins of the torque. Both torque terms are dependent on the thickness of the FM and HM layers as well as on the temperature, the angle between the current and the magnetization and on the quality of the interface. Characteristic dependences on these parameters are expected for the SHE-SOT and for iSGE-SOT [26]. Nevertheless, the experimental results do not in all cases agree and the origin of the SOT contributions in most systems is still under debate.

3. The Au/Fe/MgO sample system

The system of choice in the present study of current-induced effects in epitaxial heterostructures is a Au/Fe bilayer grown on MgO(001) single crystal substrate. In this chapter, the reported properties of ultra-thin Fe films grown on Au(001) and MgO(001) are briefly reviewed (Sec. 3.1) followed by a characterization of the growth conditions for both systems using standard surface analysis techniques (Sec. 3.2).

3.1 Review of literature

Ultra-thin Fe films grown epitaxially on Au(001) and on MgO(001) are characterized by a small lattice mismatch (Sec. 3.2.2), which enables high quality epitaxial growth. These two material combinations have been thus widely studied as model systems for ultra-thin film phenomena and the literature about the growth and magnetic properties of Fe/Au(001) and Fe/MgO(001) systems is vast.

On the one hand, the **Fe/Au(001)** system was employed in the studies of quantum well states [97, 98] and interlayer exchange coupling [98–100]. In a recent publication [47] we demonstrated that in the Fe/Au(001) system opening and closing of the magnetization-dependent spin-orbit gaps located near the Fermi level can be observed. Several experimental studies revealed that for Fe films grown on Au(001) at room temperature Au atoms segregate to the surface for Fe film thickness $t_{Fe}=15\text{-}20$ ML [101]. The Au overlayer leads to important changes of the magnetic properties of the Fe films. For example, a reduced magnetic moment of the Fe film as compared to the value for Fe/MgO(001) can be expected according to calculations [102, 103] and a changed magnetic anisotropy of the Fe film was observed [104], which was further supported by theoretical studies [105–107]. It has been shown that the segregation of Au does not significantly change the hysteresis loop of 20 monolayer (ML) Fe film on a Au(001) single crystal [108]. A noble-metal capping layer induces changes of the magnetic moment only in the top ferromagnetic layer at the interface [109]. Nonetheless, the Au segregation in the Fe/Au(001) system can be reduced by lowering the temperature during the growth [47].

On the other hand, the **Fe/MgO(001)** system exhibits a predominantly sharp interface with O only partially intermixing into the first Fe layer [110, 111]. Therefore, the Fe/MgO interface can be well described theoretically, which helped to understand the band structure-origin of the large tunneling magneto-resistance (TMR) in Fe/MgO/Fe crystalline magnetic tunnel junction (MTJ)s (see e.g. [112]). The calculations of the band

structure for the two crystalline lattices show that the MgO layer acts as a symmetry filter for electrons and leads to a large TMR of up to 200 % [11, 12]. These experiments encouraged further studies of the magneto-resistance effects in thin Fe films grown on MgO(001). An Fe thin film capped with MgO exhibits anisotropic magneto-resistance (AMR) values of up to 1 % at 30 K, which increase with decreasing Fe thickness as a consequence of confinement effects [66]. In contrast, for Fe films capped with Pt the observed AMR value is in agreement with the bulk value. For Fe thin film grown on other substrates the angular dependence of AMR related to the current direction with respect to the in-plane crystalline directions of the Fe film was demonstrated. The obtained AMR values vary between 0.07 % and 0.15 % [62, 65].

The **magnetic properties** of the Fe layer show a thickness dependence. In Fe/MgO(001) and for Fe thicknesses below 5 ML the Curie temperature T_C was observed to fall below the room temperature due to the lowered coordination number [113, 114]. At room temperature an Fe film with less than 3 ML thickness exhibits a superparamagnetic hysteresis, because of the non-continuous coverage [29]. The onset of the four-fold magneto-crystalline anisotropy (MCA), which is typical for epitaxial Fe films grown on MgO(001) substrate, was reported at 4 ML Fe films [29], while complete coverage of the MgO(001) substrate was observed beyond 6 ML Fe thickness [29]. For an Fe coverage beyond 10 ML the T_C saturates almost to the bulk value ($T_C \sim 800$ K) [113, 114].

At the ultra-thin-film limit, the film morphology and anisotropy terms induced by the interface or surface may increase and change the magnetic anisotropy of the Fe films. A small interface anisotropy $K_s \sim 1.7 \times 10^{-3}$ erg/cm² was observed for Fe/MgO(001) due to the misfit dislocations [29]. An additional uniaxial anisotropy can be induced by deposition of Fe under an oblique angle [115–117] or due to surface steps on the MgO(001) substrate also when grown at normal incidence [118]. Cebollada *et al.* studied a 200 Å thick Fe film on MgO, where they varied the film morphology by annealing [119]. A different local morphology of the annealed films changed the magnetization reversal process resulting in higher coercive and saturation fields, loss of squareness of the hysteresis, while the effective four-fold anisotropy constant decreased only slightly [119].

The reported interface anisotropy constants responsible for the polar (in-plane to out-of-plane) **spin reorientation transition (SRT)** for ultra-thin Fe film are listed in Sec. 5.2.1 (Table 5.1). The perpendicular magnetic anisotropy (PMA) state was observed in MgO/Fe/MgO(001) up to $t_{Fe} = 9 \pm 1$ Å critical Fe thickness, when deposited at $T < 150$ K [120]. The PMA state in Fe/Au(001) was observed for $t_{Fe} < \sim 3$ ML [104]. The in-plane reorientation of the four-fold magnetic anisotropy of Fe(001) (easy axis rotation from Fe[001] to Fe[110] direction) was observed in Fe/Au(001) for $t_{Fe} < \sim 7$ ML [57]. As shown by Maruyama *et al.* [121], the PMA of epitaxial MgO/Fe(2-4 ML)/Au could be electrically controlled. The demonstrated electrically induced in-plane to out-of-plane anisotropy change may have a potential as a switching mechanism in the MTJ structures [121] and

was therefore further investigated also in other materials [122–124].

Fe-based heterostructures have also been a subject of current-induced magnetization switching experiments. A switching mechanism in patterned Fe films proposed by Yoo *et al.* is based on the current-induced Oersted field in an overlaying patterned Au wire [22]. The authors have shown that multiple stable states can be induced by the Oersted field and suggest that the measured intermediate planar Hall effect (PHE) voltage is a consequence of the induced domain structure in the Fe wire (not shown by the authors) [22]. In a different study, the authors employed Fe films grown on a vicinal GaAs surface, which induced an anisotropy to the measured PHE related to an additional anomalous Hall effect (AHE) contribution [30–32]. The cubic MCA of the Fe film together with the AHE asymmetry results in four stable states of the system which are distinguished by the measured PHE voltage. Recently, an interfacial spin-orbit torque (SOT) has been observed to occur in a single-crystalline layer of Fe grown on GaAs substrate, which is of the inverse spin galvanic effect (iSGE) origin due to the inversion asymmetry of the system [28]. These results make the single-crystalline Fe films an interesting candidate for further studies of the mechanisms of electrical control of the magnetization as pursued in the present thesis.

3.2 Growth characterization using surface analysis techniques

The Fe/Au(001) system was often studied as a model ferromagnetic metal (FM)/heavy metal (HM) system [125]. A challenging task is to obtain a sharp Fe-Au interface, because the Au atoms tend to segregate to the surface. The results of several studies of Fe/Au(001) growth were summarized by Bonell *et al.* [101]. The majority of studies agree that one monolayer (ML) of Au remains on the surface of 15-20 ML Fe films when deposited at room temperature, which is related to the lower surface energy of Au. In this section, a study of Fe/Au(001) growth will be presented and the reversed stacking with an ultra-thin Fe layer grown on MgO(001) substrate will be discussed as a promising alternative for the studies of the current-induced switching phenomena.

3.2.1 Microscopic study of Fe/Au(001) growth

The study of growth of thin Fe films (up to 10 ML) on a Au(001) single crystal was carried out using a combination of spatially resolved experimental techniques, namely the photoemission electron microscopy (PEEM) and the low energy electron microscopy (LEEM). Details on PEEM and LEEM techniques can be found in Ref. [126–128]. The experimental work was conducted at the Nanospectroscopy beamline of the Elettra synchrotron in Trieste, Italy. The experimental set-up allows diffraction and spectroscopy

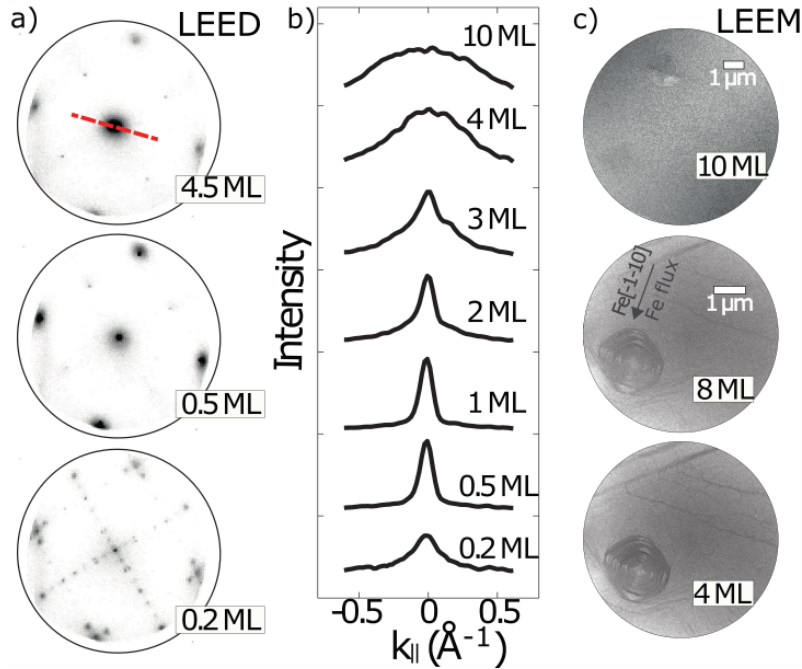


Figure 3.1: **a)** The low energy electron diffraction (LEED) patterns at 50 eV kinetic energy taken during growth at different deposition times. **b)** The angular profiles of the LEED (0,0) spot for different Fe coverage. **c)** LEEM images taken at room temperature using 12 eV electron kinetic energy at different Fe film thicknesses. For 10 ML coverage the steps propagating from the Au(001) substrate are no longer visible. Adapted from Ref. [125].

studies with lateral resolution in the micrometer regime, e.g. microprobe low energy electron diffraction (μ -LEED) and microprobe x-ray photoemission spectra (μ -XPS). Because of the geometry of the microscope [129], imaging and spectroscopical studies can be conducted simultaneously with in-situ material deposition in ultra high vacuum (UHV) or during an annealing procedure. The experimental results presented in this section have been published in an article by Gospodaric et al. in Physical Review B in February 2018 (Ref. [125]). The results of the reported study will be summarized in the following.

The Fe films were grown using molecular beam epitaxy (MBE) in UHV conditions at room temperature on a Au(001) single crystal, prepared by cycles of sputtering and subsequent annealing. The surface quality was characterized by means of LEED and LEEM. A well-ordered clean Au(001) surface was characterized with the LEED pattern with the typical reconstruction of the Au(001) crystal face [130, 131]. The Fe deposition direction was at 74° angle to the sample surface normal along the Fe $[\bar{1}\bar{1}0]$ direction (marked in Fig. 3.1 c).

The epitaxial growth of Fe was observed for coverage above 1 ML to follow the relation Fe $[100]||$ Au $[110]$ and Fe $[010]||$ Au $[1\bar{1}0]$. The characteristic LEED pattern of the body-centered-cubic (BCC) Fe lattice remains well defined for Fe film thicknesses from 1-10 ML. The angular profile of the LEED (0,0) spot (marked with red line in Fig. 3.1 a) varies

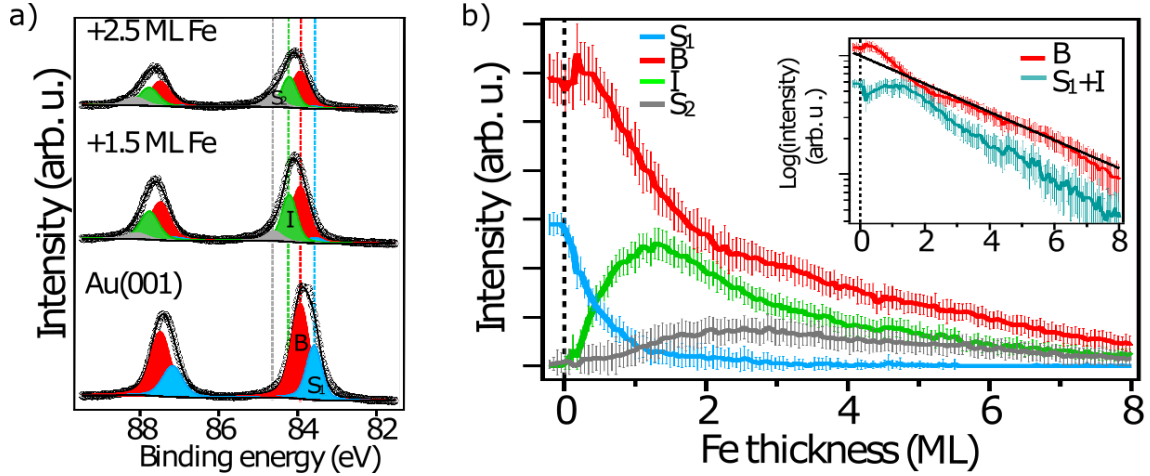


Figure 3.2: a) Fit of the X-ray photoemission spectroscopy (XPS) spectra from pure Au(001) surface and two chosen thicknesses of the Fe film. The components of the fit: B (Au bulk), I (Fe/Au interface), S₁ (Au surface), and S₂ (Au/Fe) are described in the text. b) Intensity of the components of the fit with the corresponding standard deviation error bars plotted versus Fe film thickness. Inset shows the component B and the sum of the components S₁ and I plotted on the logarithmic scale. Black line represents theoretical attenuation of Au signal by Fe layer for IMFP equal to 5.22 Å. Adapted from Ref. [125]

with increasing Fe film coverage, as demonstrated in Fig. 3.1 b. The changing profile may be a consequence of varying interlayer distance during growth, as observed in other studies [132–135]. Beyond 3 ML Fe coverage the angular profile becomes broad. This may be caused by increased surface roughness, but also by the modified scattering conditions due to Au-Fe intermixing at the surface.

LEEM images acquired during the Fe film growth show the distinct step bunches on the surface of the Au single crystal propagating up to 8 ML Fe coverage (Fig. 3.1 c) and a pyramidal defect visible also at 10 ML coverage. The XPS spectra were acquired during growth in order to study the evolution of the surface composition. At the beginning of the Fe evaporation an apparent shift to higher binding energies of the Au 4f doublet was observed. We conclude that the shift is due to different coverage dependence of the four components of the Au 4f peaks. The area under each of the components (S₁, B, I and S₂) versus Fe thickness is plotted in Fig. 3.2 b. The analysis of the coverage dependence of the component S₂, which stems from the Au overlayer, indicates a presence of a sub-ML amount of Au atoms on top of the Fe film for up to 3 ML coverage. Beyond 3 ML Fe thickness the S₂ begins to decrease, indicating that the Au atoms of the overlayer intermix into the layers of the deposited Fe film. Nonetheless, theoretical attenuation of the Au signal by the Fe film (black line) is a good approximation of the linear decrease on the logarithmic scale of the intensity of the component B (stemming from the Au bulk) and the sum of intensities of component S₁ (stemming from Au surface) and the interface component I, Fig. 3.2 b.

The microscopy study of the annealing procedure of the 10 ML Fe film on Au(001) showed increased presence of Au on the Fe surface for temperatures beyond 200°C. We obtain a 1.6-2.3 ML thickness of the Au overlayer after annealing to 300°C. The difference in the thickness of the Au top layer arises due to the distinct segregation process, which we observed in PEEM and LEEM. Namely, we observed formation of 1-5 μm -long *cracks* in the Fe film at $\sim 190^\circ\text{C}$. These Fe-poor regions act as segregation channels for the Au atoms at higher temperatures. Further explanation can be found in Ref. [125].

In conclusion, the growth of Fe on Au(001) at room temperature was found to proceed epitaxially with an Au overlayer forming from 1-3 ML Fe coverage. Beyond this Fe thickness the Au atoms start to intermix into the layers of the deposited Fe film. Because of the Fe-Au intermixing and the increased segregation of Au during annealing, the fabrication of a Fe/Au(001) system with an atomically-clean interface and a well defined structural asymmetry (normal to the layers) poses a big challenge. This problem can be avoided when the Fe film is deposited at cryogenic temperatures [111]. Nevertheless, additional annealing of the heterostructure induces Au segregation towards the surface. Since thermal effects are expected to play a role in the transport experiments due to Joule heating, the chosen sample system must be stable at increased temperatures. Therefore, a *reversed stacking sequence*, namely Au/Fe/MgO(001) was chosen for transport experiments for the studies of the current-induced effects.

3.2.2 Epitaxial growth of Fe and Au on MgO(001)

For the layer stacking with a Au layer on top of the Fe film the MgO(001) single crystal was chosen as the substrate. A commercial MgO(001) single crystal with 1 mm thickness was polished and cut so that the MgO[100] direction was along the side edge of the substrate. On top of the 10x10 mm² MgO(001) substrate two 9x3 mm² Cr contact pads were sputter-deposited using a mask on the top and bottom side of the substrate, see Fig. 3.3. The Cr pads were pre-deposited onto the substrate in a separate sputtering chamber by Thomas Jansen in Peter Grünberg Institut (PGI)-6. These two pads can be used for future investigations of the electronic band-structure in combination with transport measurements, discussed in the outlook of this thesis (Ch. 7). They can be used as electric contacts in the UHV chamber (pressure $< 1 \cdot 10^{-10}$ mbar) using a self-made sample holder with electrical connectors, see Ref. [136].

The substrate was transferred from the sputtering chamber into a UHV system of the angle-resolved photoemission spectroscopy (ARPES) apparatus for surface analysis. This system is equipped with surface preparation techniques (Ar-ion sputtering gun, UHV heater) and several experimental surface analysis techniques (LEED, Auger spectroscopy, ARPES, XPS), see Ref. [136] for a detailed description. The MgO(001) substrate was prepared by annealing to 530°C for 20 min in UHV conditions to remove any adsorbents and achieve the MgO(001) face of high crystalline quality. At this temperature the adsorbed molecules, mainly H₂O and carbohydrates, are detached from the surface, degas

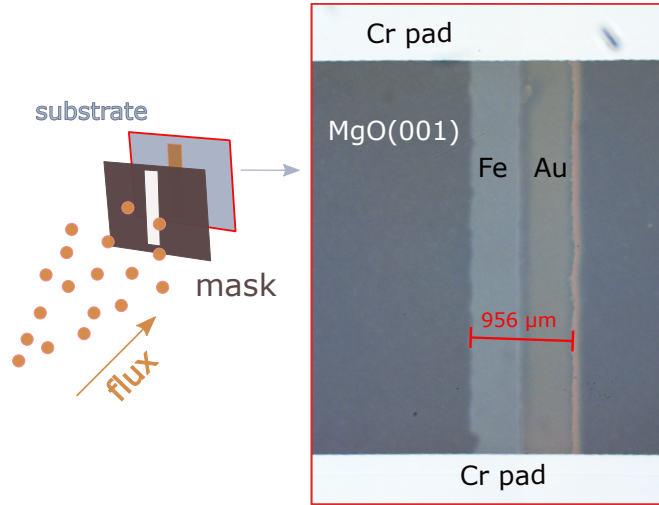


Figure 3.3: Image of the Fe(1.3 nm) and Au(~ 2 nm) stripes between the sputter-deposited Cr pads on the MgO(001) single crystal substrate. The Fe and Au stripes were deposited using molecular beam epitaxy (MBE) and a mask with a stripe shape placed in front of the substrate.

into the surrounding volume and are eventually evacuated from the system by the turbomolecular pumps. In the atmosphere of $1 \cdot 10^{-10}$ mbar pressure the surface will be covered by a monolayer of molecules in several hours [136].

Molecular beam epitaxy

The Fe and Au films were evaporated *in-situ* using molecular beam epitaxy (MBE) evaporators mounted on the ARPES apparatus. A piece of high purity material in the shape of a rod or in a crucible is placed in the evaporator and heated up by electron bombardment. This is a standard heating principle, where an electric current is applied to a thin filament wire, which due to the thermionic emission (Edison effect) acts as a source of electrons. A high voltage between the filament and the rod or the crucible accelerates the electrons towards the material. In this way the electrons collide with the material and heat it up. The emission current and the flux of the ionized evaporated material can be precisely controlled by adjusting the filament current and the high voltage allowing to achieve homogeneous deposition of the material onto the substrate. This technique plays an important role in the development of the thin film physics because it enables low deposition rates (in the order of 1 ML per second) and evaporation in UHV conditions, which together fulfill the requirements to produce ultra-thin films of high crystalline quality.

The deposition rate of the Fe and Au layers was calibrated by determining the thickness of a deposited film using X-ray reflectometry (XRR) in the laboratory of Gregor Mussler in PGI-9. The two films were deposited separately and next to each other at room temperature through a mask placed in front of the substrate to achieve a wire-like stripe, see the inset in Fig. 3.3. The film thicknesses were 1.3 nm for Fe and ~ 2 nm for

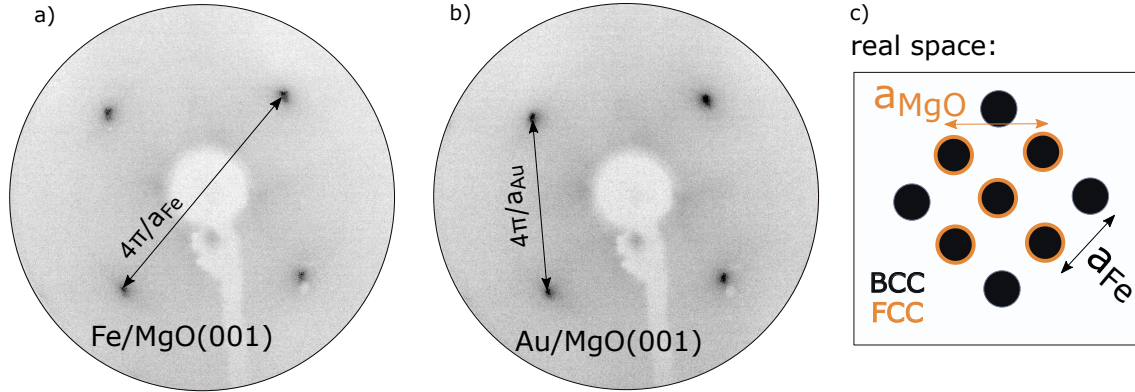


Figure 3.4: The LEED patterns as obtained from the **a)** the Fe stripe and **b)** the Au stripe using 133 eV electron kinetic energy. **c)** The real space lattice matching of the body-centered cubic (BCC) Fe(001) face with lattice constant a_{Fe} and the face-centered cubic (FCC) MgO(001) face with lattice parameter a_{MgO} .

Au.

Low-energy electron diffraction (LEED)

The crystalline quality of the films was controlled by LEED, a widely used surface analysis technique for determination of the surface atomic structure, i.e. the periodic arrangement of the atoms in the first top layers of a crystal. More details on the technique can be found in Ref. [137]. The LEED patterns shown in Fig. 3.4 a,b were obtained by directing a monochromatic beam of electrons emitted from a LaB₆ cathode and collimated and accelerated to 133 eV by a lens system towards the sample at normal incidence. The elastically backscattered electrons were visualized on the fluorescent screen, visible in Fig. 3.4 a,b. The interaction of the electrons with the atoms at the surface is in the first order approximation considered as a two-dimensional geometrical diffraction of elastically scattered waves with the de Broglie wavelength $\lambda_B = h/E$ (E is energy measured in eV). This means that the elastically backscattered electrons with energy E will form a diffraction pattern of the atomic lattice following the Bragg condition for constructive interference

$$n\lambda_B = a \cdot \sin\theta \quad (3.1)$$

with n being an integer number and a being the interatomic distance on the surface. From the condition for constructive interference in Eq. 3.1 follows that a wave with λ_B scattered on the atoms separated by lattice spacing a interacts with its backscattered wave producing peaks only at angles θ which fulfill Eq. 3.1. The LEED pattern is thus not a direct measure of the lattice but of its reciprocal transformation with a lattice spacing inversely proportional to the lattice constant a .

The MgO(001) single crystal has a FCC atomic lattice. Its (001) surface has atoms

oriented as depicted by black circles with orange border in Fig. 3.4 c. The reported lattice constant is $a_{MgO} \approx 4.2 \text{ \AA}$ [138]. At room temperature Fe grows in a BCC lattice and the atoms in the (001) face arrange as shown by the black circles in Fig. 3.4 c. The reported lattice constant is $a_{Fe} = 2.87 \text{ \AA}$ [133,139], almost a factor of 2 smaller than a_{MgO} . However, Fe can grow epitaxially on MgO(001) face with a 45° rotated lattice, as shown in the inset of Fig. 5.1 b. This is because the lattice constant a_{Fe} matched well with the half of the diagonal of the FCC lattice of MgO ($d_{MgO}/2 = \sqrt{2} \cdot a_{MgO}/2 = 2.97 \text{ \AA}$), which gives the lattice mismatch of

$$\eta = \frac{a_{Fe} - d_{MgO}/2}{d_{MgO}/2} = -3.4\%. \quad (3.2)$$

This is a higher value as compared to the lattice mismatch between Fe lattice and the Au(001) substrate. The relatively high mismatch η together with the unfavorable relation of the surface free energies (2.9 J/m^2 for Fe and 1.1 J/m^2 for MgO [140,141]) could lead to a preferential island growth of the first Fe layers on MgO and thus to broken continuity of the Fe film in the ultra-thin regime. This may cause the observed differences in the magnetic and transport properties between the 1.0, 1.3 and 1.5 nm Fe films described in Sec. 5 and Ch. 6.

For Fe/Au(001) the calculation of η is similar, because Au adapts the FCC crystal structure as MgO, but with a lattice constant of $a_{Au} = 4.08 \text{ \AA}$ (the half of the diagonal is $d_{Au}/2 = 2.88 \text{ \AA}$) [132,142]. This leads to a mismatch of

$$\eta = \frac{a_{Fe} - d_{Au}/2}{d_{Au}/2} = -0.3\%. \quad (3.3)$$

The obtained LEED patterns from the Fe and Au stripes show sharp spots in a cubic arrangement. It can be shown that the reciprocal lattice for a BCC structure with the lattice constant a is a FCC structure with lattice constant $4\pi/a$. Therefore, the LEED pattern of Fe(001) face exhibits an FCC pattern with lattice constant $4\pi/a_{Fe}$ and the LEED pattern of Au shows a BCC pattern with lattice parameter $4\pi/a_{Au}$. Keeping in mind that the Fe lattice is rotated for 45° with respect to the Au lattice, the Fe and Au reciprocal lattice constants can be read as depicted in the LEED patterns in Fig. 3.4 a,b. The obtained ratio of the lattice parameters $a_{Au}/a_{Fe} = 1.4$ is in a good agreement with the reported values [101,132,142].

X-ray absorption spectroscopy (XAS)

The Fe films on MgO(001) substrate were grown in UHV conditions, where the gas density is extremely low (e.g at 10^{-10} mbar there are more than ten orders of magnitude less molecules per cubic meter than at ambient pressure). Therefore, when the produced thin film heterostructures are removed from UHV chamber they are exposed to an increased density of molecules. A thin Fe film is highly reactive with O_2 and H_2O present in air and

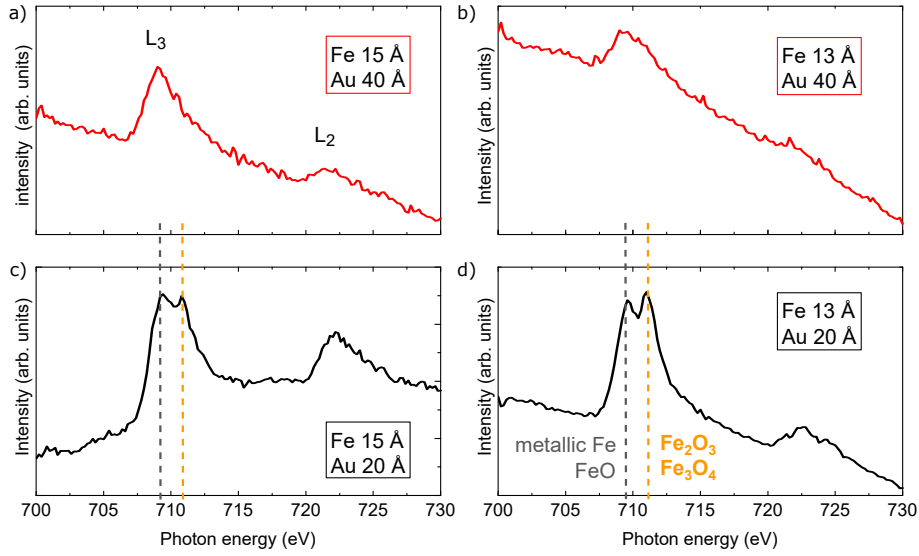


Figure 3.5: a) X-ray absorption spectra at Fe $L_{2,3}$ -edge measured from Au/Fe/MgO(001) heterostructures with varying Fe and Au layer thicknesses. The peaks of the L_3 and L_2 edges are more pronounced for the samples with 15 Å Fe layer thickness in **a** and **c**. For the 20 Å Au capping layer (in **c** and **d**) we find two peaks at the L_3 -edge, which correspond to the oxidation states of Fe with different valence state, as marked in **d**.

forms iron-oxides and iron-hydroxides when exposed to air. Contrary to Fe, Au is much less reactive and, when thick enough, can be used as a capping layer for many materials in order to protect them from oxidation. However, in the case when the Au layer is only several monolayers thick (needed in the SOT heterostructures, for example) its continuity might be broken.

Therefore, the influence of the Au layer thickness on the Fe film properties was investigated by X-ray absorption spectroscopy (XAS) at the beamline UE56-1_SGM of the storage ring BESSY II in Berlin. Here, only a brief description of the experimental technique will be provided, more on this topic can be found in Ref. [143]. In XAS experiments photons with varying energy of several hundreds of eV are directed to the sample. Depending on the elements and their chemical bonding in the sample the photons with specific energies will be absorbed by the system. This element specific energy dependence of the X-ray absorption provides the chemical sensitivity of XAS. By measuring the X-ray absorption edge of an element, its oxidation state may as well be identified.

The XAS $L_{2,3}$ -edge of Fe was measured for samples with 1.3 nm and 1.5 nm Fe layer thickness and a Au capping layer with 2 nm and 4 nm thickness. The XAS spectra acquired from the samples with 4 nm Au capping layer (Fig. 3.5 a,b) are characterized by two broad peaks at ~ 709 eV and ~ 721 eV photon energy. These two peaks correspond to electronic transitions between the occupied 2p core levels and the unoccupied 3d-like states in the electronic structure of Fe. The peak signal to background ratio for the thinner Fe film sample is reduced, therefore at the L_2 -edge the peak at 721 eV is almost not visible.

3.2. Growth characterization using surface analysis techniques

For the thinner Au capping layer, the XAS spectra in Fig. 3.5 c,d show a more pronounced peak at the L_2 -edge. This is because of the reduced scattering of electrons in the top Au layer, which increases the Fe signal. Moreover, the L_3 -edge for the sample with 2 nm Au thickness consists of two peaks separated for ~ 1 eV. The additional peaks arise from different oxidation states of Fe, namely FeO, Fe₂O₃ and Fe₃O₄ [144]. This means that the oxidation of Fe is increased in the samples with the thinner, 2 nm capping Au layer.

In conclusion, the presented in situ growth characterization of Fe/Au(001) and Fe/MgO(001) epitaxial systems has confirmed the high crystalline quality of the MBE grown Fe films. The microscopic study of Fe/Au(001) has shown an increased segregation of Au at temperatures beyond 200°. Therefore, the reversed stacking, namely Au/Fe, is preferred for transport investigations in order to ensure the stability of the structure also at elevated temperatures, which are a consequence of thermal effects due to Joule heating in transport experiments. Ultra-thin Fe films grown on MgO(001) arrange in a BCC lattice rotated for 45° with respect to the FCC lattice of MgO. A 2 nm capping layer of Au is not sufficient to prevent oxidation of the underlying Fe film and therefore, a 4 nm top Au layer was used in the heterostructures, which were lithographically patterned into Hall bars for further magneto-transport measurements. The patterning of Au/Fe/MgO(001) heterostructures and the experimental methods used for the magnetic characterization of the system will be described in next chapter.

4. Experimental methods for magnetic characterization

Two main experimental techniques were employed to study the magneto-transport properties and the current-induced effects in Au/Fe/MgO(001) patterned into Hall bars. *Magneto-transport measurements* were used to measure the magneto-resistance effects such as the anisotropic magneto-resistance (AMR), the planar Hall effect (PHE) and the anomalous Hall effect (AHE). Additionally, *Kerr microscopy* combined with the transport setup (in a single instrument) was employed to investigate the magnetic domain structure. Both experimental techniques are presented in the following.

4.1 Fabrication of Hall bars

The samples under investigation in this thesis were grown by Thomas Jansen (Peter Grünberg Institut (PGI)-6). The Fe films with thicknesses $t_{\text{Fe}}=1.0$ nm, 1.3 nm, 1.4 nm, 1.5 nm were deposited at room temperature using MBE, as described in Sec. 3.2. On top of the Fe film a 4 nm thick layer of Au was deposited. The rate of the MBE deposition was 0.1 Å/s. The epitaxy was controlled by low energy electron diffraction (LEED) and the cubic pattern similar to the one in Fig. 3.4 with slightly broader spots was observed from the top Au layer. Note, that a good indication of the crystalline quality of the Fe film is the observation of a well defined cubic magnetic anisotropy along the principle axes of the crystal, which will be discussed in Sec. 5 and in Ch. 6.

The photolithography of the Hall bar pattern was done in the clean room of PGI-7 at Forschungszentrum Jülich. The lithography process included several steps, which are illustrated in Fig. 4.1. For the photolithography of the Hall bar pattern a protective photoresist layer was used on top of the areas with the desired pattern and the rest was etched away with reactive ion-beam etching (RIBE) Fig. 4.1 a-c. The Hall bar pattern was aligned to the sample so that the Hall bars were along the Fe[1 $\bar{1}$ 0] direction. A 20 nm MgO layer was deposited on top of the samples to protect the Hall bars from oxidation (Fig. 4.1 d). Afterwards, the remaining photoresist (together with the MgO layer on top) was removed in the lift-off process, Fig. 4.1 e.

A negative photolithography step followed for patterning of the contact pads. For this purpose, a mask with the shape of the contact pads was used so that during the negative process only the parts of the Hall bars for the contact pads were not covered by the photoresist, see Fig. 4.1 f. On top, a 300-500 nm thick Au layer was sputter deposited and the remaining photoresist was again removed in the lift-off process, see Fig. 4.1 g and h. An image of the final Hall bar pattern used is shown in Fig. 4.2 b.

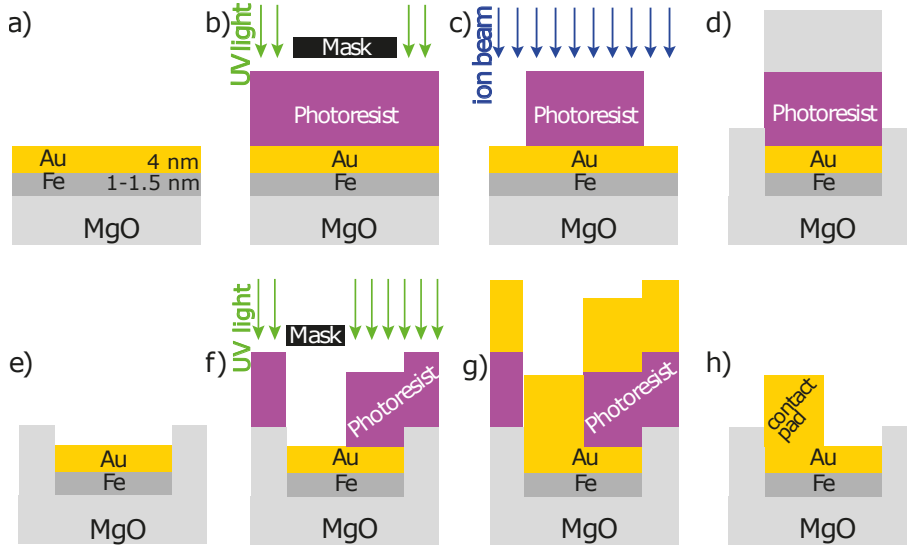


Figure 4.1: The Hall bar structures were patterned from the molecular beam epitaxy (MBE) grown heterostructures (a) by photolithography. b) The sample was coated with photoresist material and exposed to UV light under a mask with the Hall bar pattern. c) The exposed photoresist was removed with a developer and the material underneath was dry etched with a reactive ion beam (RIE). d) MgO was deposited to protect the Fe film from oxidation at the sides. e) The MgO deposited on top of photoresist was removed in the *lift-off* process. f) With the negative photolithography, the photoresist was developed to cover entire sample except the areas of the contact pads. g) A thicker layer (300 - 500 nm) of Au was sputter-deposited on the sample and removed with the lift-off process from the areas covered with the photoresist (h).

4.2 Magneto-transport measurements

The magnetic and electronic properties of materials can be characterized by measuring the magneto-resistance effects, such as AMR, PHE or AHE (discussed in more detail in Sec. 2.4). The magneto-transport measurements are typically performed by detecting the electrical response of a sample to an externally applied magnetic field B . Therefore, the sample is electrically connected to a current generator and a voltmeter, and placed in a magnetic field with a variable intensity and direction.

The magneto-transport measurements in the present thesis were performed at low temperatures using a liquid-He cryostat. The cryostat is located between two water-cooled electromagnets of a Helmholtz coil, in the area of a uniform magnetic field, see Fig. 4.2 a. The Helmholtz coils contain an iron yoke, which allows one to achieve a uniform magnetic field of up to ~ 2 T by regulating the electric current applied to the electromagnets. The sample is mounted on a rotatable rod in the cryostat, which is connected to a step motor for automatic rotation of the sample. In this way the orientation of the sample with respect to the magnetic field direction can be controlled.

For a reliable and stable electric contact, the samples with the patterned Hall bars

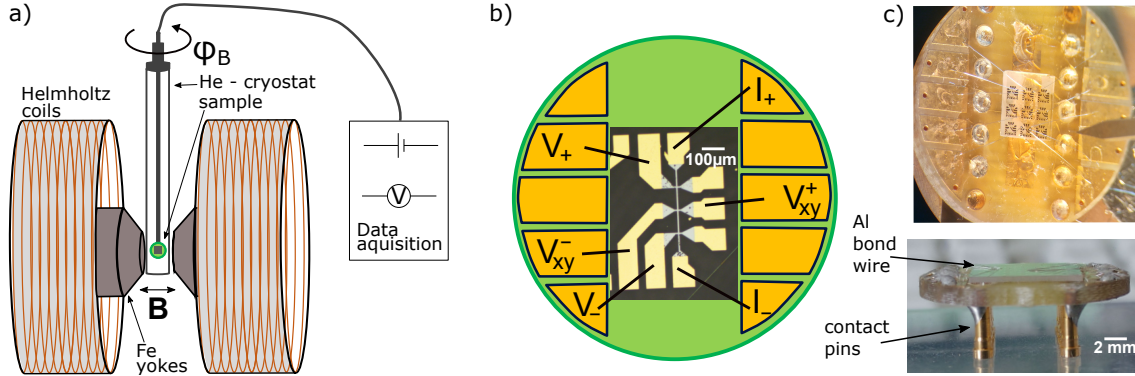


Figure 4.2: **a)** Schematic illustration of the magneto-transport experimental setup. The sample is mounted on a chip carrier (in green) on the bottom of the He-cryostat rod, which is placed between the electromagnets of the Helmholtz coil with iron yokes. The rotatable cryostat rod contains the cables leading from the contact pads on the chip carrier to an external voltage generator/meter, marked with the corresponding symbols. **b)** A schematic of the chip carrier with a microscopic image of an exemplary Hall bar with three Hall crosses. The current is applied between I_- and I_+ , the longitudinal voltage is measured between V_- and V_+ and the transversal Hall voltage between V_{xy}^- and V_{xy}^+ . **c)** Photographs of the chip carrier with a mounted sample containing 9 Hall bar structures. The bottom image is a side view of the chip carrier where the contact pins and the Al bonding wires can be seen. The latter were bonded almost flat to the sample surface to allow for transport measurements in front of the Kerr microscope.

are mounted onto a chip carrier using Al bonding wires. The chip carrier is mounted to the end of the cryostat rod, which is a bulk copper piece, which can be heated with a resistance heater to control the temperature at the sample. Each pin of the chip carrier is connected to a wire leading through the inside of the cryostat rod and a feed-through to a current generator (Keithley 2636) and a voltage meter (HP Agilent Keysight, 3458A). The magnetic field in the close vicinity of the sample was controlled via a magnetometer (Magnet-Physik FH 55) with a Hall probe.

The Hall bar pattern was designed in a way that along the bar three Hall crosses can be used for magneto-transport measurements, but also the longitudinal magnetoresistance can be measured in a four-point geometry, Fig. 4.2 b. The *longitudinal voltage* is measured between the contacts V_- and V_+ , while the *transversal voltage* V_{xy} is measured in the Hall geometry between the contacts marked with V_{xy}^- and V_{xy}^+ . The following experimental geometries were used for the acquisition of the data presented in this thesis:

- *Magnetic field scan:* A chosen constant direct current (DC) is applied along the Hall bar (between I_- and I_+ in Fig. 4.2 b) while the voltage is measured in dependence of a varying external magnetic field. The magnetic field is scanned in discrete steps along a selected direction (in-plane or perpendicular to the surface) with an amplitude ranging from $-B$ to B and vice versa. For each step in B , the voltage is read out, either between the V_- and V_+ contacts for the longitudinal resistance or between V_{xy}^- and V_{xy}^+ contacts for the transversal resistance.

- *Magnetic field scan angular dependence:* The *magnetic field scan* (see above) experimental procedure is repeated for each step of the rotation of the sample around its surface normal. In this way, the magnetic field is scanned along different in-plane directions.
- *Magnetic field rotation:* A constant magnetic field is applied parallel to the sample plane and the sample is rotated around the surface normal in steps of 5° or 10° . At each angle the DC current I is applied between the L and I_+ contacts and is varied from $-I$ to I . For each current the transversal voltage was measured between the V_{xy}^- and V_{xy}^+ contacts.
- *Switching* A current resulting in a high current density ($>10^6$ A/cm 2) is applied between the L and I_+ contacts for a short period of time (<1 s). Subsequently, the transversal voltage between the V_{xy}^- and V_{xy}^+ contacts is read out by applying a smaller current density ($<10^6$ A/cm 2). Usually a small constant magnetic field of up to ~ 5 mT is applied either parallel or perpendicular to the Hall bar in order to induce a certain rotation of the magnetization.

4.3 Kerr microscopy

Kerr microscopy is a microscopic technique used for observation of the magnetic domain structure in magnetic materials. It is based on the interaction of light with spin-polarized electrons. The manifestations of this interaction were first observed by Faraday already in 1845 [145] and 30 years later by Kerr [146] using light reflected from magnetized materials. The latter observations are today known as the magneto-optical Kerr effect (MOKE). Almost a century later it was established that the observed magneto-optical effects are a consequence of the spin-orbit coupling [147]. In this section, following a short introduction to MOKE, the specific Kerr microscopy setup used in this thesis will be presented.

4.3.1 Magneto-optical Kerr effect (MOKE)

As observed by Kerr [146], linearly polarized light reflected from a magnetized sample experiences a rotation of the polarization with respect to the polarization of the incident light. This rotation, also called the *Kerr rotation* φ_K , is related to the interaction of photons with the spin-polarized band structure of the magnetized material. The magnetization of the material can be either induced by an external magnetic field or can be spontaneously present, as for example in ferromagnets. The magnetic ordering in the material leads to time-reversal symmetry breaking, which manifests via spin-orbit coupling (SOC) as magnetization-dependent asymmetry of the electronic band structure of the system.

The effect of the magnetization on the symmetry of the system could not occur without the SOC [148]. Because SOC couples the spin and orbital character of the electronic

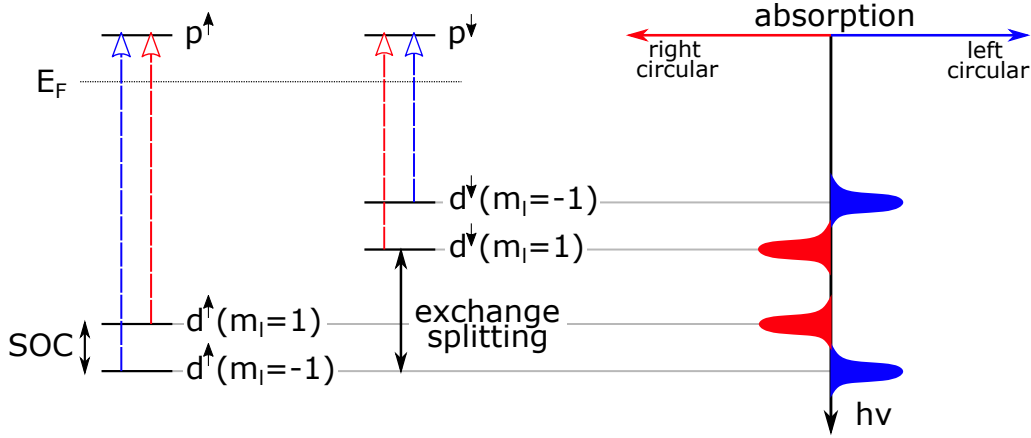


Figure 4.3: Illustration of the p-d optical transitions in a ferromagnetic material, which follow the dipole selection rules for the left (blue) and right (red) circular light. Because of the exchange and spin-orbit interaction splitting of the d levels, the absorption of the photons for each circular polarization varies with the photon energy $h\nu$.

states, changes to the spin of the electrons will also affect their orbital angular momentum. In Sec. 2.4.1 the magnetization-dependent symmetry of a ferromagnet was shown to manifest itself in the anisotropy of the phenomenological electric conductivity tensor of the system, which can be used for description of the magneto-resistance effects. The symmetry breaking due to spontaneous magnetization and SOC are reflected also in the optical properties of the material. In analogy to magneto-resistance, the *magneto-optical* effects can be described using the anisotropic optical conductivity tensor [148,149].

The optical conductivity tensor is a phenomenological description of the optical properties of a material. The tensor elements are related to the absorption of the photons with the energy $h\nu$ (h is the Planck constant and ν is the frequency of the electromagnetic wave of light) by the electrons transiting between the occupied and unoccupied states in the band structure of the material. In a bulk crystal the transitions are limited to the transitions between the states with the same wave vector \vec{k} (i.e. vertical transitions). Moreover, the transitions need to correspond to the dipole selection rules [148,149], which in the case of the 3d ferromagnetic metals allow the transitions between s- and p- and between p- and d-like states. The probability of each transition is determined by the matrix element, which depends on the symmetries of the initial occupied and final unoccupied states as well as on the polarization and energy of the incident photon.

The magneto-optical Kerr effect is associated to the off-diagonal elements of the tensor, which are determined by the difference in the absorption of the photons with opposite circular polarization [149]. In bulk ferromagnetic metal (FM) crystals the difference in absorption arises from the simultaneous presence of the exchange interaction and SOC. An illustrative example, given in Ref. [149], is to analyze the optical transitions to p levels from the exchange split d states in the atomic picture, sketched in Fig. 4.3. The exchange interaction shifts the d levels with minority spin character closer to the Fermi level. More-

over, the SOC splits the degenerate d levels according to their m_l quantum number, so that the state with $m_l=1$ ($m_l=-1$) obtains a higher energy for majority (minority) spin states. The dipole selection rules allow transitions from the majority d state with $m_l=1$ to majority p states mediated only by the left circular light and from the majority d state with $m_l=-1$ to majority p states mediated by the right circular light. The opposite rules apply to the minority states. Because the initial states of the discussed transitions are split in energy by the exchange and spin-orbit interaction (SOI), the absorption of the left and right circular light varies with the given photon energy, see Fig. 4.3. Linearly polarized light can be described as a sum of left- and right-handed circular light by adjusting the phase between them. After the interaction with the system, the photons with left- and right-handed circularity experience different absorption. After the interaction their sum leads to a rotated polarization, i.e. Kerr rotation φ_K , and a change of the ellipticity, i.e. Kerr ellipticity ϵ_K .

The Kerr effect usually has a very small magnitude (φ_K is typically of the order of 0.1° [150]). In general, however, the Kerr rotation is proportional to the magnetization component parallel to direction of the reflected light, see Fig. 4.4 a. If the magnetization is reversed, also the Kerr rotation reverses. Hence, by analyzing the Kerr rotation φ_K , information on the orientation of the magnetization can be obtained.

A detailed discussion on how to employ MOKE to resolve the magnetization orientation in microscopy can be found in Ref. [58]. Different geometries of MOKE can be used for Kerr microscopy. The MOKE geometry depends on the orientation of the magnetization and the light incidence angle Θ_0 on the surface. When the magnetization of the sample is aligned with the surface normal, MOKE is strongest when the incident light is aligned to the surface normal as well. This is known as the *polar* Kerr effect. The difference in the Kerr rotation is highest for parallel and anti-parallel alignment of the incident light direction and the orientation of the magnetization. For an in-plane magnetization, the MOKE signal is increased for grazing angle of the incident light ($\Theta_0 > 0$) and when the magnetization direction lies in the incidence plane of the light, see Fig. 4.4 a. This geometry is known as the *longitudinal* Kerr effect and it will be used for the studies of the magnetic properties in this work. In specific cases, also *transverse* geometry can be used, where the incidence plane is perpendicular to the orientation of the magnetization.

4.3.2 Kerr microscopy experimental setup

The basic components of the MOKE microscopy setup used in this thesis are sketched in Fig. 4.4 b. The light (1) is directed through collecting lenses and a polarizer (2) to obtain a linearly polarized coherent beam. It is then reflected towards the sample, passing the focusing objective lens (3). The reflected light from the sample travels through the same objective to the imaging detector (4). On its way it passes another polarizer, here employed as an analyzer, which enables detection of the Kerr rotation of the reflected light.

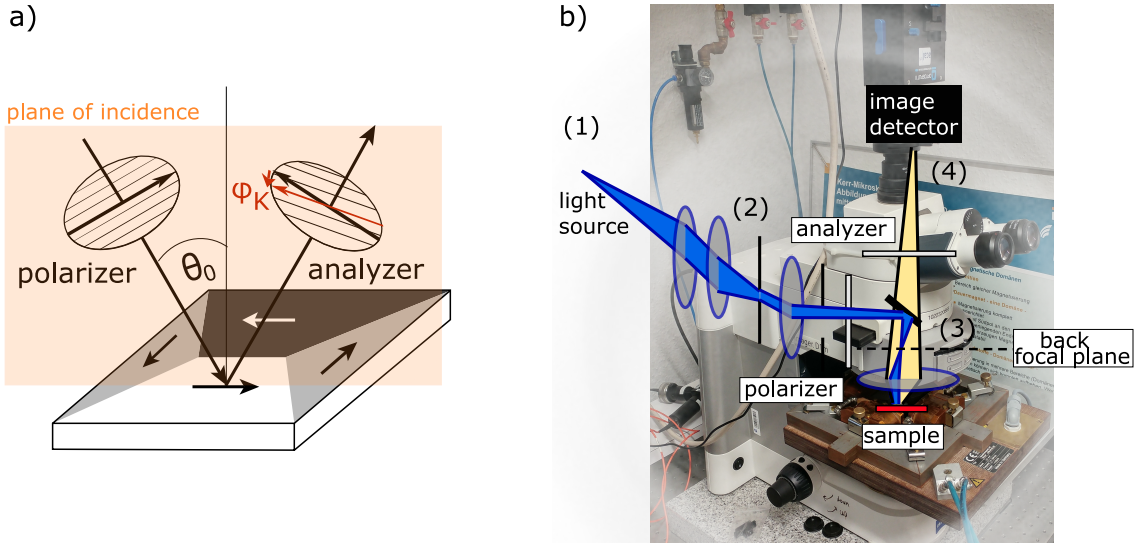


Figure 4.4: a) Schematics of the *longitudinal* Kerr geometry. The angle between the surface normal and the direction of incident light is $\Theta_0 > 0$. Before reaching the sample the light is linearly polarized by a polarizer, which is in this example oriented parallel to the incidence plane. The interaction with the sample results into a magnetization-dependent Kerr rotation φ_K of the light polarization. The polarization of the reflected light can be analyzed with another polarizer, the *so-called* analyzer. b) A photo of a commercial Kerr microscope with an illustration of the optical path of the light.

The desired MOKE geometry can be selected by imaging the light source onto the back focal plane of the objective (sketched in Fig. 4.4 b) with a polarizer and analyzer set perpendicular to each other. In this way a so-called *Maltese cross* is observed¹, see Fig. 4.5 b. Using a mechanical aperture one can select the light coming from the central area or either one of the arms of the Maltese cross to be used for illumination. If the central area is chosen for illumination, the *polar Kerr effect* can be observed, because the light will pass through the center of the objective lens towards the sample. If the light from one of the arms is chosen, it will pass the objective lens away from its center and under an angle. In the latter configuration an oblique illumination is achieved with a projection of the light polarization onto the sample surface and the *longitudinal Kerr effect* can be observed.

The above described mechanical alignment process on the Maltese cross can be avoided if light-emitting diode (LED) lamps are used as a light source. The Kerr microscopy images presented in this work were acquired using a MOKE microscope at IFW Dresden under supervision from Prof. Dr. Rudolf Schäfer and Dr. Ivan Soldatov. As presented in detail in Ref. [151], light from eight unpolarized LED lamps is guided by glass fibers into a cross-like arrangement to mimic a Maltese cross. In this way, the incidence angle of light Θ_0 is set by simply switching on or off the selected LED lamps as it is shown in Fig. 4.5 b for

¹The Maltese cross is a reciprocal formation of all the different incident angles of light on the objective lens.

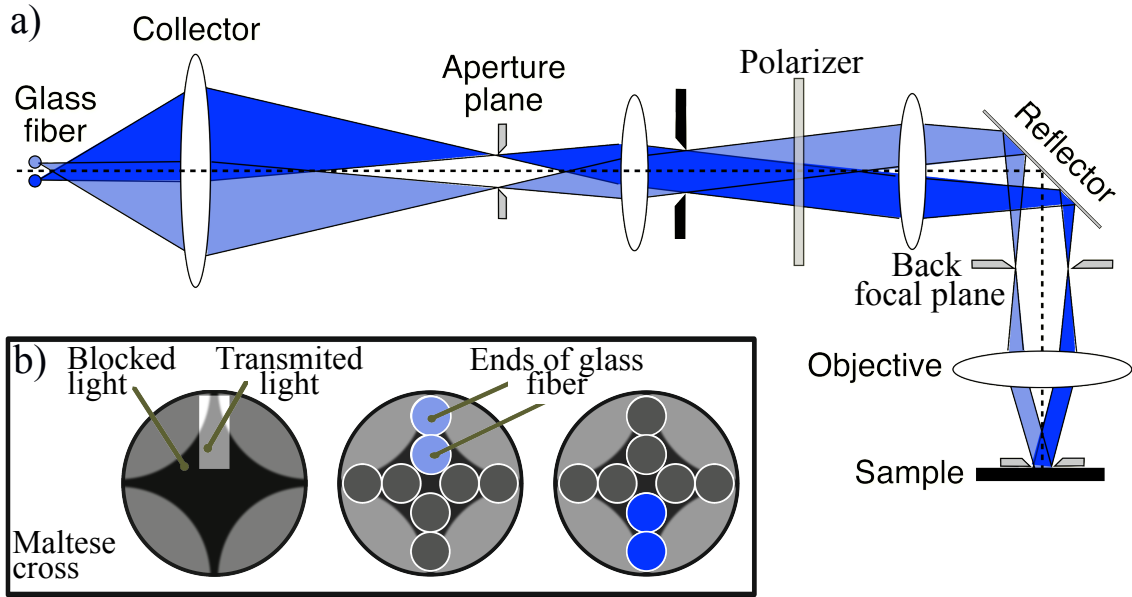


Figure 4.5: a) Illustration of the optical path of light in a Kerr microscope from the end of the fiber glass directing the light from the LED located to the top arm (light blue) and to the bottom arm (dark blue) of the Maltese cross as shown in b). The light from the top (bottom) leads to illumination of the sample from the left (right) in the sketch. b) Kerr geometry alignment set on the Maltese cross observed in the back focal plane (left) compared to the alignment by switching on/off the LED lamps on the top or bottom. With both procedures an oblique illumination of the sample is selected as shown in a). With permission adapted from Ref. [151].

the example of the longitudinal Kerr geometry.

Moreover, the novel LED light source can be used to achieve the so-called *pure in-plane* contrast in longitudinal Kerr microscopy. In any oblique geometry of incidence light onto the sample surface, the light polarization has a projection onto the in-plane as well as the out-of-plane direction of the sample surface. Therefore, the measured Kerr rotation (and along with it also the magnetic sensitivity) has contributions from both, in-plane and out-of-plane magnetization. This mixed sensitivity leads to a reduced contrast, which can be an obstacle especially for magnetic imaging of very thin films with an already low signal-to-noise ratio. The two contributions can be disentangled by summing (out-of-plane) or subtracting (in-plane) the images obtained using oblique incidence of light on the sample from the left and from the right (light and dark blue light path in Fig. 4.5).

The direction of incidence together with the angle of the analyzer define the direction of the magnetization, which gives higher intensity of the reflected light (i.e. bright domain), see Fig. 4.6. For the same orientation of the analyzer and opposite direction of light incidence the direction of the magnetization for the bright domains is reversed. Therefore, subtraction of the image obtained with illumination from the right from the image with illumination from the left results in a pure in-plane sensitivity (see Ref. [151,152] for further explanation). Furthermore, with this procedure, the magnetic contrast is doubled. This

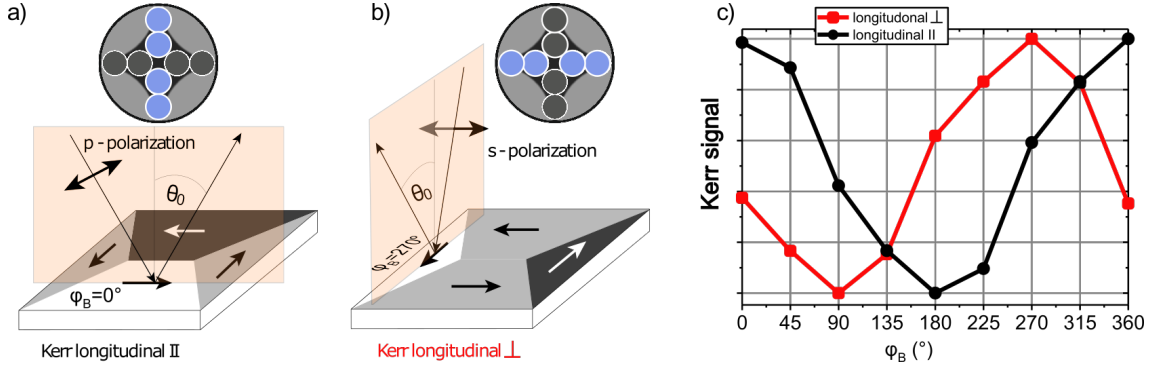


Figure 4.6: The pure in-plane geometry for Kerr microscopy. The chosen combination of LED lamps defines the direction of the Kerr sensitivity. The orientation of the polarizer is fixed to be parallel to the top-bottom orientation of the LED lamps and therefore gives **a)** p-polarized light for the top-bottom combination of the cross and **b)** s-polarized light for the left-right combination of the cross selected for illumination of the sample, see also Fig. 4.5. **c)** Kerr signal measured for different directions φ_B of the applied magnetic field close to saturation ($B \sim 10$ mT). In the Kerr longitudinal \parallel geometry (black) the Kerr signal shows a maximum for $\varphi_B = 0$ and in the Kerr longitudinal \perp geometry (red) the maximum is at $\varphi_B = 270^\circ$.

is an important improvement in Kerr microscopy of ultra-thin magnetic films, showing usually only a weak in-plane Kerr contrast.

The magnetic sensitivity was set by choosing either the top and bottom or left and right pair of LED lamps to obtain the pure in-plane contrast. The orientation of the polarizer was fixed to the direction parallel to the top bottom orientation of the LED lamps, giving either p-polarization or s-polarization of light (sketched in Fig. 4.6 a,b). The sample was fixed on a holder in front of the objective and between the coils of a small quadrupole electromagnet, which was used to provide an in-plane field B in any chosen direction φ_B of up to 40 mT. By measuring the Kerr signal, i.e. rotation of the polarization of light reflected from the sample, for different directions of the applied saturating magnetic field the direction of the Kerr contrast can be identified. The measured Kerr signal for two orientations of the incidence plane of light are shown in Fig. 4.6 c. The signal is proportional to the sine of φ_B , i.e. the direction of the magnetization in the sample plane.

Kerr microscopy combined with transport setup

To combine the Kerr microscopy with the transport measurements the sample with the Au/Fe/MgO(001) Hall bars mounted on the magneto-transport chip carrier (see Sec. 4.2) was placed in front of the objective lens of the Kerr microscope. The connecting pins of the chip carrier were connected with a Keithley multimeter to apply or measure voltages. In this way, Kerr microscopy images can be acquired simultaneously with transport measurements. The obtained angular dependence of the planar Hall resistance R_{xy} (see Sec. 2.4.2) measured in the Kerr microscopy setup is shown in Fig. 4.7 b. Moreover, the magnetic domain structure can be studied not only as a function of external magnetic fields but

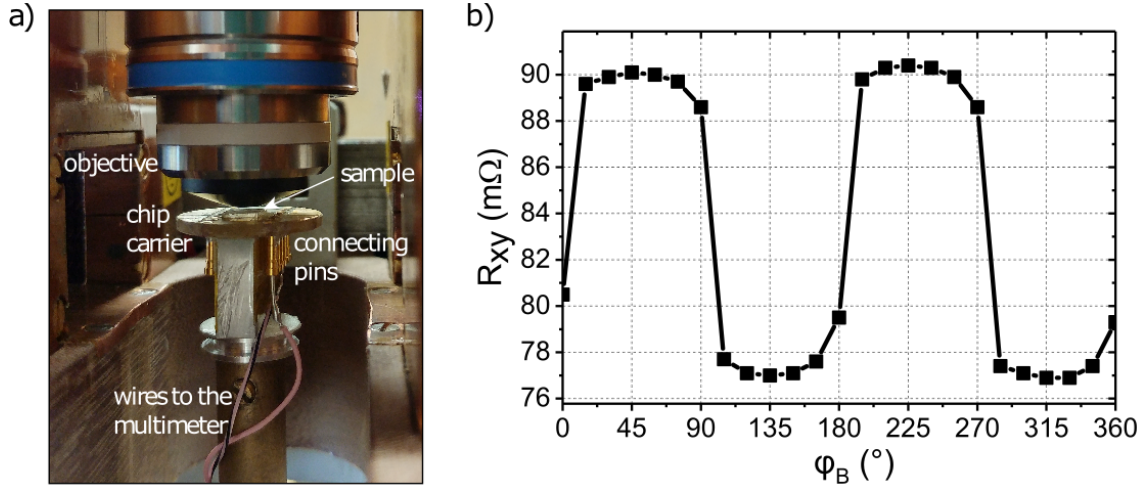


Figure 4.7: a) Sample with Au/Fe/MgO(001) Hall bars mounted on the chip carrier in front of the objective lens of the Kerr microscope. The pins of the chip carrier are wired to a Keithley multimeter. b) The planar Hall effect measured in the Kerr microscopy setup. A saturating magnetic field of 40 mT was applied along different in-plane directions and the transversal resistance R_{xy} was measured in the *magnetic field rotation* geometry (see Sec. 4.2). The longitudinal current was 1 mA.

also as a function of external electric fields. This enables spatially resolved microscopic investigations of current induced effects in magnetic thin films.

5. Magnetic properties of Au/Fe/MgO(001)

The main aim of the present study is to investigate the current-induced effects in a single crystalline model system containing a ferromagnetic layer with T_C well above the room temperature and a well-defined in-plane magnetic anisotropy. Therefore, it is of particular interest to characterize the magnetic anisotropy in the Au/Fe/MgO(001) epitaxial heterostructures with Fe layer thickness between 1-1.5 nm. In this chapter the characterization of the magnetic properties of the system is shown. The magneto-transport characterization provides information averaged over a region of the electrically contacted Hall cross. Additionally, the microscopic information is needed for gaining understanding towards the complete picture of the magnetization reversal and the domain structure of the Hall bars.

The magnetic state of Au/Fe/MgO(001) Hall bars was characterized based on the extracted hysteresis loops from Kerr images (Sec. 5.1). Further, the AHE was measured to confirm the in-plane magnetic anisotropy (Sec. 5.2) and the PHE measurements were employed to determine the anisotropy constants of the in-plane cubic magnetic anisotropy (Sec. 5.3). Finally, the magnetic domain structure of the Hall bars was studied using Kerr microscopy and, in combination with magneto-transport measurements, the influence of the domain structure on the PHE was investigated (Sec. 5.4).

5.1 Magnetic hysteresis in Kerr microscopy

In Kerr microscopy, hysteresis loops can be extracted from a selected region of interest (ROI) in the field of view by acquiring a stack of Kerr images for different values of the external magnetic field. Figure 5.1 a shows the portion of the Au/Fe(1.5 nm) Hall bar visible in the field of view of the Kerr microscope using a 50x zoom lens. The ROI was chosen to be the part of the Hall bar wire indicated by the yellow frame. In the chosen Hall bar orientation, the Fe[1 $\bar{1}$ 0] direction is along the bar and the principal directions Fe[100] and Fe[010] are along the diagonals of the Hall bar as described in Sec. 3.2.2 and 4.1.

The extracted hysteresis loops for the magnetic field applied along the Fe[100] and Fe[110] directions at room temperature are shown in Fig. 5.1 b. The Kerr sensitivity was set parallel to the external field B_{ex} direction. The measured Kerr signal is therefore proportional to the projection of the magnetization on the direction of the applied field, see Sec. 4.3. Because the magnetic layer, which is the origin of the Kerr signal, is ultra thin ($t_{Fe}=1.5$ nm), the measured intensity shows a relatively high noise level. For the magnetic field B_{ex} applied along the Fe[100] direction a square hysteresis loop was obtained with a

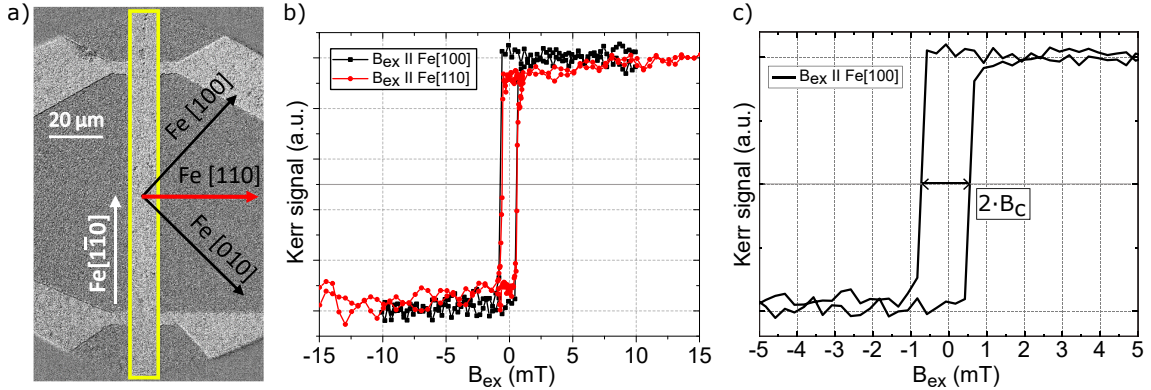


Figure 5.1: Magnetic hysteresis loops obtained using a Kerr microscope from the Au/Fe(1.5nm) Hall bar wire sketch in **a)**. The principal directions of the MgO and Fe(001) lattice are marked with arrows. **b)** Hysteresis loops acquired with field applied along the Fe[100] easy axis (black) and Fe[110] hard axis (red). **c)** Zoom into the acquired easy axis hysteresis loop.

sharp magnetization jump from Fe[$\bar{1}00$] to Fe[100] (black loop in Fig. 5.1 b and c). Such a hysteresis loop is typical for a magnetization reversal along the *easy magnetization axis*. Similarly, for the B_{ex} scan along the Fe[110] direction the hysteresis also shows a sharp magnetization jump, which is however followed by a minor, gradual increase (decrease) of the Kerr signal for the positive (negative) side of the B_{ex} scan (red loop in Fig. 5.1 b). This gradual change of the Kerr intensity after the magnetization jump is due to the coherent rotation of the magnetization towards the direction of the applied B_{ex} . The reduced remanence, visible as a decreased Kerr signal at $B_{ex}=0$, and the coherent rotation are both characteristic for the magnetization reversal along the *hard magnetization axis*. The difference in the Kerr signal in the two loops after the magnetization jump appears small because it is proportional to the cosine of the angle θ between the magnetization and the field B_{ex} direction (for $\theta=0^\circ-45^\circ$ the Kerr signal reduces for up to $\sim 30\%$). Nevertheless, the Fe[100] axis can be identified as an easy magnetization axis and the Fe[110] as a hard magnetization axis. The coercive field B_c of the 1.5 nm Fe film was determined from the easy axis hysteresis loop as shown in Fig. 5.1 c. From the width of the hysteresis loop a value of $B_c = 0.65 \pm 0.07$ mT can be extracted.

The details of the magnetization reversal along the Fe[110] hard axis (i.e. perpendicular to the Hall bar) are revealed by comparing the hysteresis loops obtained for different directions of the Kerr sensitivity. The hysteresis loops for B_{ex} applied along the Fe[110] hard axis are shown in Fig. 5.2. The Kerr contrast was set either parallel to the B_{ex} direction (Fig. 5.2 a) or parallel to the Fe[100] easy axis (Fig. 5.2 b). The full line marks the Kerr signal obtained for the positive scan of the magnetic field (i.e. from $B_{ex}<0$ to $B_{ex}>0$) and the dash-dotted line marks the negative scan (i.e. from $B_{ex}>0$ to $B_{ex}<0$). The two hysteresis loops in Fig. 5.2 a,b appear different. Major differences are in the Kerr signal at saturation and in the number of sharp changes of the Kerr signal, i.e. sharp jumps of the magnetization.

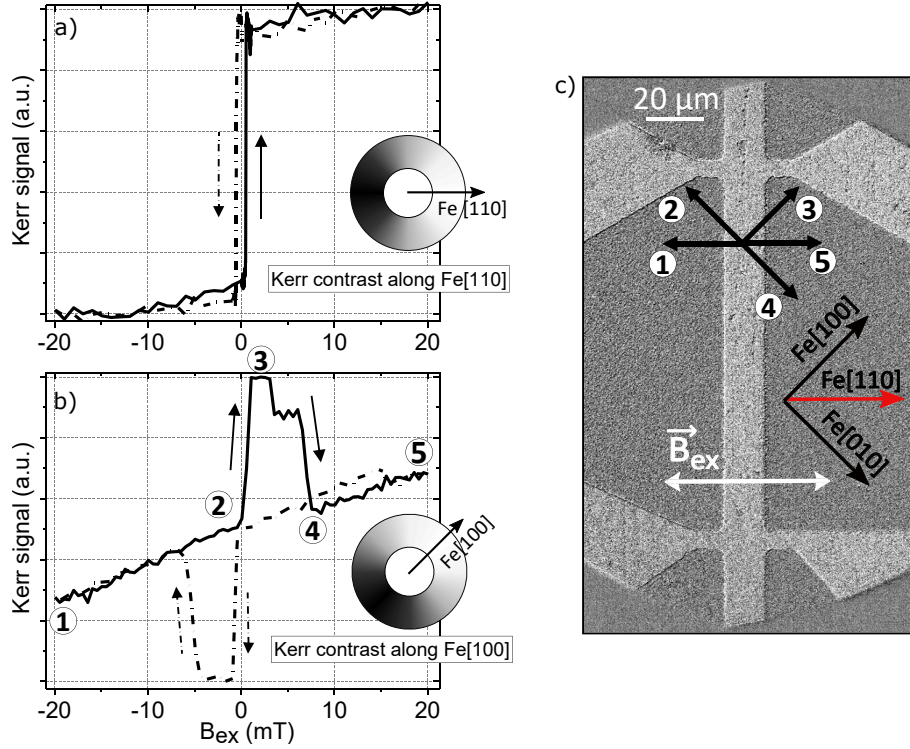


Figure 5.2: Kerr microscopy hysteresis loops obtained from the Au/Fe(1.5nm) Hall bar with magnetic field applied along the Fe[110] direction. The Kerr contrast was set along the Fe[110] direction in **a)** and along the Fe[100] direction in **b)**. In **c)** main crystallographic directions are marked as well as the 5 steps of the *double-jump* magnetization reversal process (see text). The corresponding points on the hysteresis loop are marked in **b)**. The full line marks the Kerr signal obtained for the positive scan of the magnetic field and the dash-dotted line marks the negative scan.

The hysteresis loop with the Kerr sensitivity set parallel to the B_{ex} direction (Fig. 5.2 a) resembles the loop for hard axis magnetization reversal shown in Fig. 5.1 b in red. Instead, when the Kerr sensitivity is set along the Fe[100] easy axis, the positive B_{ex} scan of the hysteresis loop (full line in Fig. 5.2 b) can be described in 5 steps. Starting at $B_{ex} \sim -20$ mT (step 1), the magnetization can be assumed to be approximately aligned with B_{ex} direction along the Fe[$\bar{1}\bar{1}$ 0]. When the magnetic field is gradually decreased, the magnetization coherently rotates towards the closest easy direction. This results in a gradual increase of the Kerr signal up to the step 2. The closest easy axis is most probably in this case determined by a small misalignment of B_{ex} with respect to the Hall bar. The gradual increase of the Kerr signal indicates that the closest easy axis is the Fe[0 $\bar{1}$ 0], because of its orientation perpendicular to the Kerr sensitivity direction. After crossing zero field the magnetization jumps from Fe[0 $\bar{1}$ 0] \rightarrow Fe[100] (step 3), which results in a sharp increase of the Kerr intensity, because the magnetization aligns with the direction of the reflected light. With further increase of B_{ex} a second jump of the magnetization

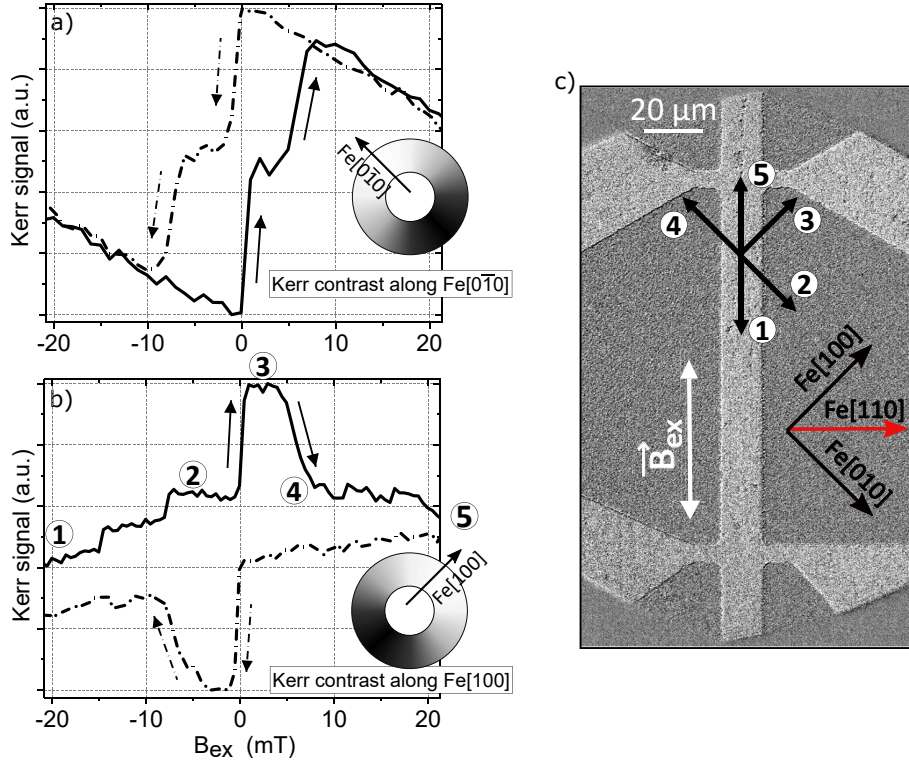


Figure 5.3: Magnetization reversal hysteresis loop for magnetic field applied along the direction parallel to the Au/Fe(1.5 nm) Hall bar and Kerr contrast set a) along the Fe[010] direction and b) along the Fe[100] direction. The hysteresis loops are complementary to each other and show the details of the double-jump magnetization reversal. c) A typical Kerr image of a portion of the Hall bar, on which the crystallographic directions are indicated and the steps of the double-jump magnetization reversal are marked corresponding to the steps of the hysteresis loop in b).

is observed at ~ 6 mT (step 4). Because the Kerr intensity at the position 4 after the jump reaches an intermediate value, the corresponding orientation of the magnetization can only be perpendicular to the direction of the reflected light, i.e. the Fe[010] direction (see grey scale ring in 5.2 b). Further increase of B_{ex} coherently rotates the magnetization towards the magnetic field direction (step 5). The steps of the magnetization reversal are sketched in Fig. 5.2 c.

A similar magnetization reversal process is observed also when the external magnetic field B_{ex} is scanned along the Fe[110] direction, i.e. parallel to the Hall bar. In Fig. 5.3 a,b the hysteresis loops for B_{ex} applied along this hard axis are shown. Here, the Kerr contrast was set along the two easy directions, namely the Fe[010] (Fig. 5.3 a) and the Fe[100] (Fig. 5.3 b). Because the sample was kept at the same position with respect to the microscope the hysteresis loops in 5.3 a and b can be directly compared. Together, the two loops represent the full picture of the magnetization reversal, which can be described by the following 5 steps (see Fig. 5.3 c) as introduced already for the magnetization

reversal along the Fe[110] hard axis. After the saturation of the magnetization along the Fe[$\bar{1}10$] the magnetization rotates towards the Fe[010] (step 1 to 2), the sense of rotation is most probably a consequence of a small misalignment of the magnetic field direction with respect to the Hall bar, see Sec. 5.3. The rotation of the magnetization towards the Fe[010] axis results in a gradual decrease of the Kerr signal to the minimum value when the Kerr contrast is set to the Fe[0 $\bar{1}0$] direction (see Fig. 5.3 a). On the other hand, the rotation leads to an intermediate value of the Kerr signal in the case of Kerr contrast along the Fe[100] direction (step 2 in 5.3 b). The first sharp jump in Kerr signal (step 2 \rightarrow 3) is related the magnetization jump from Fe[010] \rightarrow Fe[100]. This results in maximum intensity for Kerr contrast along Fe[100] and intermediate contrast value for sensitivity along Fe[0 $\bar{1}0$]. The second sharp jump in Kerr signal (step 3 \rightarrow 4) is related to the magnetization jump from Fe[100] \rightarrow Fe[0 $\bar{1}0$], which results in maximum intensity for Kerr contrast set along the Fe[0 $\bar{1}0$].

Figures 5.2 and 5.3 demonstrate the magnetization reversal along the hard magnetization axes in the Au/Fe/MgO(001) Hall bars. The Fe[110] and Fe[$\bar{1}10$] axes (i.e. parallel and perpendicular to the Hall bar) can be identified as the hard magnetization axes, because when reducing the applied B_{ex} along these two directions, the magnetization tilts towards one of the easy magnetization axes, i.e. along the Fe[100] and Fe[010] directions. The magnetization reversal along the hard axes proceeds with two magnetization jumps in each direction of the magnetic field scan. This process will be referred to as the *double-jump* magnetization reversal throughout this thesis. The acquired hysteresis loops confirm that the magnetic anisotropy in the Hall bars is governed by the four-fold magneto-crystalline anisotropy of the Fe(001) film at room temperature. Moreover, the comparison of the hysteresis loops with different directions of the Kerr sensitivity clearly shows the 45° rotation of the Fe(001) crystal lattice with respect to the MgO(001) orientation, see also Sec. 3.2.2.

However, in the case of a perfect four-fold magnetic anisotropy and a precise alignment of the magnetic field along the hard axis, the second jump of the magnetization (e.g. step 3 \rightarrow 4) observed in Fig. 5.2 b and 5.3 b cannot be explained (see Appendix C). For this an additional anisotropy has to be introduced. The reason for an asymmetry can be a misalignment of the applied magnetic field or an additional uniaxial anisotropy, which makes one of the easy axes “easier”. The additional uniaxial magnetic anisotropy can originate from to the film structure, the interfaces to Au or MgO or the shape anisotropy, as discussed in Sec. 2.2 and 3.1.

We estimate the geometrical misalignment, necessary to explain the observed second jump of the magnetization, from the value of the B_{ex} at the second jump ($B_{2nd} \sim 6$ mT). Assuming the same coercive field for all easy directions $B_c \sim 0.65$ mT, a simple geometry requirement for the observation of the second switch is $B_{2nd} \cdot (\sin\varphi - \cos\varphi) = B_c$. The angle φ is the angle between the external B_{ex} and the easy axis and $\varphi = 45^\circ$ in perfect alignment of B_{ex} to the hard magnetization axis. For the obtained experimental values of B_c and

5.1. Magnetic hysteresis in Kerr microscopy

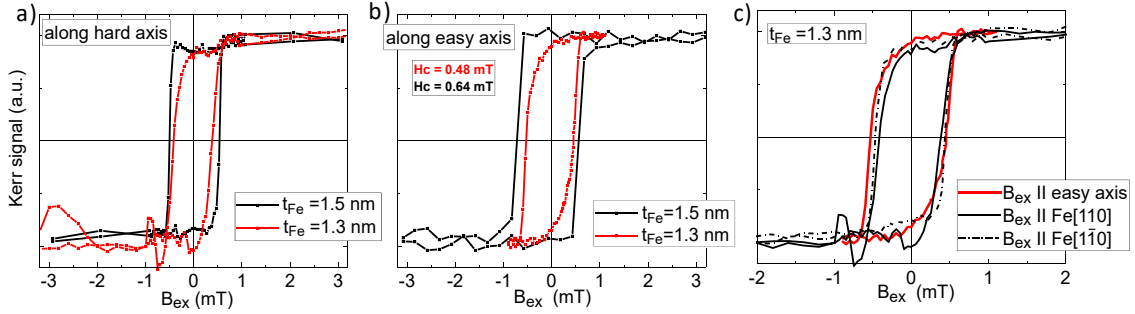


Figure 5.4: **a)** The hard axis hysteresis loops for Au/Fe Hall bars with 1.5 nm Fe thickness (black) and 1.3 nm Fe thickness (red). The Kerr contrast was set parallel to the applied field direction. **b)** Comparison of the easy axis hysteresis loops for Hall bars with 1.5 nm and 1.3 nm Fe thickness. **b)** The hysteresis loops for Au/Fe(1.3 nm) Hall bar with magnetic field scanned along the easy axis (red) and both hard axes (full and broken black lines).

B_{2nd} we obtain a misalignment of $\sim 4^\circ$, which is a reasonable value.

In the above discussion of the double-jump reversal a single magnetic domain picture was adapted. However, the considered Au/Fe Hall bars were observed to break into magnetic domains. While the phenomenological single domain picture describes well the main characteristics of the observed hysteresis loops, certain features can only be explained when the magnetic domain structure of the Hall bar is considered, see Sec. 5.4.

Kerr microscopy of the Au/Fe Hall bars with 1.3 nm Fe thickness revealed some difference in the magnetic properties compared to the Hall bars with the 1.5 nm Fe layer. The comparison of magnetic hysteresis loops is shown in Fig. 5.4. Despite the small thickness difference of nominally ~ 1 ML (considering an interlayer spacing of Fe-Fe $d_{Fe} \sim 1.4$ Å [132, 135, 142]), the shape of the extracted hysteresis loops from the Au/Fe(1.3 nm) Hall bars is more rounded compared to the loops from the Hall bars with Fe thickness of 1.5 nm. This is most probably due to a difference in the film morphology of the Fe layer. A change in the squareness of the hysteresis was, for example, reported in Ref. [29] to be induced by annealing of the ultra-thin Fe films to high temperatures. They observed a rounded hysteresis for Fe films, which were composed of interacting islands after annealing. This means that the roundness of the hysteresis is a consequence of averaging over several ferromagnetic Fe islands, which due to their different size and shape show different coercivity. Therefore, the rounded hysteresis loop might be an indication of a partial discontinuity of the 1.3 nm Fe film.

Moreover, the coercivity and roundness of the hysteresis loops for the Au/Fe(1.3 nm) Hall bars does not seem to depend on the crystalline direction, see Fig. 5.4 b. The hysteresis loops for B_{ex} along the easy axis exhibits the same roundness as the loops for B_{ex} along the hard axes. This property of the hysteresis loops is in contrast to the observations from the Hall bars with $t_{Fe}=1.5$ nm in Fig. 5.1 b. The loss of squareness of the easy axis hysteresis loop has been observed for magnetic films consisting of interacting

islands of different sizes. For example, the simulations in Ref. [29] show that hysteresis loops along an easy and a hard axis can appear identical when the islands form clusters of different sizes. A broader distribution of cluster sizes increases the coercivity, which results in increased roundness of the easy axis hysteresis loop. In this way, the shape of the hysteresis loop can seem to be independent on the crystalline direction. Moreover, for the Hall bars with 1.3 nm Fe film the coercivity is slightly reduced, see Fig. 5.4 b. This indicates that the thickness of the interacting Fe islands is probably below the expected 1.3 nm thickness and only several ML in height.

To conclude, the Kerr microscopy of the Au/Fe/MgO(001) Hall bars identifies the presence of in-plane cubic magneto-crystalline anisotropy with easy magnetization axes along the principal directions of the Fe film. Hall bars with 1.5 nm Fe layer exhibit a square hard-axis hysteresis loop and a coercive field of $B_c = 0.65 \pm 0.07$ mT. The magnetization reversal along the hard magnetization axis shows two sharp jumps of the magnetization for 90° between the in-plane easy directions and proceeds via formation and growth of domains. The reduced coercivity and crystalline-direction independent hysteresis loops observed for the 1.3 nm Fe films indicate a discontinuity of these films. The magneto-transport measurements and the Kerr microscopy of the magnetic domain structure presented in Sec. 5.3 and 5.4 provide further evidence of island formation in the 1.3 nm films.

5.2 Anomalous Hall effect characterization

In order to confirm that the magnetic easy axes in the Au/Fe/MgO(001) Hall bars with Fe thickness of 1-1.5 nm are aligned to the plane of the film, the AHE was measured in the magneto-transport setup, see Sec. 4.2. The external magnetic field B_{ex} ranging from -1500 mT to +1500 mT was applied along the Fe film normal and a small probing current density j was applied along the Hall bar ($j \sim 10^6$ A/cm²). Simultaneously, the induced transversal voltage V_{xy} was measured between two contacts across the Hall bar. The normalized AHE resistance R_{AHE} was obtained by dividing the measured V_{xy} by the applied longitudinal current and normalizing it to the limiting values. The results are shown in Fig. 5.5 a.

The measured R_{AHE} follows the same s-shaped response for the positive and the negative scan of B_{ex} . A linear behavior of the R_{AHE} is observed for small magnetic fields with the steepest slope for $t_{Fe} = 1.0$ nm. For high magnetic fields (>1000 mT) a plateau in R_{AHE} is reached. This indicates a full saturation of the magnetization along the B_{ex} direction, i.e. along the normal of the film. The saturating magnetic field scales proportionally with the Fe layer thickness. For $t_{Fe} = 1.5$ nm the saturating magnetic field in the out-of-plane direction is ~ 1000 mT. For $t_{Fe} = 1.0$ nm and 1.3 nm the saturating field is slightly reduced as compared to $t_{Fe} = 1.5$ nm and the AHE loops exhibit a more

5.2. Anomalous Hall effect characterization

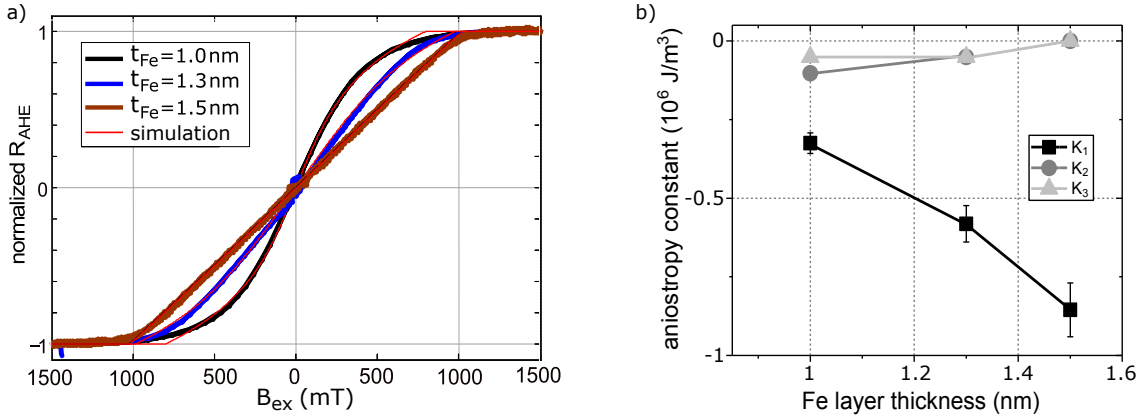


Figure 5.5: **a)** Measurements of the anomalous Hall effect (AHE) at 280 K on Au/Fe/MgO(001) Hall bars with different Fe layer thicknesses (black: $t_{Fe} = 1.0$, blue: 1.3 nm and dark red: 1.5 nm). An additional planar Hall resistance is observed in R_{AHE} measured from the Hall bar with $t_{Fe} = 1.3$ nm (blue) due to a misalignment of the external magnetic field. The AHE curves were simulated (thin red lines) by minimizing the Stoner-Wohlfarth equation for uniaxial anisotropy (see Appendix B). **b)** The out-of-plane magnetic anisotropy constants K_1 , K_2 , K_3 were determined from the best fit simulated curves. A constant saturation magnetization ($\mu_0 M_S = 2.1$ T) was used for all Fe thicknesses.

rounded shape for the regions close to the plateau. None of the measured AHE loops shows any hysteresis which means that there is no remanence in the out-of-plane direction. This is a clear indication of an in-plane magnetic easy axis.

The difference in out-of-plane saturating fields and the different shapes of the AHE loops for the samples with $t_{Fe} = 1.0$, 1.3 and 1.5 nm indicate an Fe thickness dependence of the magnetic anisotropy. To quantify the thickness dependence, the anisotropy constants were determined by minimizing the Stoner-Wohlfarth equation for the magnetic potential energy of a system with uniaxial magnetic anisotropy, see Appendix B. Equation 1.2 in Appendix B for the magnetic potential energy E_m gives

$$\begin{aligned}
 E_m = & -M_S B_{ex} \cdot \cos(0^\circ - \Theta_M) \\
 & -K_1 \cdot \cos^2(\Theta_M) \\
 & -K_2 \cdot \cos^4(\Theta_M) \\
 & -K_3 \cdot \cos^6(\Theta_M).
 \end{aligned} \tag{5.1}$$

The angle Θ_M is the angle between the film normal and the magnetization. The magnetic anisotropy terms up to the third order (i.e. sixth power of cosine function) with anisotropy constants $K_{1,2,3}$ were included in order to fit the measured data. The anisotropy constants $K_{1,2,3}$ corresponding to the best fitting simulated AHE curves (in red in Fig. 5.5 a) have negative values and for a small B_{ex} give a minimum of E_m at $\Theta_M = 90^\circ$, i.e. parallel to film plane. Therefore, the negative $K_{1,2,3}$ correspond to an in-plane magnetic easy axis. The constant K_1 decreases with increasing t_{Fe} , while the constants $K_{2,3}$ exhibit a positive

slope of the t_{Fe} dependence, see Fig. 5.5 b.

5.2.1 Contributions to the magnetic anisotropy

Each anisotropy constant $K_{1,2,3}$ can contain contributions from more than one anisotropy effect discussed in Sec. 2.2 and will be commented in the following. Firstly, the effect of the saturation magnetization value $\mu_0 M_S = 2.1$ T is considered, which was chosen as a constant value to obtain $K_{1,2,3}$ for all studied thicknesses. The reported thickness dependence of M_S [153] leads to a variation of $K_{1,2,3}$ within the error margin depicted in Fig. 5.5 b and therefore cannot explain the observed thickness dependence of $K_{1,2,3}$. The error of the $K_{1,2,3}$ values has the largest contribution from the uncertainty of the fitting parameters for the simulations (see Appendix B for details).

The $K_{1,2,3}$ constants with negative values keep the magnetization parallel to the film plane. The amplitude of the first term K_1 is two orders of magnitude larger compared to the in-plane cubic anisotropy constant K_4 (see Sec. 5.3). This is expected for thin magnetic films with high shape anisotropy contribution and a second-order cubic magnetic anisotropy. However, the data shows that the strong in-plane easy axis anisotropy decreases in amplitude for thinner Fe films. The second and third anisotropy constants $K_{2,3}$ for the 1.5 nm Fe film are difficult to determine within the precision of the simulation. Nonetheless, their absolute value increases for thinner films.

For varying values of the $K_{1,2,3}$ anisotropy constants, the magnetic potential energy E_m in Eq. 5.1 exhibits minima for different Θ_M . The minima of E_m define the magnetic phase of the system. The magnetic phases for different combinations of K_1 and K_2 are marked in Fig. 5.6 a (the constant K_3 is a minor correction to the magnetic potential energy landscape). This graph is a commonly used representation of the anisotropy constants in the anisotropy space spanned by K_1 and K_2 (found e.g. in Ref. [120, 154] and others). The third term K_3 does not change the global minimum of the magnetic energy.

The obtained experimental anisotropy constants K_1 and K_2 for decreasing Fe film thickness follow a linear trend. If extrapolated toward lower Fe coverage (as shown with the red line in 5.6 a) the trend predicts the magnetic anisotropy to transform from the in-plane into the perpendicular anisotropy via a *canted* easy-axis magnetization state. The so-called *polar* spin reorientation transition (SRT) to the perpendicular magnetic anisotropy (PMA) is achieved for $K_2 > -K_1/2$, which can be calculated by minimizing the magnetic energy in Eq. 5.1 and setting B_{ex} to zero. For positive K_1 and $K_2 < -K_1/2$ the anisotropy energy has a minimum at a canted Θ_M , different to 0° and 90° (as shown in the inset of 5.6 a). Another transition to the PMA state is possible via the *coexistence* state, where the anisotropy has two local minima at $\Theta_M=0^\circ$ and $\Theta_M=90^\circ$. This state is achieved for negative K_1 and $K_2 > -K_1/2$. When K_1 turns positive and $K_2 > -K_1/2$ the magnetization state is in the PMA. For the studied thicknesses range the actual reorientation of the easy magnetization axis was not observed.

The SRT is mediated by different anisotropy contributions, namely the magneto-

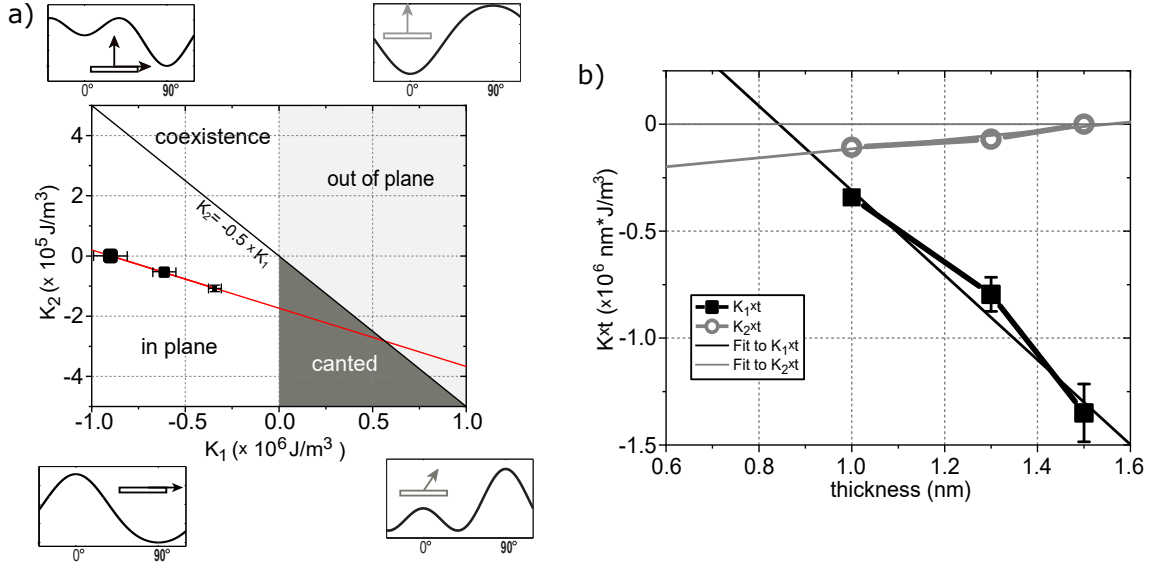


Figure 5.6: a) The anisotropy space spanned by the first-order anisotropy term K_1 and second-order anisotropy term K_2 . The regions of preferred magnetization orientation are marked and a corresponding magnetic energy angular landscape is plotted next to each region. The angle is defined with respect to the film normal (i.e. at 0° the magnetization points perpendicular to the film surface). The experimental data is plotted with black squares and the marker size corresponds to the Fe layer thickness, i.e. biggest marker for $t_{Fe}=1.5$ nm. b) Plot of the magnetic anisotropy constants K_1 and K_2 multiplied by thickness t in dependence on the thickness. This data was fitted with a linear function of $K \cdot t = K^V \cdot t + K^S$ to obtain the volume K^V and the interface K^S terms of the anisotropy constant (see Eq. 5.2).

crystalline anisotropy, the shape anisotropy due to dipole-dipole interaction and the interface or surface anisotropy [155], see Sec. 2.2. In general, these contributions have different thickness, temperature and magnetic field dependencies and promote different orientations of the easy magnetization axis. To separate the contribution originating from the bulk from the interface and surface terms, the anisotropy constants K_1 and K_2 can be separated into a volume term $K_{1,2}^V$ and an interface/surface term $K_{1,2}^S$ as (see Eq. 2.16)

$$K_{1,2} = K_{1,2}^V + \frac{K_{1,2}^S}{t}. \quad (5.2)$$

The volume (K_V) and surface (K_S) contributions can be extracted from the measured anisotropy constants K_1 and K_2 by multiplying with the film thickness t and applying a linear regression. A linear fit of $t \cdot K_{1,2}$ thickness dependence gives the $K_{1,2}^V$ as the slope and the $K_{1,2}^S$ as the intercept of the linear function with the $t=0$ axis (see Fig. 5.6 b).

From a linear fit of the $K_1 \cdot t$ data we obtain the volume contribution $K_1^V = -(1.9 \pm 0.3) \cdot 10^6 \text{ J/m}^3$ and the interface term $K_1^S = (1.6 \pm 0.4) \cdot 10^{-3} \text{ J/m}^2$. For a thin magnetic film the important contributions to the volume term K_1^V are the magneto-crystalline K_{MCA} and the shape anisotropy K_{sh} term [36,38]. The latter is for a magnetic

K_1	experimental (this work)	literature	Ref.
K^V (J/m ³)	$-(1.9 \pm 0.3) \cdot 10^6$	$-1.8 \cdot 10^6$ (K_{sh})	M_S from [153]
K^S (J/m ²)	$(1.6 \pm 0.4) \cdot 10^{-3}$	$1.47 \cdot 10^{-3} =$ $0.47 \cdot 10^{-3}$ ($K^S(\text{Fe}/\text{Au})$) $+ 1 \cdot 10^{-3}$ ($K^S(\text{Fe}/\text{MgO})$)	[55] [53,120,156,157]

Table 5.1: Table of anisotropy constants for the *out-of-plane* magnetic anisotropy.

thin film estimated as $K_{sh} = -M_S^2/2\mu_0$ in Sec. 2.2. For the previously assumed value for the saturation magnetization $M_S = 2.1$ T the shape anisotropy is $K_{sh} = -1.8 \cdot 10^6$ J/m³ and agrees well with the experimental K_1^V .

The volume anisotropy contribution for the studied thickness range is thus dominated by the shape anisotropy term with an additional smaller cubic anisotropy term K_4 . Because the K_4 term includes the film normal as an easy magnetization axis, a positive value is expected. A large additional positive contribution to K_1^V was observed in MgO/Fe/MgO and attributed to the magneto-elastic anisotropy [120], which is not observed in this study.

The interface contribution K_1^S can also be separated further into contributions from the Fe/MgO and the Fe/Au interfaces. For the latter a $K^S(\text{Fe}/\text{Au}) \sim 0.47$ erg/cm² ($0.47 \cdot 10^{-3}$ J/m² in SI units) was reported by Heinrich *et al.* [55]. The literature values for $K^S(\text{Fe}/\text{MgO})$ are of the order of 1 erg/cm² (10^{-3} J/m² in SI units) [53,120,156]. Simply summing up this two interface anisotropy terms gives $K^S \sim 1.47 \cdot 10^{-3}$ J/m², which is within the error of the experimental value determined in this work. Both interface contributions promote the PMA state when the Fe thickness is decreased. Therefore, the interface anisotropy seems to be the driving mechanism of the SRT in the system.

Higher-order anisotropy terms were needed for a good fit to the measured AHE loops, which indicates that the transitions from the in-plane to out-of-plane easy axis is more complex. The second and third order anisotropy terms also show a thickness dependence. However, their surface and volume contributions are ten times smaller compared to K_1^V and K_1^S , therefore they are not considered here. The effects of the higher order terms are discussed in detail in Ref. [155]. Such higher order corrections are used for describing a real thin magnetic film, where the magnetization is not perfectly collinear due to the presence of the surface or because of structural imperfections [154,155]. When the film growth deviates from the perfect layer-by-layer coverage, patches of Fe film with varying thickness may be present on the surface, which favor different orientations of the easy axis.

In summary, the measurements of the AHE in the Au/Fe/MgO(001) Hall bars confirmed an in-plane easy magnetization axis for Fe film thickness between 1-1.5 nm at room temperature. The magnetic anisotropy constants of the system were determined by simulation of the magneto-transport measurements. Negative values of $K_{1,2,3}$ were

5.3. In-plane magnetic anisotropy investigated via the planar Hall effect

obtained, promoting the in-plane easy axis. The Fe thickness dependence of $K_{1,2}$ reveals that the volume component of K_1 is dominated by the shape anisotropy and promotes the in-plane magnetic anisotropy while the interface term agrees with the literature values of the Fe/MgO and Fe/Au interface anisotropy constants which promote PMA. The second order term K_2 determines the type of the SRT transition as depicted in the graph of the K_1 - K_2 anisotropy space in Fig. 5.6 a. For the measured thickness range the data indicates an SRT via a canted state with an easy magnetization cone.

5.3 In-plane magnetic anisotropy investigated via the planar Hall effect

The magnetic anisotropy in the film plane of the Au/Fe/MgO(001) heterostructures was further investigated via the PHE. The origin of the PHE was explained in Sec. 2.4.2.

The PHE measurements are conducted in the Hall-geometry, see Sec. 4.2. In the experiments presented here, the current I was applied along direction Fe[$\bar{1}\bar{1}0$] parallel to the Hall bar wire. The Hall voltage V_{xy} was measured in the direction perpendicular to the Hall bar, i.e. along the Fe[110] direction, and the PHE transversal resistance R_{xy} was calculated as $R_{xy} = V_{xy}/I$. For PHE from a single-domain sample, the planar Hall voltage V_{xy} is directly related to the direction of the in-plane magnetization with respect to the direction of the applied current density j_x as (see Eq. 2.28 in Sec. 2.4.2)

$$E_y = j_x(\rho_{\parallel} - \rho_{\perp}) \cdot \sin\varphi_M \cos\varphi_M. \quad (5.3)$$

Here, the current density $j = (j_x, 0, 0)$ flows in the Fe[$\bar{1}\bar{1}0$] direction, the ρ_{\parallel} (ρ_{\perp}) is the longitudinal resistivity, when the magnetization is parallel (perpendicular) to the current direction. The angle φ_M is the angle between j and the direction of the in-plane magnetization \vec{M} (see sketch of the experiment in Fig. 2.4).

The results of the PHE measurements are depicted in Fig. 5.7. A magnetic field of 400 mT was applied in the in-plane direction and rotated around the normal of the film for 360° in steps of 5° , i.e. the *magnetic field rotation* mode of the magneto-transport measurements introduced in Sec. 4.2. Because 400 mT is beyond the saturating magnetic field, the magnetization of the film is aligned parallel to the applied field direction, therefore $\varphi_M = \varphi_B$. The resulting R_{xy} follows the $\sin\varphi_M \cdot \cos\varphi_M$ dependence from Eq. 5.3.

The PHE measurements at 250 K from Hall bars with different Fe layer thicknesses (1-1.5 nm) exhibit an approx. 10% increase of the amplitude of the PHE for higher Fe coverage, see Fig. 5.7 a. An offset was subtracted from the measured PHE resistance R_{xy} which arises due to a small misalignment of the bonding contacts giving a contribution from the longitudinal resistance. The obtained angular dependence of R_{xy} agrees well with the prediction from Eq. 5.3. Additionally, a small contribution with a $\sin\varphi_B$ -dependence can be observed, most significant for $t_{Fe}=1.5$ nm. This term can arise due to a small

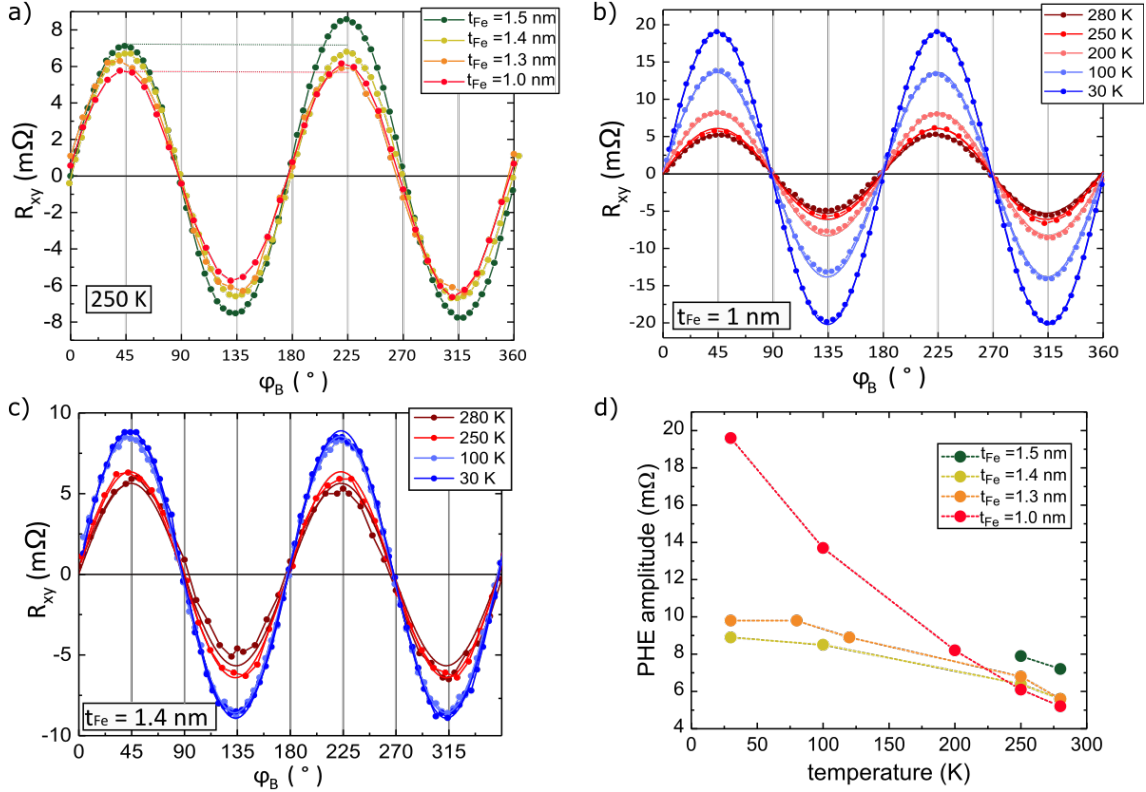


Figure 5.7: **a)** The Planar Hall effect (PHE) measurement at 250 K for Au/Fe/MgO(001) Hall bars for different Fe layer thickness. The current was applied along the wire of the Hall bar in the Fe[110] direction and the resistance R_{xy} was measured between the contacts perpendicular to the current direction. The deviation from the expected $\sin\varphi_M \cdot \cos\varphi_M$ dependence is induced by a sample misalignment of up to 1° . **b)** The temperature dependence of the PHE was measured for samples with different Fe layer thicknesses t_{Fe} . The PHE amplitude was observed to increase strongly with decreasing temperature for sample with $t_{Fe}=1$ nm. **c)** For a sample with $t_{Fe}=1.4$ nm the PHE amplitude was observed to be approximately constant for temperatures below ~ 150 K. The temperature dependence of the PHE amplitude is summarized in **d)** for all t_{Fe} .

misalignment of the sample giving rise to an out-of-plane projection of the applied magnetic field. The amplitude of the additional $\sin\varphi_B$ term can be compared to the measured anomalous Hall voltage (see Fig. 5.5 a). It may be estimated that already a small out-of-plane misalignment of 0.5° - 1° of the 400 mT magnetic field can result in an out-of-plane magnetic field of $\sin(0.5^\circ$ - $1^\circ)$ \cdot 400 mT \sim 1-5 mT. This field is sufficient to induce the observed additional $\sin\varphi_B$ term to the PHE.

In Fig. 5.7 b,c the PHE angular dependence is plotted for the samples with $t_{Fe}=1$ nm and $t_{Fe}=1.4$ nm measured at temperatures between 30 K and 280 K. The amplitude of the PHE was obtained by fitting the measured PHE with a $\sin\varphi_B \cdot \cos\varphi_B$ function. The temperature dependence of the PHE amplitude is plotted in Fig. 5.7 d for all investigated samples. The PHE shows a strong temperature variation for the 1 nm Fe coverage.

5.3. In-plane magnetic anisotropy investigated via the planar Hall effect

At this thickness, the PHE amplitude strongly increases at lower temperatures and for higher Fe coverage the increase of the amplitude is slower. This can be attributed to the discontinuity of the 1 nm Fe film. The magneto-resistance properties of discontinuous ultra-thin ferromagnetic films exhibit strong temperature, thickness and island size dependence, which arises from the interplay of the exchange interaction within each of the islands and the thermal excitations which control the interaction between the islands [158, 159]. A superparamagnetic state was observed for islands of ultra-thin ferromagnetic films at low temperatures [29, 158]. The superparamagnetic state could induce giant magneto-resistance (GMR)-like effects to the conductivity which would increase the difference between ρ_{\parallel} and ρ_{\perp} and in this way increase the PHE amplitude. Further magneto-transport measurements (e.g. B_{ex} dependence, AMR temperature dependence...) are required for a better understanding of the observed temperature and thickness dependence of the PHE amplitude.

The planar Hall transversal resistance R_{xy} and the in-plane direction of the magnetization φ_M have a direct relation as defined by Eq. 5.3. Therefore, the PHE measurement can be used to determine the orientation of the in-plane magnetization and the magnetic anisotropy of a magnetic film. When an external magnetic field B_{ex} is applied along a chosen crystalline direction of the film and gradually increased, the magnetic response of the system to the B_{ex} can be studied by measuring the R_{xy} . Figure 5.8 a shows the scans of B_{ex} along the two hard axes and the two easy axes present in the Au/Fe/MgO(001) epitaxial Hall bar with $t_{Fe}=1.5$ nm. The full lines are measurements of the R_{xy} for the positive B_{ex} scan and the dash-dotted lines for the negative scan. For the hard axis B_{ex} scans along the Fe[$\bar{1}10$] and Fe[110] directions, the magnetic field encloses an angle of $\varphi_B=0^\circ$ and $\varphi_B=90^\circ$ with the applied current direction, respectively. The planar Hall resistance R_{xy} for both B_{ex} directions shows the *double-jump* magnetization reversal, which was observed also in the magnetic hysteresis loops obtained using Kerr microscopy (see Fig. 5.2 and 5.3). It is a direct indication of the cubic magneto-crystalline anisotropy (MCA) of the Fe(001) film.

In the Sec. 5.1 the two jumps of the magnetization during the hard axis reversal process were identified. Both jumps are 90° -jumps between the easy magnetization directions. In the PHE measurement of the hard axis magnetization reversal in Fig. 5.8 a, the second jump is observed at a slightly higher B_{ex} for $\varphi_B=90^\circ$ compared to the scan for $\varphi_B=0^\circ$, which is a consequence of a difference in the in-plane misalignment between the two experiments. An additional observation is the difference in the amplitude of the R_{xy} jump between the two hard axis scans. The most probable reason for this is the difference in the shape of the magnetic domains, which form during each of the magnetization reversal processes (see Sec. 5.4). A larger misalignment could lead to formation of a larger number of smaller domains, which would influence the measured R_{xy} . The formation of domains also explains the roundness of the second jump in both magnetic field scans. An increased

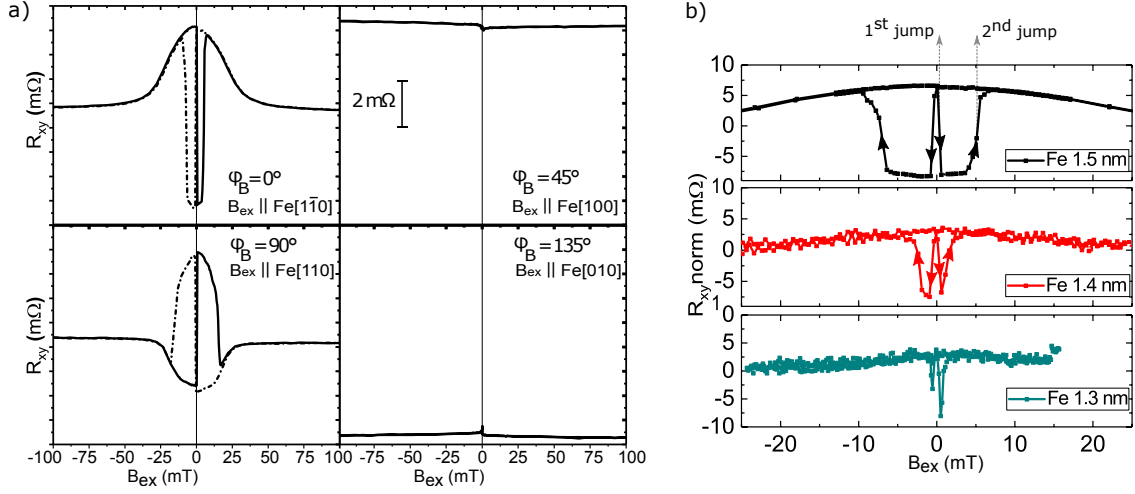


Figure 5.8: a) The room temperature planar Hall measurement of the magnetization reversal along two hard magnetization directions with $\varphi_B=0^\circ$ and $\varphi_B=90^\circ$ and two easy magnetization directions with $\varphi_B=45^\circ$ and $\varphi_B=135^\circ$ with respect to the Hall bar for the Au/Fe/MgO(001) with 1.5 nm Fe layer thickness. The full line corresponds to the positive magnetic field scan and the dash-dotted line to the negative field scan measurement. b) The $\varphi_B=0^\circ$ hard axis magnetization reversal scan of the planar Hall resistance R_{xy} at 250 K for Hall bars with 1.5 nm, 1.4 nm and 1.3 nm Fe layer thickness. For Hall bars with Fe layer thickness of 1 nm the double-jump magnetization reversal was observed only below 50 K.

roundness is observed for the $\varphi_B=90^\circ$ scan, which indicates the presence of an increased number of domains during this magnetization reversal. The formation of domains for different directions of B_{ex} is further discussed in Sec. 5.4.

The two easy magnetization axes of the cubic MCA are confirmed by B_{ex} scans along the Fe[100] and Fe[010] directions, which enclose an angle $\varphi_B=45^\circ$ and $\varphi_B=135^\circ$, respectively, with the current direction. The PHE resistance R_{xy} remains at a constant value for all values of B_{ex} along these two directions, see Fig. 5.8. At $B_{ex} \sim 0$ a small variation of R_{xy} is observed which can be attributed to a fraction of domains in which the magnetization reversal via two 90° jumps is resolved. The two easy magnetization axes of the cubic MCA are energetically equivalent, therefore it is reasonable to expect that the magnetization may switch to any of the easy directions during the reversal process. For example, during the magnetization reversal along the Fe[100] easy axis the magnetization may switch first from the Fe[$\bar{1}00$] \rightarrow Fe[010] and subsequently from Fe[010] \rightarrow Fe[100]. Therefore, R_{xy} may vary close to $B_{ex}=0$ also for the easy axis magnetization reversal.

The in-plane magnetic anisotropy in the Au/Fe Hall bars can be further studied using the magneto-transport measurements of the PHE. Figure 5.8 b shows a comparison of the PHE measurements of the hard axis magnetization reversal in Hall bars with different Fe layer thicknesses ($t_{Fe}=1$ nm, 1.4 nm and 1.5 nm). The magnetic field of the first magnetization jump (just after crossing zero field) does not significantly change with decreasing

5.3. In-plane magnetic anisotropy investigated via the planar Hall effect

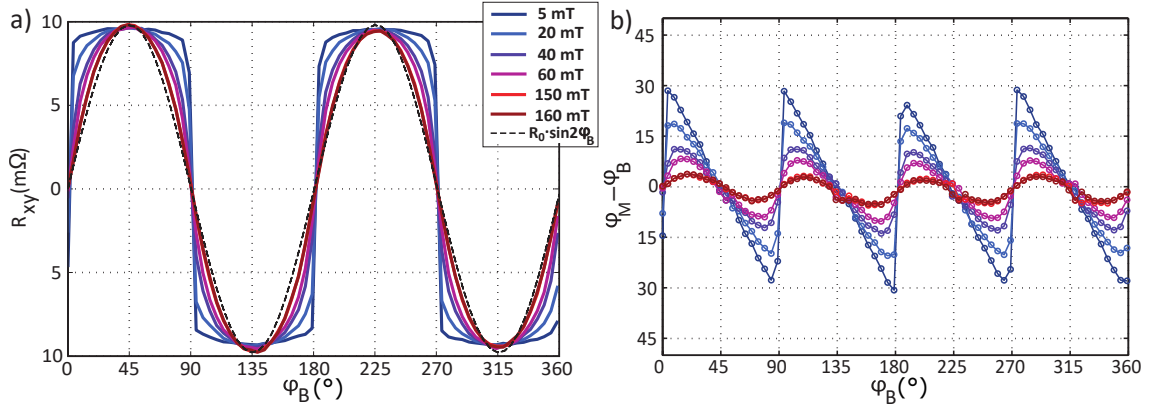


Figure 5.9: **a)** PHE measurement from the Au/Fe(1.3 nm)/MgO(001) Hall bar at 30 K for different external magnetic fields from 5 to 160 mT are compared to $R_0 \sin \varphi_B$ with $R_0 = 9.6 m\Omega$ (broken line). The angle φ_B is measured between the applied current $I = 15$ mA and the external magnetic field direction. **b)** The difference between the magnetization direction with φ_M and the external magnetic field direction with φ_B was calculated for the different magnetic fields from the deviation of the measured R_{xy} from the calculated R_{xy} in Eq. 5.3. The difference $\varphi_B - \varphi_M$ scales inversely proportional to the applied magnetic field.

Fe thickness. However, the magnetic field of the second jump increases with higher Fe coverage for a factor of 10 between the 1.3 nm and 1.5 nm Fe thickness. The increase of the second switching field indicates an increase of the magnetic anisotropy constant, which is most probably a consequence of the improved continuity of the thicker Fe films. The magnetic anisotropy constant was investigated by applying an in-plane magnetic field lower than the saturating field. This analysis will be shown in the following.

5.3.1 Magnetic torque analysis of the in-plane anisotropy

When the applied in-plane magnetic field B_{ex} is lower than the saturating field, the magnetization of the probed material is not aligned parallel to \vec{B}_{ex} . The magnetization is tilted off the direction of B_{ex} and the magnitude of the tilt depends on the strength and direction of the magneto-crystalline and other anisotropy fields acting on the magnetization of the film. Based on the observation of the double-jump reversal of the magnetization along the hard magnetization axis, an additional uniaxial anisotropy may be present in the system investigated here. Existence and strength of the anisotropy field can be studied by the *magnetic torque analysis* via the PHE measured with B_{ex} below saturation (see e.g. Ref. [152, 160]).

The results of the PHE measurements shown in Fig. 5.9 a demonstrate how the response of the magnetization changes when B_{ex} is reduced below the saturation value. The saturating field increases with decreasing temperature, see also Fig. 6.6. At 30 K and for $B_{ex} > 200$ mT the R_{xy} follows the expected $\sin \varphi_B \cdot \cos \varphi_B$ dependence, see Eq. 5.3. For smaller B_{ex} , the measured R_{xy} shows a deviation from the expected angular dependence, which amplitude is inversely proportional to the applied magnetic field, i.e. smaller the

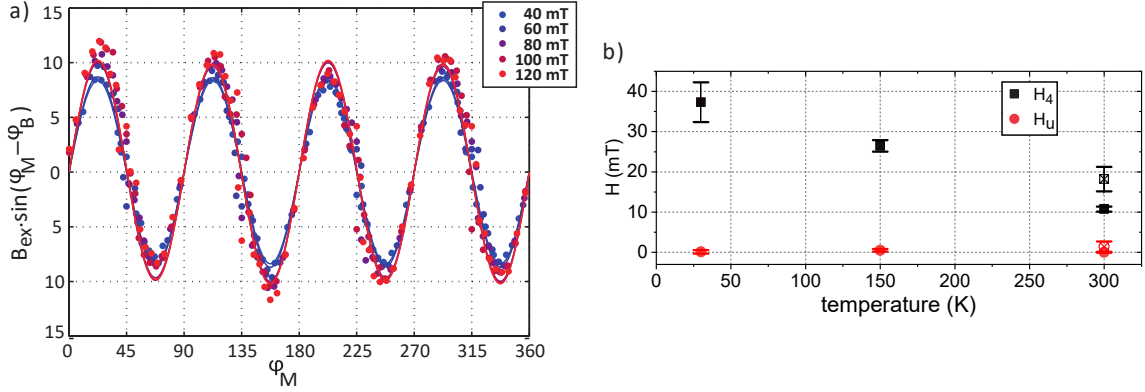


Figure 5.10: a) The sine function of the angle difference between the magnetization direction φ_M and the angle of the applied magnetic field φ_B multiplied by B_{ex} gives a very similar dependence on φ_M for all magnetic fields between 40-120 mT. The full lines are fits to the data with a function $y = A_1 \cdot \sin(2x + C_1) + A_2 \cdot \sin(4x)$. The uniaxial and the cubic anisotropy fields were obtained from the constants A_1 and A_2 of the best fit using the relationship $A_1 = \frac{H_u}{2}$ and $A_2 = \frac{H_4}{4}$, respectively. The obtained anisotropy fields at 30 K, 150 K and 300 K are plotted in b). The full symbols are H_u and H_4 obtained for a Hall bar with Fe thickness $t_{Fe}=1.3$ nm and the empty symbols are resulting fields for $t_{Fe}=1.5$ nm at 300 K.

field larger the R_{xy} deviation. For small B_{ex} the direction of the magnetization (φ_M) is not parallel to B_{ex} (φ_B). Therefore, the deviation observed in the PHE resistance is due to the tilt between the applied B_{ex} and the magnetization. The tilt is largest for the smallest B_{ex} and it depends on φ_B . The smallest deviation is observed for angles around $\varphi_B = 45^\circ, 135^\circ, 225^\circ$ and 315° , i.e. along easy magnetization directions of Fe(001) film, which agrees with the presence of the four-fold MCA acting on the magnetization.

From the difference between the measured angular dependence of R_{xy} and the expected dependence calculated from Eq. 5.3 the tilt of the magnetization can be calculated and is shown in Fig. 5.9 b) for the different values of the external magnetic field. Assuming a presence of a four-fold MCA and an additional uniaxial anisotropy in the Fe(001) film, the Stoner-Wohlfahrt model (see Appendix A) gives the magnetic energy E_m of the system written as a sum of the two anisotropy terms as follows

$$E_m = -M_S B_{ex} \cdot \cos(\varphi_B - \varphi_M) + K_u \cdot \sin^2(\varphi_M - \varphi_{K_u}) + \frac{K_4}{4} \cdot \cos^2 2\varphi_M. \quad (5.4)$$

The first term in Eq. 5.4 is the Zeeman term for the magnetic energy in the applied field B_{ex} with an angle φ_B to the Fe[$\bar{1}10$] direction. The second and the third terms are the uniaxial anisotropy and the four-fold cubic anisotropy energy, respectively. The uniaxial anisotropy with the constant K_u is acting along the direction with the angle φ_{K_u} with respect to the Fe[$\bar{1}10$] and the cubic anisotropy with the constant K_4 results in two orthogonal easy magnetization axes along the Fe[100] and Fe[010] directions.

In the equilibrium state, the magnetization of the film will stabilize along the direction with the lowest magnetic energy E_m defined in Eq. 5.4. The φ_M^{min} with the lowest energy

5.3. In-plane magnetic anisotropy investigated via the planar Hall effect

is found by calculating the derivative over φ_M of the magnetic energy and setting it to zero. This gives

$$\frac{\partial E_m}{\partial \varphi_M}(\varphi_M^{min}) = 0 \quad (5.5)$$

$$B_{ex} \cdot \sin(\varphi_M^{min} - \varphi_B) = \frac{H_u}{2} \cdot \sin(2(\varphi_M^{min} - \varphi_{K_u})) + \frac{H_4}{4} \cdot \sin(4\varphi_M^{min}). \quad (5.6)$$

Here, the uniaxial and the cubic anisotropy fields are introduced as $H_u = \frac{2K_u}{M_S}$ and $H_4 = \frac{2K_4}{M_S}$. Equation 5.6 can be understood also as defining the equilibrium between the applied *magnetic-field torque* (left hand side of Eq. 5.6) and the torques due to the magnetic anisotropy fields (right hand side of Eq. 5.6). In a stationary state and for B_{ex} smaller than the saturating field, the tilt of the magnetization from the B_{ex} direction is thus due to the anisotropy fields. The magnetic field torque on the left hand side of Eq. 5.6 was calculated by multiplying the sine function of the measured tilt $\varphi_M - \varphi_B$ (shown in Fig. 5.9 b) by the external magnetic field B_{ex} . The obtained φ_M -dependence of the torque was fitted with a function $y = A_1 \cdot \sin(2x + C_1) + A_2 \cdot \sin(4x)$ where the two constants A_1 and A_2 equal $A_1 = \frac{H_u}{2}$ and $A_2 = \frac{H_4}{4}$, respectively. The best fit to the angular dependence of the magnetic field torque at 30 K for $t_{Fe} = 1.3$ nm is shown in Fig. 5.10 a.

The anisotropy fields H_u and H_4 evaluated from the best-fit A_1 and A_2 constants are plotted in Fig. 5.10 b. The analysis was repeated for measurements at 150 K (samples with $t_{Fe} = 1.3$ nm) and at room temperature (sample with $t_{Fe} = 1.3$ nm and $t_{Fe} = 1.5$ nm). The uniaxial anisotropy field resulted to be a minor correction to the predominant cubic anisotropy with a 1-2 orders of magnitude larger anisotropy field. The extracted values from the room temperature measurements read $H_u(1.3 \text{ nm}) = 0 \pm 0.11$ mT and $H_4(1.3 \text{ nm}) = 10.8 \pm 0.6$ mT for $t_{Fe} = 1.3$ nm and $H_u(1.5 \text{ nm}) = 1 \pm 1$ mT and $H_4(1.5 \text{ nm}) = 18 \pm 3$ mT for $t_{Fe} = 1.5$ nm. The difference in the error is due to a different resolution of the measurement, which is set by the magnetic field scan rate (i.e. step size, waiting time and resolution set at the magnetometer). Because of the small value of the uniaxial correction to the magnetic anisotropy, the precision of the experiment was insufficient to determine its exact value or its direction (φ_{K_u}).

The cubic anisotropy field for the sample with $t_{Fe} = 1.3$ nm increases at lower temperatures and reaches an almost four times higher value at 30 K, while the uniaxial field remains below 1 mT at all measured temperatures. The increase of K_4 at low temperatures can be explained by the decrease of the thermal excitations of the spin system [36, 161]. The increasing temperature induces spin fluctuations (e.g. magnons), which are related to deviations of the orientation of the spins from their direction in the ground state at zero temperature. At low temperatures less of the spin fluctuations are excited, which results in an increased total magnetization.

For a direct comparison with literature values, the cubic anisotropy constant can

be calculated from $K_4 = \frac{H_4 M_S}{2}$. For the saturation magnetization we used the value $M_S = 1710 \text{ emu/cm}^3$ (2.1 T in SI units) obtained in Ref. [153] for a 1.3 nm Fe film grown on MgO(001) capped with 100 Å MgO. The resulting cubic anisotropy constants at room temperature are $K_4(1.3 \text{ nm}) = 0.9 \cdot 10^4 \text{ J/m}^3$ and $K_4(1.5 \text{ nm}) = 1.5 \cdot 10^4 \text{ J/m}^3$ for the two samples with different Fe layer thicknesses and are compared to reported values of K_4 in Table 5.2.

The K_4 anisotropy constant for the 1.5 nm Fe film is higher as compared to K_4 for the 1.3 nm Fe film. Scaling of the anisotropy constant with Fe thickness is observed also in the literature values (see Ref. [153, 160, 162] and Table 5.2). The thickness dependence at low coverage is usually brought about by the interface anisotropy term. For the in-plane anisotropy constant of a magnetic thin film with thickness t the same phenomenological separation into a volume K_V and a surface or interface K_S contributions as introduced in Sec. 2.2 and 5.2 can be used, so that

$$K_4 = K_V + \frac{K_S}{t}. \quad (5.7)$$

In the studied system two interface contributions can be expected, namely from the Fe/MgO and Au/Fe interfaces. Because we observe a decrease of the K_4 with lower t , the total surface contribution K_S in the Au/Fe/MgO system is expected to have a negative value. In fact, it was observed for Au/Fe/Au(001) system that the negative K_S lowers the effective anisotropy constant K_{eff} when the Fe thickness is decreased and leads to an easy-axes reorientation transition (90° rotation of both easy axes) at a critical Fe thickness [57]. For this type of K_S an additional uniaxial anisotropy is not expected to be present as it corresponds to an equal rotation of both easy axes.

Another property of the films, which may influence the magnetic anisotropy, is the film morphology. It has been reported that the film roughness (determined by the top layers of the film) does not considerably change the anisotropy constant for Fe films with 10 nm thickness [163]. For different growth conditions of Fe on MgO(001) and of the Au capping layer the obtained K/M value was $\sim 20 \text{ mT}$ [163], i.e. $H_4 \sim 40 \text{ mT}$. In the present work, Fe films with $t_{Fe} \leq 1.5 \text{ nm}$ are studied, for which indications of discontinuity have been observed, see Sec. 5.1 and 5.4. For discontinuous ultra-thin ferromagnetic films

Fe thickness (nm)	K_4 (J/m ³)	Ref.
1.3	$0.9 \cdot 10^4$	this work
1.5	$1.5 \cdot 10^4$	this work
4.2	$2.67 \cdot 10^4$	[160]
25	$3.23 \cdot 10^4$	[162]
bulk	$4.8 \cdot 10^4$	[162]

Table 5.2: Table of the cubic anisotropy constants K_4 .

a reduced magnetic anisotropy energy has been reported, which was attributed to the magnetic interaction between the islands of the film [158, 159].

In brief, the PHE analysis of the in-plane magnetic anisotropy confirmed the presence of the cubic anisotropy with easy magnetization axes along the principle directions of the Fe(001) film, which is expected due to the high crystalline quality of the film. The extracted magnetic anisotropy constant $K_4=(0.9 \pm 0.05) \cdot 10^4 \text{ J/m}^3$ for $t_{Fe}=1.3 \text{ nm}$ increases at lower temperatures and with thickness, which agrees with the observation that the 1.5 nm Fe films have an improved continuity. The value of an additional uniaxial anisotropy is below the precision of the employed magneto-transport measurements. This indicates that a small misalignment of the experiment, rather than an uniaxial anisotropy, is responsible for observation of the double-jump magnetization reversal process.

5.4 Magnetic domain structure

In previous sections, the magnetic anisotropy of the Au/Fe/MgO(001) Hall bars was characterized based on the hysteresis loops extracted from the Kerr microscopy images (Sec. 5.1) and magneto-transport measurements (Sec. 5.2 and 5.3). While the major features of the observed loops can be explained by considering a single domain Fe(001) film with in-plane cubic MCA influenced by the interface effects, which give rise to the Fe-layer thickness dependence of magnetic anisotropy, some of the observations in the loops point towards a multi-domain state of the Fe(001) film. These observations include the additional “plateaus” in the Kerr hysteresis loops (Fig. 5.2, Fig. 5.3), increased roundness of the loops from 1.3 nm Fe film (Fig. 5.4) and the roundness and angular dependence of the PHE loops (Fig. 5.8). Therefore, a microscopic investigation sensitive to the orientation of the in-plane magnetization is required to study the magnetic state of the system.

The lateral distribution of the orientation of the magnetization can be studied by Kerr microscopy (see Sec. 4.3) with a lateral resolution down to $\sim 0.1 \mu\text{m}$. When Kerr images are acquired as a function of a varying external magnetic field B_{ex} , they show the changes in the magnetic domain structure induced by the field. First, the Kerr microscopy investigation of the Hall bars with $t_{Fe}=1.5 \text{ nm}$ and $t_{Fe}=1.3 \text{ nm}$ will be shown followed by a combined magneto-transport and Kerr microscopy study of the PHE.

5.4.1 Magnetic domains in Au/Fe(1.5 nm) Hall bars

The hysteresis loops acquired from the Hall bars with $t_{Fe}=1.5 \text{ nm}$ indicate an improved continuity of the Fe film as compared to the thinner film with $t_{Fe}=1.3 \text{ nm}$ (see Sec. 5.1). However, the PHE measurements show signatures of domain formation during the magnetization reversal process also for the Hall bars with $t_{Fe}=1.5 \text{ nm}$ (Sec. 5.3, Fig. 5.8). The magnetization reversal along the Fe[110] hard axis of the Au/Fe(1.5 nm)/MgO(001)

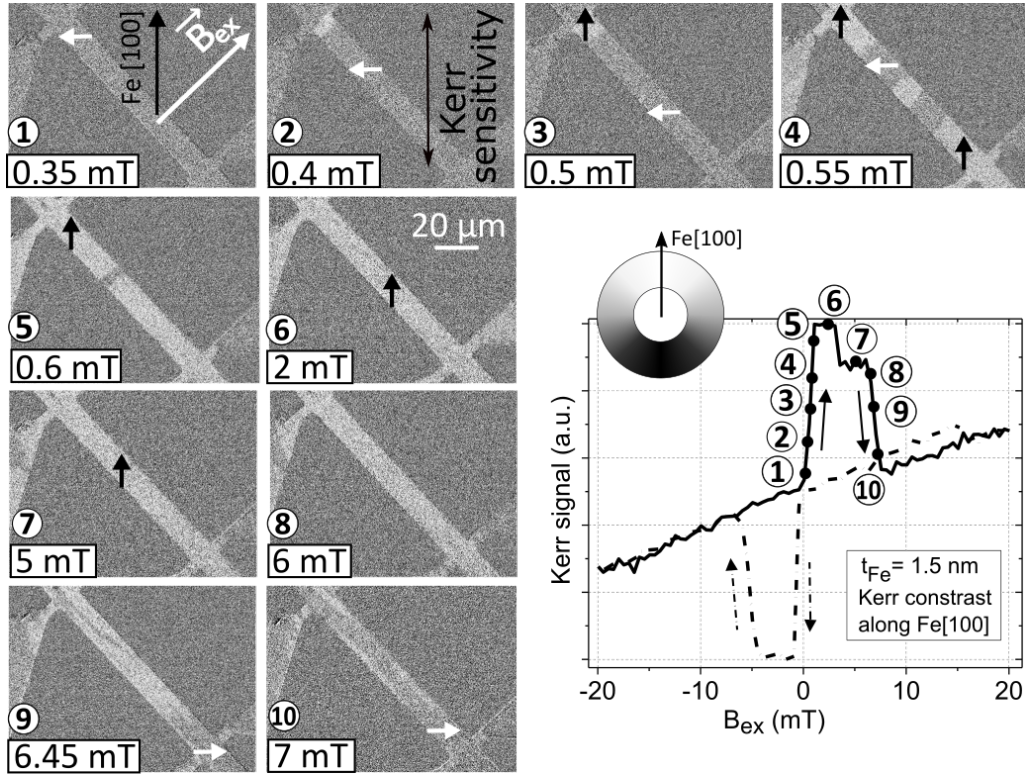


Figure 5.11: The magnetization reversal along the $\text{Fe}[110]$ hard axis in $\text{Au}/\text{Fe}(1.5 \text{ nm})/\text{MgO}(001)$ was imaged using Kerr microscopy. Kerr sensitivity was set along the $\text{Fe}[100]$ easy axis (see inset of the graph). The hysteresis loop (bottom right) was extracted from the acquired Kerr images from the area of the Hall bar. The sequence of the snapshots of the Hall bar (1-10) is marked at corresponding B_{ex} values on the graph and shows the formation of easy axis domains after saturation of the magnetization along $\text{Fe}[1\bar{1}0]$ direction.

as observed in Kerr microscopy is shown in Fig. 5.11. The Kerr sensitivity was set such that the magnetization with a projection along the $\text{Fe}[100]$ easy axis appears bright, while the magnetization with a projection on the $\text{Fe}[010]$ easy axis appears dark (see the sketch of intensity in the inset). The images 1-10 were acquired after the film was saturated along the $-\vec{B}_{ex}$ direction, i.e. along the $\text{Fe}[\bar{1}\bar{1}0]$ hard axis. The Hall bar appears homogeneously dark in image 1, because the magnetization points along the $\text{Fe}[0\bar{1}0]$ easy direction, perpendicularly to the Kerr sensitivity axis. Note, that the magnetization may also point along the $\text{Fe}[010]$ direction, which is perpendicular to the Kerr sensitivity axis as well and thus results in the same Kerr contrast.

The bright domains start to appear after crossing zero field at $B_{ex}=0.4 \text{ mT}$ (image 2 in Fig. 5.11). The first switched, bright domain is observed next to the Hall bar cross (i.e. the crossing of the longitudinal channel with the transversal contacts). This can be explained as resulting from the stray field due to 90° edges of the Hall cross as well as due to the presence of the contact pads with large areas of magnetic material. The central area of the Hall cross is therefore a probable source of pinning points for the magnetization. This

region was observed to facilitate nucleation of switched domains also in other experiments (see e.g. Fig. 5.12).

Increasing B_{ex} along Fe[110] hard axis induces further growth of the bright domains and nucleation of new domains (images 3-8 in Fig. 5.11). At $B_{ex} \sim 2$ mT the bright domains extend over the entire length of the Hall bar. The magnetization in the bright domains is aligned to the Fe[100] easy direction. Images 7 and 8 show the magnetic state at $B_{ex}=5$ mT and $B_{ex}=6$ mT, which correspond to a small decrease of intensity (intermediate “plateau”) observed in the hysteresis loop. A visible change in intensity can be identified only on the contact pads. However, the decrease in intensity marks the onset of the second switch of the magnetization. Because the Kerr sensitivity was set along the Fe[100], the second switch of the magnetization from Fe[100]→Fe[010] can also be observed. When the magnetization switches towards Fe[010] its projection on the Kerr sensitivity axis is close to zero and therefore results in darker Kerr contrast (dark domains in images 9 and 10).

Interestingly, during the second magnetization switch the domain walls are oriented preferentially along the Hall bar, which is in contrast to the shape of the domain walls observed in the images 1-8 of the first magnetization switch. Both observed magnetization switches (Fe[0 $\bar{1}$ 0]→Fe[100] and Fe[100]→Fe[010]) involve formation of domains with magnetization rotated for 90°. Therefore, the domains are separated by the 90° domain walls, which means that the magnetization rotates for 90° when crossing the domain wall. In fact, for a cubic system with two easy axes the 90° domain walls are energetically favorable over the 180° domain walls [58]. The orientation of the walls is most probably determined by magneto-statics and can be explained by considering the magnetization inside the bright and dark domains, which will be discussed in more detail in the following (see Fig. 5.13 and the explanation in text).

The magnetization reversal along the same Fe[110] hard axis was imaged also by setting the Kerr sensitivity along the axis parallel to B_{ex} (see Fig. 5.12). With this settings the highest magnetic contrast is obtained between the magnetization parallel and anti-parallel to the Fe[110] direction. These two orientations of the magnetization are achieved when B_{ex} is close to the saturating field along the hard axis. Moreover, in this geometry, the easy directions Fe[100] and Fe[010] lead to the same Kerr contrast (see the sketch of the Kerr intensity wheel in the inset of the graph). Therefore, the double-jump feature of the magnetization reversal process cannot be distinguished in this measurement. However, magnetization along Fe[0 $\bar{1}$ 0] leads to opposite Kerr contrast compared to magnetization parallel to Fe[100]. Thus, the domains with magnetization switched from Fe[0 $\bar{1}$ 0] to Fe[100] are seen as bright domains forming at $B_{ex} > 0.35$ mT (images 2-7). The domains formed during this reversal process exhibit the straight 90° domain walls perpendicular to the Hall bar as observed earlier. The first reversed domain again nucleates close to the Hall bar cross (image 2).

Even though the hysteresis loops in Fig. 5.11 and Fig. 5.12 display different features, the Kerr microscopy images of the domain structure reveal that both hysteresis loops result

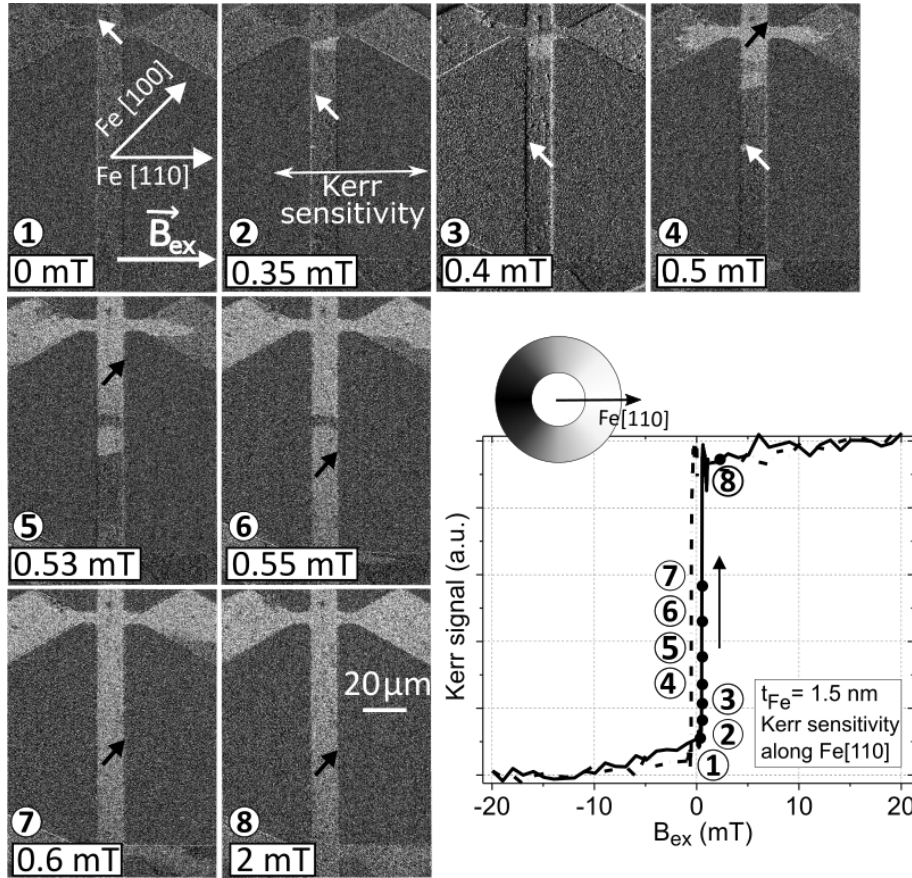


Figure 5.12: Kerr microscopy images of the magnetization reversal along the Fe[110] hard axis of the Au/Fe(1.5 nm)/MgO(001) Hall bar. The Kerr sensitivity was set parallel to the external magnetic field B_{ex} . The corresponding B_{ex} of the snapshot sequence are marked on the hysteresis loop with numbers 1-8 (bottom right). The Kerr images show the domain structure for different $B_{ex} > 0$ after saturation of the magnetization along Fe[110]. The inset of the graph shows the Kerr intensity wheel for the set geometry of the experiment.

from the same magnetization reversal process. The Kerr microscopy analysis shows, that the hard axis magnetization reversal proceeds via formation of domains. The domains with reversed magnetization start to form at $B_{ex} \sim 0.35$ mT after B_{ex} crosses zero field. At this magnetic field, the magnetization in some parts of the Fe film undergoes a 90° flip from one easy direction to another. The flips of the magnetization occur first at the positions of increased stray fields (Hall cross center) or at the location of structural defects and imperfections of the film, where the magnetic field is not homogeneous. Between the magnetic domains the 90° domain walls form, which are orientated perpendicular to the Hall bar for the first switch and approximately along the Hall bar for the second switch.

The orientation of the 90° domain walls seems to be a consequence of the direction of the magnetization within the corresponding domains. To investigate this relationship we induced different magnetic domain structure by applying B_{ex} along the two hard axes.

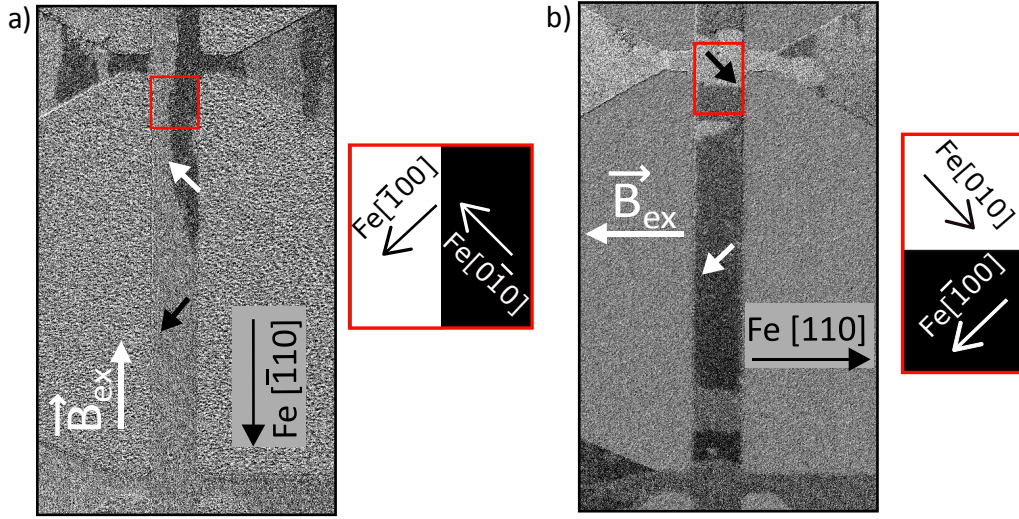


Figure 5.13: **a)** Kerr microscopy image of the Au/Fe(1.5nm)/MgO(001) Hall bar with magnetic field $B_{ex}=0.51$ mT applied in direction parallel to the Hall bar, after saturation along Fe[$\bar{1}10$], i.e. along $-\vec{B}_{ex}$. The Kerr sensitivity is set along Fe[$\bar{1}10$] direction. The magnetization along the Hall bar is not homogeneous, but split into domains. The domain walls have a preferential orientation parallel to the B_{ex} axis. The sketch on the right illustrates the orientation of the magnetization in the bright and dark domains. **b)** The same region of the Hall bar was imaged also with a magnetic field applied perpendicular to the Hall bar after saturation along $-\vec{B}_{ex}$. The Kerr sensitivity is set in the direction of $-\vec{B}_{ex}$. The domain wall orientation follows the axis of B_{ex} .

In Fig. 5.13 the snapshots of the domain structure at $B_{ex}=0.51$ mT are shown, which were acquired after saturation of the magnetization along $-\vec{B}_{ex}||\text{Fe}[\bar{1}10]$ (a) and along $-\vec{B}_{ex}||\text{Fe}[110]$ (b). When reducing B_{ex} , the magnetization rotates from the saturated state towards the closest easy direction (Fe[$\bar{1}00$] in Fig. 5.13 a and Fe[010] in Fig. 5.13 b). After crossing zero field the reversed, dark domains were formed with magnetization rotated towards the Fe[0 $\bar{1}0$] (a) and towards Fe[$\bar{1}00$] (b).

Interestingly, the domain walls tend to form parallel to the B_{ex} direction, i.e. parallel to the Hall bar in Fig. 5.13 a and perpendicular to the Hall bar in 5.13 b. The observed domain structures seem to follow the *closed-flux* magnetization configuration, which is observed in small magnetic elements with dimensions beyond the single-domain limit [58]. The most commonly known closed-flux configuration is the Landau state observed in magnetic thin films patterned into a square (see e.g. Ref. [58] and [38]). The closed-flux pattern is a consequence of the fact that the energetically lowest magnetization state is a closed magnetic circle [38] (see also Sec. 2.3). The orientation of the magnetization within each of the domains is determined by the magnetic anisotropy of the Fe film and so is the type of the domain walls. Because of the strong in-plane magnetic anisotropy the domain walls are most probably of Néel type. The shape of the domains, however, is here mostly determined by the stray fields produced due to the limited dimensions of the Hall bar and induce the observed alignment of the domain walls to the B_{ex} direction. This is often the

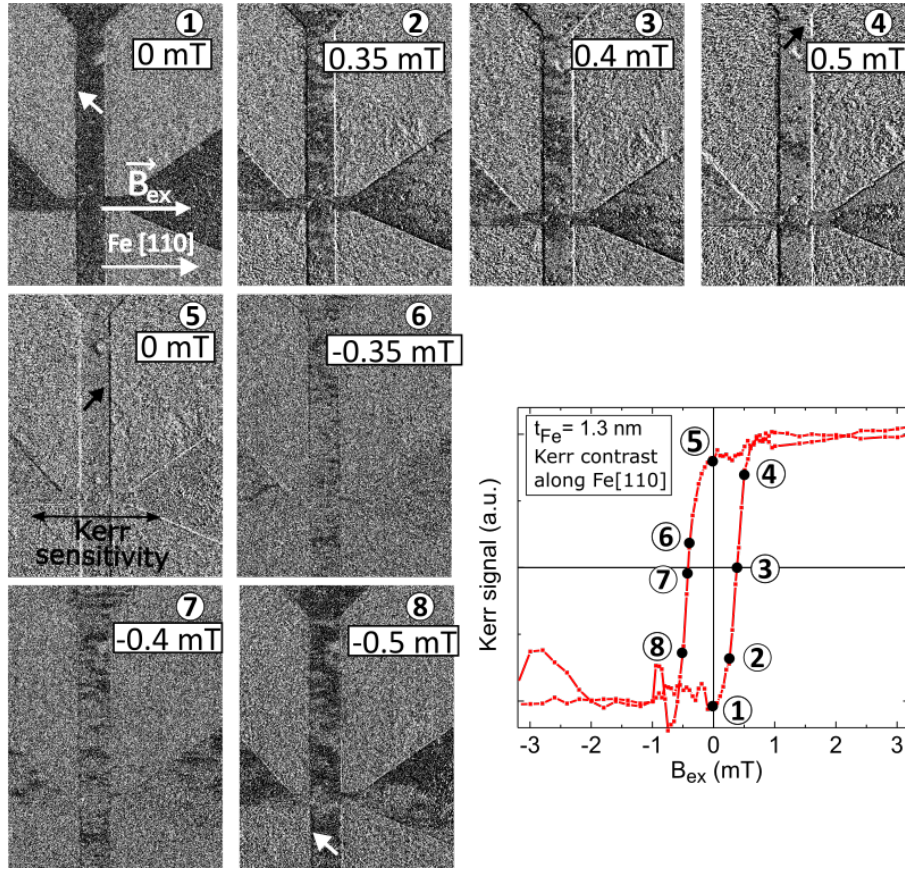


Figure 5.14: Kerr microscopy of the magnetization reversal along the Fe[110] hard axis of the Au/Fe(1.3 nm)/MgO(001) Hall bar. The Kerr sensitivity was set parallel to the direction of the external field B_{ex} . On the hysteresis loop (bottom right) extracted from the acquired Kerr images the B_{ex} values of the corresponding Kerr snapshots are marked with numbers 1-4 for the positive B_{ex} and number 5-8 for the negative B_{ex} scan.

case for magnetic thin film elements [58].

Moreover, the magnetic domains with domain walls aligned to the Hall bar (Fig. 5.13 a) appear to have more irregular shape compared to the domain walls aligned perpendicular to the Hall bar (b). This may be a consequence of the fact that the parallel domain walls are less stable due to the stray fields produced by the magnetization within the domains. In the Au/Fe/MgO(001) Hall bars studied here, the configuration of the magnetization is determined by the competition of the stray field and the magnetic anisotropy. The latter favors magnetization alignment along one of the easy directions, while the stray field allows for a multi-domain state. It is interesting to note that as a consequence, magnetic domains arranged as perpendicular stripes can be formed, which are similar to the suggested *race-track* memory domain structure [164].

5.4.2 Magnetic domains in Au/Fe(1.3 nm) Hall bars

A more irregular configuration of the magnetic domains was observed in the Au/Fe/MgO(001) Hall bars with 1.3 nm Fe layer thickness. An exemplary hard axis magnetization reversal in this sample is shown in Fig. 5.14. The Kerr contrast was set in the direction of the Fe[110] hard axis, so that the domains with projection of the magnetization on this hard direction appear bright. The reversed magnetic domains start to form at ~ 0.35 mT after crossing zero field (image 2 for positive scan and image 6 for negative scan) as observed also in the Hall bar with 1.5 nm Fe layer.

However, at Fe layer thickness of 1.3 nm the domain walls are not straight lines. The orientation of the domain walls appear to follow the direction of the external field as observed also in the 1.5 nm Fe film, while the size of the nucleated domains is much smaller in the 1.3 nm film. The reversed domains seem to nucleate at structural defects scattered along the Hall bar. A strong influence of the structural defects on the nucleation and configuration of the domains for the thinner Fe film is consistent with the increased roundness of the extracted hysteresis loop (bottom right of Fig. 5.14) and its independence on the crystalline direction observed earlier (Sec. 5.1). The observation of the small, irregularly shaped magnetic domains provides further evidence for the broken continuity of the 1.3 nm Fe films. In this case, averaging of the Kerr signal over an area containing domains with different magnetic orientations leads to a rounded hysteresis loop independent on the direction of the applied external field.

5.4.3 Domain structure and the planar Hall effect

The magneto-transport measurements based on the PHE, which were presented in Sec. 5.3, were discussed assuming a single domain state of the Hall bar. However, the single domain picture is inconsistent with the observation of domain formation along the Hall bars, which was revealed by Kerr microscopy. Consequently, a multi-domain picture needs to be considered also in the interpretation of the PHE measurements and of the hysteresis loops acquired using Kerr microscopy, where the signal is averaged over an area of the Hall bar. The hysteresis loops have been compared to the Kerr images in the previous two sections. However, an interesting question remains, which area of the Hall bar contributes to the PHE voltage measured in the magneto-transport setup, when it is composed of domains with different orientations of the magnetization. A better understanding can be gained from an experiment combining PHE measurements and Kerr microscopy, introduced in Sec. 4.3.2.

The magnetic domain configuration of the Au/Fe(1.5 nm) Hall cross was imaged using Kerr microscopy (see Fig. 5.15). The magnetization within the bright (dark) domains is aligned parallel to the Fe[100] (Fe[0 $\bar{1}$ 0]) direction. Additionally, the PHE voltage V_{xy} induced between the transversal contacts (V_{xy}^+ and V_{xy}^-) was measured for each of the domain configurations. The values of V_{xy} measured from a set of subsequently induced

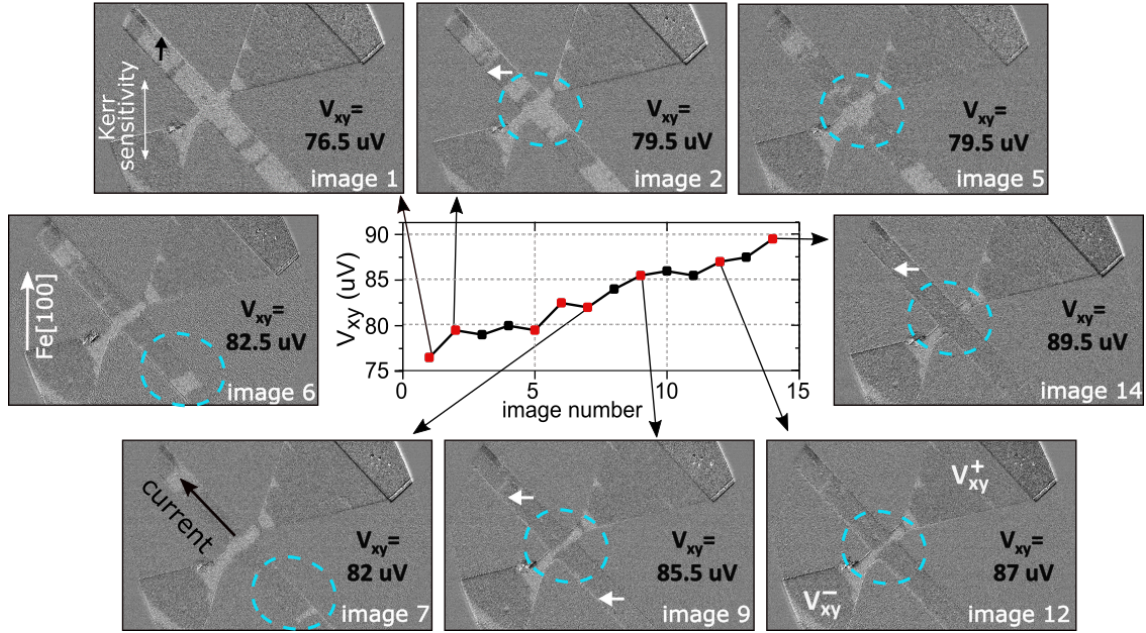


Figure 5.15: A set of Kerr microscopy images of the Au/Fe(1.5 nm)/MgO(001) Hall cross with different domain configurations induced by applying different current densities (see Sec. 6.4). The Kerr sensitivity was set along the Fe[100] easy axis as marked on image 7. The magnetization in the bright domains is oriented along the Fe[100] (black arrow in image 1) and in the dark domains along the Fe[0 $\bar{1}$ 0] (white arrows in image 2,9 and 14). Simultaneously, a longitudinal probing current of 1 mA was used to measure the PHE voltage V_{xy} between the contacts V_{xy}^- and V_{xy}^+ marked on image 12. The corresponding V_{xy} for each Kerr image is marked in red on the plot of the subsequent PHE measurements.

domain configurations is shown in the graph in Fig. 5.15.

The magnetization within the bright domains in Fig. 5.15 is rotated for 90° with respect to the magnetization in the dark domains and therefore, these two domains will induce a different PHE voltage (compare images 1 and 14 and their corresponding V_{xy}). Consequently, when the domain configuration along the Hall bar changes, the corresponding PHE voltage gradually changes as well. This can be seen from the selected Kerr images and the V_{xy} measured from these domain configurations (red dots). Prior to the acquisition of each subsequent Kerr image a domain configuration with an increasing fraction of dark domains was induced along the Hall bar by applying different current densities (see also Sec. 6.4).

The increasing V_{xy} seems to follow the growing portion of the dark domains observed in the subsequent Kerr images. However, the voltage V_{xy} corresponding to Kerr images 2, 3, 4 and 5 exhibits only a small variation even though the domain configuration along the Hall bar visibly changes (e.g. compare the areas within the blue circle on images 2 and 5 in Fig. 5.15). Similarly, the V_{xy} corresponding to images 6 and 7 remains approximately unaffected by the observed change of the domain configuration (within blue circles). On the other hand, only a small variation in the domain configuration in central area of the

Hall cross can be distinguished between images 9, 12 and 14, for which the corresponding V_{xy} exhibits a gradual increase. This indicates that only a limited area of the Hall bar determines the PHE voltage measured between the contacts V_{xy}^- and V_{xy}^+ .

The measurements of the PHE are conducted in the Hall geometry, which means that an electric current is applied along the Hall bar and the induced voltage V_{xy} is measured perpendicular to the current, between two transversal contacts located on either side of the Hall bar, see image 12 in Fig. 5.15. These four contacts, i.e. two for applying the current and two for the V_{xy} measurement, build up the Hall cross. When a homogeneous current density is applied along the length of the Hall bar, the measured PHE voltage between the transversal contacts depends on the orientation of the magnetization in the *Hall cross center*, i.e. the region strictly limited by the width of the transversal contacts (blue area marked in Fig. 5.16 c). However, in a Hall bar structure the applied current density can be shunted by the “passive” transversal contacts as shown by simulations in Ref. [165–167]. The current shunting occurs in the diffusive current regime due to the spreading of the current into the transversal contacts. As a consequence, the current density in the Hall cross center decreases and a finite current density is found in the transversal contacts away from the cross [165–167]. Therefore, the measured V_{xy} can depend on the orientation of the magnetization in the areas of the transversal contacts where the current density spread is not negligible. Moreover, the measured V_{xy} scales with the current density (see Eq. 2.28) and would decrease due to the current shunting. Additionally, because of the spreading of the current into the transversal contacts, its direction may vary even in the areas next to the Hall cross center, see Ref. [167]. The current density distribution and its direction may be further affected by structural defects along the Hall bar. This may lead to contributions to V_{xy} from the areas extended away from the Hall cross center into the direction of the Hall bar (e.g. orange area in Fig. 5.16 c).

Nonetheless, Neumann and Meinert have shown that the current leakage towards the transversal contacts depends on the ratio between the width of the transversal contacts and the width of the Hall bar [167]. For ratios up to 0.5, they have shown that the current density is only slightly distorted from a homogeneous distribution at the Hall cross center, while it becomes strongly inhomogeneous for ratios close to 1, for which the current density decreases down to 50 % of the value away from the Hall cross center [167]. The Hall cross used in the present experiment has the width ratio of $6.5 \mu\text{m}/18 \mu\text{m}=0.36$, see Fig. 5.16 c. Therefore, in a first approximation, a homogeneous current density along the Hall bar can be assumed in the analysis. However, for a precise determination of the Hall bar area, which generates the measured PHE voltage, a more realistic current density distribution needs to be considered, which can be obtained by simulations of the current flow through a Hall cross with a given width ratio. In the following, the observed domain configurations in the Hall bar and the measured V_{xy} will be compared and analyzed.

The obtained PHE voltages for the corresponding Kerr images in Fig. 5.15 vary in

amplitude between the extrema of the PHE measured at saturation (see e.g. Fig. 5.16 a) and seem to depend on the fractions of the bright and dark domains within the relevant region of the Hall bar. In order to confirm the dependence of the PHE voltage on the domain fractions, the latter were estimated from the measured PHE voltages and compared to the fractions observed in Kerr images. To calculate the fractions of the domains from the measured PHE voltages, it was assumed that the Hall bar with a single dark domain would result in PHE voltage of V_{max}^{PHE} and the Hall bar in bright domain state would give V_{min}^{PHE} measured in an external field $B_{ex}=40$ mT in the Kerr microscopy setup, see Fig. 5.16 a. The two extrema were identified from the angular dependence of the PHE by applying B_{ex} along different in-plane directions.

If the region of the Hall bar responsible for the measured PHE voltage contains $x_V\%$ of the dark domains and $(100-x_V)\%$ of the bright domains, we assume that the resulting PHE voltage V_{xy} can be written as

$$V_{xy} = x_V \cdot V_{max}^{PHE} + (100 - x_V) \cdot V_{min}^{PHE}. \quad (5.8)$$

By applying Eq. 5.8 to the set of measured V_{xy} the percentage x_V of the dark domains (black squares) was obtained as shown in Fig. 5.16 b.

The fraction of the dark domains was extracted also from the Kerr images acquired simultaneously with each of the V_{xy} measurements. The approximation of a homogeneous current density along the Hall bar was used and all regions of a selected area of the Hall bar were considered to contribute with an equal weight to the measured V_{xy} . The images were normalized to the maximum and minimum gray values along the Hall bar of the complete image sequence, so that the dark domains were normalized to 1 and the bright domains to 0. In this way, averaging the pixel values of a selected region in the Kerr image directly gives the dark domain percentage x_{Kerr} .

The dark domain percentage x_{Kerr} obtained from the Hall cross center limited by the Hall bar width and the width of the transversal contacts (blue dots in Fig. 5.16 b) exhibits a good match to x_V for the majority of the analyzed Kerr images. When the portion of the Hall bar was enlarged along the wire, the extracted x_{Kerr} increased and lead to an overestimated dark domain percentage. For example, an area of the Hall bar extended from the Hall cross center for $30 \mu\text{m}$ in each direction along the Hall bar (orange rectangle) resulted in a larger dark domain fraction as compared to x_V for all of the analyzed Kerr images (orange dots in Fig. 5.16 b). Extending the rectangle further along the Hall bar lead to additional increase of the extracted x_{Kerr} values (not shown here).

This results indicate that the measured PHE voltage is mainly determined by the configuration of magnetic domains at the Hall cross center. The domain structure of the Hall bar at larger distances ($>10 \mu\text{m}$) from the Hall cross center does not contribute to the measured V_{xy} . Therefore, changes of the domain configuration at $>10 \mu\text{m}$ away from the Hall cross center cannot be unambiguously detected by measuring the PHE voltage between the transversal contacts V_{xy}^+ and V_{xy}^- . The small mismatch between x_{Kerr} from

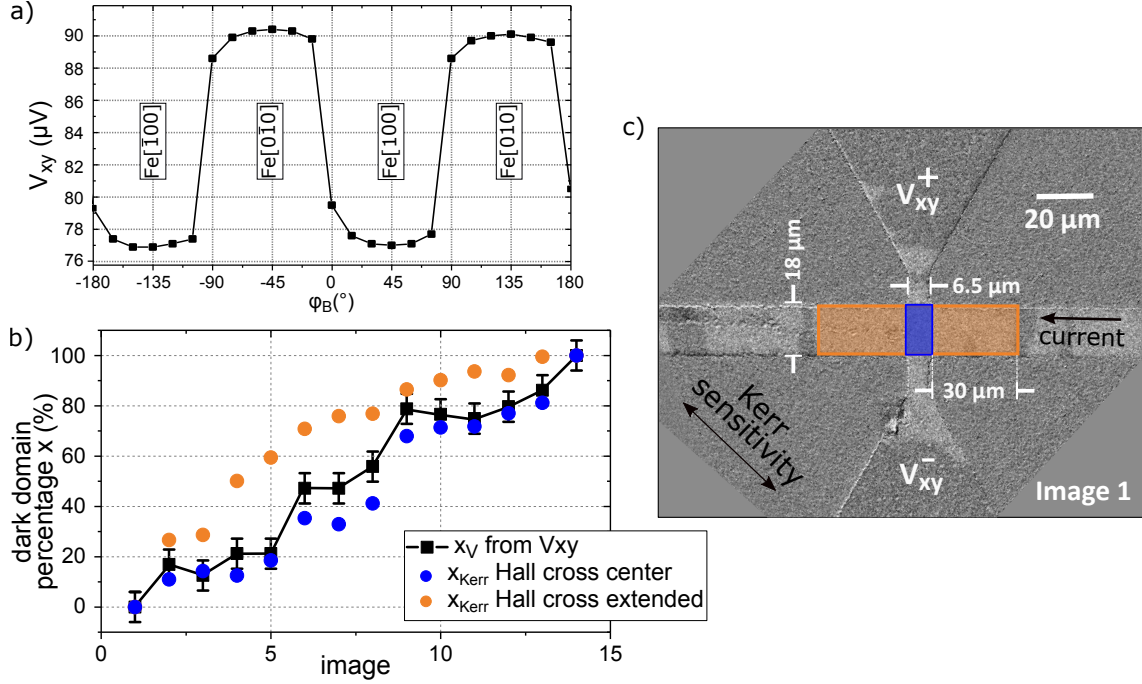


Figure 5.16: a) The PHE measurement in the Kerr microscopy setup from the Au/Fe(1.5 nm)/MgO(001) Hall bar. A longitudinal probing current of 1 mA was used to measure the PHE voltage V_{xy} between the contacts V_{xy}^+ and V_{xy}^- (marked in c) for different directions of 40 mT external in-plane magnetic field with angle φ_B to the current direction. b) The dark domain percentage for a set of subsequent Kerr images calculated from the measured V_{xy} (black squares) compared to the estimated dark domain percentage obtained by averaging the intensity of selected regions of the Hall cross marked in c).

the Hall cross center (blue) and x_V may arise from the unhomogeneous current density distribution at the Hall cross center due to current leakage [167], which was neglected in the present analysis. Moreover, a contribution to V_{xy} may originate also from the area of the transversal contacts, to which the current spreads [167]. Moreover, variation of the current direction in the areas of the Hall bar next to the Hall cross center may add to V_{xy} measured between the transversal contacts. In the region of the Hall cross center, several competing effects may lead to contributions to the measured V_{xy} . Therefore, a precise determination of the area of the Hall cross responsible for the detected PHE voltage is not a trivial task. In the future, by careful manipulation of the domain structure close to the Hall cross center and additional simulations of the current density in the Hall bar, a more quantitative analysis is planned to be conducted.

To put these observations into a perspective, the limited area of the Hall bar contributing to the PHE voltage may offer a practical way to locally probe the in-plane magnetization in a confined area of a material. Keeping in mind the similarity of the domain shape in the Hall bars with 1.5 nm Fe layer thickness to the proposed race-track memory [164] (see

Fig. 5.11, Fig. 5.12, Fig. 5.13), the PHE-readout could be employed to probe the in-plane magnetization in a domain, nucleated along a stripe of a magnetic material and moved along the stripe using a suitable mechanism of domain motion. Moreover, down-scaling of the Hall cross can be considered, because the majority of the Hall bar does not contribute to the PHE voltage (devices in this thesis have Hall bars in length of 0.8 mm). However, the down-scaling of the devices towards the nm-regime requires a dedicated study. The domain shape and size depends on the magnetic anisotropy of the system, which would considerably change in the nm-regime. Nonetheless, by varying the size of the Hall bar, and therefore the magnetic anisotropy, it would be possible to adjust the magnetic fields necessary for magnetization switching and/or inducing the domain motion.

In summary, the Hall bars with 1-1.5 nm Fe thickness exhibit a purely in-plane magnetic easy axis with in-plane anisotropy constant $K_1=(0.3\cdot 10^6-0.9\cdot 10^6)$ J/m³ with a dominant contribution from the shape anisotropy. In the film plane the four-fold magnetic anisotropy dictates the orientation of the magnetization with the cubic anisotropy constant of $K_4=0.9$ (1.5) $\cdot 10^4$ J/m³ for $t_{Fe}=1.3$ (1.5) nm. The in-plane easy magnetization directions of the Hall bars correspond to the extrema of the PHE due to the chosen alignment of the MgO(001) substrate. The PHE measurements demonstrate the *double-jump* magnetization reversal along the hard magnetization axis, which is, most probably, observed due to a small misalignment of the experimental geometry. It has been observed that the 1.3 nm Fe film is not continuous, but the film quality improved for $t_{Fe}=1.5$ nm. This is most evident from the Kerr microscopy analysis of the Hall bars. The Kerr images revealed that the field-induced magnetization reversal proceeds via nucleation and growth of magnetic domains, which exhibit a more regular shape and a larger size for the 1.5 nm Fe film compared to the 1.3 nm Fe layer. The measured PHE voltage is determined mainly by the domain configuration in the Hall cross center.

6. Magnetization switching in Au/Fe/MgO(001) by applied current density

It has been shown in Ch. 5 that the magnetization reversal process along the hard axes of the Au/Fe/MgO(001) heterostructures proceeds via a *double-jump* magnetization reorientation mechanism. The reversal proceeds with two jumps between the easy magnetization directions, which are followed by rotation of the magnetization towards the external field direction, when the magnetic field approaches the saturating value. The magnetization direction during the reversal process was probed via MOKE (in Kerr microscopy) and by applying a longitudinal low current density and measuring the transversal PHE voltage (in magneto-transport measurements). In both experiments, the applied current density along the Hall bar was kept low ($j < 10^6$ A/cm²) or zero in order to maintain the current-induced effects (i.e. fields, torques or thermal effects) on the magnetization small. Thus, it is reasonable to assume that the observed magnetization reversal presented in Ch. 5 is driven purely by the external magnetic field.

This chapter, however, focuses on the current-induced effects, which can be observed when the previous magneto-transport measurements are repeated using higher current density $j > 10^7$ A/cm² applied along the Hall bar. For reasons of clarity, the key results will be listed in the following, while the details of the thorough analysis of the current-induced fields, magnetization reorientation, and domain formation, studied using magneto-transport measurements and Kerr microscopy, can be found in the individual sections of this chapter.

The PHE measurements in the *magnetic-field-scan* mode using $j > 10^6$ A/cm² (Sec. 6.1) exhibit a **left-right asymmetry** of the hysteresis loops, i.e. between negative and positive magnetic field scans, and an additional shift in R_{xy} between the two scans at temperatures lower than 50 K. The amplitude of the left-right asymmetry scales with the applied current density and is assigned to the Oersted field generated by the current in the Au layer of the Hall bar. The R_{xy} shift may be a result of a current-induced effective field in the out-of-plane direction, which is indicated also in the measurements of the PHE angular dependence (Sec. 6.1.4) and could originate from the increased spin Hall effect (SHE) in Au at low temperatures.

Kerr microscopy of the Hall bars with applied current density up to $j = 3 \cdot 10^7$ A/cm² at room temperature reveals an **Oersted field of up to 1 mT** in the direction perpendicular to the current (Sec. 6.2). Interestingly, the spatially-resolved hysteresis loops extracted from the Kerr images additionally show that the effective field acting on the magnetization

at the Hall cross center can vary from the Oersted field extracted from the remaining Hall bar, which may have a significant effect on the current-induced switching.

Expanding on these findings, current-driven hysteresis loops are demonstrated (Sec. 6.3), which show that the Oersted field can be employed not only to tilt the magnetization of the Fe layer, but also for **reorientation of the magnetization** between two orthogonal easy directions by inducing formation of switched domains.

Finally, **current-induced multi-level switching** of the magnetic state is demonstrated by applying current density pulses in the range between $1.5 \cdot 10^7 \text{ A/cm}^2 < j < 3.5 \cdot 10^7 \text{ A/cm}^2$ to the Hall bar (Sec. 6.4). Different levels are distinguished by measuring the PHE resistance and can be related to multi-domain states of the magnetization in the Fe layer, which are stable in the absence of external fields.

We note, that in the sections of this chapter describing the results of the room-temperature measurements we use the term *current-induced* to refer to the effects, which were observed to scale with the current density applied to the Au/Fe/MgO(001) Hall bars. The current density generates an Oersted field, which can reach values comparable to the room-temperature coercive field of the system. Therefore, the term *current-induced switching* in this thesis is not strictly limited to have a direct relation to spin currents generated by the applied charge current density, which is often the case in literature.

6.1 Asymmetry of the high-current PHE hysteresis loops

According to Ampere's law an electric current applied along a wire produces a magnetic field B_{Oe} , which scales proportionally to the current density j ($B_{Oe} \propto j$). Moreover, in FM/heavy metal (HM) systems, a current applied parallel to the layers was demonstrated to induce torques on the magnetization of the FM layer (see Sec. 2.5.2). Both effects are expected to influence the magnetization reversal process and can be studied, for instance, by magneto-transport measurements of the PHE with a high probing current applied to the Hall bar. If the applied electric current does not induce any magnetic fields or torques or the induced effects are negligibly small, the magnetization reversal process, observed e.g. in the *magnetic-field-scan* mode (see Sec. 4.2), would be expected to be independent on the probing current density. Otherwise, if the current-induced effects are not negligible, the magnetization reversal process is expected to be altered.

Therefore, the PHE measurement of the magnetization reversal along the Fe[1 $\bar{1}$ 0] hard axis in Au/Fe(1.3 nm)/MgO(001) Hall bars was repeated using an increasing probing current from $I=3 \text{ mA}$ to $I=15 \text{ mA}$, see Fig. 6.1. For the Hall bar device with $20 \mu\text{m}$ width and 5.3 nm thickness of the conducting layer (4 nm Au , 1.3 nm Fe), the applied electric currents correspond to current densities from $j=0.3 \cdot 10^7 \text{ A/cm}^2$ to $j=1.4 \cdot 10^7 \text{ A/cm}^2$. Upon increasing j a strong asymmetry between the magnetization reversal for the positive (from $B_{ex} < 0$ to $B_{ex} > 0$, black dots) and negative (from $B_{ex} > 0$ to $B_{ex} < 0$, red dots) magnetic field scan is observed, see Fig. 6.1.

6.1. Asymmetry of the high-current PHE hysteresis loops

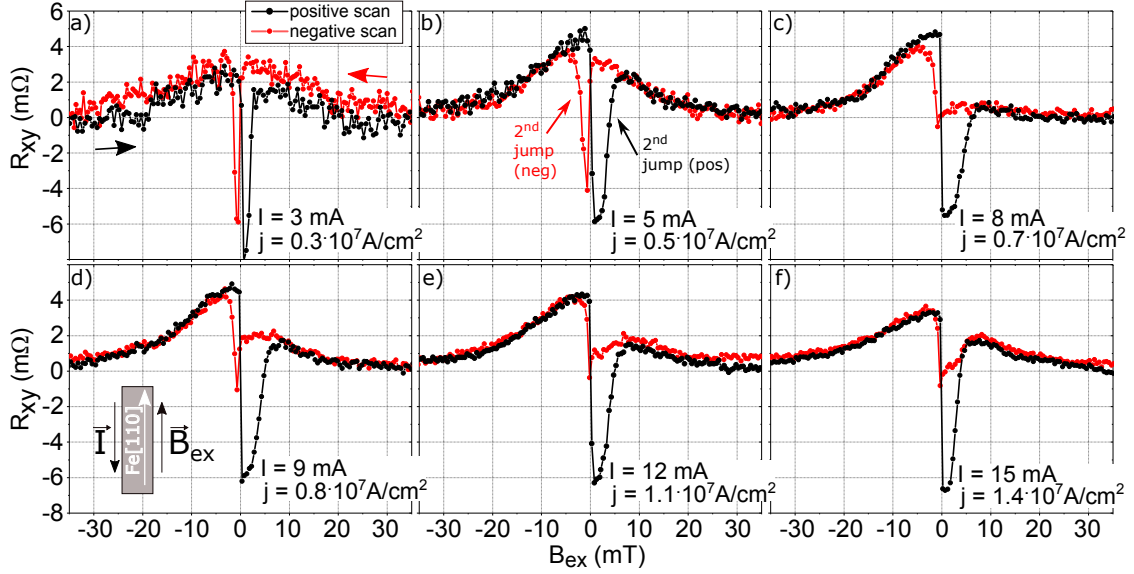


Figure 6.1: Magnetization reversal along the hard axis $\text{Fe}[\bar{1}\bar{1}0]$ in $\text{Au}/\text{Fe}(1.3 \text{ nm})/\text{MgO}(001)$ Hall bar probed via PHE in the magnetic-field-scan mode at 250 K as described in Sec. 4.2. The longitudinal probing current I along the Hall bar was equal to 3, 5, 8, 9, 12 or 15 mA as indicated on the corresponding graph. Increasing the probing current density induces a larger asymmetry between the positive magnetic field scan (black dots) and negative magnetic field scan (red dots) magnetization reversal. The applied current and the positive external field are parallel to the $\text{Fe}[\bar{1}\bar{1}0]$ hard direction, see sketch in the inset of d).

The PHE hysteresis loop acquired using 3 mA probing current exhibits the double-jump magnetization reversal for both B_{ex} scans. A small asymmetry in the width of the double-jump dip is observed between the positive and the negative B_{ex} scans already for $I=3$ mA. The amplitude of the asymmetry increases for higher probing currents. This *left-right asymmetry* means, in other words, that the second switch of the magnetization occurs at a smaller B_{ex} during the negative field scan compared to the positive field scan, see PHE loops for $j < 0.6 \cdot 10^7$ A/cm² in Fig. 6.1 a,b.

For the positive magnetic field scan (black dots), the double-jump dip remains present for all probing currents. The reorientation of the magnetization during the second jump is more gradual compared to the first jump immediately after crossing zero B_{ex} . For higher probing currents ($I=8-15$ mA in c-f), R_{xy} after the second jump does not reach the value obtained for the magnetization saturated along the easy axis (compare R_{xy} before the first jump and after the second jump).

For the negative field scan (red dots) the magnetization reversal process strongly differs from the double-jump scheme observed using a low probing current densities. When B_{ex} decreases from the positive saturation value towards 0 the transversal resistance R_{xy} gradually increases, which indicates a rotation of the magnetization towards one of the easy directions. However, for probing current densities between $j=0.7 \cdot 10^7$ A/cm² to

$j=1.4 \cdot 10^7$ A/cm² the R_{xy} value for saturation along the easy direction is not reached. A narrow double switch is observed at a small negative B_{ex} after crossing zero field for $j=0.7 \cdot 10^7$ A/cm² and $j=0.8 \cdot 10^7$ A/cm² (c and d). For the higher probing current densities ($j > 1 \cdot 10^7$ A/cm² in e and f) a double jump of the magnetization is observed before crossing zero field during the negative field scan. The amplitudes of the corresponding R_{xy} jumps are smaller compared to the amplitudes of the jumps during positive magnetic field scan (black dots). For $j > 1 \cdot 10^7$ A/cm², the switching fields for both directions of the magnetic field scan are approximately the same and positive.

The observed current density dependence of the PHE hysteresis loop clearly shows that the current-induced effects on the magnetization reversal process are not negligible and thus require further investigation. In the following, a detailed analysis of the dependence of the left-right asymmetry on the current density, B_{ex} direction and temperature will be discussed. The results have shown that the observed asymmetry can be assigned to the current-induced Oersted field, which causes changes of the magnetization reversal process.

6.1.1 Comparison to Stoner-Wohlfarth simulations

To gain a better understanding of the obtained PHE hysteresis loops in Fig. 6.1 the hard axis magnetization reversal was calculated from the Stoner-Wohlfarth model. Additionally to the energy terms from the four-fold anisotropy and the Zeeman term (see Appendix C), a **constant magnetic field** B_{\perp} in the direction perpendicular to the applied current I was considered to contribute to the total magnetic energy of the system, see Eq. 1.5 in Appendix C. This added field stands for a current-induced field (or a field-like torque) responsible for the effects observed in the experiment.

In the simulation, the following anisotropy constants were used: $K_u=0$ and $K_4=9 \cdot 10^3$ J/m³. The magnetic field angle was set to $\varphi_B=5^\circ$ and the saturation magnetization $\mu_0 M_S=2.1$ T. The additional in-plane field B_{\perp} in the direction perpendicular to $\vec{I} \parallel \text{Fe}[1\bar{1}0]$ ($\varphi_{B_{\perp}}=90^\circ$) was varied. The simulated PHE loops show, that B_{\perp} indeed induces a *left-right asymmetry*, which scales with B_{\perp} , see Fig. 6.2. The same sign of the asymmetry as compared to the experiment was obtained using $B_{\perp} < 0$, i.e. $\vec{B}_{\perp} \parallel \text{Fe}[\bar{1}\bar{1}0]$, in the simulation. For the probing current $I=15$ mA the double jump for the negative field scan (red dots) is strongly shifted to higher B_{ex} , so that the first magnetization jump occurs at a positive magnetic field, overlapping with the second jump of the positive field scan (black dots), see Fig. 6.2 b and d. The second jump of the magnetization occurs after crossing zero field.

The steps of the magnetization reversal during the negative field scan are sketched in the inset of Fig. 6.2 c and d, which show the evolution of the magnetization angle φ_M in response to the applied B_{ex} as calculated from the Stoner-Wohlfarth model. Firstly, during the positive field scan (black line) the second switch ($\varphi_M=-45^\circ \rightarrow 45^\circ$) shifts to an increased $B_{ex} > 0$ for the higher current density. Secondly, the magnetization reversal during the negative field scan (red line) follows a different set of steps depending on

6.1. Asymmetry of the high-current PHE hysteresis loops

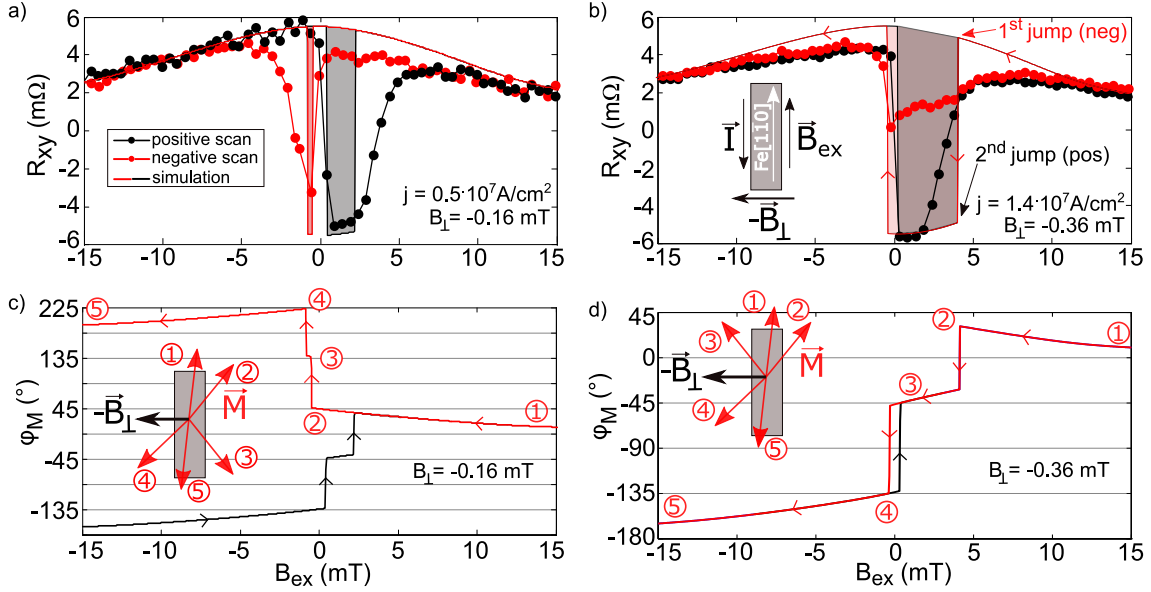


Figure 6.2: The experimental PHE hysteresis loops measured at 250 K on the Au/Fe(1.3 nm)/MgO(001) Hall bar using **a)** $j=0.5 \cdot 10^7 \text{ A/cm}^2$ and **b)** $1.4 \cdot 10^7 \text{ A/cm}^2$. The positive (black dots) and negative (red dots) experimental magnetic field scans along the $\text{Fe}[1\bar{1}0]$ hard axis are compared to simulated PHE signal (black and red solid line), calculated from the Stoner-Wohlfarth model (Appendix C). An additional current-induced in-plane magnetic field B_{\perp} was considered in the simulation in the direction perpendicular to the current as sketched in the inset of b). The angle φ_M between the magnetization and the $\text{Fe}[1\bar{1}0]$ direction calculated by minimizing the Stoner-Wohlfarth equation with **c)** $B_{\perp}=-0.16 \text{ mT}$ and **d)** $B_{\perp}=-0.36 \text{ mT}$ for the positive (black) and negative (red) magnetic field scan. The insets show the steps 1-5 of the magnetization reversal for the negative field scan.

the applied current. For $j=0.5 \cdot 10^7 \text{ A/cm}^2$ (c) the first magnetization jump occurs at $B_{ex} < 0$ (2 \rightarrow 3) and corresponds to $\varphi_M = 45^\circ \rightarrow 135^\circ$, while for the higher current density (d) it corresponds to $\varphi_M = 45^\circ \rightarrow -45^\circ$ and occurs at $B_{ex} > 0$. During the second switch (3 \rightarrow 4) the magnetization jumps from $\varphi_M = 135^\circ \rightarrow 225^\circ$ for lower current density and from $\varphi_M = -45^\circ \rightarrow -135^\circ$ for the higher current density. Note, that the angles $\varphi_M = 225^\circ = -135^\circ$, therefore the final step of the magnetization reversal (4 \rightarrow 5) is the same for both applied current densities.

In short, the magnetization reversal for $j < 0.5 \cdot 10^7 \text{ A/cm}^2$ proceeds along opposite sides of the Hall bar for the positive and negative B_{ex} scans. On the other hand, for the higher current density (d) the simulated variation of φ_M during the negative B_{ex} scan almost exactly follows the steps of the magnetization reversal for the positive B_{ex} scan. This is due to the unidirectional anisotropy introduced to the system by B_{\perp} . The additional field lowers the magnetic energy for φ_M closer to the B_{\perp} direction, which promotes the magnetization reversal via easy directions closer to B_{\perp} . The effect is especially pronounced when B_{ex} is decreased towards zero and when the probing current density is high, inducing a higher B_{\perp} .

On the one hand, the contribution to the magnetic potential energy of \vec{B}_{ex} and \vec{B}_{\perp} could be replaced with an effective magnetic field calculated as a sum of the two vectors $\vec{B}_{eff} = \vec{B}_{ex} + \vec{B}_{\perp}$. When \vec{B}_{ex} is swept the effective field \vec{B}_{eff} changes its direction. For example, for high \vec{B}_{ex} above the saturating value, $\vec{B}_{eff} \parallel \vec{B}_{ex}$ and when \vec{B}_{ex} is reduced the small misalignment of the Hall bar with respect to \vec{B}_{ex} defines the direction of the first rotation of the magnetization (1→2 in the sketch in Fig. 6.2 d). This rotation is in the same sense for both magnetic field scans, i.e. towards an easy direction along the same diagonal. For small \vec{B}_{ex} , the effective field rotates towards \vec{B}_{\perp} for both, positive and negative magnetic field scans and forces the magnetization to align along its direction. Close to the zero field the response of the magnetization is a consequence of the competition between \vec{B}_{\perp} and the anisotropy fields.

On the other hand, \vec{B}_{\perp} can be understood as a small magnetic field, which induces nucleation of magnetic domains with 90° rotated magnetization. In this picture, the magnetization reversal proceeds by growth of domains with switched magnetization. The direction of \vec{B}_{\perp} defines the direction of the magnetization in the switched domains. In support of the multi-domain picture is also the observation that the simulated PHE hysteresis loop does not explain all the features of the experimental hysteresis loops obtained with a current density beyond $0.5 \cdot 10^7$ A/cm². The sharpness of the simulated magnetization jumps is not observed in the experiment, where the changes of the PHE resistance are rather gradual, indicating formation of domains in the Hall cross center. Moreover, for the negative field scan in the region $-5 \text{ mT} < B < 5 \text{ mT}$ the PHE resistance R_{xy} does not reach the values expected for $\varphi_M = \pm 45^\circ$ as it is the case for the positive scan. For the experimental PHE hysteresis loop acquired using $I=15$ mA the values of R_{xy} do not reach the extrema also for the positive scan (black dots in Fig. 6.2 c). This deviations from the simulated PHE hysteresis loop indicate that magnetization reversal includes multi-domain states, which are especially significant for the negative field scan. This is most probably due to the orientation of the additional in-plane field B_{\perp} , which for the negative magnetic field scan points opposite to the preferred rotation of the magnetization, as sketched in the inset of Fig. 6.2 d (rotation from 1→2 has the opposite sign compared to \vec{B}_{\perp}).

Furthermore, the PHE hysteresis loops were simulated using different B_{\perp} values in order to find the best fitting curves to the experimental PHE hysteresis loops acquired with probing currents $I=3-15$ mA (Fig. 6.1). Other parameters in the equation for the magnetic potential energy (Eq. 1.5 in Appendix C) were kept constant. The extracted B_{\perp} values from the best matching simulated curves are plotted against the corresponding probing currents in Fig. 6.3 (black dots). The error bars were determined by B_{\perp} values for which the agreement between the simulation and the experimental data changes for less than 5% compared to the best fitting. The error increases with increasing current and reaches values up to 0.14 mT for $I=15$ mA.

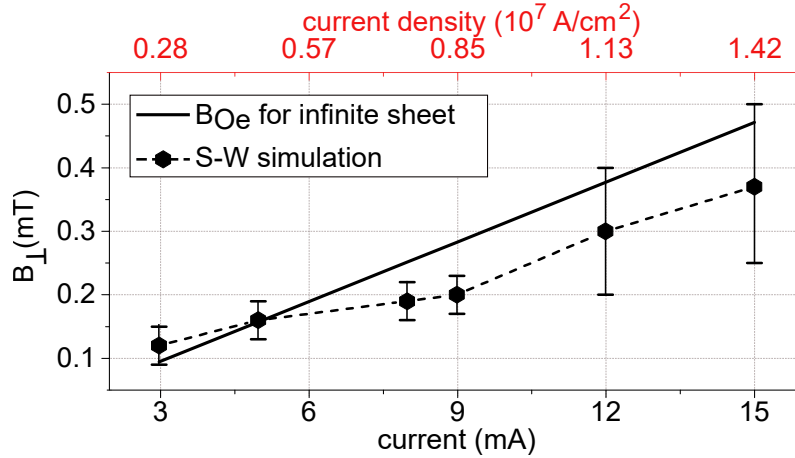


Figure 6.3: The current-induced in-plane magnetic field B_{\perp} as determined from the simulation (black dots) of the planar Hall hysteresis loops for Au/Fe(1.3 nm)/MgO acquired at 250 K with magnetic field applied along the Fe[110] hard axis and as calculated from the Ampere's law approximation for an infinite conducting sheet (black line) for different applied current densities. The latter was calculated as $B_{Oe} = \mu_0 I / (2w)$, where I is the current along the x-axis and $w = 20 \mu\text{m}$ is the width of the Hall bar.

The simulated B_{\perp} values can be compared to a simplified Oersted field calculation (black line in Fig. 6.3). For this, the Hall bar is considered as an infinite conducting sheet, which is a reasonable approximation, since the ratio between the thickness and the width/length of the Hall bar is very high (in the order of 1:10000). This approximation of the Oersted field is often used to estimate the upper limit of the Oersted field in FM/non-magnetic metal (NM) bilayers [95, 168]. To obtain the upper limit it is assumed that the applied current flows in the NM layer and induces an Oersted field at the position of the adjacent FM layer. In the case of Fe/Au/MgO(001) Hall bars this is a fair approximation, because of the higher conductivity of the thicker Au layer. Following Ampere's law in the infinite conductive sheet approximation the Oersted field generated by current I can be calculated as $B_{Oe} = \mu_0 I / (2w)$, where $w = 20 \mu\text{m}$ is the width of the Hall bar. The reasonable agreement between the data and the simplified infinite sheet approximation indicates that the Oersted field may have a dominating effect on the magnetization reversal process when a high current density is applied to the Hall bar, see Fig. 6.3. However, for increasing probing current density the infinite sheet approximation starts to deviate from the obtained B_{\perp} from the simulations. This deviation may be related to the mismatch between simulation and data due to the domain formation or due to additional current-induced effects such as heating.

6.1.2 Dependence on the direction of the external magnetic field

With the aim of further characterization of the observed current-induced field B_{\perp} the PHE hysteresis loops were investigated for different directions of the external magnetic field B_{ex} .

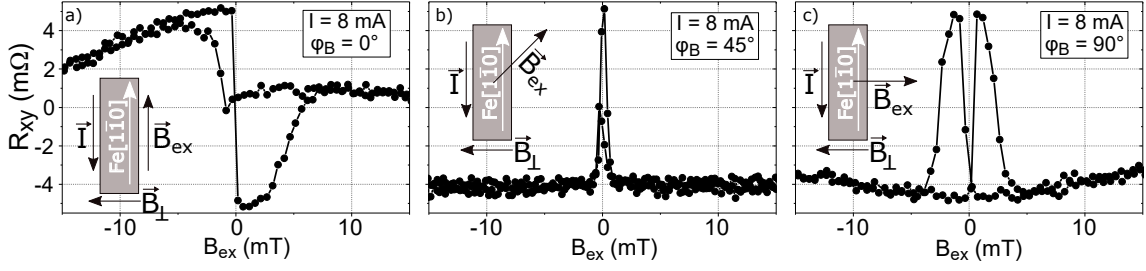


Figure 6.4: The PHE hysteresis loops acquired at 250 K from Au/Fe(1.3 nm)/MgO(001) Hall bars using probing current of 8 mA and magnetic field B_{ex} applied along the direction with **a)** $\varphi_B=0^\circ$, **b)** 45° and **c)** 90° angle to the Fe[1 $\bar{1}$ 0] hard axis, see inset of each graph for the corresponding geometry of the experiment.

These measurements were conducted in the mode *magnetic field scan angular dependence* as described in Sec. 4.2. The PHE hysteresis loops shown in Fig. 6.4 were acquired using probing longitudinal current of 8 mA and B_{ex} applied at angles $\varphi_B=0^\circ$, 45° and 90° to the Fe[1 $\bar{1}$ 0] direction. For $\varphi_B=45^\circ$ and $\varphi_B=90^\circ$ the left-right asymmetry vanishes. In fact, for the magnetic field scan along $\varphi_B=45^\circ$, i.e. B_{ex} along the easy axis Fe[100], two sharp jumps of the magnetization are observed at $B_{ex} \sim \pm 0.5$ mT, while for $\varphi_B=90^\circ$ the second magnetization jumps are more gradual and fully saturate at $B_{ex} \sim \pm 5$ mT.

The reduced asymmetry of the PHE hysteresis loops for $\varphi_B > 40^\circ$ is not surprising when the additional in-plane magnetic field B_\perp is considered. When \vec{B}_{ex} direction is close to $\varphi_B=90^\circ$ then the angle between \vec{B}_{ex} and the current-induced \vec{B}_\perp reduces to zero. This means that the direction of the total effective magnetic field acting on the magnetization does not vary when B_{ex} is reduced, but only changes its strength. Therefore, the PHE response to the magnetic field scan starts to resemble more the PHE hysteresis loop obtained using a small probing current density.

When the external magnetic field \vec{B}_{ex} and \vec{B}_\perp are oriented along the same axis, a constant shift of the hysteresis loop is expected, from which B_\perp can be estimated. The shift of the PHE hysteresis loops acquired using $I=8$ mA with positive and negative polarity along the Hall bar (marked as $I=+8$ mA (black dots) and $I=-8$ mA (red dots) in Fig. 6.5) reverses upon reversal of the polarity of the current. Because the magnetization reversal proceeds via the same steps independent on the applied current polarity and the periodicity of the PHE is 180° , a similar shape of the PHE loops is acquired for both polarities of the probing current.

The region $-6 \text{ mT} < B < 6 \text{ mT}$ of the magnetic field scans was measured with a higher resolution for both current polarities and both directions of the scan, see Fig. 6.5 b. Note that each of the magnetic field scans reached the saturating magnetic fields (either positive or negative), but it is not shown in the graphs. The hysteresis loops are shifted either to positive or negative magnetic fields depending on the polarity of the applied current direction. This is an additional confirmation that the observed features of the high current PHE hysteresis loops indeed scale with the applied current density. The shift of the PHE

6.1. Asymmetry of the high-current PHE hysteresis loops

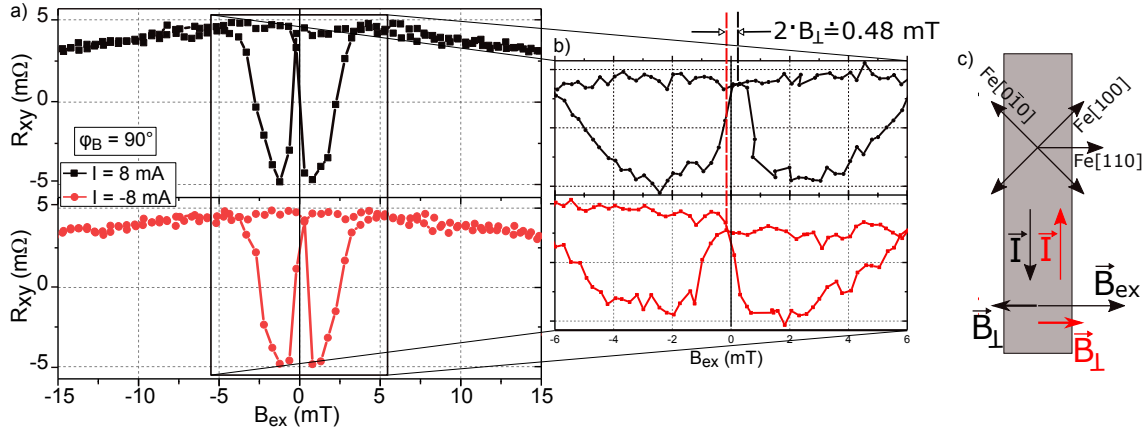


Figure 6.5: a) The magnetization reversal along the direction perpendicular to the Hall bar, i.e. along Fe[110] direction ($\varphi_B=90^\circ$). The planar Hall resistance R_{xy} was measured by applying a probing current $I=8$ mA either in the direction antiparallel (black dots) or parallel (red dots) to the Fe[110]. b) The measurement with a smaller step in the magnetic field reveals a shift of the PHE hysteresis loops towards positive (negative) magnetic fields for the parallel (antiparallel) alignment of the applied current. Note, the magnetic field scans shown in b) reached the saturating magnetic field values for both current polarities and both senses of the magnetic field scan. c) Sketch of the experiment.

hysteresis loop with positive current in respect with the one with negative current was evaluated to be ~ 0.48 mT. Taking into account that the reversed direction of the probing current also reverses the direction of the current-induced in-plane field B_\perp (in the presented case, \vec{B}_\perp reverses from -90° for $I=8$ mA to 90° for $I=-8$ mA), the observed shift between the hysteresis loops equals $2 \cdot B_\perp$. Therefore, we obtain a value of $B_\perp(I=8 \text{ mA})=0.24$ mT, which agrees very well with the $B_{Oe}(8 \text{ mA})=0.25$ mT calculated for the approximation of the infinite conducting sheet and matches well with the $B_\perp(I=8 \text{ mA})=0.19$ mT, which was used in the simulation of the experimental PHE hysteresis loop (shown in Fig. 6.1).

6.1.3 Temperature dependence of the current-induced left-right asymmetry

The amplitude of the left-right asymmetry, which was observed to be a consequence of a current-induced field B_\perp , scales with the applied current density. Moreover, it is expected to depend on the strength of the magnetic anisotropy of the system. This is because the PHE hysteresis loop for the hard axis magnetization reversal depends strongly on the anisotropy fields in the system. In the Au/Fe/MgO(001) heterostructures an in-plane cubic magnetic anisotropy was observed with the anisotropy constant K_4 , which increases at low temperatures, see Sec. 5.3. This means, that the coercive field B_c along an easy direction also increases at low temperatures. Therefore, the amplitude of the left-right asymmetry of the PHE hysteresis loops induced by a constant current density is expected to decrease when the temperature of the sample is lowered.

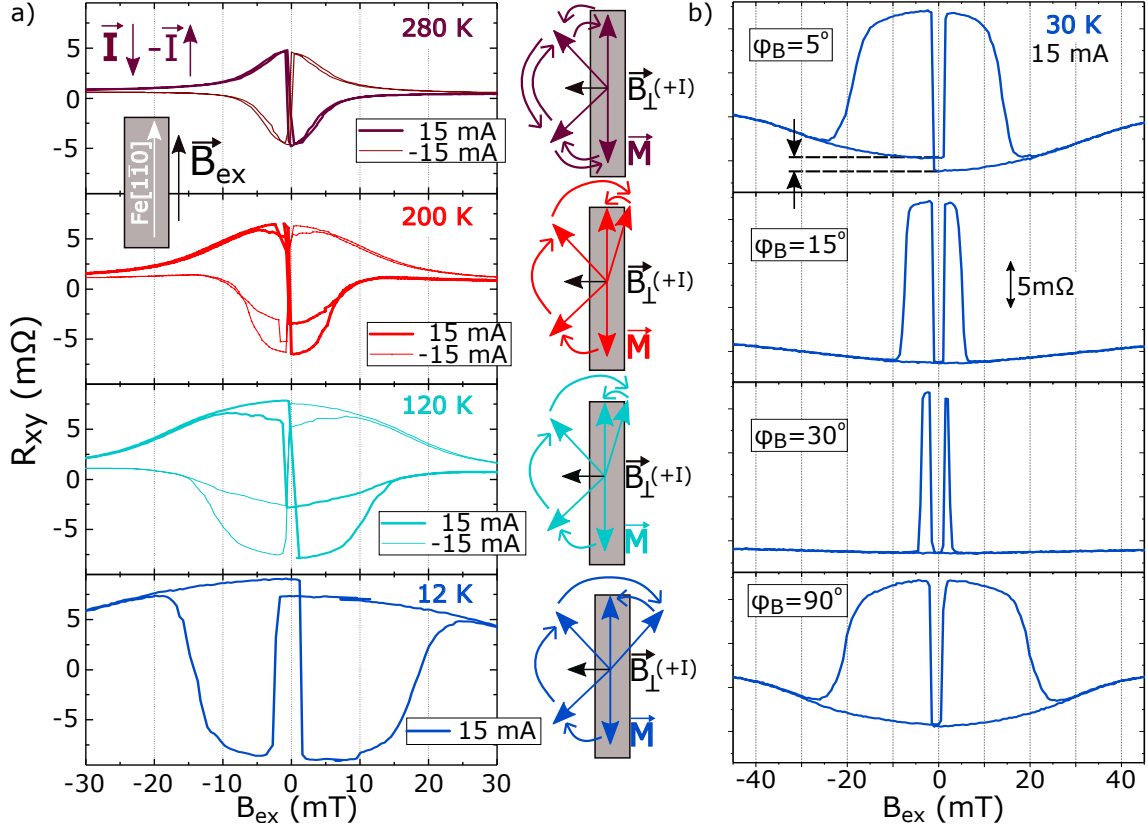


Figure 6.6: **a)** PHE hysteresis curves acquired at 280 K (dark red), 200 K (light red), 120 K (light blue) and 12 K (dark blue) from Au/Fe(1.3 nm)/MgO(001) Hall bars using a probing current of ± 15 mA, as marked on the graphs. The magnetic field was scanned along the Fe[110] hard axis as sketched in the inset. On the right to each graph the magnetization reversal process is sketched for current applied opposite to the Fe[110] direction (\vec{I}) for the positive magnetic field scan (for 280 K, 200 K, 120 K and 12 K) and for the negative scan for 280 K. **b)** The PHE hysteresis loops acquired at 30 K from the same Hall bar using a current \vec{I} of 15 mA and magnetic field scanned at angle $\varphi_B = 5^\circ, 15^\circ, 30^\circ$ and 90° to the Fe[110] direction as marked on the graphs. On the first graph the shift in the PHE resistance R_{xy} is marked with dashed lines.

To validate this hypothesis the PHE hysteresis loops were acquired at different sample temperatures using a probing current $I = \pm 15$ mA (Fig. 6.6 a). B_{ex} was scanned along the Fe[110] hard axis (sketched in the inset). The shape of the loops shows a clear temperature dependence. At temperatures $T > 200$ K the second magnetization reorientation is observed at $B_{ex} < 10$ mT, while at lower temperatures ($T < 150$ K) the second transition of the magnetization sets in for $B_{ex} > 10$ mT. This indicates an increase of the coercive field B_c at lower temperatures. Additionally, the increase of B_c at low temperatures leads to higher saturating fields, which align the magnetization along the Fe[110] hard axis.

Moreover, the magnetization reversal process detected via PHE varies with temperature. The probing current of $I = 15$ mA corresponds to current density of $2.8 \cdot 10^7$ A/cm²

and induces an Oersted field $B_{Oe}=0.47$ mT according to the infinite conducting sheet approximation, see Fig. 6.3. At 280 K the magnetization reversal is modified by the current-induced field so that only a single switch of the magnetization per magnetic field scan occurs at a small B_{ex} after crossing zero (dark red line in Fig. 6.6). At this temperature the B_c of the cubic anisotropy is low and the current-induced field B_{\perp} is strong enough to force the magnetization to preserve a positive projection on the direction of the B_{\perp} throughout the reversal process, see sketch. In other words, the Zeeman energy due to B_{\perp} lowers the magnetic potential energy for the easy magnetization directions closest to B_{\perp} and increases the potential barrier for the jumps towards the other easy directions.

When the sample is cooled below 200 K, the PHE hysteresis loops show a changed magnetization reversal process compared to the one at 280 K (see the loops in light red for 200 K and light blue for 120 K in Fig. 6.6 a). Firstly, the PHE loops at $T < 200$ K are broadened in B_{ex} by a factor of 2 compared to the loop at 280 K, which indicates an increase of B_c . Secondly, the PHE hysteresis loops show an asymmetry between the positive and negative B_{ex} scans (observed also at 250 K as shown in Figs. 6.1 and 6.2 a,b). The second reorientation of the magnetization (at $|B_{ex}| > 5$ mT) seems to involve a rotation towards the easy axis with a negative projection onto the \vec{B}_{\perp} (see illustrations in Fig. 6.6 a). Therefore, in the temperature range between 100-200 K, B_{\perp} induced by $I=15$ mA modifies the magnetization reorientation despite the increased B_c . Note, that the different amplitude of the R_{xy} signal between the positive and negative B_{ex} scans (at $|B_{ex}| < 10$ mT) is most probably a consequence of domain formation.

When the sample temperature was decreased to 12 K (dark blue line) the *double-jump* reversal process was observed for both senses of the magnetic field scan. In fact, the shape of the PHE hysteresis loop acquired with $I=15$ mA at 12 K resembles the hysteresis loop acquired with a much smaller probing current ($I=3$ mA) at higher temperatures, see e.g. Fig. 6.1. Therefore, the variation of the PHE hysteresis with an increasing probing current density (in Fig. 6.1) is in a way similar to the modification of the hysteresis loop when only the temperature is decreased, while the current density is kept constant.

Interestingly, when the temperature is decreased below 50 K, a shift in the PHE resistance is observed between the positive and the negative magnetic field scans additionally to the discussed left-right asymmetry. This can be seen in Fig. 6.6 a at 12 K (dark blue) and in Fig. 6.6 b, where the PHE loops acquired at 30 K and for different directions of B_{ex} are shown. The R_{xy} shift is clearly visible for B_{ex} scanned along an axis close to the Fe[1 $\bar{1}$ 0] hard axis ($\varphi_B < 10^\circ$). The shift reduces to zero when the angle φ_B between B_{ex} and the hard axis is further increased.

Using the simulation based on the Stoner-Wohlfarth equation for a system with a four-fold magnetic anisotropy and in an externally applied magnetic field B_{ex} , the shift in R_{xy} observed in the PHE hysteresis loops at 30 K can be partially reproduced, see Appendix C.2. The equation for the magnetic potential energy was equipped with the Zeeman term due to the external magnetic field B_{ex} and a current-induced field B_{\perp} , and

magnetic anisotropy terms. Additionally, an out-of-plane field B_{oop} was defined to be dependent on the angle between the magnetization and the current direction following the equation for the damping-like term of the current-induced torques, see discussion in Sec. 6.1.4 and in Appendix C.2. According to this definition, the B_{oop} would reach a maximum when the current and the magnetization are aligned and decrease to zero when they are perpendicular. This additional field could tilt the magnetization out of the film plane and give rise to an AHE voltage. The simulations showed that the additional B_{oop} -term indeed results in a shift in R_{xy} as observed in data for $\varphi_B < 10^\circ$. However, the shift in the simulated PHE hysteresis loops does not decrease with φ_B as observed in the experiment, but stays constant for all direction of B_{ex} , see Fig. C.7 and the discussion in Appendix C.2. Therefore, the model of the current-induced out-of-plane term used in the simulation cannot reliably explain the origin of the observed R_{xy} shift in the PHE loops. However, the agreement between the data and simulation for $\varphi_B < 10^\circ$ is an indication of a possible current-induced field component in the direction perpendicular to the film plane at $T < 50$ K. Furthermore, additional signatures of B_{oop} observed in PHE measurements will be discussed in next section.

6.1.4 Indication of a current-induced out-of-plane field

One way to further characterize the possible out-of-plane component B_{oop} of the current-induced field is to employ the *magnetic field rotation* mode of the magneto-transport measurements, see Sec. 4.2. In this mode it is possible to study the magnetization-angle dependence of the current-induced fields, because the orientation of the magnetization is controlled by an external saturating field. It is assumed that in a FM/HM bilayer with an in-plane magnetization easy axis a significant current-induced field in the out of plane direction is most probably of damping-like character and therefore dependent on the in-plane direction of the magnetization as $\vec{B}_{oop} \propto \hat{\sigma} \times \vec{m}$, where $\hat{\sigma} = \hat{j} \times \hat{z}$, see Sec. 2.5.2 and Ref. [96, 169]. The amplitude of \vec{B}_{oop} can be therefore written as $B_{oop} = B_{oop}^0 \cos(\varphi_M)$ where φ_M is the in-plane angle between the magnetization and the current direction. A strong enough B_{oop} can act against the in-plane anisotropy field and the applied B_{ex} and tilt the magnetization out of the film plane. The out-of-plane component of \vec{M} could induce AHE which gives an additional contribution to R_{xy} .

To a large extent the analysis presented in this section follows the reported characterization of current-induced fields in Ref. [96, 169]. Our results at $T < 50$ K indicate an additional contribution to R_{xy} , which amplitude scales with the applied current and depends on the orientation of the in-plane magnetization. The additional R_{xy} can be a consequence of a tilt of the magnetization due to an out-of-plane field of (2.6 ± 0.5) mT induced by currents $I > 20$ mA. Because of the assumptions included in the analysis of the PHE measurements and the mismatch between the experiment and simulation, the presence of the B_{oop} cannot be unambiguously confirmed. In the following, a detailed explanation of the analysis and its results will be given.

6.1. Asymmetry of the high-current PHE hysteresis loops

When the magnetization has an in-plane and an out-of-plane component the measured transversal resistance R_{xy} is a sum of the PHE resistance R_{PHE} and the AHE resistance R_{AHE} as

$$R_{xy} = R_{PHE} + R_{AHE}. \quad (6.1)$$

In the presence of an external magnetic field \vec{B}_{ex} and the current-induced fields \vec{B}_{\perp} and \vec{B}_{oop} the magnetization will be affected by the effective magnetic field \vec{B}_{eff}

$$\vec{B}_{eff} = \vec{B}_{ex} + \vec{B}_{\perp} + \vec{B}_{oop}. \quad (6.2)$$

If a constant \vec{B}_{ex} is applied parallel to the film plane at an angle φ_B to the current direction, the in-plane components of \vec{B}_{eff} will be $B_{eff}^x = B_{eff} \cos(\varphi_M) = B_{ex} \cos(\varphi_B)$ and $B_{eff}^y = B_{eff} \sin(\varphi_M) = B_{ex} \sin(\varphi_B) + B_{\perp}$, see the sketch in Fig. 6.7 c. Here it is assumed that the magnetization is aligned to the effective magnetic field and therefore $\varphi_{B_{eff}} = \varphi_M$. Combining the two in-plane components of \vec{B}_{eff} we can write [96]

$$\begin{aligned} \frac{\sin(\varphi_M)}{\cos(\varphi_M)} &= \frac{B_{ex} \sin(\varphi_B) + B_{\perp}}{B_{ex} \cos(\varphi_B)}, \\ \tan(\varphi_M) &= \frac{\sin(\varphi_B) + B_{\perp}/B_{ex}}{\cos(\varphi_B)}. \end{aligned} \quad (6.3)$$

The Eq. 6.3 shows that the in-plane orientation of the magnetization φ_M depends on the ratio between the B_{\perp} and B_{ex} . The current-induced B_{\perp} scales with the applied current density j , see Sec. 6.1.1. The current-induced modulation of φ_M will depend also on the sign of the applied current as $B_{\perp}(-j) = -B_{\perp}(j)$. Therefore,

$$\begin{aligned} \varphi_M(+j) &= \text{atan}\left(\frac{\sin(\varphi_B) + B_{\perp}/B_{ex}}{\cos(\varphi_B)}\right), \\ \varphi_M(-j) &= \text{atan}\left(\frac{\sin(\varphi_B) - B_{\perp}/B_{ex}}{\cos(\varphi_B)}\right). \end{aligned} \quad (6.4)$$

The difference in the AHE resistance measured with a positive $+j$ and a negative $-j$ current density can be written as [96]

$$\begin{aligned} R_{AHE,diff} &= R_{AHE}(+j) - R_{AHE}(-j) = \frac{dR_{AHE}}{dB_z} B_{oop}^0 (\cos\varphi_M(+j) + \cos\varphi_M(-j)) \\ &\approx 2 \frac{dR_{AHE}}{dB_z} B_{oop}^0 \cos(\varphi_B) \end{aligned} \quad (6.5)$$

In Eq. 6.5 the approximation of small B_{\perp}/B_{ex} ratio was used and the $\frac{dR_{AHE}}{dB_z}$ is the slope of the AHE curve measured with an B_z applied perpendicular to the film plane [96].

Similarly, the difference in the PHE contribution for a positive and a negative applied

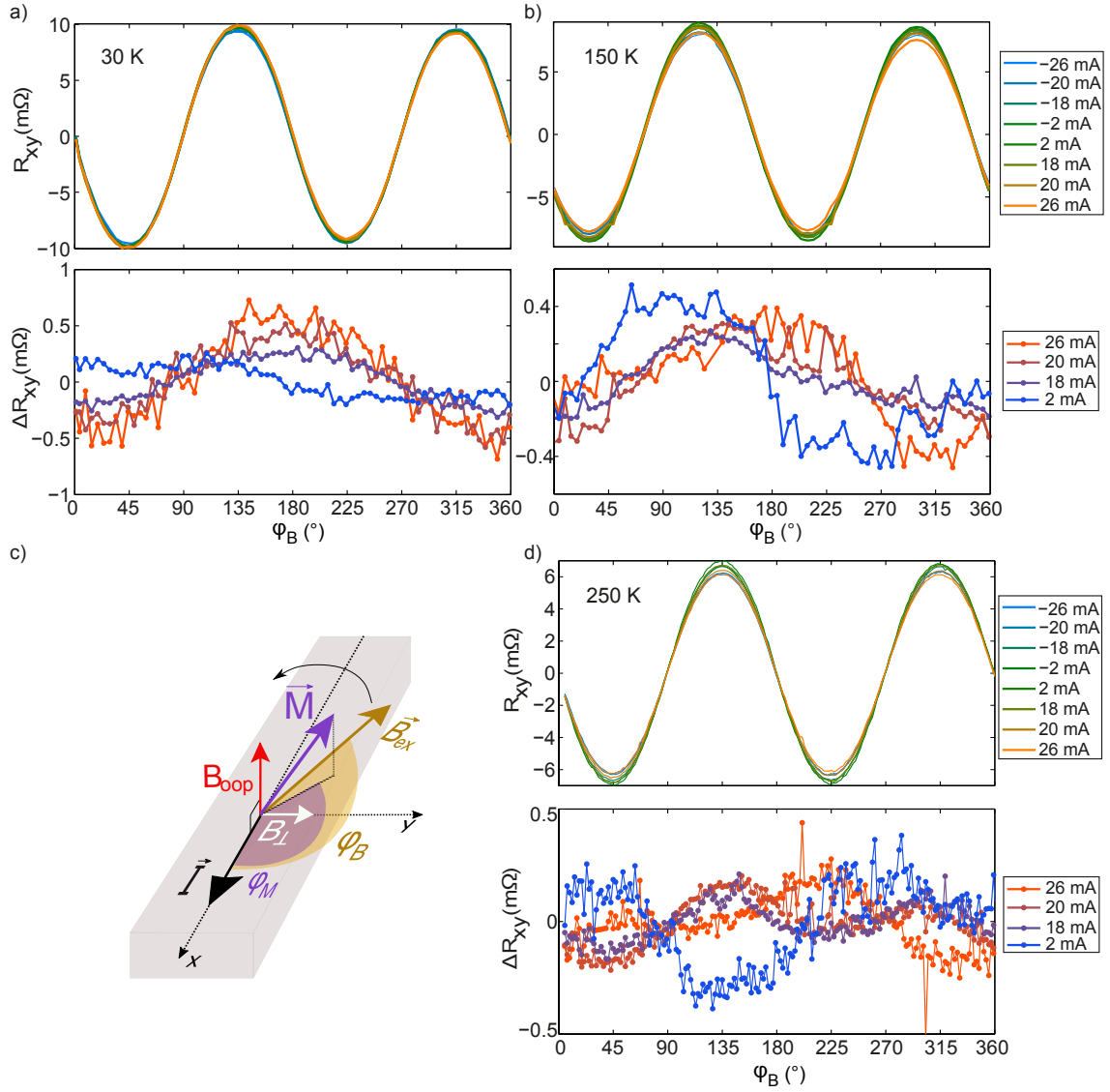


Figure 6.7: The planar Hall resistance R_{xy} measured at a) 30 K, b) 150 K and d) 250 K in dependence on the angle of the external in-plane magnetic field $B_{ex}=400$ mT. The angular dependence of R_{xy} was measured with current parallel (\vec{I} , green to orange colors) and antiparallel ($-\vec{I}$, blue colors) to $Fe[1\bar{1}0]$ direction, as sketched in c). The difference in R_{xy} with positive and negative current is plotted for the chosen probing current densities below the plot of R_{xy} for each corresponding temperature. The expected in-plane \vec{B}_{\perp} and out-of-plane \vec{B}_{oop} current-induced fields are sketched in c).

current density can be written as

$$R_{PHE,diff} = R_{PHE}(+j) - R_{PHE}(-j) \quad (6.6)$$

However, in the analysis described in Ref. [96, 169] the effects of any magnetic anisotropy present in the system are disregarded, because polycrystalline samples were used. The presence of cubic anisotropy fields modulates the angular dependence of the PHE resistance as was discussed in Sec. 5.3. The measured anisotropy fields were in the order of 10-40 mT and therefore much larger compared to the estimated $B_{\perp} < 1$ mT. Thus, $R_{PHE,diff}$ is expected to be small for $B_{ex} > 100$ mT.

Figure 6.7 shows the angular dependence of the transversal resistance using a varying probing current with positive $R_{xy}(+I)$ and negative polarity $R_{xy}(-I)$ (see color scale) measured at 30 K, 150 K and 250 K. For each of the probing current densities the difference $\Delta R_{xy} = R_{xy}(+I) - R_{xy}(-I)$ was calculated and is shown for each temperature below the corresponding PHE plot. Clearly, ΔR_{xy} has a strong current and temperature dependence. At 30 K we observe a $\cos(\varphi_B)$ -dependence of ΔR_{xy} , see Fig. 6.7 a. The amplitude of the cosine function proportionally increases with the probing current density. At higher temperatures ΔR_{xy} exhibits a more complex angular dependence. At 150 K (b) ΔR_{xy} develops a $\cos(\varphi_B)$ -like dependence when the probing current is increased, while for lower current densities a phase shift of the $\cos(\varphi_B)$ -dependence is observed. The shape of the angular dependence of ΔR_{xy} at 250 K remains complex and with a small amplitude for all probing current densities (d).

One of the reasons for the changing shape of the angular dependence of ΔR_{xy} with higher current densities at 150 K and 250 K may be the presence of more than one current-induced field components. In that case, the tilt of the magnetization would be determined by an effective field, i.e. a sum of the current-induced fields with different angular dependencies, which may additionally have different directions and scale differently with the applied current density. This would lead to a complex angular dependence of the total ΔR_{xy} . However, at 30 K we observe a cosine shape of the angular dependence of ΔR_{xy} for all applied current densities. Thus, at this temperature, we can apply Eq. 6.5 to fit the experimental ΔR_{xy} and estimate B_{oop}^0 .

The measurement of ΔR_{xy} at 30 K was fitted with the function $A_1 \cdot \cos(\varphi_B) + A_2$. The data with the best fitting functions are shown in Fig. 6.8 a for 26 mA, 20 mA, 14 mA and 8 mA probing current. The offset A_2 of the best fit cosine functions reached a maximum of $A_2^{max} \sim 0.03$ m Ω and is therefore contained in the error of the amplitude A_1 (error ~ 0.1 m Ω).

The amplitude of the current-induced out-of-plane field B_{oop}^0 was calculated from Eq. 6.5 as

$$B_{oop}^0 = \frac{A_1(I)}{2 \frac{dR_{AHE}}{dB_z}}. \quad (6.7)$$

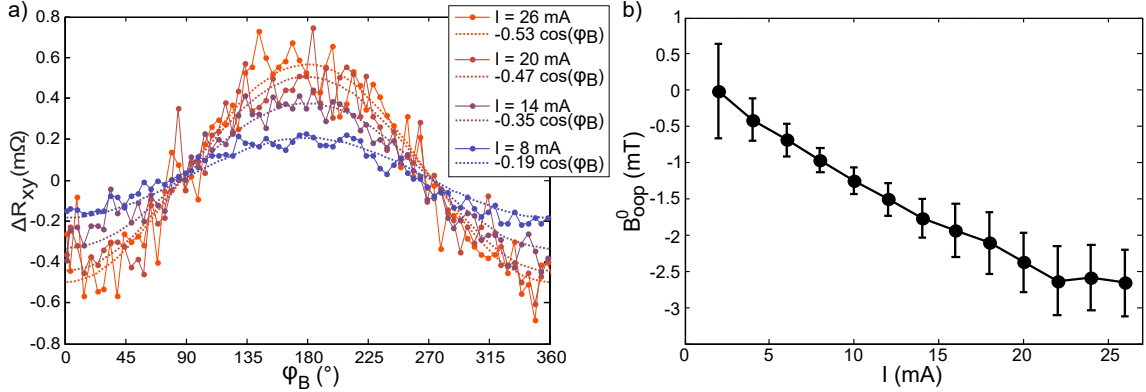


Figure 6.8: a) Angular dependence of the difference ΔR_{xy} between the planar Hall voltage R_{xy} measured with positive and R_{xy} measured with negative current for various probing current densities (dots) was fitted with a function $A_1 \cdot \cos(\varphi_B) + A_2$ (dotted line). External magnetic field of 400 mT was applied parallel to the film plane (see sketch in Fig. 6.6 c) b) The amplitude of the current-induced out-of-plane field B_{oop}^0 was obtained for each probing current from the amplitude of the cosine-function A_1 as $B_{oop}^0 = A_1 / (2 \cdot 0.1 \text{ mT/m}\Omega)$.

The slope $\frac{dR_{AHE}}{dB_z}$ was estimated from the room temperature measurement of the AHE on the Au/Fe(1.3 nm)/MgO Hall bar, for which the normalized curve is shown in Fig. 5.5. For CoFeB it was reported that the dR_{AHE}/dB_z at 10 K is for 15% larger than the room temperature value [169]. Therefore, we estimate that $dR_{AHE}/dB_z(30 \text{ K}) \sim 1.1 \cdot 0.1 \text{ m}\Omega/\text{mT}$. Using this value in Eq. 6.7 the obtained amplitude of the current-induced out-of-plane field reaches up to $(2.6 \pm 0.5) \text{ mT}$ for 26 mA probing current. The obtained B_{oop}^0 value may be an overestimation due to the small AHE slope, which was used in the calculation. However, when employing the same dR_{AHE}/dB_z value in the Stoner-Wohlfarth simulation of the PHE hysteresis loops acquired at 30 K (Fig. 6.6) we obtain a similar estimation of the B_{oop}^0 , see Appendix C.2.

The good agreement in the B_{oop}^0 estimation of the two analysis methods is a good indication of the presence of an out-of-plane component of the current-induced field. This component, however, is observed when the temperature is reduced below 50 K. The reason for this may be two-fold. Firstly, at reduced temperature the in-plane anisotropy field in the system reduces (in some cases it even rotates perpendicular to the plane [120]). This leads to a decrease of the critical magnetic field required to tilt the magnetization out of the film plane. Therefore, the effect of the current-induced B_{oop} increases at lower temperatures. Secondly, the current-induced spin-orbit torques (SOT) were observed to have a temperature dependence, which differs for different physical origins of the torques and for the different terms of the torques (damping-like (DL) or field-like (FL), for example). In Ta-based heterostructures it has been observed that the FL term strongly decreases with reduced temperature, while the DL term remains mostly unaffected [170, 171]. This

6.2. Characterization of the current-induced field in Kerr microscopy

was explained based on the origin of the torques from the SHE in Ta [26]. In contrast, for structures containing a layer of Pt, both terms either remained almost constant with temperature in as-grown sample or increased with temperature in annealed sample [27]. The possible increase of a DL-term, which is observed in this work at 30 K agrees also with the temperature-dependent SHE observed in Au [172]. Compared to approximately constant spin Hall angle (SHA) observed in Pt, the authors of Ref. [172] reported on an increasing SHA in Au at reduced temperature. In the SHE-picture, the DL-term is directly related to the SHE in the NM layer. Therefore, an increased SHA could induce a larger DL-torque.

To sum up, the PHE-based magneto-transport measurements have demonstrated that at room temperature a high current density applied to Au/Fe/MgO(001) Hall bars changes the hard axis magnetization reversal. The observed changes in PHE loops can be explained by a current-induced field B_{\perp} of up to 0.5 mT in the direction perpendicular to the current, which was confirmed by simulations based on the Stoner-Wohlfarth model and the observed dependence of PHE loops on the B_{ex} direction. The dominant contribution to the current-induced B_{\perp} arises from the Oersted field generated by a current in the Au layer. The influence of the Oersted field on the magnetization reversal is reduced at low temperatures due to higher anisotropy fields. At $T < 50$ K the PHE measurements acquired with high current densities show indications of an additional current-induced field in the out-of-plane direction.

6.2 Characterization of the current-induced field in Kerr microscopy

The Kerr microscopy of Au/Fe/MgO Hall bars in Sec. 5.4 revealed that the field-induced magnetization reversal along the hard axis proceeds via magnetization rotation towards the closest easy axis followed by formation and growth of domains. On the other hand, the current-induced fields (B_{\perp} and B_{oop}) were shown to have a considerable influence on the field-induced magnetization reversal process observed via the PHE measurements. Therefore, a combined microscopic and magneto-transport study is required to investigate the current-induced effects on the magnetization reversal process and the domain structure. In fact, the Kerr microscopy setup at IFW Dresden offers the possibility to simultaneously perform transport measurements, as shown in Sec. 4.3. In this section, the results of the Kerr-microscopy study of a Hall bar with 1.5 nm Fe layer thickness will be presented. The Hall bar structure was electrically contacted as shown in Fig. 4.7. The setup currently operates only at room temperature, therefore temperature-dependent studies were not possible.

The current-induced field \vec{B}_{\perp} was observed in the direction perpendicular to the lon-

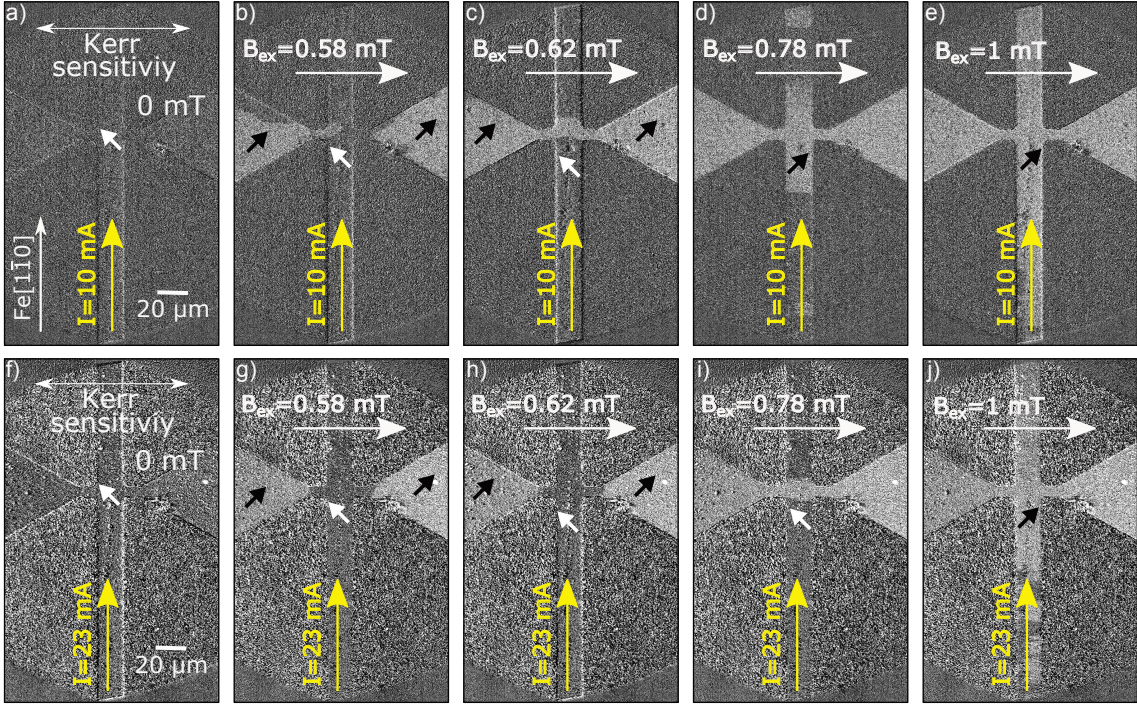


Figure 6.9: The magnetization reversal along Fe[110] hard axis of the Au/Fe(1.5 nm)/MgO(001) Hall bar observed in the Kerr microscope when a current $I=10$ mA (a-e) and $I=23$ mA (f-j) was applied as marked with the yellow arrows. The magnetic field B_{ex} was scanned from -20 mT to +20 mT. The presented images were acquired after crossing zero field (a and f), at 0.58 mT (b and g), 0.62 mT (c and h), 0.78 mT (d and i) and at 1 mT (e and j), marked with the white arrow. The Kerr sensitivity was set along B_{ex} direction, therefore we can identify the brighter and darker domains as marked with the small white and black arrows.

gitudinal current (see Sec. 6.1). Therefore, when a magnetic field B_{ex} is applied perpendicular to the Hall bar it is aligned either parallel or antiparallel to \vec{B}_{\perp} , see sketch in Fig. 6.10. In this geometry, the changes to the magnetization reversal induced by \vec{B}_{\perp} were investigated under the Kerr microscope. The Kerr sensitivity was set to give the highest magnetic contrast between the magnetization oriented parallel and antiparallel to B_{ex} and the electric current was applied along the Hall bar in the direction parallel to Fe[1 $\bar{1}$ 0] (yellow arrows in Fig. 6.9).

The Kerr images shown in Fig. 6.9 can be directly compared to the ones in Fig. 5.12, because they were acquired from the same Hall bar and the direction of the external magnetic field as well as the Kerr sensitivity was set in the same way. While during the acquisition of the Kerr images shown in Fig. 5.12 no current was applied along the Hall bar, the images in Fig. 6.9 were obtained while a constant DC of $I=10$ mA (a-e) and $I=23$ mA (f-j) was applied continuously throughout the measurement. Independent of the applied current density the magnetization reversal proceeds via formation of domains with domain walls preferentially parallel to B_{ex} direction, as discussed already in Sec. 5.4. Note, that the dark and bright domains in Fig. 6.9 correspond to the magnetization along

6.2. Characterization of the current-induced field in Kerr microscopy

the easy directions Fe[0 $\bar{1}$ 0] and Fe[100] diagonal to the Hall bar. Further confirmation, that the magnetization is oriented along the easy axis within the domains, is the gradual change of the Kerr signal at higher B_{ex} indicating a coherent rotation of the magnetization from one of the easy axes towards the hard axis parallel to B_{ex} , see Fig. 6.10 b.

Under the applied current density the first switched domains appear at the areas of the contact pads at $B_{ex} \sim 0.5$ mT after crossing zero field (black arrows in Fig. 6.9 b and g). For $I=10$ mA (current density $j=1.5 \cdot 10^7$ A/cm²), the first switched domains along the Hall bar appear at the Hall cross center almost simultaneously with the switching of the contact pads. As discussed earlier, the stray field of the large contact pads and the edges at the Hall cross center create nucleation points for switched domains. At $B_{ex}=0.6$ mT (Fig. 6.9 c) the Hall cross center is almost completely switched and a single bright domain is observed in this region. Further increase of B_{ex} leads to expansion of the bright domain and nucleation of additional switched domains along the Hall bar until at $B_{ex} \sim 1$ mT the magnetization in the entire visible area of the Hall bar is reoriented as shown by the black arrow in Fig. 6.9 e.

The increased current density ($j=3.5 \cdot 10^7$ A/cm² in Fig. 6.9 f-j) leads to a slightly delayed reversal of the magnetization along the Hall bar, compared to the magnetization in the areas of the contact pads. The switched bright domains appear at the Hall cross center at $B_{ex} \sim 0.8$ mT in Fig. 6.9 i. At $B_{ex}=1$ mT some dark, not yet switched domains remain present along the Hall bar, see Fig. 6.9 j. The difference in the reversal process between the contact pads and the Hall bar is brought about by the applied current density. Because the Hall bar area switches at higher B_{ex} compared to the contact pads, the current-induced field \vec{B}_\perp seems to point in the opposite direction than B_{ex} . In this way it hinders the reversal of the magnetization along the Hall bar until B_{ex} is strong enough to cancel \vec{B}_\perp , i.e. when $B_{ex} \sim 0.8$ mT.

For a more quantitative analysis of the magnetization reversal in Kerr microscopy with applied current density, the hysteresis loops were extracted from the acquired Kerr images. For this, the area along the Hall bar was chosen (orange boarder in Fig. 6.10 a). Hysteresis loops from Kerr image stacks collected using a varying applied current density during the magnetic field scan were extracted from the same area of the Hall bar. The Kerr signal versus B_{ex} is plotted in Fig. 6.10 b, the inset shows the enlarged zero field region of the hysteresis loops.

Firstly, the Kerr signal in the hysteresis loops in Fig. 6.10 b does not remain constant after the magnetization switch at ~ 0.6 mT, but gradually increases until approximately 10 mT, which is a characteristic shape of a hard axis hysteresis loop. Therefore, in the Kerr images in Fig. 6.9 acquired at $B_{ex} < 1$ mT, the magnetization cannot be considered as aligned to the B_{ex} direction, but rather to the easy magnetization axes.

Moreover, the enlarged region of the hysteresis loops around $B_{ex}=0$ mT shows a shift of the loops proportional to the increasing applied current, see inset of Fig. 6.10 b. The shift in B_{ex} of the loops appears to be asymmetric in respect to zero field, i.e. for positive B_{ex}

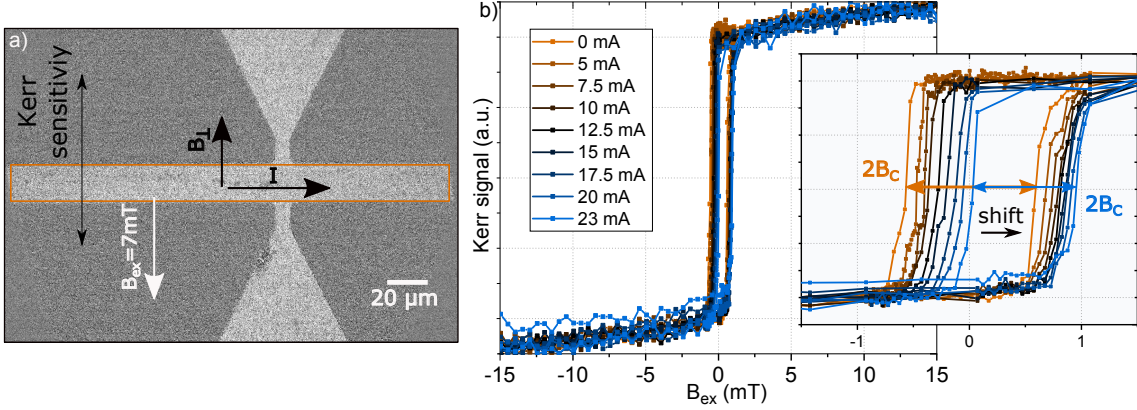


Figure 6.10: **a)** Kerr microscopy image acquired using a magnetic field of $B_{ex}=7$ mT close to saturation along the Fe[110] hard axis (white arrow) and a current density applied in the direction of Fe[$\bar{1}\bar{1}0$] longitudinal to the Hall bar. The Kerr sensitivity was set along the axis of the external magnetic field and the Kerr signal for the hysteresis loops in **b)** was extracted from the area marked in orange. **b)** The hard axis hysteresis loops were acquired using a varying current density applied to the Hall bar. The inset shows the enlarged region around $B_{ex}=0$ mT, where the shift (black arrow) and a decrease of the coercive field ($I=0$ mA in orange and $I=23$ mA in light blue) are visible.

the shift seems smaller compared to the negative B_{ex} . This can be seen when comparing the hysteresis loops for $I=0$ (orange) and for $I=23$ mA (light blue) in the inset of Fig. 6.10 b. This is due to an additional decrease of the width of the hysteresis loops with higher applied current densities. We extracted the coercive field B_c as the half of the width of the loops as shown in the inset. By this definition, the field B_c does not relate to the applied B_{ex} at which the magnetization switches for 90° , but is a measure of the width of the hysteresis loop. Because both, a shift in B_{ex} and a change of B_c are induced by a higher current density applied to the Hall bar, the change of the hysteresis loops appears asymmetric with respect to zero field, see schematics in Fig. 6.12 d.

The shift of the center of the hysteresis loops has a linear dependence on the applied current as shown in Fig. 6.11 a. The slope of the best fit linear function was (0.043 ± 0.006) mT/mA, i.e. (0.030 ± 0.006) mT/ $(10^6$ A/cm $^2)$. The error was determined from the error of the read-out of the shift. The linear increase of the shift with the applied current density and the direction of the shift towards higher magnetic fields strongly indicate that it is caused by an additional current-induced magnetic field B_\perp along Fe[$\bar{1}\bar{1}0$] direction, i.e. opposite to the external magnetic field as sketched in Fig. 6.10 a. The magnetization in the Hall bar is modulated by the total magnetic field $\vec{B}_{tot} = \vec{B}_{ex} + \vec{B}_\perp$. For positive B_{ex} the total magnetic field is $B_{tot} = B_{ex} - B_\perp$. The magnetization switch is then observed at $B_{ex} = B_{switch} + B_\perp$, which is for B_\perp higher as without the applied current, where it is observed at B_{switch} . For $B_{ex} < 0$, the total field is $B_{tot} = B_{ex} + B_\perp$ and the magnetization switches at $B_{ex} = -B_{switch} + B_\perp$. Therefore, the observed shift of the hysteresis loops is a direct measure of the current-induced B_\perp . The obtained values are

6.2. Characterization of the current-induced field in Kerr microscopy

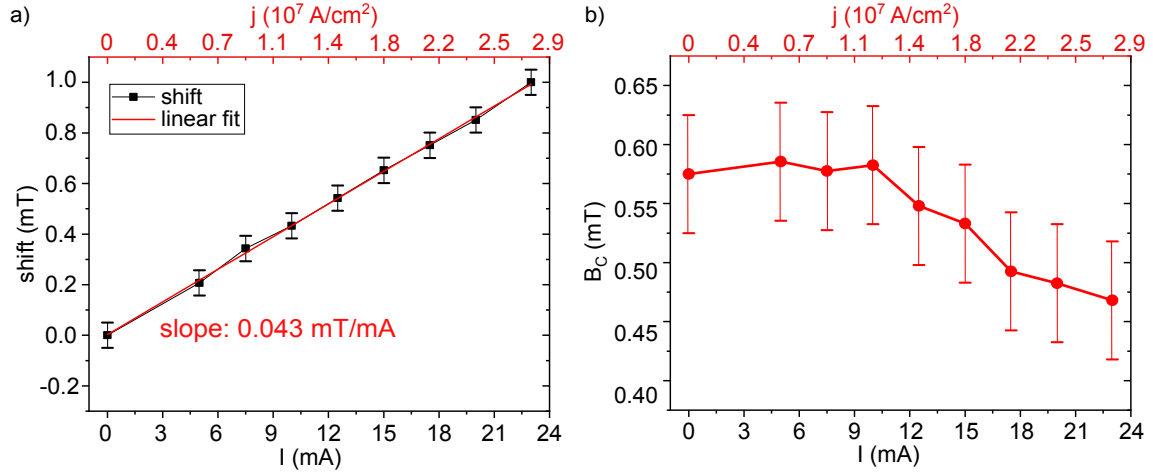


Figure 6.11: a) The hysteresis loops extracted from the Hall bar region in the stacks of Kerr images acquired at room temperature from Au/Fe(1.5 nm)/MgO(001) were observed to shift to higher magnetic field proportionally to the applied current. The observed shift shows a linear dependence on the current. The current density was determined for a Hall bar width of 12 μm and total thickness of 5.5 nm. b) The width of the hysteresis loops was observed to change when a higher current density is applied longitudinal to the Hall bar. The width of the loop equals $2 \cdot B_c$. The coercive field B_c stays constant for currents up to 10 mA and for higher currents begins to gradually decrease, which indicates the onset of increased sample heating.

larger approximately by a factor of 2 compared to B_{\perp} obtained from the simulated PHE hysteresis loops of the Au/Fe(1.3 nm)/MgO at 250 K, see Fig. 6.2 and 6.3. This difference may be related to the different thickness ratio between the two samples (one with 1.3 nm and other with 1.5 nm Fe layer) or, more probably, to the temperature difference between the two experiments.

The coercive field B_c , which was extracted from the measured hysteresis loops, keeps an approximately constant value of ~ 0.57 mT for currents up to $I=10$ mA. For higher currents B_c starts to decrease and drops to ~ 0.47 mT at $I=23$ mA. The decrease of coercivity is an indication of a change in temperature of the sample. When the temperature of the system increases, its thermal energy increases proportionally. The thermal energy gives the magnetic moments in the system more freedom to overcome the magnetic potential energy barrier and move from a magnetic state with a local energy minimum to a state with different orientation of the magnetization. This results in a decreased coercive field B_c . A high current density leads to resistive- or Joule heating, which is proportional to the applied current and the resistance of the material. However, Joule heating seems to have no significant effect on the system when the applied current is below 10 mA (i.e. below $1.5 \cdot 10^7$ A/cm²). For these currents the heating power provided by the applied electric current seems to be compensated by heat dissipation through the contact pads and the bonding wires.

The combined Kerr microscopy and magneto-transport analysis of the PHE in the Au/Fe(001) Hall bars has shown that the Hall cross center most significantly influences the measured PHE voltage, see Sec. 5.4.3. For the same region of the Hall bar, simulations of the electric current flow have been reported, which show spreading of the current into the transversal contacts and a reduced current density in the center of the Hall cross [165–167]. A decrease of the current density would lead to a reduced B_{\perp} . The hysteresis loops acquired using a Kerr microscope can be extracted by choosing a different ROI of the Hall bar. In this way, the hysteresis loops from the regions with no current (i.e. contact pads) and with applied current (i.e. Hall bar) can be compared. Moreover, different areas along the Hall bar can be selected to compare the current-induced B_{\perp} . The hysteresis loops extracted from the area of a contact pad¹ (black), the full Hall bar (orange for $I=5$ mA, dark blue for $I=15$ mA and light blue for $I=23$ mA) and the area of the Hall cross center (brown) are shown in Fig. 6.12.

The hysteresis loops from the contact pad region (solid black line) do not shift to higher B_{ex} when the applied current density is increased, see Fig. 6.12 a-c. They show a sharper transition of the magnetization during the switch, which means that the nucleated, switched domains are on average larger, which makes the switch of the magnetization in the contact pads more abrupt. The coercive field B_c slightly decreases with higher current density, which indicates that Joule heating affects the contact pads as well. This agrees with the observation, that heat dissipation via contact pads and bonding wires compensates the Joule heating for currents up to 10 mA. The extracted B_c versus the applied currents is plotted in Fig. 6.13 b for the hysteresis loops from different regions of the Hall bar. At the contact pad region (black dots), B_c starts to decrease for currents beyond ~ 12 mA and it decreases less as compared to B_c from the full wire (orange dots), for example.

Interestingly, the hysteresis loops acquired from the Hall cross center (brown dots) show a slightly smaller shift to higher B_{ex} compared to the loops from the full wire (orange dots) in Fig. 6.13 a) for all applied currents. Moreover, the hysteresis loops extracted from the Hall cross center and full wire exhibit a different change in the coercive field B_c (Fig. 6.13 b). The difference in B_c explains the asymmetry of the B_{ex} -shift between the left ($B_{ex}<0$) and the right side ($B_{ex}>0$) of the hysteresis loops indicated with brown arrows in Fig. 6.12. The effect of both, a magnetic field shift and a change in the coercivity, is for different scenarios sketched in Fig. 6.12 d.

The difference in the B_{ex} -shift and in the variation of B_c with current between the Hall cross center and the Hall bar indicates that in these two regions a different effective field and a different effective Joule heating have an influence on the magnetization reversal. Firstly, the Hall cross center is located closer to the contact pads and has a direct connection to them via the transversal contacts (gray area between the pad and cross region in the inset

¹Contact pad areas consist of the same Au/Fe bilayer as the Hall bar and are covered with a Cr adhesion layer (1 nm) and a Au contact layer (50 nm).

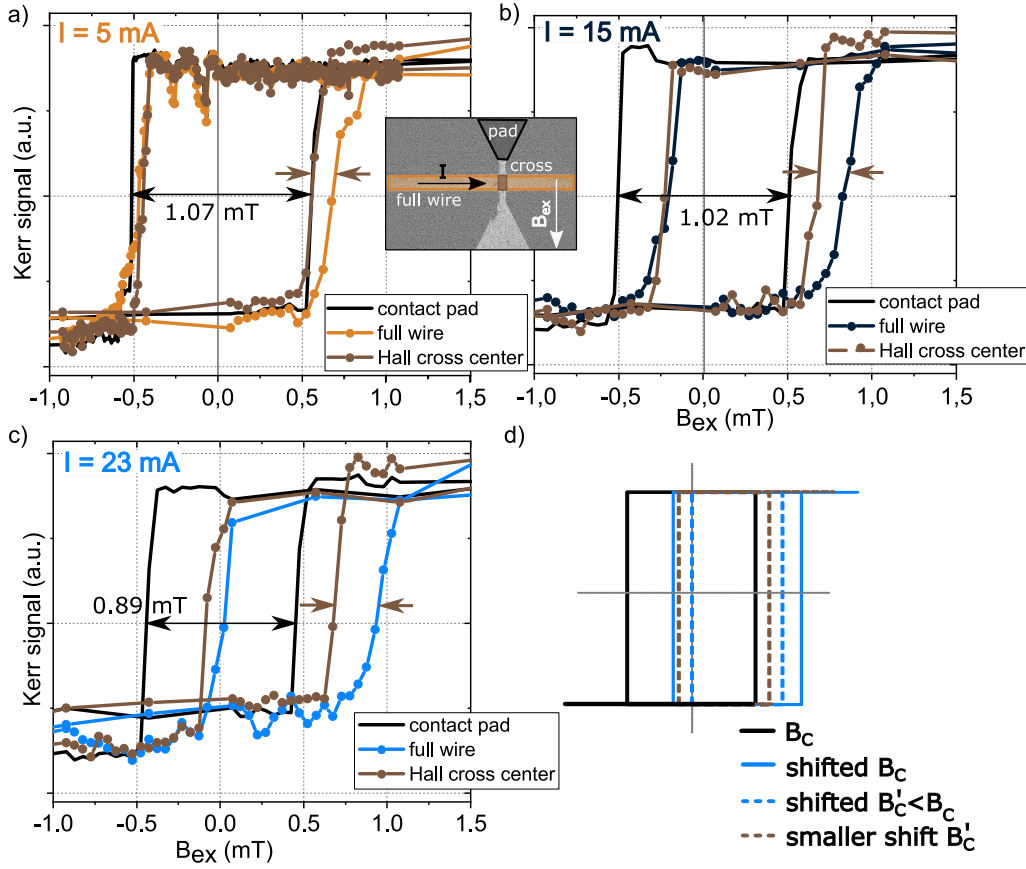


Figure 6.12: Hysteresis loops extracted from the stacks of Kerr images acquired from a Au/Fe(1.5 nm)/MgO(001) Hall bar at room temperature. During the acquisition of the images a current of a) 5 mA, b) 15 mA and c) 23 mA was applied longitudinally to the Hall bar. The hysteresis loops were extracted from different regions of the Hall bar marked in the inset of a). The color scheme for the hysteresis loops from the full wire is taken from Fig. 6.10. d) An illustration of the change of the hysteresis loop when a magnetic field shift (blue line) and a reduced coercive field (blue dotted line) are observed simultaneously.

of Fig. 6.13). The magnetization reversal in the contact pad region is not affected by the current-induced Oersted field. Therefore, during the B_{ex} scan with $\vec{B}_{ex} \parallel -\vec{B}_{Oe}$ the magnetization in the contact pads reverses at smaller B_{ex} compared to the Hall bar regions (see Fig. 6.9). The stray field due to the magnetization in the contact pad influences the magnetization reversal in the areas in its proximity. In this way, the magnetization in the contact pads may reduce the B_C for the magnetization switch in the Hall cross center during the positive B_{ex} scan. However, the Hall cross center is also in direct contact with the remaining area of the Hall bar. Reorientation of magnetization in the Hall bar regions close to the cross center may as well influence its magnetization. Therefore, the shape of the hysteresis loop extracted from the Hall cross center depends on the magnetization reversal in the areas in its close proximity, i.e. contact pads and neighboring Hall bar regions.

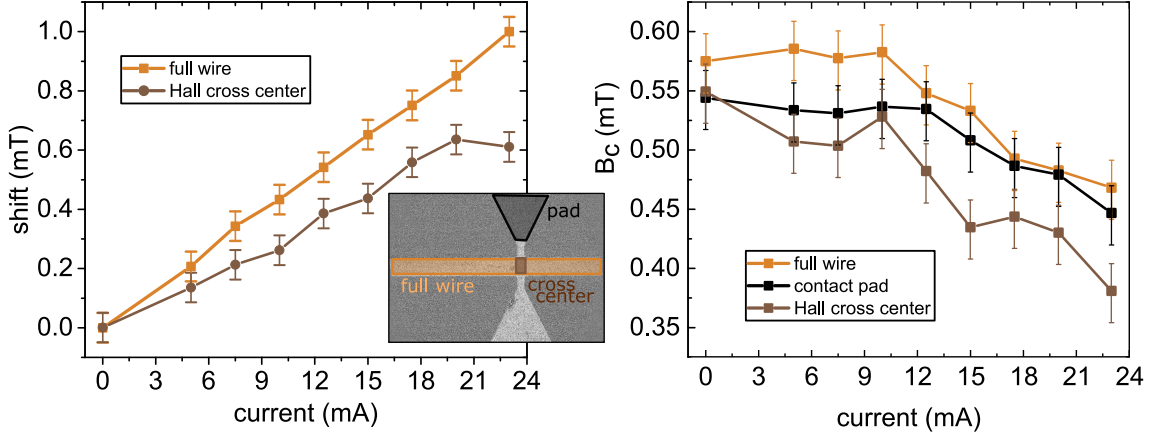


Figure 6.13: a) The shift of the hysteresis loops acquired while applying a current longitudinal to the Hall bar for the full wire region (orange) and the Hall cross center (brown), see inset. The hysteresis loops from the contact pad are not shifted. The error was determined from the read-out error. b) The coercive field B_c extracted from the hysteresis loops from different regions on the Hall bar.

Additionally, the magnetization reversal in the Hall cross center depends also on the current density. Simulations in Ref. [165–167] show current shunting in the Hall cross center, i.e. spreading of the current to the transversal contacts, which could lead to a decrease of the current density at the Hall cross center generating a smaller Oersted field as compared to the remaining Hall bar and leading to a reduced Joule heating. Because of the influence of the neighboring magnetic regions and the current shunting, the magnetization reversal in the Hall cross center exhibits a more complex dependence on the current-induced field and thermal effects. Therefore, the B_{ex} -shift of the hysteresis loops from the Hall cross center cannot be interpreted as a direct measure of the current-induced Oersted field.

In contrast, the hysteresis loop from the full Hall bar is less affected by the magnetization in the contact pads. The B_{ex} -shift extracted from the full wire hysteresis loops (orange dots in Fig. 6.13 a) is a good measure of the current-induced B_{Oe} , while the decrease in B_c indicates the onset of effective Joule heating of the Hall bar for $I > 10$ mA. A decrease of B_c with higher I was observed for hysteresis loops from all regions of the device (see Fig. 6.13 b), which is a consequence of increased thermal effects at higher I , present even in the contact pad region. A decrease of the B_{ex} -shift for the Hall cross center at $I = 23$ mA (see Fig. 6.13 a) may be related to the increased effective Joule heating of the contact pads.

The influence of the magnetization in the areas in proximity of the Hall cross center to its magnetization reversal process may have important consequences also when the magnetization reorientation is induced by the applied current in the absence of an external magnetic field. For example, it can be anticipated that the magnetization in the contact pads, which does not reorient under an applied current along the Hall bar, can hinder the

reorientation of the magnetization in the Hall cross center. A current-induced field may therefore lead to reorientation of the magnetization in the Hall bar, while the magnetization in the Hall cross center would remain oriented parallel to the magnetization in the contact pad area. Such response of the Hall bar to the applied I was indeed observed in Kerr microscopy, see Figs. 5.15 and 6.17.

In brief, the analysis of the magnetic hysteresis loops presented in this section contributes an important aspect to the general picture of the current- and field-induced magnetization reversal in Au/Fe/MgO(001) Hall bars. The B_{ex} -shift of the hysteresis loops, which is proportional to the applied current, provides further evidence of a current-induced magnetic field B_{\perp} perpendicular to the Hall bar. The field B_{\perp} corresponds to an Oersted field generated by the applied current and reaches up to 1 mT at room temperature. The current-induced field is therefore comparable to the coercive field $B_c \sim 0.6$ mT for the 90° switch of the magnetization in the Au/Fe/MgO(001) Hall bars from one easy direction to another (see Sec. 6.2). Joule heating of the Hall bar was observed to increase for $I > 10$ mA and to lead to a reduced effective B_c . In the Hall cross center, the effective B_c and the shift of the hysteresis loop are influenced by the magnetization orientation in the adjacent contact pads. In absence of an external field, nucleation of switched domains along the Hall bar could be induced by an in-plane current because of the comparable magnitudes of the current-induced B_{\perp} and the B_c , which is reduced due to Joule heating. This heat-assisted nucleation of switched domains induced by a current density $j > 1.5 \cdot 10^7$ A/cm² followed by growth of the domains induced by an increasing current can be employed to achieve purely-electrical switching of the magnetization. As will be shown in the following, the magnetization in Au/Fe/MgO(001) can indeed be switched by application of a current density to the Hall bar.

6.3 Current-driven magnetization reorientation

The MBE grown Fe(001) thin films with two approximately identical easy magnetization axes along the principal in-plane crystallographic directions (the Fe[100] and Fe[010]) are well suited to test the current-induced magnetization reorientation. Firstly, the initial state of the system can be set by applying a saturating B_{ex} along one of the easy directions, which remains stable also in zero field. Secondly, an applied current density in the absence of B_{ex} induces a magnetic field perpendicular to the Hall bar, which can switch the magnetization for 90° from the initial easy direction to a different one, which is as well stable in zero field.

For the measurements demonstrated in Fig. 6.14, the initial state of the magnetization was set along the Fe[100] direction (\vec{M}_1) using a field of 500 mT. In order to conduct a controllable and reproducible switching experiment we applied a small constant magnetic

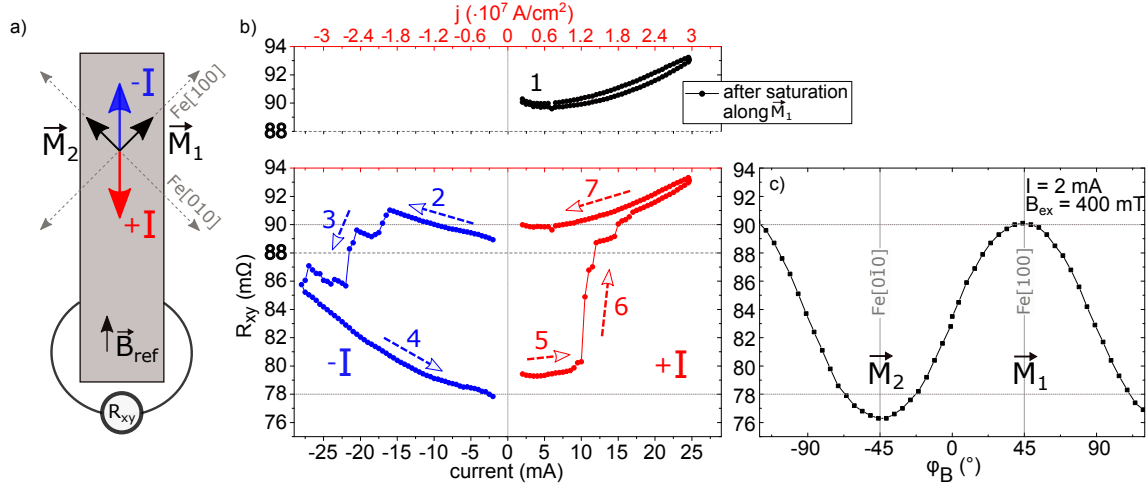


Figure 6.14: a) Sketch of the experiment. A constant reference magnetic field $B_{ref}=0.8$ mT was applied in the $Fe[1\bar{1}0]$ direction throughout the experiment. b) Measurement of the PHE resistance R_{xy} in Au/Fe(1.5 nm)/MgO(001) at 280 K after saturation of the magnetization along the $Fe[100]$ direction (\vec{M}_1) for increasing probing current. The numbers 1-7 mark the sequence of the measurements. First, a positive probing current $+I$ (i.e. antiparallel to B_{ref}) was scanned (1, black dots). Afterwards, a negative current $-I$ was scanned (2-4, blue dots) and a gradual reorientation of the magnetization along $Fe[0\bar{1}0]$ (\vec{M}_2) was observed. The positive current scan was repeated (5-7, red dots) immediately after the negative current scan. c) The angular dependence of the PHE resistance R_{xy} measured with a probing current $I=2$ mA and a saturating external magnetic field ($B_{ex}=400$ mT).

field $B_{ref}=0.8$ mT along the $Fe[1\bar{1}0]$ direction. This external magnetic field acts as a reference for the switching direction, because it limits the possible final orientations of the magnetization after an applied current density from four directions down to two. In other words, the small B_{ref} modifies the potential energy landscape by lowering the energy minima for the two closest easy magnetization directions. For B_{ref} along $Fe[1\bar{1}0]$ the energy of the system is lowest when the magnetization points along $Fe[0\bar{1}0]$ or along $Fe[100]$ easy direction. Note, that a magnetic field $B_{ref}<5$ mT along the $Fe[1\bar{1}0]$ is not sufficient to induce a 90° switch of the magnetization from $\vec{M}_1 \rightarrow \vec{M}_2$ marked in Fig. 6.14 a. This switch would correspond to the second jump of the double-jump magnetization reversal, which was observed at fields $B_{ex}>6$ mT along the hard magnetization axis in Sec. 5 for 1.5 nm Fe layer thickness. Moreover, the additional reference magnetic field is required in order to hinder the reorientation of the magnetization for 180° . A 180° rotation of the magnetization leads to the same PHE resistance R_{xy} and is therefore not distinguishable in the magneto-transport measurements.

While the constant B_{ref} was applied parallel to the Hall bar with magnetization along \vec{M}_1 , a positive DC current $+I$ (red arrow in Fig. 6.14 a) was gradually increased up to 24 mA (1). At each applied positive current the transversal PHE resistance R_{xy} was read-out (black dots in Fig. 6.14 b). R_{xy} increased with a quadratic current dependence and returned to the starting value once the current was decreased back to 0. However, when

the current direction was reversed to point parallel to \vec{B}_{ref} (negative current $-I$, blue arrow in Fig. 6.14 a), R_{xy} first slightly increased with increasing current (2) and for $-I < -15$ mA the value of R_{xy} started to drop (3). Two plateaus can be seen with a slight quadratic increase of R_{xy} with the applied negative current. When the probing current was reduced back to zero (4), R_{xy} continued to drop, now with a quadratic current dependence and reached $R_{xy} = 78$ m Ω , a value ~ 12 m Ω lower compared to the R_{xy} at the beginning of the negative current scan.

The quadratic increase of the R_{xy} with increasing current density is related to the resistive (or Joule) heating of the system by the applied current (as observed in Sec. 6.2) and it is independent of the direction of the current. The *quadratic background* in the R_{xy} measurements was observed for increasing positive current ($+I$) right after the saturation along \vec{M}_1 (black dots). Nonetheless, R_{xy} remains close to 90 m Ω throughout the current scan, which is the value of PHE resistance measured at saturation of the magnetization along Fe[100] easy axis (peak in PHE measurement in Fig. 6.14 c). However, the drop of R_{xy} at high negative currents (blue dots) cannot be explained by a heating effect. The transversal resistance R_{xy} drops down to 78 m Ω , which is a value measured when the magnetization is saturated close to the Fe[0 $\bar{1}$ 0] easy axis (dip in PHE measurement in Fig. 6.14 c). Therefore, the increased negative current induced a reorientation of the magnetization from \vec{M}_1 to \vec{M}_2 .

The current-induced reorientation of the magnetization was confirmed by repeating the positive current scan (red dots in Fig. 6.14 b) immediately after the negative current scan was completed, which has switched the majority of domains to \vec{M}_2 . Following the red empty arrow at the beginning of the positive current scan (5), the measured $R_{xy} \sim 79$ m Ω stays approximately constant. When $+I$ was increased beyond 10 mA (6) the PHE resistance abruptly jumped to higher values until it reached $R_{xy}(\vec{M}_1) = 90$ m Ω at ~ 15 mA. For higher $+I$ the small increase of PHE resistance is dominated by the quadratic background, which is observed also when the $+I$ current is reduced down to zero (7), where R_{xy} finally stabilizes at $R_{xy}(\vec{M}_1) = 90$ m Ω . Therefore, the $+I$ scan has induced the reorientation of the magnetization from \vec{M}_2 to \vec{M}_1 .

Effect of the reference field B_{ref}

The effect of the constant B_{ref} applied along the Fe[1 $\bar{1}$ 0] direction can be seen in Fig. 6.15 a. Increasing the field up to 3 mT (gray dots) does not significantly change the current-induced hysteresis loop. Higher B_{ref} reduces the critical current density at which the switched domains at the Hall cross center start to nucleate. For $B_{ref} = 5.75$ mT (dark red dots), the current-induced reorientation of the magnetization appears unstable when the current is reduced back to zero. Due to the high B_{ref} , the effective field acting on the domains is strong enough to induce nucleation of switched domains also for a low current density. The asymmetry in the PHE response between the positive current ($+I$) and negative current ($-I$) scans is a consequence of a misalignment, which has a more

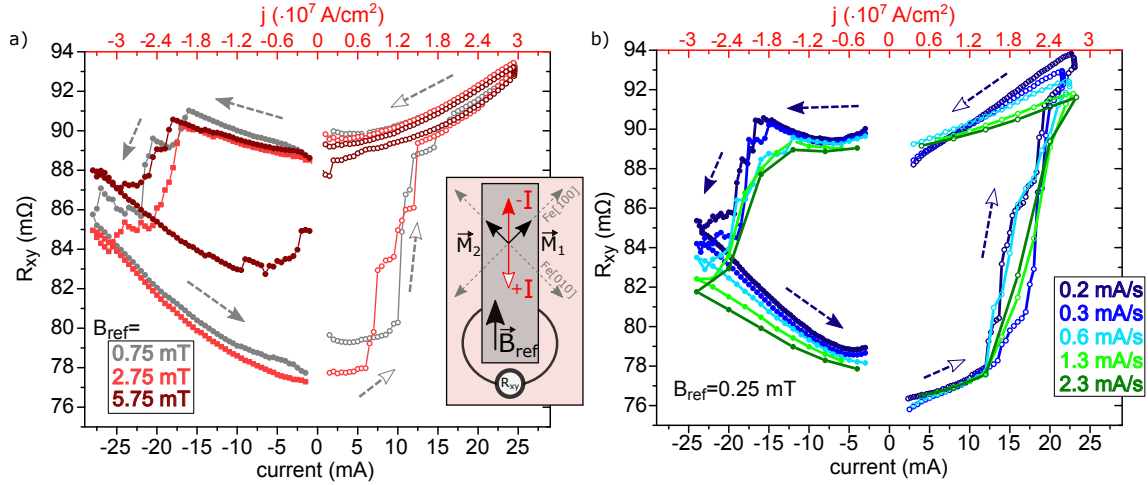


Figure 6.15: Current-induced hysteresis loops were measured at 280 K on Au/Fe(1.5 nm)/MgO(001) Hall bars. The current was swept from 1 mA up to 24 mA and reduced back to 1 mA in the direction Fe[$\bar{1}10$] (+ I , empty circles) or in the opposite direction ($-I$, full circles), see sketch of the experiment in **a**). In **a**) the strength of the reference magnetic field B_{ref} applied along the Hall bar in Fe[$\bar{1}10$] direction was varied. In **b**) the current sweep rate was increased from 0.2 mA/s to 2.3 mA/s. The empty arrows show the sequence of the measurement with the positive current (+ I) and the full arrows for the negative current ($-I$).

significant influence for higher B_{ref} , see Fig. 6.15 a. This asymmetry was improved by rotating the sample for 1-3°, which can be seen in Fig. 6.15 b.

Thermal effects

Fig. 6.15 b shows the current-driven hysteresis loops acquired using different rates of the current sweep. For the + I (empty dots) and $-I$ (full dots) current scans with the sweep rate of 2.3 mA/s the quadratic background of R_{xy} response is reduced compared to the current sweeps with lower rates. The quadratic background dominates the R_{xy} response at the start of the current sweep and the end of the sweep when the applied current density is reduced to 0 (the arrows mark the sequence of the measurement for each current sweep). Because of the reduced quadratic background the maximal reached R_{xy} value during the sweep decreases with faster sweep rate.

The heating power P applied to the system by the electric current scales as $P \propto R \cdot I^2$ (Joule's law). Some of the produced heat can be dissipated through the contact pads and bonding wires with a good thermal contact. However, when the applied power exceeds the dissipation rate of the system, the temperature of the Hall bar increases. This is especially true, when a high current density is applied to the Hall bar for a longer time (for the 0.2 mA/s sweeping rate the high current density was applied for approximately 5 min). Therefore, it can be assumed, that the quadratic background at the beginning of the current sweeps (up to $j=1.2 \cdot 10^7 \text{ A/cm}^2$) with different sweep rates is approximately

equal due to heat dissipation. The difference in the quadratic background increases at higher current densities and it is most clearly visible when the applied current is reduced gradually back to zero, which leads for the system to cool down.

Reproducibility and intermediate states

The measurements of the *current-driven* hysteresis loops described above were repeated several times for the Au/Fe/MgO(001) heterostructures with 1.3 nm and 1.5 nm Fe layer thickness. Each time, the $+I$ current scan reversed the magnetization from \vec{M}_2 to \vec{M}_1 and the $-I$ current scan from \vec{M}_1 to \vec{M}_2 , see Fig. 6.15. After each of the scans the magnetization was in a stable state, i.e. aligned along the easy magnetization direction, which was measured as a constant R_{xy} after the completed $-I$ or $+I$ scans. The observed plateaus with “intermediate” values of PHE resistance, i.e. values which do not correspond to either $R_{xy}(\vec{M}_1)$ or $R_{xy}(\vec{M}_2)$ can be explained within the multidomain picture by considering a formation of domains within the central area of the Hall cross. For the field-driven hysteresis loops, the magnetization reversal via domain nucleation and growth was confirmed in Kerr microscopy, see Sec. 5.4 and Sec. 6.2. Similarly, the domain nucleation and growth was observed for the current-driven hysteresis loop as will be demonstrated in Sec. 6.4.

To summarize, magnetization reorientation from an initial state along one easy direction, which was set by a high magnetic field previous to the measurement, to a 90° rotated easy direction was induced by an increasing current density. The mechanism of the remagnetization process can be described as follows: a current density of up to $\sim 1.5 \cdot 10^7 \text{ A/cm}^2$ induces heating of the system and possibly a reduction of the coercivity for a 90° switch of the magnetization. The orientation of the magnetization of the switched domains is determined by the current polarity with respect to the initial magnetization direction. Further increase of the current density induces a sufficient Oersted field for nucleation of 90° switched domains, which grow proportionally to the applied current density until the effective current-induced field is strong enough (of the order of some mT) so that the central area of the Hall cross, relative for the PHE resistance (see Sec. 5.4), is completely switched. This additional feature, namely to manipulate the domain structure by an applied current density, would offer further application possibilities for this or similar systems and will be discussed further in Ch. 7.

6.4 Reversible magnetization switching with high current density

The *current-driven* hysteresis loops in the previous section, Sec. 6.3, were acquired by applying a DC current sweep, which was used for manipulation of the magnetic state of the Hall bar and simultaneously for probing the orientation of the magnetization by

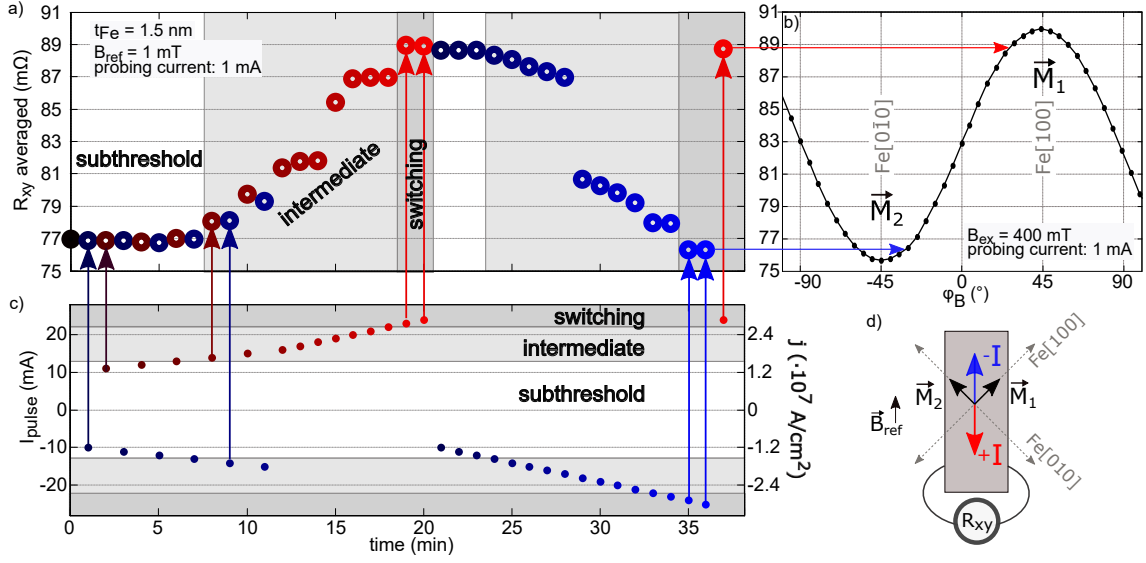


Figure 6.16: a) PHE resistance R_{xy} measured using 1 mA probing current in Au/Fe(1.5 nm)/MgO(001) Hall bar at 280 K after applying high current density "pulses" for approximately 1 s with positive polarity (red dots) and negative polarity (blue dots). The plotted R_{xy}^{avg} stands for averaged R_{xy} measured over a span of 60 s after the current pulse. The vertical arrows relate the measured R_{xy}^{avg} to a corresponding high-current pulse in c). The color brightness of the dots scales with the current pulse density. We observe three regimes of current-induced effects, the *subthreshold* (white), *intermediate* (bright gray) and *switching* (dark gray area). b) PHE dependence on the magnetization direction measured at 280 K by applying a saturation magnetic field of 400 mT along different in-plane directions. d) Sketch of the experiment.

measuring the PHE resistance. Therefore, a further confirmation of the stability of the observed current-induced magnetic state in the absence of the high current density is required. For external fields $B_{ex} \leq 2$ mT, a probing current of density $\leq 1.2 \cdot 10^6$ A/cm 2 does not induce changes to the orientation of the magnetization in the Hall cross (see Sec. 6.3). Therefore, the PHE resistance R_{xy} measured using a low probing current merely provides the information on the stable magnetic state of the system.

The magnetic state of the Au/Fe(1.5 nm)/MgO(001) Hall bar was probed using $I=1$ mA, corresponding to current density $j=1.2 \cdot 10^6$ A/cm 2 . The state was probed directly *after* applying a high current density of $j \geq 1 \cdot 10^7$ A/cm 2 . The high current density was applied for a duration of $t \sim 1$ s and is therefore in this section referred to as a high current *pulse*. The PHE read-out using the low probing current was acquired for about 60 s or longer. This type of magneto-transport measurements was introduced in Sec. 4.2 as the *switching-mode*.

The data points in Fig. 6.16 a show the averaged value of the PHE resistance R_{xy}^{avg} (each value is an average ~ 50 data points in a time span of 60 s) after an applied pulse of high current density. The sequence of the applied current pulses is plotted in Fig. 6.16 c. Again, a small reference magnetic field $B_{ref}=1$ mT was applied along the Hall bar in the

6.4. Reversible magnetization switching with high current density

Fe[1 $\bar{1}$ 0] direction (see sketch of the experiment in Fig. 6.16 d). The current pulse density and polarity was varied, while the probing current was kept constant.

The manipulation of the magnetization by the high current pulses can be roughly divided into three regimes

- *Subthreshold regime*: (white background) Current pulses with $j < 1.5 \cdot 10^7$ A/cm² (dark red for positive polarity of the current $+I$ and dark blue dots for $-I$) did not induce a distinguishable change to the magnetic state, which was defined prior to the switching experiment by saturating the magnetization along the Fe[0 $\bar{1}$ 0] or \vec{M}_2 direction (black dot) with $B_{ex}=500$ mT.
- *Intermediate regime*: (bright gray background) After current pulses with “intermediate” current density between $j=1.5 \cdot 10^7$ A/cm² and $j=2.5 \cdot 10^7$ A/cm², a change of R_{xy}^{avg} is detected. The measured values of R_{xy}^{avg} after the pulse do not correspond to R_{xy} obtained for magnetization along one of the easy directions (either \vec{M}_1 or \vec{M}_2). These *intermediate states* are a consequence of a multi-domain state of magnetization at the Hall cross center, which was induced (or changed) by the current pulse.
- *Switching regime*: (dark gray background) After current pulses with $j > 2.5 \cdot 10^7$ A/cm² (bright red and bright blue dots) the measured R_{xy}^{avg} matches the values close to the dip/peak of the PHE angular dependence, see Fig. 6.16 b. These values of R_{xy} were measured not only after a series of pulses with increasing j but also after applying a singular pulse with $j > 2.5 \cdot 10^7$ A/cm² to the Hall bar (bright red point in Fig. 6.16 a). Here, the single $+I$ pulse with $j=3 \cdot 10^7$ A/cm² induces reorientation of the magnetization from \vec{M}_2 (bright blue dots) to \vec{M}_1 (bright red dot). Nonetheless, the obtained R_{xy} values after the pulses do not match the values of $R_{xy}(\vec{M}_{1,2})$ exactly, which is most probably because of the multi-domain state at the Hall cross center. The switching regime will be discussed in the following.

A current density beyond the critical limit of $j_c \sim 1.5 \cdot 10^7$ A/cm² induces a change of the magnetic state in the Hall cross center. After applying a pulse with $j > j_c$ the measured R_{xy} values lie between the two extrema of the PHE, see Fig. 6.16 b. The *intermediate* R_{xy} values were measured also during the high current sweeps studied in Sec. 6.3. In contrast, the intermediate R_{xy} shown in this section were measured with a small current density *after* the high current pulse. The corresponding magnetic state is thus stable also in the absence of the high current density. However, the stable states of the magnetization in Au/Fe/MgO(001) Hall bars are defined by the cubic anisotropy of the system and therefore, the intermediate states observed here can be explained only in the multi-domain picture.

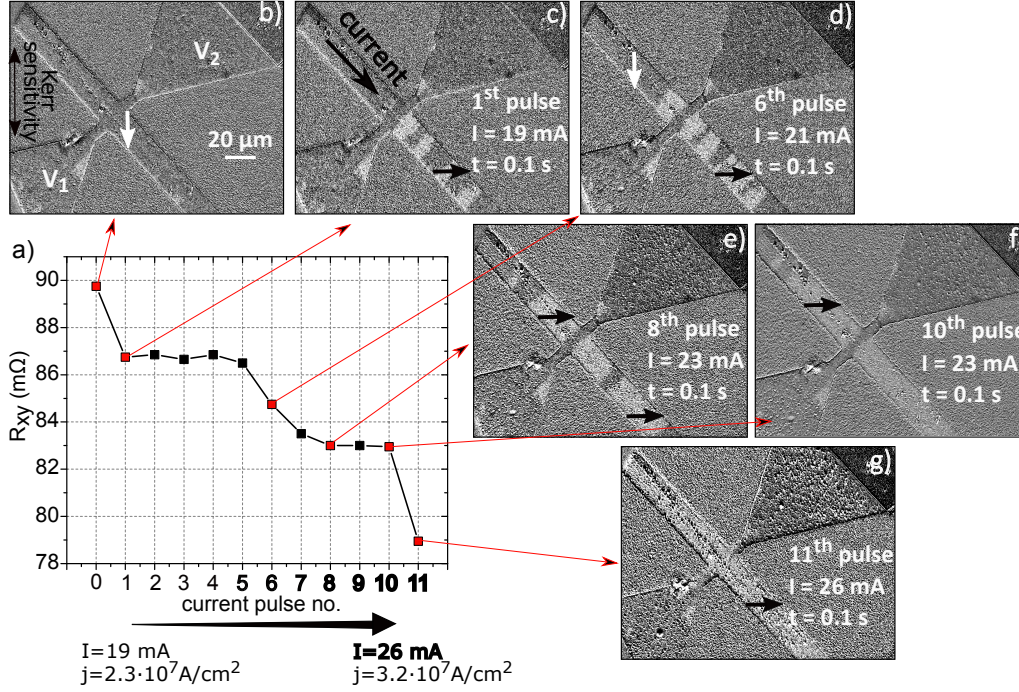


Figure 6.17: The current-induced domain structure was investigated under the Kerr microscope. A homogeneous starting state with the magnetization saturated along Fe $[\bar{1}00]$ direction ($-\vec{M}_1$, dark domains) throughout the Hall bar was set by applying a magnetic field. Afterwards, a sequence of Kerr images was acquired. Each image was obtained after applying a 0.1 s current pulse along the Hall bar as marked in image no. 2. Additionally, the PHE resistance of the induced magnetic state was measured using a 1 mA probing current between the contact pads marked in b). The PHE resistance of the selected Kerr images (b-f) is marked on the graph in red. The amplitude of the applied current pulses was increased in steps of 1 mA as indicated by the thick arrow below the graph.

Multi-state switching in zero-field

In order to visualize the current-induced multi-domain states a sequence of Kerr images of the Au/Fe(1.5 nm)/MgO(001) Hall cross was acquired at room temperature after applying pulses of increasing current density as shown in Fig. 6.17 a. The current pulse duration was 0.1 s. The magnetization along the Hall bar was initially saturated along the Fe $[\bar{1}00]$ direction, i.e. $-\vec{M}_1$ (white arrow in Fig. 6.17 b). Immediately after each pulse a Kerr image was acquired and the PHE resistance R_{xy} was measured using a probing current of 1 mA, see the description of the experimental setup in Sec. 4.3. A selected set of the Kerr images is shown in Fig. 6.17 b-g.

The current pulses 1-4 were set with a constant current density $j = 2.3 \cdot 10^7 \text{ A/cm}^2$. The first applied current pulse (c) to the Hall bar in the initial magnetic state induced bright domains (with magnetization along the Fe $[0\bar{1}0]$ direction) along the wire and next to the Hall cross center. The measured PHE resistance reduced to $R_{xy} = 86.5 \text{ m}\Omega$. The bright domains, which formed next to the Hall cross center, seem to influence the measured R_{xy} .

Additional current pulses with the same j (2-4) did not induce further changes to the domain structure close to the Hall cross center and result therefore in almost constant R_{xy} .

When the current density of the pulse was increased to $j=2.5\cdot 10^7$ A/cm² (5) the R_{xy} further decreased and the bright domains grew and new switched domains formed close to the Hall cross center, see Fig. 6.17 d. The nucleation and growth of the bright domains was observed for each further increase of current density of the pulse (Fig. 6.17 e-g). The current-induced magnetic field manipulates the domain structure close to the Hall cross center, which contributes to the measured R_{xy} . The Kerr images reveal that the bright and dark domain ratio changes in dependence on the current density of the pulse and on its polarity. The induced multi-domain states lead to *intermediate* R_{xy} , i.e. between $R_{xy}(\vec{M}_1)$ and $R_{xy}(\vec{M}_2)$. A switch of the magnetization within the Hall cross center limited by the width of the transversal contacts was observed at highest applied current densities (g). This may be related to the reported decrease of the current density at the center of the Hall cross due to current leakage into the transversal contacts [167]. Additionally, the magnetization in the area of the transversal contacts next to the Hall cross center does not switch under the applied current density and can generate a stray field, which pins the magnetization in its proximity.

As can be seen in Fig. 6.17 g, after applying a current pulse with $j=3.2\cdot 10^7$ A/cm² the bright domains grow over the full visible Hall bar area, which results in PHE resistance $R_{xy}=79$ m Ω . The value does not match the R_{xy} for magnetization saturated along the Fe[010] direction (black arrow), see Fig. 6.16. This is most probably due to the dark domains present at the transversal contacts. However, the results show that the current-induced magnetization switching in Au/Fe/MgO(001) Hall bars is possible also in zero-field.

Two-state switching

Besides the multi-level current-induced switching in the Au/Fe/MgO(001) system, a current-induced reorientation between two single-domain states is also of relevance for possible applicability of the studied system. The reproducibility of the single-domain switching was tested by applying a sequence of current pulses with $j=2.4\cdot 10^7$ A/cm² and reversed polarity of every subsequent pulse along a Hall bar with 1.5 nm Fe layer thickness, see Fig. 6.18. After each pulse, the PHE resistance was measured with a probing current density $j=1\cdot 10^6$ A/cm², see Sec. 4.2. The reference field $B_{ref}=1$ mT along the Fe[1 $\bar{1}$ 0] assists the switching process so that the critical current pulse density required to reorient the magnetization from \vec{M}_1 to \vec{M}_2 (or vice versa) is reduced as compared to the measurements shown in Fig. 6.17. However, the measured R_{xy} after the $j=\pm 2.4\cdot 10^7$ A/cm² current density pulses did not reach the limiting PHE resistance values obtained using a saturating field (on the right in Fig. 6.18). Most probably, a higher current density pulse would be required to induce a single domain state at the Hall cross center, which would

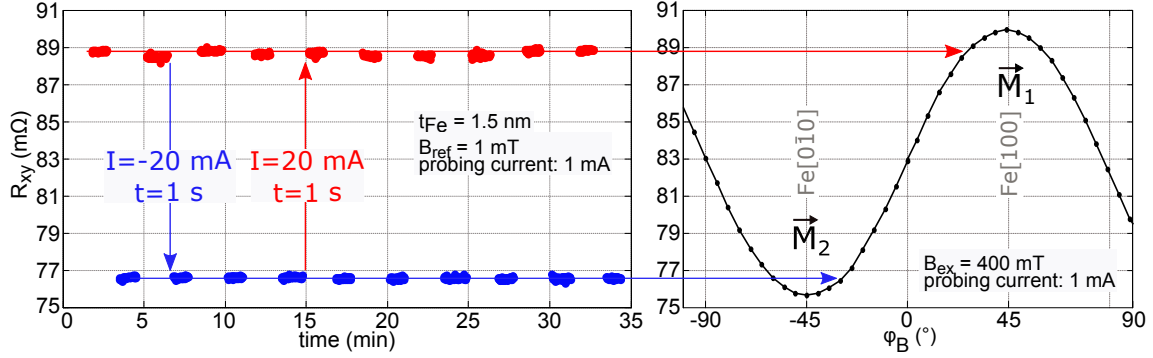


Figure 6.18: Current-induced switching of the magnetic state of the Au/Fe(1.5 nm)/MgO(001) Hall bar measured via the PHE at 280 K. The PHE resistance R_{xy} was measured using probing current $I=1$ mA (corresponding to $j=1.2 \cdot 10^6$ A/cm²) after applying a high current $I=20$ mA (corresponding to $j=2.4 \cdot 10^7$ A/cm²) of either positive (in red) or negative (in blue) polarity for ~ 1 s to the Hall bar. A constant magnetic field $B_{ref}=1$ mT was applied along the Fe[$\bar{1}\bar{1}0$] direction, see sketch in Fig. 6.17 d. Measured R_{xy} values are compared to the angular dependence of the PHE (on the right) acquired by rotating the magnetization with a saturating magnetic field ($B_{ex}=400$ mT) parallel to the film plane and using $I=1$ mA probing current.

compensate for the current leakage into the transversal contacts [167]. Nonetheless, the measurement of the current-induced switching of the magnetization shown in Fig. 6.18 confirms the stability of the current-induced magnetic states and the reproducibility of the switching mechanism.

In contrast to the current-induced switching in the Hall bars with 1.5 nm Fe layer thickness, the same current density pulses applied to the Hall bar with 1.3 nm Fe layer induce a smaller change to the magnetic state as shown in Fig. 6.19. The two states induced by $+I$ and $-I$ current pulses resulted in intermediate R_{xy} values, namely $R_{xy}=30.5$ mΩ after $+I$ pulse and $R_{xy}=26.5$ mΩ after the $-I$ pulse. The difference $\Delta R_{xy}=4$ mΩ is sufficient to differentiate between the two induced magnetic states, which contain multiple domains in the area of the Hall cross center. The current pulses induce a change of the ratio between the 90° rotated domains. This is most probably because of the small size and irregular shape of the magnetic domains observed in Kerr microscopy of the Au/Fe(1.3 nm)/MgO(001) Hall bars, see Fig. 5.14. The small domains are more easily manipulated by stray fields and therefore less stable.

Nevertheless, the current-induced magnetization switching in the Hall bars with 1.3 nm Fe layer thickness is reproducible. After each current pulse of the same polarity a similar PHE R_{xy} is measured and it remains within $\sim \pm 0.5$ mΩ during the read-out time. This means, that each current pulse with the same polarity induced a magnetic state with approximately constant ratio of the 90° rotated domains in the area of the Hall cross center. Moreover, the mechanism reverses upon reversal of the B_{ref} direction, see Fig. 6.19 c and the sketch of the experiment in Fig. 6.19 d. When B_{ref} is applied along Fe[$\bar{1}\bar{1}0$] (empty arrow in Fig. 6.19 d), the $+I$ pulse induces a higher portion of the domains with

6.4. Reversible magnetization switching with high current density

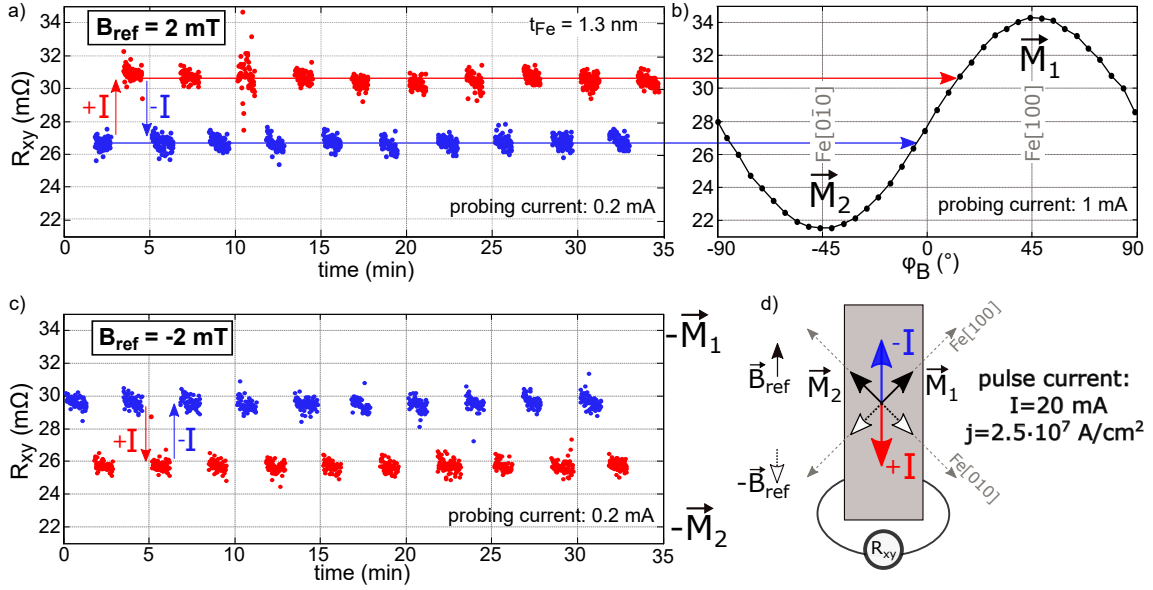


Figure 6.19: Manipulation of the magnetic state of the Au/Fe(1.3 nm)/MgO(001) Hall bar by high current density pulses (duration of 1 s) with positive (in red) and negative (in blue) polarity. The magnetic state was probed *after* the high current pulse via measuring the PHE resistance R_{xy} using $I=0.2$ mA (corresponding to $j=0.24 \cdot 10^6$ A/cm²). A constant magnetic field a) $B=2$ mT and c) $B=2$ mT was applied along the Hall bar, see sketch in d). b) Angular dependence of the PHE measured using 1 mA probing current and $B=400$ mT applied along different direction parallel to the film plane.

magnetization along Fe[010] (i.e. $-\vec{M}_2$) and the $-I$ pulse increases the ratio of domains in favor of the magnetization along Fe[100] (i.e. $-\vec{M}_1$). For reversed B_{ref} , the resulting R_{xy} values obtained after the $+I$ or $-I$ current pulses are slightly shifted to lower values. This is probably due to the different starting orientation of the magnetization, which was set by applying a high magnetic field along the $-\vec{M}_2$ direction, while for the measurements with the positive B_{ref} the magnetization was saturated along \vec{M}_1 previous to applying the high current pulses, compare Fig. 6.19 a and Fig. 6.19 c.

In conclusion, the magneto-transport measurements of the Au/Fe/MgO(001) Hall bars supported by Kerr microscopy demonstrate that a current-induced field is dominated by the Oersted field generated by a current density applied to the Hall bar. A current density $j > 1.5 \cdot 10^7$ A/cm² generates an Oersted field comparable to the coercive field B_c for the 90° switch of the in-plane magnetization between two easy directions. The switching is assisted by Joule heating, which reduces B_c . The effective field acting on the magnetization at the Hall cross center varies from the one in the remaining Hall bar, which is due to the competing effects in this region of the Hall bar. The magnetization at the Hall cross center is influenced by the stray field of the contact pads, while the effective Joule heating and current-induced Oersted field may be reduced due to current shunting [167]. The

magnetic state of Au/Fe/MgO(001) Hall bars can be manipulated by applying a current density along the Hall bar. Switching between multiple magnetic states was induced in zero-field by applying varying current density pulses along the Hall bars, which resulted in intermediate R_{xy} values. With current pulses of $j > 2.3 \cdot 10^7$ A/cm² single-domain switching can be achieved in the Hall bars with 1.5 nm Fe layer thickness. The current-induced magnetic states were shown to be reproducible and stable in the absence of external or current-induced fields.

7. Summary and Outlook

The scope of this work was to study a heavy metal/ferromagnetic metal/insulator epitaxial model system containing a single-crystalline ferromagnetic layer. The Au(4 nm)/Fe(1-1.5 nm)/MgO(001) system grown by molecular beam epitaxy was chosen due to the small lattice mismatch between the crystal structures of the three constituents, while the stacking sequence with the Au capping layer is preferred over the reversed MgO/Fe/Au, in which increased Au segregation and intermixing at the Fe/Au interface has been observed at room temperature. The photo-lithographically patterned Hall bars of Au/Fe bilayers with 1-1.5 nm thickness of the crystalline Fe(001) layer exhibit a strong in-plane easy magnetization axis driven by the shape anisotropy. In the film plane the cubic magneto-crystalline term stemming from the Fe(001) layer dominates the magnetic anisotropy, which promotes the easy magnetization directions along the principle axes of Fe(001) film. The chosen orientation of the MgO(001) substrate with respect to the Hall bar pattern sets the principle Fe(001) axes along the diagonals of the Hall bar. In this arrangement the easy magnetization axes, i.e. Fe[100] and Fe[010], overlap with the minimum and the maximum of the angular dependence of the planar Hall effect, which makes them easily distinguishable in a magneto-transport experiment in Hall bar geometry.

Furthermore, Kerr microscopy of the Au/Fe(1.5 nm)/MgO(001) Hall bars revealed the formation of regularly-shaped 90° magnetic domains during a hard axis magnetization reversal with straight domain walls oriented perpendicular to the Hall bar. The shape of the domains is governed by an interplay of the magneto-crystalline and shape anisotropies and stray fields, contrary to the defect-governed shape of the domains in a discontinuous 1.3 nm Fe film. Moreover, the electrical readout of the in-plane magnetization orientation is possible via measuring the planar Hall voltage. Kerr microscopy analysis has shown that the planar Hall voltage is mainly determined by the domain configuration within the Hall cross center. The system-driven regular arrangement of the 90° magnetic domains, which can be locally read via planar Hall effect, resembles the configuration of the domains along a strip proposed for race-track memory technologies [164] and motivates further study of potential current-induced domain dynamics and magnetization manipulation in this system.

We have observed that a current density beyond 10^7 A/cm² has a clear influence on the hard axis magnetization reversal process in Au/Fe/MgO(001) Hall bars. While at room temperature the measured changes to the reversal process can be explained by including a current-induced Oersted field in the direction perpendicular to the Hall bar, the planar Hall effect measurements at $T < 50$ K indicate a presence of an additional current-induced field of < 2.5 mT in the direction normal to the film surface. The Oersted field is generated by the current in the Au layer and the out-of-plane field may be related to a torque induced by the increased spin Hall effect in Au at low temperatures [172]. The low temperature

regime of current-induced fields in Au/Fe/MgO(001) requires a dedicated study.

Moreover, the presented study combining Kerr microscopy and magneto-transport measurements demonstrates how the current-induced Oersted field can be employed for electrical multi-state magnetization switching in Au/Fe/MgO(001) Hall bars in zero-field. The initial magnetic state of the system was observed to change when a current density $j > 1.4 \cdot 10^7 \text{ A/cm}^2$ is applied to the Hall bar. The amplitude of the change in the planar Hall voltage due to the different magnetic state scales with j , while the sign of the change reverses with the polarity of j . The new magnetic states induced by j are stable in zero field and in low-current regime. With $j > 2.5 \cdot 10^7 \text{ A/cm}^2$ switching between single-domain state at the Hall cross center can be achieved.

The mechanism behind the analog-like response of the magnetic state of the system to j is based on the current-induced manipulation of the domain structure observed in Kerr microscopy images. The current-induced Oersted field can exceed the coercive field $B_c = 0.65 \pm 0.05 \text{ mT}$ for a 90° switch of the in-plane magnetization when the applied j is increased above $1.4 \cdot 10^7 \text{ A/cm}^2$. The switching may be further assisted by Joule heating from the applied current which reduces B_c along the Hall bar and can thus initiate domain nucleation. Higher current densities increase the formation of switched domains or induce their growth. The employed current densities are comparable to the reported values for current densities generating spin orbit torques in ferromagnet/heavy metal bilayers, see e.g. Ref. [26].

In the context of novel three-terminal spintronic memory technologies [5], the studied system combines the characteristics of a non-volatile and multi-level magnetic memory, in which the magnetic state can be electrically manipulated and read-out in zero-field. The manipulation of the magnetic state in an Fe film via an Oersted-field generated by a current in a Au wire has been reported by Yoo *et al.* [22, 32]. By growing the Fe film on a vicinal GaAs surface the authors achieved an out-of-plane tilt of the easy magnetization axes, which adds an anomalous Hall effect contribution to the transversal R_{xy} and therefore four different R_{xy} values for the four easy magnetization directions were observed. However, we observe that in Au/Fe/MgO(001) multiple magnetic states can be achieved even for flat Fe(001) films. Since the Hall bars investigated in this work show non-volatile resistance values that depend on the history of the device (i.e. the amount of charge current that has been applied to it), they can be regarded as memristors. These devices could be used as multilevel electronic memories or as artificial synapses in bio-inspired (neuromorphic) computing architectures [23–25]. A similar system could be envisioned also for binary logs or as a high-current “on-off” switch.

Nevertheless, for any application purposes the device size and the switching current densities need to be further adjusted. The Oersted-field switching mechanism in Au/Fe/MgO(001), on which we report in this work, leads to comparably high switching current densities. We have shown, that the 4 nm thick Au capping layer effectively pre-

vents the oxidation of the ultra-thin Fe(001) film and that it carries the majority of the applied current, which is confirmed by the good agreement with the calculated Oersted field in the infinite conductive sheet approximation. Therefore, in the Hall bars studied in this work the Au layer serves as the conductive wire generating an Oersted field.

At room temperature, our study does not indicate a significant influence from the spin-orbit torques originating either from the Fe/Au interface or from the Au film. The latter origin is related to the spin Hall effect in Au, which is in most studies reported to have a smaller amplitude compared to Pt or Ta [88, 172]. The spin Hall angles in Pt and Au exhibit opposite temperature dependencies [172], which indicates that the dominant contributions to the spin Hall effect arise from different mechanisms in the two materials [172–174]. Furthermore, spin-orbit torque studies employing Pt/Co bilayers have pointed out the importance of the transparency of the Pt/Co interface for the spin current generated by the spin Hall effect in Pt [27, 175]. The ferromagnet/heavy-metal interface transparency is strongly material dependent and is linked to the matching of the electronic band structures of the two materials close to the Fermi level.

Interaction of electronic states across the interface affects also the presence and efficiency of the interfacial spin-orbit torque. In the example of Pt/Co interface, which is often referred to as the model system for spin-orbit torques [21], calculations have shown that the strong spin-orbit coupling in Pt induces an additional spin polarization in the first layers of Co via hybridization of orbitals at the interface [176]. The strong spin-orbit coupling in the intrinsic band structure of Pt results in pronounced spin-orbit gaps in the states with mostly d-orbit character at the Fermi level [174]. In another example, theoretical calculations of the Fe/GaAs(001) interface show a strong dependence of the spin-orbit interaction on the direction of the magnetization in Fe layer [177]. For the same system the interfacial spin-orbit torque assigned to the Rashba-type spin-orbit interaction at the interface has been observed experimentally at room temperature [28]. In the case of the bulk band structure of Fe(001) film grown on Au(001) single crystal we have observed magnetization dependent spin-orbit gaps close to the Fermi level [47]. The opening and closing of the gaps in the band-structure of the Fe(001) film is influenced by the intrinsic spin-orbit coupling in Fe and the symmetry reduction due to the surface. Our observations can be linked to the reported magnetization-dependent asymmetries in the interfacial band structure of some ultra-thin ferromagnetic films arising from the interplay between the exchange interaction and Rashba-like spin-orbit interaction at their interfaces [178, 179]. Such interplay of the exchange and spin-orbit interaction has been placed to the core of the spin-orbit torque phenomena, which motivates further investigations of the interfacial band structure of the single-crystalline Fe(001) films grown on Au(001) or MgO(001) and its engineering (e.g. by doping, adjusting layer thicknesses,...).

As outlook, the switching mechanism in Au/Fe/MgO(001) systems would require some further investigations in order to identify the individual contributions to the current-

induced torques. The better understanding of the switching process could lead to improvements of the system parameters (such as Hall bar size or switching currents) making it suitable for any actual application. Firstly, the components of the current-induced fields, especially the possible out-of-plane field term observed at $T < 50$ K, would need a detailed study in order to distinguish the Oersted field term from other current-induced contributions. One way of separating the contributions is to reduce the Oersted field at the position of the Fe layer with, for example, an additional metal layer in the heterostructure. In a Au/Fe/MgO(film)/Au/MgO(001) structure an in-plane current would generate an Oersted field from the “lower” Au layer grown on the MgO(001) substrate as well as from the capping Au layer. By carefully adjusting the thickness of the two Au layers, their Oersted fields would cancel at the position of the Fe layer. The spin Hall effect and interface-related contributions could then be studied by investigating the dependence of the current-induced fields on temperature and on Au and Fe layer thicknesses. To probe the presence of interfacial effects, an angle-resolved photoemission spectroscopy (ARPES) study of the electronic band structure at the Au/Fe(001) interface may be used thanks to the high crystalline quality of the films. First preliminary results have been obtained on the Fe/Au(001) system and an Fe stripe grown in-situ on MgO(001).

Another worthwhile investigation of the Au/Fe/MgO(001) devices is to test the improvements or limitations to the observed switching mechanism brought about by changes of the design and size of the Hall bars. For example, the scalability of the system remains an open question. While the reduction of the size of the Hall bar is technologically trivial, the magnetic anisotropy of the system together with the crystalline quality may change in the nm-size regime. On the other hand, reduced size of the Hall bar may lead to lower coercive fields and thus to lower switching currents. Moreover, the importance of the anisotropy field for the switching mechanism can be tested by a comparative study using a polycrystalline Fe film (achieved perhaps on a different insulating substrate).

Additionally, the efficiency of the observed switching process may be improved by considering a different material combination. Firstly, a different capping layer (e.g. Pt or Ta) may lead to increased components from the spin-orbit torques to the current-induced fields. A capping layer with lower conductivity as compared to the 4 nm Au layer, which was employed in this study, can decrease the Oersted field contribution. Secondly, if a higher efficiency of the switching mechanism can be achieved, a ferromagnetic layer with higher coercive fields could be used in order to improve the stability of the magnetic state at room temperature and in presence of stray fields. A higher coercive field was observed for Fe(001) film with increased thickness, where the cubic magnetic anisotropy is well defined due to improved continuity. Future experiments are planned on a 1.5 nm Fe(001) film capped with 4 nm Pt layer. Preliminary Kerr microscopy images of this sample have already been obtained.

Appendix: Simulations of the magnetic potential energy

A Stoner-Wohlfarth equation

In the Stoner-Wohlfarth model the system is assumed to be in a single domain state, so that the magnetization is constant throughout the volume. For example, it can reproduce well the magnetic response to an external magnetic field of weakly interacting small magnetic particles. If their size is similar to the domain wall width $d = \pi\sqrt{A/K_u}$, where A is the exchange stiffness and K_u is the magneto-crystalline anisotropy [38], a magnetic domain wall is not stable. Such small particles with a parallel internal spin alignment will respond to an external magnetic field with a coherent rotation of the magnetization. The rotation will depend on the magnetic anisotropy present due to the crystal structure and shape.

The Stoner-Wohlfarth model can be used also for larger magnetic samples to simulate their magnetic hysteresis. However, some limitations of the model need to be kept in mind. The model predicts the coercivity and anisotropy fields to be equal and usually results in square hysteresis loops. This is a consequence of the assumption of a uniform and constant magnetization. In macroscopic samples the magneto-static interactions and morphological imperfections impair a homogeneous magnetization. The formation of domain walls is preferred and, in an external magnetic field, the magnetic response cannot be described with a coherent rotation of the spins. Therefore, the magnetic hysteresis loops modeled based on the Stoner-Wohlfarth equation exhibit an increased squareness and predict too high coercive fields [36, 38, 58].

The Stoner-Wohlfarth model adapts the phenomenological description of magnetic anisotropy to define the magnetic potential energy E_m of the system. In the example of a uniaxial magnetic anisotropy with anisotropy constant K the magnetic energy per unit volume can be written as

$$E_m = -M_S B \cos(\varphi_M - \varphi_B) + K_u \cdot \sin^2 \varphi_M. \quad (1.1)$$

Here, the first term describes the interaction of the magnetization \vec{M} with the external magnetic field B applied at an angle φ_B to the easy magnetization axis (at $\varphi=0^\circ$). The second term describes the gain or loss of energy depending on the angle φ_M enclosed by the magnetization and the easy magnetization axis. The magnetic energy landscape at zero magnetic field has two minima, either at $\varphi_M = 0^\circ$ and $\varphi_M = 180^\circ$ for $K_u > 0$ or at $\varphi_M = 90^\circ$ and $\varphi_M = 270^\circ$ for $K_u < 0$, see Fig. A.1 b. In the latter case, the magnetic easy axis is found at $\varphi=90^\circ$.

The magnetic energy landscape is changed when a magnetic field B is applied. In Fig.

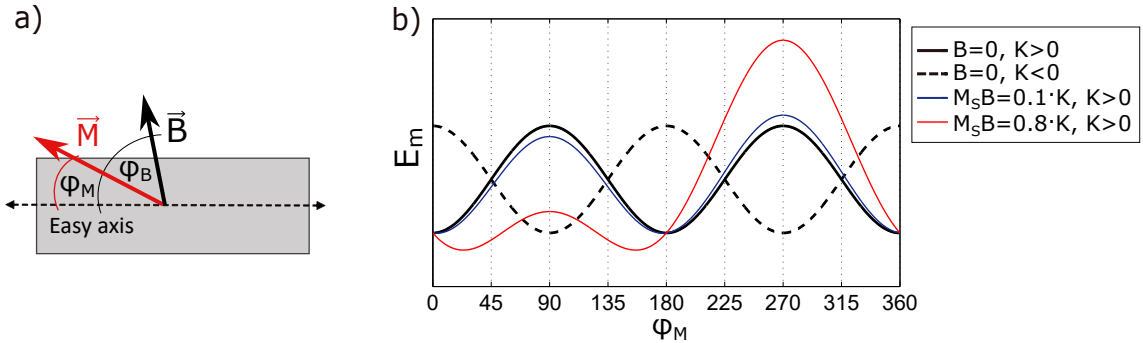


Figure A.1: Magnetic potential energy landscape calculated from the Stoner-Wohlfarth equation for a sample with a uniaxial anisotropy in 2D, sketched in **a)**. The magnetization \vec{M} and the external magnetic field \vec{B} enclose angles φ_M and φ_B , respectively, with the direction of the easy axis. The magnetic energy dependence on φ_M was calculated from the Eq. 1.1 using the parameters listed in the graph legend **b)**.

A.1 an example of the energy landscape for a magnetic field along $\varphi_B = 90^\circ$ is shown. A small magnetic field compared to the anisotropy constant with $M_S B = 0.1 K_u$ induces only a small difference in E_m at $\varphi_M = 90^\circ$ and $\varphi_M = 270^\circ$, while a magnetic field comparable to the anisotropy field ($M_S B = 0.8 K_u$) considerably changes the difference in the maxima and shifts the minima of E_m closer towards $\varphi_M = 90^\circ$, i.e. parallel to the direction of the external field.

For simulation of a hysteresis loop, i.e. when the applied magnetic field strength is varied between $-B$ and B with a fixed φ_B , the orientation of the magnetization at each applied B is found by calculating the angle φ_M^{min} at which the energy $E_m(\varphi_M^{min}, B, \varphi_B)$ has a minimum value. For the angle φ_M^{min} the conditions $\frac{\partial E_m}{\partial \varphi_M} = 0$ and $\frac{\partial^2 E_m}{\partial \varphi_M^2} > 0$ need to be fulfilled. The minimum magnetic energy state is a stationary state for the magnetization direction. In this way φ_M^{min} in dependence on B and φ_B can be calculated and can be used to simulate the magnetic hysteresis loop. This is shown in Fig. A.2 for the example of the uniaxial anisotropy. Here, Eq. 1.1 was used to find φ_M^{min} for each φ_B and $M_S B / K_u$ parameters and $\cos \varphi_M^{min}$ was calculated, which represents the projection of \vec{M} onto the easy axis. The simulated φ_M^{min} response can also be used to interpret the magneto-transport effects, which depend on the angle between the magnetization and the current direction. This will be shown in the following for the anomalous Hall effect (AHE) and planar Hall effect (PHE).

B Anomalous Hall effect hysteresis simulation

The in-plane magnetic anisotropy of the Au/Fe/MgO heterostructures was investigated by measuring the AHE. The origin of this effect was commented in Sec. 2.4.3 and the experimental setup was shown in Sec. 4.2. Here, the calculated rotation of the magneti-

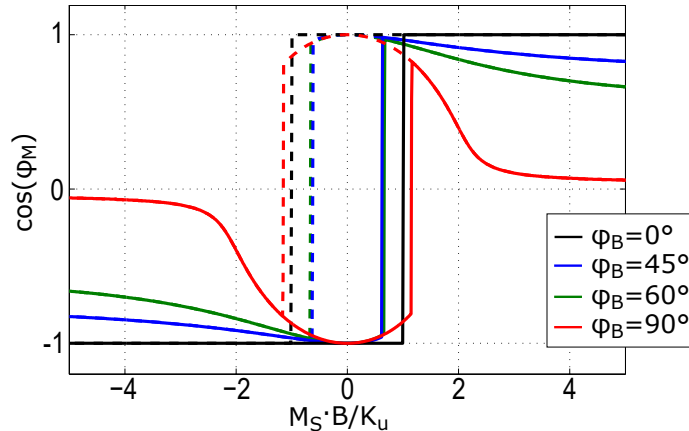


Figure A.2: The calculated minima of the magnetic potential energy for four different magnetic field directions depending on the $M_S B / K_u$ parameter from the Stoner-Wohlfarth equation Eq. 1.1 for uniaxial magnetic anisotropy. The $M_S B / K_u$ parameter was scanned from -5 to 5 (solid line) and back to -5 (broken line) in order to simulated a magnetic hysteresis loop. The cosine of the calculated φ_M^{min} was plotted, which represents the projection of \vec{M} onto the easy axis direction.

zation as a response to a magnetic field applied along the film normal will be presented. The simulation of the out-of-plane hysteresis loop was done based on the Stoner-Wohlfarth equation discussed in the previous section (Sec. A).

Usually, in thin film studies, the film normal is defined as the *unique axis* [38]. Therefore, we define $\Theta=0^\circ$ along the film normal and Θ_M as the angle between \vec{M} and the film normal. We assume an easy magnetization axis at $\Theta=90^\circ$, i.e. parallel to the film plane. The magnetic field B is applied along the film normal, therefore $\Theta_B=0^\circ$. The equation for the magnetic potential energy E_m is a sum of the Zeeman energy and of the first, second and third order expansion terms of the uniaxial magnetic anisotropy. For easy magnetization axis at $\Theta=90^\circ$ the energy E_m can be written as

$$\begin{aligned}
 E_m = & -M_S B \cdot \cos(0^\circ - \Theta_M) \\
 & -K_1 \cdot \cos^2(\Theta_M) \\
 & -K_2 \cdot \cos^4(\Theta_M) \\
 & -K_3 \cdot \cos^6(\Theta_M).
 \end{aligned} \tag{1.2}$$

The second and third order anisotropy constants K_2 and K_3 were included for a better fit to the measured AHE loops. The Θ_M^{min} with minimal E_m for a given magnetic field B were calculated using a MATLAB code. The sine of the Θ_M^{min} gives the normalized AHE signal for a given B . The match to the measured AHE loops was found by trial insertion of K_1/M_S , K_2/M_S and K_3/M_S parameters. The best fits are shown in Fig. B.3.

The simulated AHE curves are in good agreement with the measurements. The best fit anisotropy constants K_1 , K_2 and K_3 have a negative value, which agrees with the

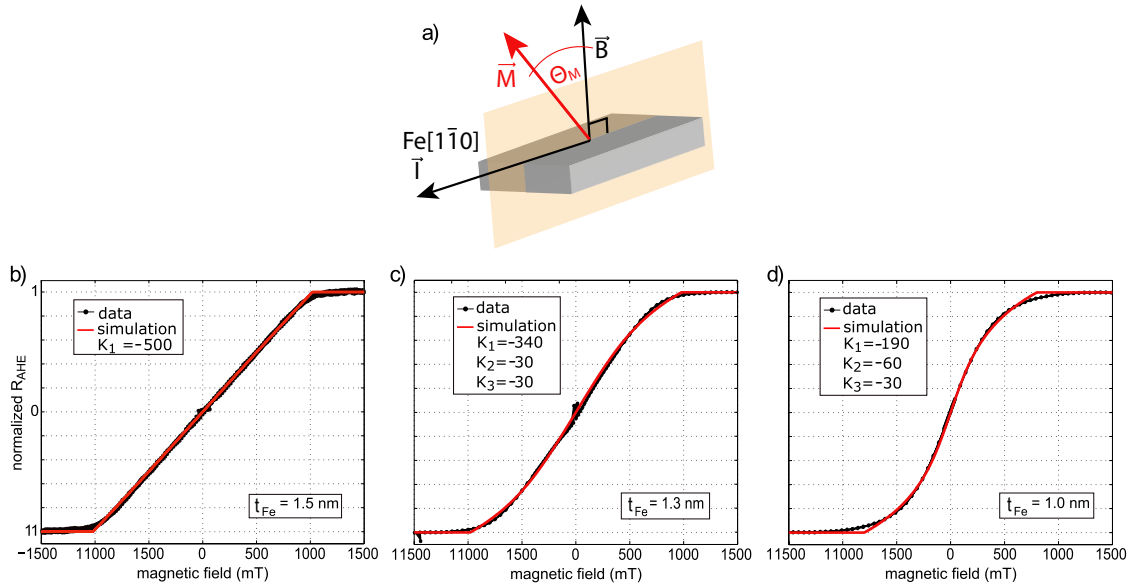


Figure B.3: a) Sketch of the geometry for the anomalous Hall effect measurement. The same geometry was used also for the Stoner-Wohlfarth calculations of the stationary states, i.e. calculations of the angles Θ_M between the film normal and the magnetization \vec{M} in the plane spanned by \vec{B} and \vec{I} (marked in orange), which have the minimal magnetic potential energy. In b), c) and d) the measured AHE loops at 280 K from Hall bars with $d_{Fe} = 1.5, 1.3$ and 1.0 nm are plotted with the best fit simulated AHE curve. The anisotropy constants K_1, K_2 and K_3 used in the calculation are written in the legend of each of the plots. Here, the saturation magnetization was set to 1 and the $K_{1,2,3}$ are in the units of mT.

easy magnetization axis parallel to the film plane. However, the calculated curves result in sharper reorientation of the magnetization compared to the measurement. Especially around the onset of the plateau, i.e. the saturation of the magnetization along the film normal, the simulated curve exhibits a sharper transition to the saturated state, while the measurements show a more gradual transition. This mismatch can be a consequence of the assumption of a single-domain state of the sample, which is made when using the Stoner-Wohlfarth equation for calculating E_m . Moreover, structural defects and sharp edges of the Hall bar structure, which act as pinning points for the magnetization, are not considered in the calculation. Also, thermal excitations which lead to a reduction of the magnetization and may influence the magnetization reversal process are not included. The resulting best fit anisotropy constants are discussed in Sec. 5.3.

C Planar Hall effect hysteresis simulation

The in-plane cubic asymmetry of the Au/Fe/MgO(001) Hall bars was studied with magneto-transport measurements based on the PHE, which were presented in Sec. 5.3. The four-fold and uniaxial anisotropy constants for the Hall bars with 1.5 nm and 1.3 nm

Fe layer thickness were extracted from the analysis of the data and are summarized in Table C.1.

anisotropy constant	$t_{\text{Fe}} = 1.3 \text{ nm}$	$t_{\text{Fe}} = 1.5 \text{ nm}$
$K_4 \text{ (}\cdot 10^3 \text{ J/m}^3\text{)}$	(9.2 ± 0.5)	(15 ± 2)
$K_u \text{ (}\cdot 10^3 \text{ J/m}^3\text{)}$	(0 ± 0.1)	(0.8 ± 0.8)

Table C.1: Table of the experimentally obtained anisotropy constants (see Sec. 5.3).

The measured PHE loops can be simulated in the single domain picture using the Stoner-Wohlfarth expression for the magnetic energy E_m of a two-dimensional system with a four-fold magnetic anisotropy, additional uniaxial anisotropy and interaction of the magnetization with the externally applied in-plane magnetic field B . This expression was already used for the analysis of the PHE measurements (Eq. 5.4), and we repeat it for clarity

$$E_m = -M_S B \cdot \cos(\varphi_B - \varphi_M) + K_u \cdot \sin^2(\varphi_M - \varphi_{K_u}) + \frac{K_4}{4} \cdot \cos^2 2\varphi_M. \quad (1.3)$$

Similarly to the simulations of the AHE loops, the PHE hysteresis loops were simulated by calculating the φ_M^{min} with minimum energy E_m for each applied B . The starting point of the simulation was to calculate the $\varphi_{M,1}^{\text{min}}$ for $-B$. Next, the magnetic field was increased for a chosen step ΔB and the angle $\varphi_{M,2}^{\text{min}}$ was calculated by finding the minimum of $E_m(-B + \Delta B)$. This procedure was repeated for all steps of the gradually increasing B and also for the negative scan of the applied field. The range of φ_M to which the magnetization can coherently rotate from $\varphi_{M,i}^{\text{min}}$ for an applied magnetic field B_{i+1} was limited to the interval between $\varphi_{M,i}^{\text{min}} - 70^\circ$ and $\varphi_{M,i}^{\text{min}} + 70^\circ$. This constrains the rotation of \vec{M}_{i+1} to the nearest angle with local energy minimum and not to the angle with the global energy minimum. Moreover, due to the four-fold symmetry of the magnetic potential energy landscape usually more than one global minimum is found. In this case, the simulated φ_M could oscillate between the angles with equal global minima, which is not a physical observation.

Instead of varying the anisotropy parameters, the experimentally obtained values for K_4 and K_u in Table C.1 were inserted into Eq. 1.3. The simulated hard axis magnetization reversal for a positive and negative magnetic field scan along Fe[1 $\bar{1}$ 0] direction is shown in Fig. C.4. The angle φ_M between the magnetization and Fe[1 $\bar{1}$ 0] direction is plotted versus the applied magnetic field B . For the positive B scan the magnetization rotates from $\varphi_M = -180^\circ$ towards $\varphi_M = 135^\circ$ and jumps to $\varphi_M = -45^\circ$ after crossing zero field. The second jump to $\varphi_M = 45^\circ$ is calculated to occur at $B=1.4 \text{ mT}$, from here the magnetization rotates towards $\varphi_M = 0^\circ$ when the field is gradually increased. The same steps are observed for all magnetic field scans shown in Fig. C.4 and agree well with the observations in Kerr microscopy of the hard axis magnetization reversal in Sec. 5.1. In the simulations the direction of the uniaxial anisotropy was determined to be along the easy axis Fe[100]

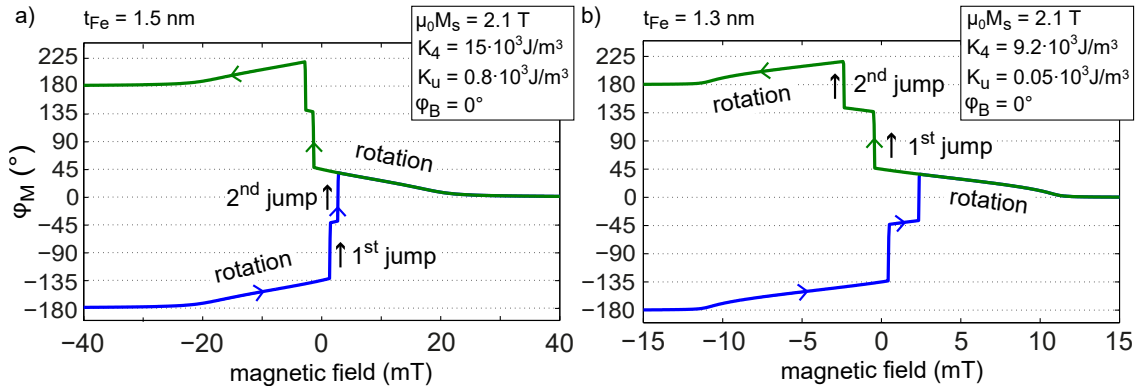


Figure C.4: **a)** A Stoner-Wohlfahrt modeled magnetization reversal calculated by minimizing the magnetic potential energy defined in Eq. 1.3 using the experimentally obtained anisotropy parameters for the Hall bar with 1.5 nm Fe layer thickness (listed in the inset). The steps of the magnetization reversal between $\varphi_M = -180^\circ$ and $\varphi_M = 180^\circ$ (blue curve) are marked in the graph. For the negative scan of the magnetic field (green curve) the magnetization reversal proceeds via the same steps. **b)** The same simulation using the parameters K_4 and K_u obtained experimentally for the Hall bar with 1.3 nm Fe layer thickness. The magnetization reversal for positive (in blue) and negative (in green) magnetic field scan proceeds via the same steps as marked in a.

($\varphi_{K_u} = 45^\circ$). Because φ_{K_u} could not be unambiguously extracted from the analysis in Sec. 5.3, it was determined from the best fit simulation of experimental data.

From the simulated magnetic-field dependence of φ_M , the PHE resistance can be calculated for each magnetic field B_i considered by inserting the corresponding value for $\varphi_{M,i}$ into the equation for the PHE voltage (derived from Eq. 5.3)

$$R_{xy} = R_{PHE} \cdot \sin(\varphi_{M,i}) \cos(\varphi_{M,i}) \quad (1.4)$$

The R_{PHE} prefactor in Eq. 1.4 is the PHE amplitude, which was experimentally determined in Sec. 5.3. The results of the simulations of the PHE loops acquired with magnetic field applied along the current direction Fe[1 $\bar{1}$ 0] are shown in Fig. C.5. The simulated PHE loops using the experimentally obtained values for K_4 , K_u and R_{PHE} for the Hall bars with $t_{Fe} = 1.3$ nm and $t_{Fe} = 1.5$ nm match the general shape of the experimental data (see Fig. C.5 a and b). The gradual rotation of the magnetization before the first and after the second jump (in Fig. C.4) gives the rounded shape of the PHE response, while the sharp jumps of φ_M observed in Fig. C.4 correspond to the sharp changes in the PHE signal.

A better match between the simulated and experimental PHE loops was obtained when a misalignment angle between the Fe[1 $\bar{1}$ 0] direction and the applied magnetic field was added ($\varphi_B \neq 0$). The experimental data for $t_{Fe} = 1.5$ nm was best simulated using a mismatch of 2° and an increased cubic anisotropy constant K_4 , while the uniaxial anisotropy was set to zero (see Fig. C.5b). Similarly, the simulated PHE loop for $t_{Fe} = 1.3$ nm with

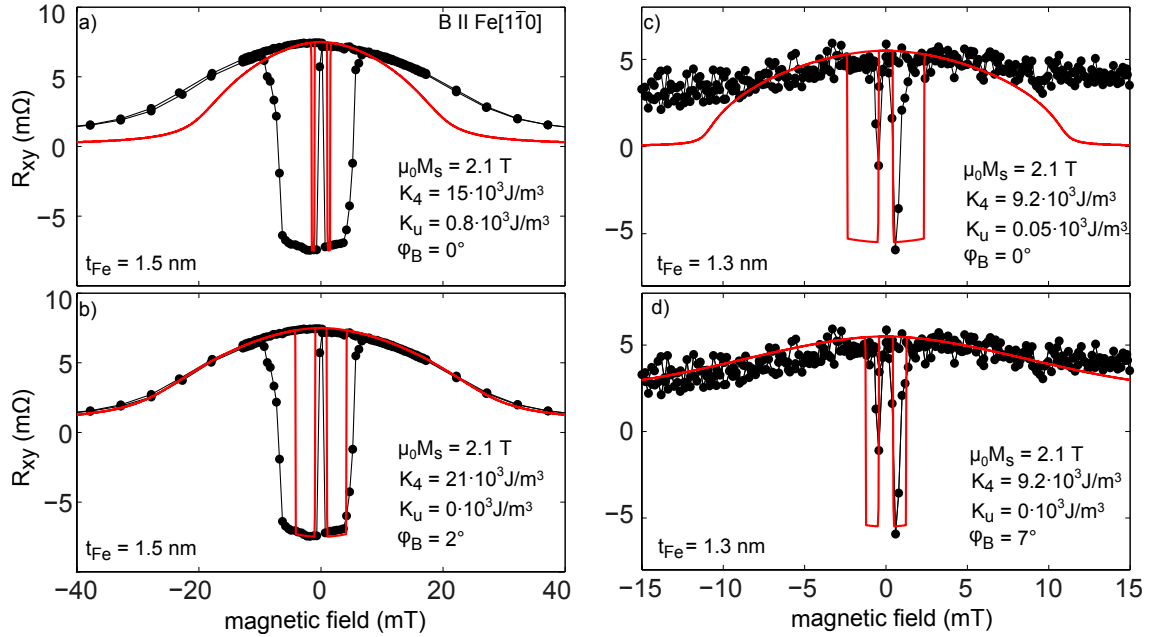


Figure C.5: Experimental and simulated planar Hall effect loops for magnetic field scan along the Fe[110] direction, i.e. parallel to the applied current of 3 mA, acquired from the Hall bar with Fe layer thickness of 1.5 nm (a and b) and 1.3 nm (c and d). The Stoner-Wohlfarth simulation using the experimentally obtained anisotropy constants K_4 and K_u (in a and c) is compared to the simulation with adjusted parameters for a better match to the data (in b and d). In the simulation with non-zero K_u , a $\varphi_{K_u} = 45^\circ$ was used. The *left-right* asymmetry observed in the PHE measurements is marked in a.

smallest deviation from the data was obtained using a mismatch of 7° and no uniaxial anisotropy (see Fig. C.5d). This is supporting the argument that a small misalignment of the experiment is the most probable reason for the observation of the double-jump magnetization reversal.

Nevertheless, certain inconsistencies between the experimental data and the simulation remain. Firstly, the sharp magnetization jumps were in the experiment observed at slightly shifted switching fields and, secondly, especially the second magnetization jump after crossing zero field appears in the simulation as a one step switch, while in the experimental data it is a more gradual process via several intermediate states. These deviations of the simulation from the experimental data can be explained by the simplified single-domain picture, which is employed in the Stoner-Wohlfarth model. In other words, the Stoner-Wohlfarth model does not include the formation of domains in the magnetization reversal model, only sharp jump or coherent rotation of a single macro-spin with magnetization M_S . When considering also the formation of domains, the reduced switching field of the first magnetization jump after crossing zero field can be explained with the formation of switched domains at the nucleation points. The nucleation points were observed also in the region of the Hall cross (see Sec. 5.4) and therefore, the domains nucleated there can

induce changes to the R_{xy} . Additionally, in the same region also pinned domains have been observed. These may induce the gradual changes in R_{xy} during the second magnetization switch after crossing zero field. However, the single-domain Stoner-Wohlfarth model gives a good qualitative explanation of the observed PHE loops.

C.1 Current-induced in-plane field

In addition to the mentioned deviations of the simulated loops from the experimental data, the asymmetry in the experimental PHE hysteresis loops between the negative and positive magnetic field (*left-right* asymmetry marked in Fig. C.5a) is also not accounted for in the simulation. Neither the uniaxial term nor the misalignment explain the observed asymmetry, therefore an additional term needs to be considered. Because the observed asymmetry increases with the applied current density, the missing term may arise from the applied electric current, which flows through the conducting layers of the Hall bar (Fe and Au layer). From Ampere's law [38], the electric current induces a magnetic field, known as the Oersted field (see Sec. 2.1). Other mechanisms behind the current-induced terms may be related to the spin-orbit interaction (e.g. spin-orbit torques).

The effect of an additional current-induced magnetic field B_{\perp} can be simulated by adding a second Zeeman term to the Eq. 1.3 for the magnetic potential energy

$$E_m = -M_S B \cdot \cos(\varphi_B - \varphi_M) + K_u \cdot \sin^2(\varphi_M - \varphi_{K_u}) + \frac{K_4}{4} \cdot \cos^2 2\varphi_M \quad (1.5)$$

$$-M_S B_{\perp} \cdot \cos(\varphi_{\perp} - \varphi_M)$$

We can set the direction of the B_{\perp} to be perpendicular to the electric current, i.e. $\varphi_{\perp}=90^{\circ}$ to simulate the direction of an Oersted field induced by the current through the Au layer at the position of the underlying Fe film and at the same time also a possible *field-like* term of the spin-orbit torque (see Sec. 2.5).

Indeed, the simulated PHE curve for the hard direction scan of the magnetic field with the additional Zeeman term is in a good agreement with the experimental data. The comparison in Fig. C.6 shows that including a magnetic field $B_{\perp} = 0.12$ mT in the direction perpendicular to the applied current reproduces the left-right asymmetry observed in the experimental data from the Hall bar with 1.5 nm and 1.3 nm Fe thickness. To match the data from the 1.3 nm thick Fe film the angle of the B_{\perp} was set to $\varphi_{\perp}=-90^{\circ}$. This is because the PHE curve was acquired by applying a current in the direction opposite to the Fe[1 $\bar{1}$ 0]. The effect of the additional field can be understood as follows. If the magnetization jump occurs from a direction with a negative projection on the \vec{B}_{\perp} to a direction with a positive projection (e.g. Fe[$\bar{1}$ 00] \rightarrow Fe[010]) then the field B_{\perp} assists the externally applied magnetic field and the magnetization jump is shifted to a lower field and a decrease in the width of the hysteresis is observed (positive field range in Fig. C.6a and the negative range in Fig. C.6b). For the magnetization jump in the opposite direction (Fe[010] \rightarrow Fe[$\bar{1}$ 00] or Fe[100] \rightarrow Fe[0 $\bar{1}$ 0]), the magnetic field B_{\perp} hinders the rotation and a

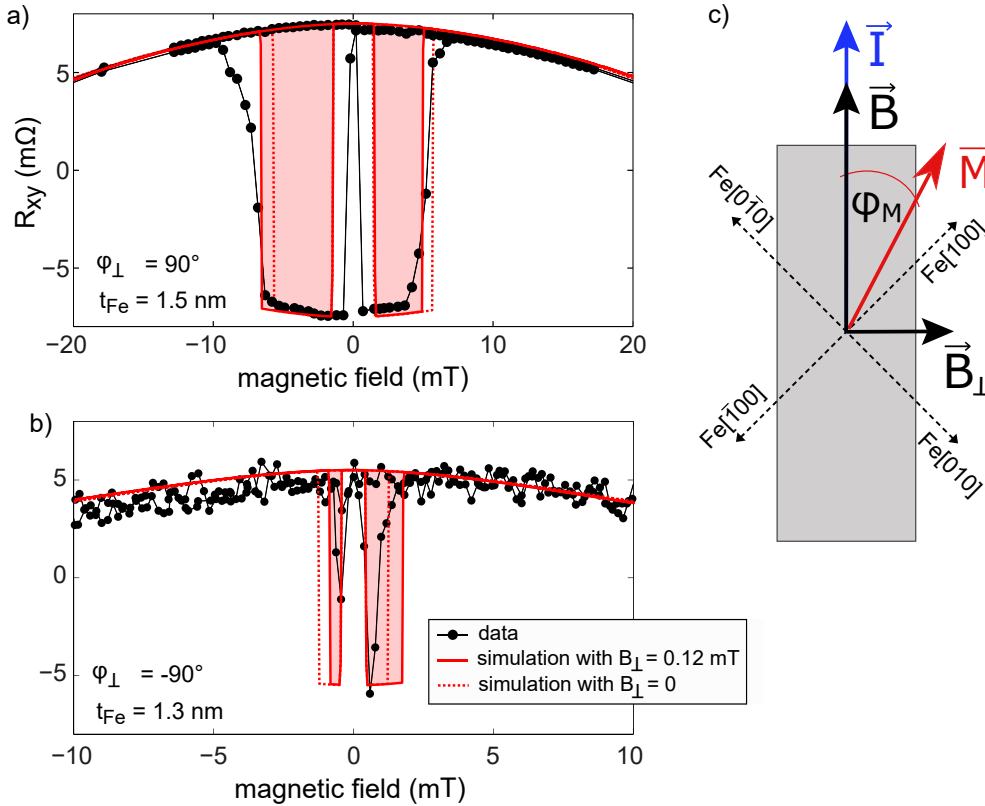


Figure C.6: The PHE curve for magnetic field scan along the $Fe[1\bar{1}0]$ hard axis parallel to the current was simulated using the magnetic potential energy with (red line) and without (red dotted line) the additional Zeeman term including $B_{\perp}=0.12$ mT magnetic field perpendicular to the current direction ($\varphi_{\perp}=90^{\circ}$). The simulated curve was calculated for the Hall bar with 1.5 nm Fe layer thickness (in **a**) and 1.3 nm Fe layer thickness (in **b**) and compared to the experimental data acquired at 250 K. In **b**) the angle $\varphi_{\perp}=-90^{\circ}$ was used in the simulation for a better match to experimental data. **c**) The geometry of the experiment and simulation.

higher external field is needed to induce the magnetization jump. This is observed as an increase of the hysteresis width in the negative field range in Fig. C.6a or in the positive range in Fig. C.6b.

C.2 Current-induced out-of-plane field

The transversal resistance R_{xy} can, in general, have two contributions, namely the planar Hall effect (PHE) resistance R_{PH} and a contribution induced by the anomalous Hall effect (AHE) R_{AHE} , when the magnetization of the sample has a component along the normal of the film plane. In the simulation of the magnetization reversal applied here, the system is considered as two-dimensional, which means that the magnetization is assumed to be parallel to the film plane. This is a reasonable approximation for the strong in-plane magnetic easy axis of the considered system, which was observed in the AHE measurements, see

Sec. 5.3.

However, the in-plane anisotropy can have a strong temperature dependence. For example, for MgO/Fe(~ 1 nm)/MgO the in-plane anisotropy constant decreases at low temperatures and below ~ 200 K the magnetic anisotropy rotates out-of-plane [120]. When the in-plane anisotropy decreases at lower temperatures, the magnetization can more easily be rotated out-of-plane. Therefore, at low temperatures, a current-induced field with a component along the film normal may tilt the magnetization out-of-plane, which would induce an AHE contribution to the measured R_{xy} .

The addition of a R_{AHE} contribution was stimulated by the observation of the shift in R_{xy} between the positive and negative magnetic field scans along the Fe[1 $\bar{1}$ 0] for temperatures < 50 K, see e.g. Fig. 6.6. For the simulation of the PHE loops at $T < 50$ K we consider a current-induced torque with a damping-like character¹. In a system with in-plane magnetization, the effective magnetic field B_{oop} of such a torque would be along the film normal. Such effective current-induced field was observed in ferromagnetic metal (FM)/heavy metal (HM) systems and was assigned to the spin Hall effect (SHE) in the HM [26], see Sec. 2.5. Here it is approximated as $\vec{B}_{oop} = B_{oop}\vec{\sigma} \times \vec{m} = B_{oop}\cos(\varphi_M)$ with $\vec{\sigma} = \vec{z} \times \vec{j}$ as the spin polarization at the interface to the HM induced by the SHE. The film normal is along \vec{z} and \vec{j} is the current density vector.

The minimization of the two-dimensional Stoner-Wohlfarth magnetic potential energy was calculated as described in previous section to obtain the in-plane angle of the magnetization φ_M in dependence on the external magnetic field. The cubic anisotropy constant was increased to $K_4 = 2.5 \cdot 10^4 \text{ J/m}^3$, which is an expected increase of K_4 from the results of the temperature dependence of the magnetic anisotropy in Sec. 5.3. The magnetization reversal was simulated for external magnetic field applied at $\varphi_B = 5^\circ$ and 15° to the Fe[1 $\bar{1}$ 0] direction and an additional in-plane magnetic field $B_\perp = 0.4$ mT. The resulting PHE hysteresis loops are shown in the second column in Fig. C.7.

To simulate the PHE curves plotted in the third column in Fig. C.7 simulated magnetic field dependence $\varphi_M(B)$ was used to calculate the transversal resistance R_{xy} as a sum of the PHE and AHE induced resistances as

$$R_{xy} = R_{PH} + R_{AHE} = R_{PHE}\sin(\varphi_M)\cos(\varphi_M) \cdot \cos^2(\Theta_M) + R_A\sin(\Theta_M) \quad (1.6)$$

The angle Θ_M is the tilt of the magnetization in the out-of-plane direction. Because of the tilt Θ_M the in-plane component of the magnetization is reduced by factor $\cos^2(\Theta_M)$ and the R_{xy} obtains an additional contribution from the AHE with an amplitude R_A and a sine-dependence on the Θ_M . The tilt Θ_M is defined by the ratio between the in-plane

¹Under the assumption, that the current-induced torque induces an out-of-plane tilt of the magnetization and acts therefore in the opposite direction of the magnetic (or Gilbert) damping, it could be termed also *antidamping* torque.

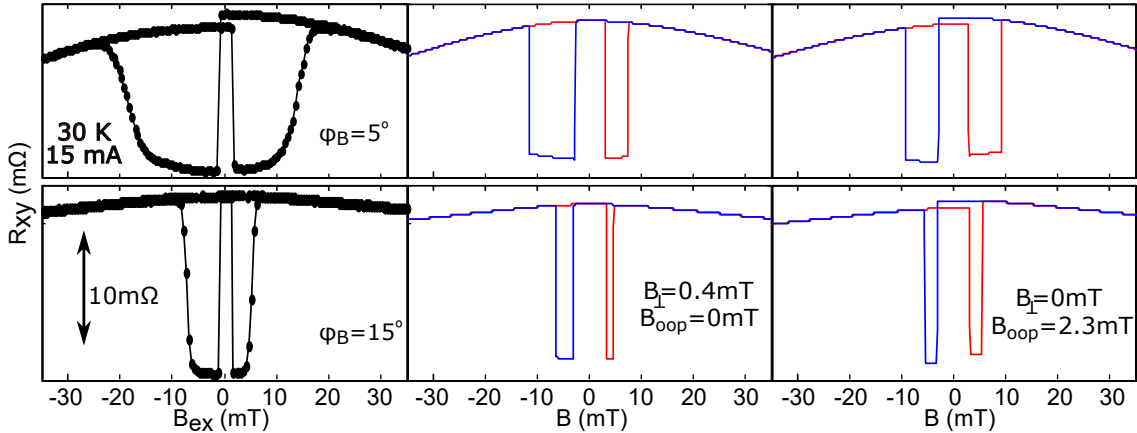


Figure C.7: PHE hysteresis loops acquired at 30 K with B_{ex} field scan along the direction with (top) $\varphi_B=5^\circ$ and (bottom) 15° to the Fe[1 $\bar{1}$ 0] hard axis (first column) and simulated from the Stoner-Wohlfarth model using an additional magnetic field $B_\perp=0.4$ mT perpendicular to Fe[1 $\bar{1}$ 0] direction (second column) or an additional magnetic field B_{oop} in the direction normal to the film plane (third column).

fields and the current-induced out-of-plane field

$$\Theta_M = \text{atan}\left(\frac{B_{oop}\cos(\varphi_M)}{B + B_{ani}}\right) \quad (1.7)$$

where B_{oop} is the amplitude of the current-induced out-of-plane field with a $\cos(\varphi_M)$ -dependence on the in-plane orientation of the magnetization.

The parameter R_A was determined from the slope dR_{AHE}/dB_z of the AHE curve (the normalized AHE curves are shown in Fig. 5.5). This estimation was used also in Ref. [96, 169] and for CoFeB it was estimated that the dR_{AHE}/dB_z slope increases for 15% when the temperature is reduced to 10 K [169]. We use $R_A = \frac{dR_{AHE}}{dB_z}(1 \text{ T}) \sim 0.1 \Omega$. The in-plane anisotropy field was set to $B_{ani}=400$ mT. This value was estimated from the experimentally obtained anisotropy constant in Sec. 5.3 at room temperature for the 1.3 nm Fe layer thickness. In Ref. [120] it was observed that the anisotropy constant drops to approximately half of the room-temperature value at 10 K. Therefore, the value for B_{ani} used in the calculation was determined as $B_{ani} = K_1/M_S$, which was obtained in Appendix B.

The simulated $R_{xy} = R_{PH} + R_{AHE}$ are shown in the third column in Fig. C.7. The additional AHE contribution due to the out-of-plane tilt gives rise to the shift in R_{xy} between the positive and the negative magnetic field scans. The size of the shift matches the experimental one when $B_{oop} \sim 2.3$ mT. The R_{xy} shift is observed only for external magnetic fields below ~ 5 mT and it is present in the simulated PHE hysteresis loops also for $\varphi_B > 15^\circ$, which is not the case for the measured loops. This indicates that the approximation of the additional B_{oop} in the model used for the simulation does not correctly describe the properties of this field. This may be due to the antidamping-

like character of the corresponding torque, which is not correctly approximated with the $\cos(\varphi_M)$ dependence of its effective field. Error may arise also due to the two-dimensional Stoner-Wohlfarth model used for the calculation of the magnetic potential energy of the system.

Bibliography

- [1] G. E. Moore. Cramming more components onto integrated circuits, Reprinted from Electronics, volume 38, number 8, April 19, 1965, pp.114 ff. *IEEE Solid-State Circuits Newsletter*, 20(3):33–35, sep 2006. 1
- [2] M. M. Waldrop. More Than Moore. *Nature*, 530(7589):144–147, 2016. 1
- [3] K. Roy, S. Mukhopadhyay, and H. Mahmoodi-Meimand. Leakage current mechanisms and leakage reduction techniques in deep-submicrometer CMOS circuits. *Proceedings of the IEEE*, 91(2):305–327, feb 2003. 1
- [4] International Roadmap for Devices and Systems (IRDS) 2017 Edition, 2017 (Accessed: October 4th, 2018). <https://irds.ieee.org/roadmap-2017>. 1
- [5] S. Fukami and H. Ohno. Magnetization switching schemes for nanoscale three-terminal spintronics devices. *Japanese Journal of Applied Physics*, 56(8):0802A1, 2017. 1, 118
- [6] G. Binasch, P. Grünberg, F. Saurenbach, and W. Zinn. Enhanced magnetoresistance in layered magnetic structures with antiferromagnetic interlayer exchange. *Physical Review B*, 39(7):4828–4830, mar 1989. 1, 8
- [7] M. N. Baibich, J. M. Broto, A. Fert, F. N. Van Dau, F. Petroff, P. Eitenne, G. Creuzet, A. Friederich, and J. Chazelas. Giant magnetoresistance of (001)Fe/(001)Cr magnetic superlattices. *Physical Review Letters*, 61(21):2472–2475, nov 1988. 1, 8
- [8] M. Julliere. Tunneling Between Ferromagnetic Films. *Physics Letters*, 54(3):225, 1975. 1
- [9] J. S. Moodera, L. R. Kinder, T. M. Wong, and R. Meservey. Large magnetoresistance at room temperature in ferromagnetic thin film tunnel junctions. *Physical Review Letters*, 74(16):3273–3276, apr 1995. 1
- [10] T. Miyazaki and N. Tezuka. Spin polarized tunneling in ferromagnet/insulator/ferromagnet junctions. *J. Magn. Magn. Mat.*, 151(3):403–410, 1995. 1
- [11] S. Yuasa, T. Nagahama, A. Fukushima, Y. Suzuki, and K. Ando. Giant room-temperature magnetoresistance in single-crystal Fe/MgO/Fe magnetic tunnel junctions. *Nature Materials*, 3(12):868–871, oct 2004. 1, 30
- [12] S.S.P. Parkin, C. Kaiser, A. Panchula, P. M. Rice, B. Hughes, M. Samant, and S. H. Yang. Giant tunnelling magnetoresistance at room temperature with MgO (100) tunnel barriers. *Nature Materials*, 3(12):862–867, oct 2004. 1, 30

- [13] L. Jiang, H. Naganuma, M. Oogane, and Y. Ando. Large Tunnel Magnetoresistance of 1056% at Room Temperature in MgO Based Double Barrier Magnetic Tunnel Junction (Retracted article. See vol. 4, artn no. 019201, 2011). *Applied Physics Express*, 2(8):83002, 2009. 1
- [14] J. C. Slonczewski. Current-driven excitation of magnetic multilayers. *Journal of Magnetism and Magnetic Materials*, 159(1-2):L1–L7, 1996. 1
- [15] L. Berger. Emission of spin waves by a magnetic multilayer traversed by a current. *Physical Review B - Condensed Matter and Materials Physics*, 54(13):9353–9358, oct 1996. 1
- [16] M. Tsoi, A. G.M. Jansen, J. Bass, W. C. Chiang, M. Seck, V. Tsoi, and P. Wyder. Excitation of a magnetic multilayer by an electric current. *Physical Review Letters*, 80(19):4281–4284, may 1998. 1
- [17] E. B. Myers, D. C. Ralph, J. A. Katine, R. N. Louie, and R. A. Buhrman. Current-induced switching of domains in magnetic multilayer devices. *Science*, 285(5429):867–870, 1999. 1
- [18] J. M. Daughton. Magnetoresistive memory technology. *Thin Solid Films*, 216(1):162–168, 1992. 1
- [19] W. J. Gallagher and S. S. P. Parkin. Development of the magnetic tunnel junction MRAM at IBM: From first junctions to a 16-Mb MRAM demonstrator chip. *IBM Journal of Research and Development*, 50(1):5–23, jan 2006. 1
- [20] K. Ando, S. Takahashi, K. Harii, K. Sasage, J. Ieda, S. Maekawa, and E. Saitoh. Electric manipulation of spin relaxation using the spin hall effect. *Physical Review Letters*, 101(3):36601, jul 2008. 1
- [21] I. M. Miron, G. Gaudin, S. Auffret, B. Rodmacq, A. Schuhl, S. Pizzini, J. Vogel, and P. Gambardella. Current-driven spin torque induced by the Rashba effect in a ferromagnetic metal layer. *Nature Materials*, 9(3):230–234, 2010. 1, 24, 119
- [22] T. Yoo, S. Khym, H. Lee, S. Lee, S. Lee, X. Liu, J. K. Furdyna, D. U. Lee, and E. K. Kim. Quaternary memory device fabricated from a single layer Fe film. *Journal of Applied Physics*, 111(7):07C704, 2012. 1, 2, 31, 118
- [23] N. Locatelli, V. Cros, and J. Grollier. Spin-torque building blocks. *Nature Materials*, 13(1):11–20, dec 2014. 2, 118
- [24] J. Grollier, D. Querlioz, and M. D. Stiles. Spintronic Nanodevices for Bioinspired Computing. *Proceedings of the IEEE*, 104(10):2024–2039, 2016. 2, 118

-
- [25] J. Torrejon, M. Riou, F. A. Araujo, S. Tsunegi, G. Khalsa, D. Querlioz, P. Borlototti, V. Cros, K. Yakushiji, A. Fukushima, H. Kubota, S. Yuasa, M. D. Stiles, and J. Grollier. Neuromorphic computing with nanoscale spintronic oscillators. *Nature*, 547(7664):428–431, jul 2017. 2, 118
- [26] A. Manchon, I. M. Miron, T. Jungwirth, J. Sinova, J. Zelezny, A. Thiaville, K. Garello, and P. Gambardella. Current-induced spin-orbit torques in ferromagnetic and antiferromagnetic systems. *ArXiv e-prints*, jan 2018. 2, 24, 25, 26, 27, 28, 97, 118, X
- [27] C. F. Pai, Y. Ou, L. H. Vilela-Leão, D. C. Ralph, and R. A. Buhrman. Dependence of the efficiency of spin Hall torque on the transparency of Pt/ferromagnetic layer interfaces. *Physical Review B - Condensed Matter and Materials Physics*, 92(6):64426, aug 2015. 2, 97, 119
- [28] L. Chen, M. Decker, M. Kronseder, R. Islinger, M. Gmitra, D. Schuh, D. Bougeard, J. Fabian, D. Weiss, and C. H. Back. Robust spin-orbit torque and spin-galvanic effect at the Fe/GaAs (001) interface at room temperature. *Nature Communications*, 7:13802, dec 2016. 2, 31, 119
- [29] C. Martínez Boubeta, C. Clavero, J. M. García-Martín, G. Armelles, A. Cebollada, Ll. Balcells, J. L. Menéndez, F. Peiró, A. Cornet, and Michael F. Toney. Coverage effects on the magnetism of Fe/MgO(001) ultrathin films. *Physical Review B - Condensed Matter and Materials Physics*, 71(1):14407, jan 2005. 2, 30, 55, 63
- [30] T. Yoo, S. Khym, S. Y. Yea, S. Chung, S. Lee, X. Liu, and J. K. Furdyna. Four discrete Hall resistance states in single-layer Fe film for quaternary memory devices. *Applied Physics Letters*, 95(20):202505, 2009. 2, 31
- [31] T. Yoo, S. Khym, H. Lee, S. Chung, S. Lee, X. Liu, and J. K. Furdyna. Asymmetry in the planar Hall resistance of Fe films grown on vicinal GaAs substrates. *Journal of Applied Physics*, 107(9):09C505, 2010. 2, 31
- [32] T. Yoo, S. Khym, H. Lee, S. Lee, S. Kim, J. Shin, S. Lee, X. Liu, and J. K. Furdyna. Use of the asymmetric planar hall resistance of an Fe film for possible multi-value memory device applications. *Journal of nanoscience and nanotechnology*, 11(7):5990–5994, jul 2011. 2, 31, 118
- [33] S. Blundell. *Magnetism in condensed matter*. Oxford ; New York : Oxford University Press, 2001., 2001. 4, 5, 7, 8, 21
- [34] C. M. Schneider and J. Kirschner. Chapter 9 - Magnetism at Surfaces and in Ultrathin Films. In K. Horn and M. Scheffler, editors, *Electronic Structure*, volume 2 of *Handbook of Surface Science*, pages 511–668. North-Holland, 2000. 5, 6

- [35] N. W. Ashcroft and N. D. Mermin. *Solid state physics*. Fort Worth : Harcourt College Publ., college edition, 2000. 5, 15, 16
- [36] R. Skomski. *Simple Models of Magnetism*, volume 1. 2010. 6, 7, 9, 10, 12, 13, 59, 67, I
- [37] M. Müller. *Electronic Structure of Ferromagnet-Insulator Interfaces: Fe/MgO and Co/MgO*. PhD thesis, Universität Duisburg-Essen, aug 2007. 7
- [38] J. Stöhr and H. C. Siegmann. *Magnetism: From fundamentals to nanoscale dynamics*, volume 152. Springer-Verlag Publisher, Berlin, 2006. 7, 8, 9, 10, 11, 12, 13, 14, 18, 23, 59, 73, I, III, VIII
- [39] S. Blügel. C1 Reduced Dimensions I: Magnetic Moment and Magnetic Structure. In S. Blügel, T. Brückel, and C. M. Schneider, editors, *Magnetism goes Nano - Electron Correlations, Spin Transport, Molecular Magnetism*, volume 26 of *Schriften des Forschungszentrums Jülich . Reihe Materie und Material / Matter and Material*. Forschungszentrum, Zentralbibliothek, Jülich, 2005. 8
- [40] C.A.F. Vaz, J.A.C. Bland, and G. Lauhoff. Magnetism in ultrathin film structures. *Reports on Progress in Physics*, 71(5):056501, 2008. 8
- [41] L. M. Falicov, D. T. Pierce, S. D. Bader, R. Gronsby, K. B. Hathaway, H. J. Hopster, D. N. Lambeth, S.S.P. Parkin, G. Prinz, M. Salamon, I. K. Schuller, and R. H. Victora. Surface, Interface, And Thin-Film Magnetism. *Journal of Materials Research*, 5(6):1299–1340, jun 1990. 8
- [42] J. Nogués and I. K. Schuller. Exchange bias. *J. Magn. Magn. Mater.*, 192(2):203–232, 1999. 8
- [43] P. Grünberg, R. Schreiber, Y. Pang, U. Walz, M. B. Brodsky, and H. Sowers. Layered magnetic structures: Evidence for antiferromagnetic coupling of Fe layers across Cr interlayers. *Journal of Applied Physics*, 61(8):3750–3752, nov 1987. 8
- [44] N. D. Mermin and H. Wagner. Absence of ferromagnetism or antiferromagnetism in one- or two-dimensional isotropic Heisenberg models. *Physical Review Letters*, 17(22):1133–1136, nov 1966. 9
- [45] G. Van Der Laan. Microscopic origin of magnetocrystalline anisotropy in transition metal thin films. *Journal of Physics Condensed Matter*, 10(14):3239–3253, 1998. 11, 12, 13
- [46] G. Bihlmayer. C2 : Reduced Dimensions II : Magnetic Anisotropy. In S. Bluegel, T. Brueckel, and C. M. Schneider, editors, *Magnetism Goes Nano: Electron Correlations, Spin Transport, Molecular Magnetism*, volume 26 of *Schriften des*

-
- Forschungszentrums Juelich . Reihe Materie und Material / Matter and Material*, page C2. Forschungszentrum, Zentralbibliothek, Juelich, 2005. 11
- [47] E. Mlynczak, M. Eschbach, S. Borek, J. Minár, J. Braun, I. Aguilera, G. Bihlmayer, S. Döring, M. Gehlmann, P. Gospodaric, S. Suga, L. Plucinski, S. Blügel, H. Ebert, and C. M. Schneider. Fermi surface manipulation by external magnetic field demonstrated for a prototypical ferromagnet. *Physical Review X*, 6(4):041048, 2016. 11, 17, 18, 29, 119
- [48] P. Bruno. Physical origins and theoretical models of magnetic anisotropy. In Rainer Hölzle, editor, *Magnetismus von Festkörpern und Grenzflächen: Einführung in den Magnetismus von metallischen Festkörpern und Grenzflächen. 24. IFF-Ferienkurs vom 8. bis 19. März*, number 24, chapter 24, pages 24.1–.28. Forschungszentrum, Zentralbibliothek, 1993. 11, 12, 13
- [49] P. Bruno. Tight-binding approach to the orbital magnetic moment and magnetocrystalline anisotropy of transition-metal monolayers. *Phys. Rev. B*, 39(1):865–868, jan 1989. 11
- [50] L. Néel. Anisotropie magnétique superficielle et surstructures d’orientation. *Journal de Physique et le Radium*, 15(4):225–239, 1954. 12
- [51] B. T. Jonker, K. H. Walker, E. Kisker, G. A. Prinz, and C. Carbone. Spin-polarized photoemission study of epitaxial Fe(001) films on Ag(001). *Physical Review Letters*, 57(1):142–145, jul 1986. 12
- [52] M. Stampanoni, A. Vaterlaus, M. Aeschlimann, and F. Meier. Magnetism of epitaxial bcc iron on Ag(001) observed by spin-polarized photoemission. *Physical review letters*, 59(21):2483–2485, nov 1987. 12
- [53] H. X. Yang, M. Chshiev, B. Dieny, J. H. Lee, A. Manchon, and K. H. Shin. First-principles investigation of the very large perpendicular magnetic anisotropy at Fe/MgO and Co/MgO interfaces. *Physical Review B - Condensed Matter and Materials Physics*, 84(5), 2011. 13, 60
- [54] B. Rodmacq, S. Auffret, B. Dieny, S. Monso, and P. Boyer. Crossovers from in-plane to perpendicular anisotropy in magnetic tunnel junctions as a function of the barrier degree of oxidation. *Journal of Applied Physics*, 93(10 2):7513–7515, 2003. 13
- [55] B. Heinrich, Z. Celinski, J. F. Cochran, A. S. Arrott, and K. Myrtle. Magnetic anisotropies in single and multilayered structures (invited). *Journal of Applied Physics*, 70(10):5769–5774, 1991. 13, 60
- [56] B. Heinrich and J.F. Cochran. Ultrathin metallic magnetic films: magnetic anisotropies and exchange interactions. *Advances in Physics*, 42(5):523–639, 1993. 13

- [57] M. Brockmann, S. Miethaner, R. Onderka, M. Köhler, F. Himmelhuber, H. Regensburger, F. Bensch, T. Schweinböck, and G. Bayreuther. In-plane spin reorientation transition in ultrathin epitaxial Fe(001) films. *Journal of Applied Physics*, 81(8):5047–5049, 1997. 13, 30, 68
- [58] A. Hubert and R. Schäfer. *Magnetic Domains*. Springer-Verlag Berlin Heidelberg, 1998. 13, 45, 71, 73, I
- [59] T. R. McGuire and R. I. Potter. Anisotropic Magnetoresistance in Ferromagnetic 3D Alloys. *IEEE Transactions on Magnetics*, 11(4):1018–1038, 1975. 16, 18
- [60] P. S. Bechthold. Micromagnetism - Lecture Notes of the 40th Spring School 2009 - Spintronics : From GMR to Quantum Information. In R. Waser, C. M. Schneider, M. Morgenstern, D. Bürgler, and S. Blügel, editors, *40th IFF Springschool Lecture Notes*, volume 10, page B7. Forschungszentrum, Zentralbibliothek, Juelich, 2009. 16, 18, 19
- [61] W. Thomson. On the Electro-Dynamic Qualities of Metals:—Effects of Magnetization on the Electric Conductivity of Nickel and of Iron. *Proceedings of the Royal Society of London*, 8(0):546–550, jan 1856. 18
- [62] R. P. van Gorkom, J. Caro, T. M. Klapwijk, and S. Radelaar. Temperature and angular dependence of the anisotropic magnetoresistance in epitaxial Fe films. *Physical Review B*, 63(13):134432, mar 2001. 18, 20, 30
- [63] T. T. Chen and V. A. Marsocci. Planar magnetoresistivity and planar hall effect measurements in nickel single-crystal thin films. *Physica*, 59(3):498–509, 1972. 18
- [64] K. J. Friedland, M. Bowen, J. Herfort, H. P. Schönherr, and K. H. Ploog. Intrinsic contributions to the planar Hall effect in Fe and Fe₃Si films on GaAs substrates. *Journal of Physics Condensed Matter*, 18(9):2641–2653, 2006. 18
- [65] M. Tondra, D. K. Lottis, K. T. Riggs, Y. Chen, E. D. Dahlberg, and G. A. Prinz. Thickness dependence of the anisotropic magnetoresistance in epitaxial iron films. *Journal of Applied Physics*, 73(10):6393–6395, 1993. 20, 30
- [66] C. Martinez-Boubeta, Ll. Balcells, and A. Cebollada. Enhanced and oscillatory magnetoresistance of thin Fe(001) films. *Applied Physics Letters*, 88(13):132511, 2006. 20, 30
- [67] K. M. Seemann, F. Freimuth, H. Zhang, S. Blügel, Y. Mokrousov, D. E. Bürgler, and C. M. Schneider. Origin of the planar Hall effect in nanocrystalline Co₆₀Fe₂₀B₂₀. *Physical Review Letters*, 107(8):86603, aug 2011. 21

-
- [68] A. A. Taskin, H. F. Legg, F. Yang, S. Sasaki, Y. Kanai, K. Matsumoto, A. Rosch, and Y. Ando. Planar Hall effect from the surface of topological insulators. *Nature Communications*, 8(1):1340, 2017. 21
- [69] N. A. Sinitsyn. Semiclassical theories of the anomalous Hall effect. *Journal of Physics Condensed Matter*, 20(2):23201, 2008. 21, 22
- [70] Y. Mokrousov. *Anomalous Hall Effect*, pages 177–207. Springer International Publishing, Cham, 2018. 22
- [71] N. Nagaosa, J. Sinova, S. Onoda, A. H. MacDonald, and N. P. Ong. Anomalous Hall effect. *Reviews of Modern Physics*, 82(2):1539–1592, 2010. 22
- [72] S. Nakatsuji, N. Kiyohara, and T. Higo. Large anomalous Hall effect in a non-collinear antiferromagnet at room temperature. *Nature*, 527(7577):212–215, oct 2015. 22
- [73] A. K. Nayak, J. E. Fischer, Y. Sun, B. Yan, J. Karel, A. C. Komarek, C. Shekhar, N. Kumar, W. Schnelle, J. Kübler, C. Felser, and S.S.P. Parkin. Large anomalous Hall effect driven by a nonvanishing Berry curvature in the noncolinear antiferromagnet Mn₃Ge. *Science Advances*, 2(4), 2016. 22
- [74] J. Cumings, L. S. Moore, H. T. Chou, K. C. Ku, G. Xiang, S. A. Crooker, N. Samarth, and D. Goldhaber-Gordon. Tunable anomalous Hall effect in a nonferromagnetic system. *Physical Review Letters*, 96(19):196404, 2006. 22
- [75] N. Nagaosa. Anomalous hall effect - A new perspective. *Journal of the Physical Society of Japan*, 75(4):42001, 2006. 22
- [76] I. M. Miron, T. Moore, H. Szambolics, L. D. Buda, S. Auffret, B. Rodmacq, S. Pizzini, and J. Vogel. domain domain-wall controlled by the Rashba effect. *Nature Materials*, 10(1):1–8, may 2011. 23
- [77] L. Liu, C. F. Pai, Y. Li, H. W. Tseng, D. C. Ralph, and R. A. Buhrman. Spin-torque switching with the giant spin hall effect of tantalum. *Science*, 336(6081):555–558, 2012. 23, 24
- [78] K. Garello, I. M. Miron, C. O. Avci, F. Freimuth, Y. Mokrousov, S. Blügel, S. Auffret, O. Boulle, G. Gaudin, and P. Gambardella. Symmetry and magnitude of spin-orbit torques in ferromagnetic heterostructures. *Nature Nanotechnology*, 8(8):587–593, 2013. 24
- [79] U. H. Pi, K. W. Kim, J. Y. Bae, S. C. Lee, Y. J. Cho, K. S. Kim, and S. Seo. Tilting of the spin orientation induced by Rashba effect in ferromagnetic metal layer. *Applied Physics Letters*, 97(16):162507, 2010. 24

- [80] I. M. Miron, K. Garello, G. Gaudin, P. J. Zermatten, M. V. Costache, S. Auffret, S. Bandiera, B. Rodmacq, A. Schuhl, and P. Gambardella. Perpendicular switching of a single ferromagnetic layer induced by in-plane current injection. *Nature*, 476(7359):189–193, jul 2011. 24
- [81] C. O. Avci, K. Garello, C. Nistor, S. Godey, B. Ballesteros, A. Mugarza, A. Barla, M. Valvidares, E. Pellegrin, A. Ghosh, I. M. Miron, O. Boulle, S. Auffret, G. Gaudin, and P. Gambardella. Fieldlike and antidamping spin-orbit torques in as-grown and annealed Ta/CoFeB/MgO layers. *Physical Review B - Condensed Matter and Materials Physics*, 89(21):214419, jun 2014. 24
- [82] J. Kim, J. Sinha, M. Hayashi, M. Yamanouchi, S. Fukami, T. Suzuki, S. Mitani, and H. Ohno. Layer thickness dependence of the current-induced effective field vector in Ta|CoFeB|MgO. *Nature Materials*, 12(3):240–245, dec 2013. 24
- [83] C. F. Pai, L. Liu, Y. Li, H. W. Tseng, D. C. Ralph, and R. A. Buhrman. Spin transfer torque devices utilizing the giant spin Hall effect of tungsten. *Applied Physics Letters*, 101(12):122404, 2012. 24
- [84] P. Wadley, B. Howells, J. Železný, C. Andrews, V. Hills, R. P. Campion, V. Novák, K. Olejník, F. Maccherozzi, S. S. Dhesi, S. Y. Martin, T. Wagner, J. Wunderlich, F. Freimuth, Y. Mokrousov, J. Kuneš, J. S. Chauhan, M. J. Grzybowski, A. W. Rushforth, Kw Edmond, B. L. Gallagher, and T. Jungwirth. Spintronics: Electrical switching of an antiferromagnet. *Science*, 351(6273):587–590, 2016. 24
- [85] S. Fukami, C. Zhang, S. DuttaGupta, A. Kurenkov, and H. Ohno. Magnetization switching by spin-orbit torque in an antiferromagnet-ferromagnet bilayer system. *Nature Materials*, 15:535, feb 2016. 24
- [86] J. Han, A. Richardella, S. A. Siddiqui, J. Finley, N. Samarth, and L. Liu. Room-Temperature Spin-Orbit Torque Switching Induced by a Topological Insulator. *Phys. Rev. Lett.*, 119(7):77702, aug 2017. 24
- [87] M. I. Dyakonov and V. I. Perel. Current-induced spin orientation of electrons in semiconductors. *Physics Letters A*, 35(6):459–460, 1971. 24
- [88] J. Sinova, S. O. Valenzuela, J. Wunderlich, C. H. Back, and T. Jungwirth. Spin Hall effects. *Reviews of Modern Physics*, 87(4):1213–1260, oct 2015. 24, 119
- [89] V. V. Bel’kov and S. D. Ganichev. Magneto-gyrotropic effects in semiconductor quantum wells. *Semiconductor Science and Technology*, 23(11):1–28, 2008. 25
- [90] V. M. Edelstein. Spin polarization of conduction electrons induced by electric current in two-dimensional asymmetric electron systems. *Solid State Communications*, 73(3):233–235, 1990. 25

-
- [91] A. Manchon and S. Zhang. Theory of spin torque due to spin-orbit coupling. *Physical Review B - Condensed Matter and Materials Physics*, 79(9):94422, 2009. 26
- [92] G. Bihlmayer. Relativistic effects in solids. In *Lecture Notes of 45th IFF Spring School*, pages 1–34. 45th IFF Spring School - Computing Solids: Models, ab-initio methods and supercomputing, Forschungszentrum Jülich (Germany), 10 Mar 2014 - 21 Mar 2014, 2014. 26
- [93] H. Kurebayashi, J. Sinova, D. Fang, A. C. Irvine, T. D. Skinner, J. Wunderlich, V. Novák, R. P. Campion, B. L. Gallagher, E. K. Vehstedt, L. P. Zárbo, K. Výborný, A. J. Ferguson, and T. Jungwirth. An antidamping spin-orbit torque originating from the Berry curvature. *Nature Nanotechnology*, 9(3):211–217, mar 2014. 27
- [94] X. Qiu, Z. Shi, W. Fan, S. Zhou, and H. Yang. Characterization and Manipulation of Spin Orbit Torque in Magnetic Heterostructures. *Advanced Materials*, 0(0):1705699, 2018. 28
- [95] X. Fan, J. Wu, Y. Chen, M. J. Jerry, H. Zhang, and J. Q. Xiao. Observation of the nonlocal spin-orbital effective field. *Nature Communications*, 4:1799, apr 2013. 28, 87
- [96] M. Kawaguchi, K. Shimamura, S. Fukami, F. Matsukura, H. Ohno, T. Moriyama, D. Chiba, and T. Ono. Current-induced effective fields detected by magnetotransport measurements. *Applied Physics Express*, 6(11):113002, 2013. 28, 92, 93, 94, XI
- [97] F. J. Himpsel. Fe on Au(100): Quantum-well states down to a monolayer. *Physical Review B*, 44(11):5966–5969, 1991. 29
- [98] J. E. Ortega, F. J. Himpsel, G. J. Mankey, and R. F. Willis. Quantum-well states and magnetic coupling between ferromagnets through a noble-metal layer. *Physical Review B*, 47(3):1540–1552, 1993. 29
- [99] K. Shintaku, Y. Daitoh, and T. Shinjo. Magnetoresistance effect and interlayer exchange coupling in epitaxial Fe/Au(100) and Fe/Au(111) multilayers. *Physical Review B*, 47(21):14584–14587, jun 1993. 29
- [100] J. Unguris, R. J. Celotta, and D. T. Pierce. Oscillatory exchange coupling in Fe/Au/Fe(100). *Journal of Applied Physics*, 75(10):6437–6439, 1994. 29
- [101] F. Bonell, D. D. Lam, S. Yoshida, Y. T. Takahashi, Y. Shiota, S. Miwa, T. Nakamura, and Y. Suzuki. Investigation of Au and Ag segregation on Fe(001) with soft X-ray absorption. *Surface Science*, 616:125–130, 2013. 29, 31, 37
- [102] C. Li, A. J. Freeman, and C. L. Fu. Monolayer magnetism: Electronic and magnetic properties of Fe/Au(001). *Journal of Magnetism and Magnetic Materials*, 75(3):201–208, dec 1988. 29

- [103] R. Wu and A. J. Freeman. Magnetism at metal-ceramic interfaces: effects of a Au overlayer on the magnetic properties of Fe/MgO(001). *Journal of Magnetism and Magnetic Materials*, 137(1-2):127–133, oct 1994. 29
- [104] C. Liu and S. D. Bader. Perpendicular surface magnetic anisotropy in ultrathin epitaxial Fe films. *Journal of Vacuum Science & Technology A: Vacuum, Surfaces, and Films*, 8(3):2727–2731, 1990. 29, 30
- [105] G. Y. Guo, W. M. Temmerman, and H. Ebert. First-principles determination of the magnetization direction of Fe monolayer in noble metals. *Journal of Physics: Condensed Matter*, 3(42):8205–8212, oct 1991. 29
- [106] L. Szunyogh, B. Újfalussy, and P. Weinberger. Magnetic anisotropy of iron multilayers on Au(001): First-principles calculations in terms of the fully relativistic spin-polarized screened KKR method. *Physical Review B*, 51(15):9552–9559, apr 1995. 29
- [107] S. Gallego, L. Szunyogh, M. C. Muñoz, and P. Weinberger. Influence of Au segregation on the magnetic anisotropy of Fe/Cu₃Au(0 0 1). *Journal of Magnetism and Magnetic Materials*, 272-276(SUPPL. 1):E953–E954, 2004. 29
- [108] S. D. Bader and E. R. Moog. Magnetic properties of novel epitaxial films. *J. Appl. Phys.*, 61(3729):3729, 1987. 29
- [109] C. L. Fu, A. J. Freeman, and T. Oguchi. Prediction of strongly enhanced two-dimensional ferromagnetic moments on metallic overlayers, interfaces, and superlattices. *Physical Review Letters*, 54(25):2700–2703, jun 1985. 29
- [110] C. Wang, A. Kohn, S. G. Wang, L. Y. Chang, S. Y. Choi, A. I. Kirkland, A. K. Petford-Long, and R. C.C. Ward. Structural characterization of interfaces in epitaxial Fe/MgO/Fe magnetic tunnel junctions by transmission electron microscopy. *Physical Review B - Condensed Matter and Materials Physics*, 82(2):24428, jul 2010. 29
- [111] E. Młyńczak, K. Freindl, N. Spiridis, and J. Korecki. Epitaxial MgO/Fe(001) and Fe/MgO(001): Structures of the interfaces. *Journal of Applied Physics*, 113(2):24320, 2013. 29, 34
- [112] W. H. Butler, X.-G. Zhang, T. C. Schulthess, and J. M. MacLaren. Spin-dependent tunneling conductance of Fe/MgO/Fe sandwiches. *Physical Review B*, 63(5):054416, jan 2001. 29
- [113] Y. Y. Huang, C. Liu, and G. P. Felcher. Magnetization of ultrathin bcc Fe films on MgO. *Physical Review B*, 47(1):183–189, jan 1993. 30

-
- [114] R. Reitinger, B. Sepiol, G. Vogl, B. Pfau, L. M. Stadler, S. Stankov, F. Zontone, N. Spiridis, and J. Korecki. Morphology of Fe / MgO (001) ultrathin films. *Journal of Applied Physics*, 102(3):34310, 2007. 30
- [115] O. Durand, J.R. Childress, P. Galtier, R. Bisaro, and A. Schuhl. Origin of the uniaxial magnetic anisotropy in Fe films grown by molecular beam epitaxy. *Journal of Magnetism and Magnetic Materials*, 145(1-2):111–117, 1995. 30
- [116] Y. Park, E. E. Fullerton, and S. D. Bader. Growth-induced uniaxial in-plane magnetic anisotropy for ultrathin Fe deposited on MgO(001) by oblique-incidence molecular beam epitaxy. *Applied Physics Letters*, 66(16):2140–2142, 1995. 30
- [117] J. H. Wolfe, R. K. Kawakami, W. L. Ling, Z. Q. Qiu, R. Arias, and D. L. Mills. Roughness induced in plane uniaxial anisotropy in ultrathin Fe films. *Journal of Magnetism and Magnetic Materials*, 232(1-2):36–45, 2001. 30
- [118] J. L. Costa-Krämer, J. L. Menéndez, A. Cebollada, F. Briones, D. García, and A. Hernando. Magnetization reversal asymmetry in Fe/MgO(001) thin films. *Journal of Magnetism and Magnetic Materials*, 210(1-3):341–348, feb 2000. 30
- [119] F. Cebollada, A. Hernando-Mañeru, A. Hernando, C. Martínez-Boubeta, A. Cebollada, and J. M. González. Anisotropy, hysteresis, and morphology of self-patterned epitaxial Fe/MgO/GaAs films. *Physical Review B - Condensed Matter and Materials Physics*, 66(17):1–8, nov 2002. 30
- [120] A. Koziol-Rachwał, W. Skowroński, T. Ślęzak, D. Wilgocka-Ślęzak, J. Przewoźnik, T. Stobiecki, Q. H. Qin, S. Van Dijken, and J. Korecki. Room-temperature perpendicular magnetic anisotropy of MgO/Fe/MgO ultrathin films. *Journal of Applied Physics*, 114(22), 2013. 30, 58, 60, 97, X, XI
- [121] T. Maruyama, Y. Shiota, T. Nozaki, K. Ohta, N. Toda, M. Mizuguchi, A. A. Tulapurkar, T. Shinjo, M. Shiraishi, S. Mizukami, Y. Ando, and Y. Suzuki. Large voltage-induced magnetic anisotropy change in a few atomic layers of iron. *Nature Nanotechnology*, 4(3):158–161, jan 2009. 30
- [122] K. Nakamura, T. Akiyama, T. Ito, M. Weinert, and A. J. Freeman. Role of an interfacial FeO layer in the electric-field-driven switching of magnetocrystalline anisotropy at the Fe/MgO interface. *Phys. Rev. B*, 81(22):220409, jun 2010. 30
- [123] Y. Shiota, T. Maruyama, T. Nozaki, T. Shinjo, M. Shiraishi, and Y. Suzuki. Voltage-Assisted Magnetization Switching in Ultrathin Fe 80 Co 20 Alloy Layers. *Applied Physics Express*, 2(6):63001, 2009. 30
- [124] W.-G. Wang, M. Li, S. Hageman, and C. L. Chien. Electric-field-assisted switching in magnetic tunnel junctions. *Nature Materials*, 11:64, nov 2011. 30

- [125] P. Gospodaric, E. Młyńczak, M. Eschbach, M. Gehlmann, G. Zamborlini, V. Feyer, L. Plucinski, and C. M. Schneider. Localized segregation of gold in ultrathin Fe films on Au(001). *Physical Review B*, 97(8):85409, feb 2018. 31, 32, 33, 34
- [126] C. M. Schneider and G. Schönhense. Investigating surface magnetism by means of photoexcitation electron emission microscopy. *Reports on Progress in Physics*, 65(12):1785, 2002. 31
- [127] E. Bauer. Low energy electron microscopy. *Reports on Progress in Physics*, 57:895–938, 1994. 31
- [128] E. Bauer. Leem Basics. *Reviews Surface Review and Letters*, 5(6):1275–1286, 1998. 31
- [129] Th. Schmidt, S. Heun, J. Slezak, J. Diaz, K. C. Prince, G. Lilienkamp, and E. Bauer. SPELEEM: Combining LEEM and spectroscopic imaging. *Surface Review and Letters*, 05(6):1287–1296, 1998. 31
- [130] N. Spiridis and J. Korecki. Influence of Au reconstruction on growth of Fe on Au(100). *Applied Surface Science*, 141(3-4):313–318, 1999. 32
- [131] R. Hammer, A. Sander, S. Förster, M. Kiel, K. Meinel, and W. Widdra. Surface reconstruction of Au(001): High-resolution real-space and reciprocal-space inspection. *Physical Review B - Condensed Matter and Materials Physics*, 90(3):35446, 2014. 32
- [132] R. Opitz, S. Löbus, A. Thissen, and R. Courths. An angle-scanned photoelectron diffraction (XPD) study of the growth and structure of ultrathin Fe films on Au(001). *Surface Science*, 370(2-3):293–310, jan 1997. 32, 37, 55
- [133] A. M. Begley, S. K. Kim, J. Quinn, F. Jona, H. Over, and P. M. Marcus. Growth of ultrathin films of Fe on Au(001). *Physical Review B*, 48(3):1779–1785, 1993. 32, 36
- [134] V. Blum, Ch. Rath, S. Müller, L. Hammer, K. Heinz, J. M. García, J. E. Ortega, J. E. Prieto, O. S. Hernán, J. M. Gallego, A. L. de Parga, and R. Miranda. Fe thin-film growth on Au(100): A self-surfactant effect and its limitations. *Phys. Rev. B*, 59(24):15966–15974, jun 1999. 32
- [135] O. S. Hernán, J. M. Gallego, A. L. Vázquez De Parga, and R. Miranda. Initial growth of Fe on Au(100): Preferential nucleation, place exchange and enhanced mass transport. *Applied Physics A: Materials Science and Processing*, 66(SUPPL. 1):1117–1120, 1998. 32, 55
- [136] M. Eschbach. *Band Structure Engineering in 3D Topological Insulators Investigated by Angle-Resolved Photoemission Spectroscopy Erklärung*. Dr., Duisburg, Juelich, 2015. 34

-
- [137] F. Jona, J. A. Strozier, and W. S. Yang. Low-energy electron diffraction for surface structure analysis. *Reports on Progress in Physics*, 45(5):527–585, 1982. 36
- [138] O. Madelung, U. Rössler, and M. Schulz, editors. *Magnesium oxide (MgO) crystal structure, lattice parameters, thermal expansion*, pages 1–6. Springer Berlin Heidelberg, Berlin, Heidelberg, 1999. 36
- [139] G. A. Prinz and J. J. Krebs. Molecular beam epitaxial growth of single-crystal Fe films on GaAs. *Applied Physics Letters*, 39(5):397–399, 1981. 36
- [140] L. Z. Mezey and J. Giber. The Surface Free Energies of Solid Chemical Elements: Calculation from Internal Free Enthalpies of Atomization. *Japanese Journal of Applied Physics*, 21(11R):1569, 1982. 37
- [141] S. H. Overbury, P. A. Bertrand, and G. A. Somorjai. The Surface Composition of Binary Systems. Prediction of Surface Phase Diagrams of Solid Solutions. *Chemical Reviews*, 75(5):547–560, 1975. 37
- [142] Y. L. He and G. C. Wang. Observation of atomic place exchange in submonolayer heteroepitaxial Fe/Au(001) films. *Physical Review Letters*, 71(23):3834–3837, dec 1993. 37, 55
- [143] S. Hüfner. *Photoelectron Spectroscopy*. Springer Verlag, Berlin, 2003. 38
- [144] P. S. Miedema and F. M. F. de Groot. The iron L edges: Fe 2p X-ray absorption and electron energy loss spectroscopy. *Journal of Electron Spectroscopy and Related Phenomena*, 187:32–48, 2013. 38
- [145] M. Faraday. Experimental Researches in Electricity. Nineteenth Series. *Philosophical Transactions of the Royal Society of London*, 136(0):1–20, 1846. 43
- [146] J. Kerr LL.D. XLIII. On rotation of the plane of polarization by reflection from the pole of a magnet. *The London, Edinburgh, and Dublin Philosophical Magazine and Journal of Science*, 3(19):321–343, 1877. 43
- [147] H. R. Hulme. The Faraday Effect in Ferromagnetics. *Proceedings of the Royal Society A: Mathematical, Physical and Engineering Sciences*, 135(826):237–257, 1932. 43
- [148] H. Ebert. Magneto-optical effects in transition metal systems. *Reports on Progress in Physics*, 59(12):1665, 1996. 43, 44
- [149] P. Bruno, Y. Suzuki, and C. Chappert. Magneto-optical Kerr effect in a paramagnetic overlayer on a ferromagnetic substrate: A spin-polarized quantum size effect. *Physical Review B - Condensed Matter and Materials Physics*, 53(14):9214–9220, apr 1996. 44

- [150] C. M Schneider. Imaging magnetization dynamics. In *Magnetism Goes Nano: Electron Correlations, Spin Transport, Molecular Magnetism*, volume 26, page D5, 2005. 45
- [151] I. V. Soldatov and R. Schäfer. Selective sensitivity in Kerr microscopy. *Review of Scientific Instruments*, 88(7):73701, 2017. 46, 47
- [152] I. V. Soldatov. *Thermoelectric effects and anisotropy in magnetic films*. PhD thesis, Technische Universität Dresden, 2016. 47, 65
- [153] A. Koziol-Rachwał, T. Nozaki, V. Zayets, H. Kubota, A. Fukushima, S. Yuasa, and Y. Suzuki. The effect of the MgO buffer layer thickness on magnetic anisotropy in MgO/Fe/Cr/MgO buffer/MgO(001). *Journal of Applied Physics*, 120(8):85303, 2016. 58, 60, 67, 68
- [154] D. Wilgocka-Ślezak, K. Freindl, A. Koziol, K. Matlak, M. Rams, N. Spiridis, M. Ślezak, T. Ślezak, M. Zajac, and J. Korecki. Thickness-driven polar spin re-orientation transition in ultrathin Fe/Au(001) films. *Physical Review B - Condensed Matter and Materials Physics*, 81(6), 2010. 58, 60
- [155] P. J. Jensen and K. H. Bennemann. Magnetic structure of films: Dependence on anisotropy and atomic morphology. *Surface Science Reports*, 61(3):129–199, 2006. 58, 60
- [156] M. Klaua, D. Ullmann, J. Barthel, W. Wulfhekel, J. Kirschner, R. Urban, T. L. Monchesky, A. Enders, J. F. Cochran, and B. Heinrich. Growth, structure, electronic, and magnetic properties of MgO/Fe(001) bilayers and Fe/MgO/Fe(001) trilayers. *Physical Review B*, 64(13):134411, 2001. 60
- [157] C.-H. Lambert, A. Rajanikanth, T. Hauet, S. Mangin, E. E. Fullerton, and S. Andrieu. Quantifying perpendicular magnetic anisotropy at the Fe-MgO(001) interface. *Applied Physics Letters*, 102(12):122410, 2013. 60
- [158] C. M. Gürtler, Y. B. Xu, and J. A.C. Bland. In situ study of the temperature-dependent magnetoresistance of ultrathin epitaxial Fe films on GaAs(100). *Journal of Magnetism and Magnetic Materials*, 226-230(PART I):655–657, 2001. 63, 68
- [159] S. Krzyk, A. Schmidfeld, M. Kläui, and R. Ulrich. Magnetotransport effects of ultrathin Ni 80 Fe 20 films probed in-situ. *New Journal of Physics*, 12(2):1–8, 2010. 63, 68
- [160] B. Hu, W. He, J. Ye, J. Tang, Y.-S. Zhang, S. S. Ahmad, X.-Q. Zhang, and Z.-H. Cheng. Determination of magnetic anisotropy constants and domain wall pinning energy of Fe/MgO(001) ultrathin film by anisotropic magnetoresistance. *Scientific Reports*, 5:14114, sep 2015. 65, 68

-
- [161] J. B. Staunton, L. Szunyogh, A. Buruzs, B. L. Gyorffy, S. Ostanin, and L. Udvardi. Temperature dependence of magnetic anisotropy: An ab initio approach. *Physical Review B - Condensed Matter and Materials Physics*, 74(14):144411, oct 2006. 67
- [162] S. Mallik, N. Chowdhury, and S. Bedanta. Interplay of uniaxial and cubic anisotropy in epitaxial Fe thin films on MgO (001) substrate. *AIP Advances*, 4(9):0–6, 2014. 68
- [163] S. M. Jordan, J. F. Lawler, R. Schad, and H. Van Kempen. Growth temperature dependence of the magnetic and structural properties of epitaxial Fe layers on MgO(001). *Journal of Applied Physics*, 84(3):1499–1503, 1998. 68
- [164] S. Parkin and S. H. Yang. Memory on the racetrack. *Nature Nanotechnology*, 10(3):195–198, mar 2015. 74, 79, 117
- [165] E. K. De Vries, A. M. Kamerbeek, N. Koirala, M. Brahlek, M. Salehi, S. Oh, B. J. Van Wees, and T. Banerjee. Towards the understanding of the origin of charge-current-induced spin voltage signals in the topological insulator Bi₂Se₃. *Physical Review B - Condensed Matter and Materials Physics*, 92(20):201102, nov 2015. 77, 102, 104
- [166] A. Van Den Brink, G. Vermijs, A. Solignac, J. Koo, J. T. Kohlhepp, H. J.M. Swagten, and B. Koopmans. Field-free magnetization reversal by spin-Hall effect and exchange bias. *Nature Communications*, 7:10854, mar 2016. 77, 102, 104
- [167] L. Neumann and M. Meinert. Influence of the Hall-bar geometry on harmonic Hall voltage measurements of spin-orbit torques. *AIP Advances*, 8(9):95320, 2018. 77, 78, 102, 104, 112, 114, 116
- [168] L. Liu, T. Moriyama, D. C. Ralph, and R. A. Buhrman. Spin-Torque Ferromagnetic Resonance Induced by the Spin Hall Effect. *Phys. Rev. Lett.*, 106(3):36601, jan 2011. 87
- [169] M. Jamali, Z. Zhao, M. DC, D. Zhang, H. Li, A. K. Smith, and J.-P. Wang. Planar Hall effect based characterization of spin orbital torques in Ta/CoFeB/MgO structures. *Journal of Applied Physics*, 119(13):133902, 2016. 92, 94, 96, XI
- [170] X. Qiu, P. Deorani, K. Narayanapillai, K.-S. Lee, J. Lee, H.-W. Lee, and H. Yang. Angular and temperature dependence of current induced spin-orbit effective fields in Ta/CoFeB/MgO nanowires. *Scientific Reports*, 4:1–13, 2014. 97
- [171] J. Kim, J. Sinha, S. Mitani, M. Hayashi, S. Takahashi, S. Maekawa, M. Yamanouchi, and H. Ohno. Anomalous temperature dependence of current-induced torques in CoFeB/MgO heterostructures with Ta-based underlayers. *Physical Review B - Condensed Matter and Materials Physics*, 89(17):174424, 2014. 97

- [172] M. Isasa, E. Villamor, L. E. Hueso, M. Gradhand, and F. Casanova. Temperature dependence of spin diffusion length and spin Hall angle in Au and Pt. *Physical Review B - Condensed Matter and Materials Physics*, 91(2):24402, jan 2015. 97, 117, 119
- [173] G.-Y. Guo, S. Maekawa, and N. Nagaosa. Enhanced Spin Hall Effect by Resonant Skew Scattering in the Orbital-Dependent Kondo Effect. *Phys. Rev. Lett.*, 102(3):36401, jan 2009. 119
- [174] G.-Y. Guo, S. Murakami, T.-W. Chen, and N. Nagaosa. Intrinsic Spin Hall Effect in Platinum: First-Principles Calculations. *Phys. Rev. Lett.*, 100(9):96401, 2008. 119
- [175] W. Zhang, W. Han, X. Jiang, S.-H. Yang, and S. S. P. Parkin. Role of transparency of platinum-ferromagnet interfaces in determining the intrinsic magnitude of the spin Hall effect. *Nature Physics*, 11:496, apr 2015. 119
- [176] P. M. Haney, H. W. Lee, K. J. Lee, A. Manchon, and M. D. Stiles. Current-induced torques and interfacial spin-orbit coupling. *Physical Review B - Condensed Matter and Materials Physics*, 88(21):214417, 2013. 119
- [177] M. Gmitra, A. Matos-Abiague, C. Draxl, and J. Fabian. Magnetic control of spin-orbit fields: A first-principles study of Fe/GaAs. *Physical Review Letters*, 111(3):36603, jul 2013. 119
- [178] P. Moras, G. Bihlmayer, P. M. Sheverdyaeva, S. K. Mahatha, M. Papagno, J. Sánchez-Barriga, O. Rader, L. Novinec, S. Gardonio, and C. Carbone. Magnetization-dependent Rashba splitting of quantum well states at the Co/W interface. *Physical Review B - Condensed Matter and Materials Physics*, 91(19):195410, may 2015. 119
- [179] C. Carbone, P. Moras, P. M. Sheverdyaeva, D. Pacilé, M. Papagno, L. Ferrari, D. Topwal, E. Vescovo, G. Bihlmayer, F. Freimuth, Y. Mokrousov, and S. Blügel. Asymmetric band gaps in a Rashba film system. *Physical Review B*, 93(12):125409, mar 2016. 119

List of Abbreviations

AHE	anomalous Hall effect	MOKE	magneto-optical Kerr effect
AMR	anisotropic magneto-resistance	MRAM	magnetoresistive random-access memory
ARPES	angle-resolved photoemission spectroscopy	MTJ	magnetic tunnel junction
BCC	body-centered cubic	NM	non-magnetic metal
CMOS	complementary metal-oxide-semiconductor	PEEM	photoemission electron microscopy
DC	direct current	PHE	planar Hall effect
DL	damping-like	PMA	perpendicular magnetic anisotropy
DOS	density of states	PGI	Peter Grünberg Institut
FCC	face-centered cubic	ROI	region of interest
FL	field-like	SHA	spin Hall angle
FM	ferromagnetic metal	SHE	spin Hall effect
GMR	giant magneto-resistance	SOC	spin-orbit coupling
HDD	hard disk drive	SOI	spin-orbit interaction
HM	heavy metal	SOT	spin-orbit torque
iSGE	inverse spin galvanic effect	SRT	spin reorientation transition
LED	light-emitting diode	STT	spin-transfer torque
LEED	low energy electron diffraction	TMR	tunneling magneto-resistance
LEEM	low energy electron microscopy	UHV	ultra high vacuum
MBE	molecular beam epitaxy	XAS	X-ray absorption spectroscopy
MCA	magneto-crystalline anisotropy	XPS	X-ray photoemission spectroscopy
ML	monolayer	XRR	X-ray reflectometry
MEA	magneto-elastic anisotropy		

Publications and Conference Contributions

Articles

- A1** “Realization of a vertical topological p-n junction in epitaxial $\text{Sb}_2\text{Te}_3/\text{Bi}_2\text{Te}_3$ heterostructures”
M. Eschbach, E. Młyńczak, J. Kellner, Jörn Kampmeier, M. Lanius, E. Neumann, C. Weyrich, M. Gehlmann, **P. Gospodarič**, S. Döring, G. Mussler, N. Demarina, M. Luysberg, G. Bihlmayer, T. Schäpers, L. Plucinski, S. Blügel, M. Morgenstern, C. M. Schneider, & D. Grützmacher
Nature Communications **6**, 8816 (2015)
- A2** “Quasi 2D electronic states with high spin-polarization in centrosymmetric MoS_2 bulk crystals”
M. Gehlmann, I. Aguilera, G. Bihlmayer, E. Młyńczak, M. Eschbach, S. Döring, **P. Gospodarič**, S. Cramm, B. Kardynał, L. Plucinski, S. Blügel, & C. M. Schneider
Scientific Reports **6**, 26197 (2016)
- A3** “Fermi surface manipulation by external magnetic field demonstrated for a prototypical ferromagnet”
E. Młyńczak, M. Eschbach, S. Borek, J. Minár, J. Braun, I. Aguilera, G. Bihlmayer, S. Döring, M. Gehlmann, **P. Gospodarič**, S. Suga, L. Plucinski, S. Blügel, H. Ebert, & C. M. Schneider
Physical Review X **6**, 041048 (2016)
- A4** “ Bi_1Te_1 : a dual topological insulator”
M. Eschbach, M. Lanius, C. Niu, E. Młyńczak, **P. Gospodarič**, J. Kellner, P. Schüffelgen, M. Gehlmann, Sven Döring, E. Neumann, M. Luysberg, G. Mussler, L. Plucinski, M. Morgenstern, D. Grützmacher, G. Bihlmayer, S. Blügel, & C. M. Schneider
Nature Communications **8**, 14976 (2017)

- A5** “Direct observation of the band gap transition in atomically thin ReS₂”
M. Gehlmann, I. Aguilera, G. Bihlmayer, S. Nemsák, P. Nagler, **P. Gospodarič**, G. Zamborlini, M. Eschbach, V. Feyer, F. Kronast, E. Młyńczak, T. Korn, L. Plucinski, C. Schüller, S. Blügel, & C. M. Schneider
Nano Letters **17**, 5187-5192 (2017)
- A6** “Localized segregation of gold in ultra-thin Fe films on Au(001)”
P. Gospodarič, E. Młyńczak, M. Eschbach, M. Gehlmann, G. Zamborlini, V. Feyer, L. Plucinski, & C. M. Schneider
Physical Review B **97**, 085409 (2018)
- A7** “Does Exchange Splitting persist above T_C? A spin-resolved photoemission study of EuO”
T. Heider, T. Gerber, M. Eschbach, E. Młyńczak, P. Lömker, **P. Gospodarič**, M. Gehlmann, M. Plötzing, O. Köksal, R. Pentcheva, L. Plucinski, C. M. Schneider, & M. Müller
arXiv:1809.00631 [cond-mat.mtrl-sci] (2018)
- A8** “Kink far below the Fermi level reveals new electron-magnon scattering channel in Fe”
E. Młyńczak, M.C.T.D. Müller, **P. Gospodarič**, T. Heider, I. Aguilera, M. Gehlmann, M. Jugovac, G. Zamborlini, C. Tusche, S. Suga, V. Feyer, L. Plucinski, C. Friedrich, S. Blügel, & C. M. Schneider
Nature Communications **10**, 505 (2019)

Conference contributions

- Talk** “Calibration of highly efficient FeO-based spin polarization detector”
P. Gospodarič, E. Młyńczak, M. Eschbach, M. Gehlmann, S. Döring, L. Plucinski, & C. M. Schneider
DPG Spring Meeting, Regensburg, Germany (2016)
- Talk** “Spin-ARPES with FeO-based spin detector”
P. Gospodarič, E. Młyńczak, M. Eschbach, M. Gehlmann, S. Döring, L. Plucinski, & C. M. Schneider
VITI PhD School, Lueven, Belgium (2016)
- Talk** “Spin orbit torque in Au/Fe/MgO (001) heterostructures measured in Hall geometry”
P. Gospodarič, E. Młyńczak, D. E. Bürgler, F. Volmer, B. Beschoten, L. Plucinski, & C. M. Schneider
DPG Spring Meeting, Dresden, Germany (2017)
- Talk** “Current-induced remagnetization in epitaxial Au/Fe/MgO(001) heterostructures”
P. Gospodarič, E. Młyńczak, L. Plucinski, Y. Mokrousov, & C. M. Schneider
DPG Spring Meeting, Berlin, Germany (2018)
- Poster** “Spin-orbit coupling effects in ferromagnetic epitaxial nanostructures studied by spin-ARPES”
P. Gospodarič, E. Młyńczak, M. Eschbach, M. Gehlmann, L. Plucinski, & C. M. Schneider
IEEE Summer School, Sendai, Japan (2016)
- Poster** “Growth of Fe on Au(001) studied with spatial resolution on the sub-micrometer scale”
P. Gospodarič, E. Młyńczak, M. Eschbach, M. Gehlmann, G. Zamborlini, V. Feyer, L. Plucinski, & C. M. Schneider
LEEM PEEM 10 workshop, Monterey, USA (2016)

- Poster** “Spin-resolved ARPES with FeO-based polarimeter”
P. Gospodarič, T. Heider, E. Młyńczak, L. Plucinski, & C. M. Schneider
ToCoTronics 2018, Würzburg, Germany (2018)
- Poster** “Characterization of field- and current-induced magnetization switching in epitaxial Au/Fe/MgO(001)”
P. Gospodarič, E. Młyńczak, A. Kakay, I. Soldatov, D.E. Bürgler, R. Schäfer, L. Plucinski, J. Fassbender & C. M. Schneider
JEMS Conference 2018, Mainz, Germany (2018)

Der Lebenslauf ist in der Online-Version aus Gründen des Datenschutzes nicht enthalten.

Acknowledgements

I would like to express my sincere thanks to all the people who helped me, in one way or another, to accomplish this work. Firstly, I owe my gratitude to **prof. Dr. Claus M. Schneider** for giving me the chance to join PGI-6 institute, which gave me the opportunity to work with an international team of experienced scientists and in several well-equipped laboratories. It has been inspiring to work under your supervision.

The unique atmosphere in the group of **Dr. Lukasz Plucinski** will be lasting in my memories. I am very grateful for the mentorship which I have received throughout my PhD work from Dr. Lukasz Plucinski and from **Dr. Ewa Mlynczak**. Ewa, I am most thankful for giving me the opportunity to work on the EpiSpin project and I want to thank you for your constant support with discussions and suggestions and for your devoted guidance. It has been a pleasure to share the office with you. Lukasz, thank you for the countless discussions, explanations and all your encouragements and also for your honest expressions of opinion, which were at times much needed.

I would like to thank all PhD students, who have been a part of the group during my PhD time. **Dr. Markus Eschbach**, you have thought me countless lessons about working in the ARPES-laboratory and motivated me for my further work. I enjoyed our climbing around the ARPES chamber together. I would like to thank **Dr. Mathias Gehlmann** for all the fruitful discussions, valuable beamtime hours and his help with \LaTeX . To **Tristan Heider** I want to thank for his patient and careful way of work in the laboratory and the honest and friendly conversations. Together with **Bharti Parashar** and **Yinshang Liu**, they collegially supported me during writing of this thesis.

The samples were produced by **Thomas Jansen** who I thank for his precise work and support in the magneto-transport laboratory.

I thank **Dr. Daniel Bürgler** for many educative and helpful discussions.

Special thanks goes to **Dr. Attila Kakay** for his support and for organizing the collaboration with IFW Dresden, where **Dr. Ivan Soldatov** and **Prof. Dr. Rudolf Schäfer** assisted with their valuable knowledge and experience.

I am grateful to **Dr. Vitaliy Feyer**, **Giovanni Zamborlini**, **Matteo Jugovac**, **Dr. Slavomir Nemsak** and **Johanna Hackl** for their assistance during beamtimes.

Rene Borowski allowed me to work in the clean room of PGI-7 and offered help when needed.

I would like to thank all the members of the PGI-6 institute whom I have had the pleasure to meet during my time there for creating a friendly working environment. I thank **Bernd Küpper**, **Arnd Bremen**, **Heinz Pfeiffer** and **Norbert Schnitzler** for their technical support. I would like to acknowledge **Dr. Christian Tusche** for sharing his knowledge on laser- and spin-ARPES.

I am grateful to **Prof. Dr. Shigemasa Suga** for the inspirational discussions and

for teaching me to play ping-pong. To **Dr. Roman Adam** I thank for all the running rounds around the campus, which kept me and my mind fit.

I am endlessly thankful to my beloved **Dr. Christoph Schmitz**. This work would not be possible without your constant support on both, personal and scientific levels. Thank you for all the encouragements, your enthusiasm and for your endless love and care in the good times and also in the most difficult moments.

I am grateful to **Dr. Georg Schmitz** for reading the thesis.

Last but not least, I thank my friends and family. I am forever thankful to my mother **Tatjana Pirc** for her unconditional love and support and my brother **Jan Gospodarič** for his positive and energetic spirit. They both, even though from abroad, made me always feel loved. My dear friends **Neža** and **Lara, Anja, Mojca** and **Dina** keep my spirits up all the way from Slovenia and I thank my dear **Saba** for conquering the world with me.